Universidade de Lisboa

Faculdade de Ciências

Departamento de Engenharia Geográfica, Geofísica e Energia

Clouds and Convection in the Tropics and Subtropics: Models, Observations, and Parameterizations

Sambingo da Silva Cardoso

Doutoramento em Ciências Geofísicas e da Geoinformação
(Meteorologia)

2013

Universidade de Lisboa

Faculdade de Ciências

Departamento de Engenharia Geográfica, Geofísica e Energia

Clouds and Convection in the Tropics and Subtropics: Models, Observations, and Parameterizations

Sambingo da Silva Cardoso

Tese orientada pelo Prof. Doutor Pedro Manuel Alberto de Miranda e pelo Doutor Andrew Gettelman, especialmente elaborada para a obtenção do grau de doutor em Ciências Geofísicas e da Geoinformação (Meteorologia)

2013

to José, Ana, Lemba, and Sylvain

“Everything that is really great and inspiring is created by the individual who can labor in freedom.”

Albert Einstein

Preamble

This thesis is the result of work done by Sambingo da Silva Cardoso during his doctoral studies in Meteorology at the University of Lisbon (UL, Portugal). The investigation, performed in the framework of the GPCI (Global energy and water cycle experiment cloud system study / working group on numerical experimentation Pacific Cross-section Intercomparison) project, was carried out both in Portugal and in the United States of America (U.S.A.), respectively, at the Center of Geophysics of the University of Lisbon (CGUL), and at the National Center for Atmospheric Research (NCAR). The work was supervised by Professor Pedro Miranda (UL), and by Doctor Phil Rasch (NCAR, now at Pacific Northwest National Laboratory [PNNL, U.S.A.]), later substituted by Doctor Andrew Gettelman (NCAR). Short-term visits to the Joint Institute for Regional Earth System Science and Engineering (JIFRESSE, University of California, U.S.A.), and to the Jet Propulsion Laboratory (JPL, U.S.A.) were hosted by Doctor João Teixeira (JPL), GPCI project coordinator. GPCI was funded by the National Aeronautics and Space Administration (NASA, U.S.A.) grant X06AB74G. CGUL is funded by the Portuguese Science and Technology Foundation (FCT, Portugal). NCAR is supported by the National Science Foundation (NSF, U.S.A.). The work presented here was supported from February 2008 to February 2012 by a Doctoral Grant from FCT (SFRH/BD/37214/2007).

Scientific Articles Published in Refereed Journals

Teixeira, J., S. Cardoso, M. Bonazzola, J. Cole, A. DelGenio, C. DeMott, C. Franklin, C. Hannay, C. Jakob, Y. Jiao, J. Karlsson, H. Kitagawa, M. Köhler, A. Kuwano-Yoshida, C. LeDrian, J. Li, A. Lock, M. J. Miller, P. Marquet, J. Martins, C. R. Mechoso, E. van Meijgaard, I. Meinke, P. M. A. Miranda, D. Mironov, R. Neggers, H. L. Pan, D. A. Randall, P. J. Rasch, B. Rockel, W. B. Rossow, B. Ritter, A. P. Siebesma, P. M. M. Soares, F. J. Turk, P. A. Vaillancourt, A. Von Engeln, and M. Zhao, 2011: *Tropical and Subtropical Cloud Transitions in Weather and Climate Prediction Models: The GCSS/WGNE Pacific Cross-Section Intercomparison (GPCI)*. J. Climate, **24**, 5223–5256.

Karlsson, J., G. Svensson, S. Cardoso, J. Teixeira, and S. Paradise, 2010: *Subtropical cloud regime transitions: Boundary layer depth and cloud-top height evolution*. J. Appl. Meteor. Climatol., **49**, 1845–1858.

Other Publications

Cardoso, S., J. Teixeira, 2009: *Preliminary results from the GPCI project*. Available **online** at:
http://gcss-dime.giss.nasa.gov/gpci/modsim_gpci.html
http://gcss-dime.giss.nasa.gov/gpci/modsim_gpci_models.html
http://gcss-dime.giss.nasa.gov/gpci/GPCI-results-to-GCSS_DIME_CMAI-012008.pdf

Teixeira, J., S. Cardoso, A. P. Siebesma, and the GPCI Team, 2008: *Results from the First 2 Years of the GCSS Pacific Cross Section Intercomparison*. GEWEX News, No. **18(4)**, International GEWEX Project Office, Silver Spring, MD, 1–4.

Acknowledgements

During my long doctoral journey I had the honor of meeting and interacting with a large number of people to whom I am grateful. There is not enough space here to list all of them and the ways they have helped me. From the administrative personnel at the various institutions I visited (most notably, Christina Book, at NCAR in Boulder [U.S.A.], a friend for life!), to the graduate and undergraduate students I met at some of those research centers, not forgetting the roommates and landladies I had during my stays abroad (especially, 91 years young Louise Adams, a dear friend!), or even the, always amicable, NCAR shuttle drivers, I truly believe that every single person I met during this, not always easy, journey deserves my profound appreciation.

To Professor Pedro Miranda, from the University of Lisbon (UL), I am indebted for the continued support and guidance (muito obrigado Professor!). Doctor João Teixeira, the coordinator of the GPCI project, has been crucial in helping to define the context for my doctoral work. I here acknowledge all the support and research opportunities he offered me (muito obrigado João!). Doctor Pedro Soares from the Center of Geophysics of the University of Lisbon has always been available, and provided significant guidance at important stages of my work. Doctor Pedro Viterbo, from then Portuguese Meteorological Institute, offered helpful comments on work developed during the first doctoral year. It was with great pleasure that I worked under the supervision of both Doctor Phil Rasch, and Doctor Andrew Gettelman, while at NCAR. Their friendly and informal ways gave me with much needed confidence in my research work. I additionally thank Professor José Teixeira da Silva (UL), and Professor Fernando Santos (UL), for providing me with letters of recommendation.

Many thanks go to all the GPCI collaborators, whose model simulations and observational data are the raw material for my doctoral investigation. I am especially appreciative of the interaction with Doctors Cecile Hannay and Jennifer Kay, from NCAR, Doctor Roel Neggers from the Royal Netherlands Meteorological Institute (KNMI), Doctor Johannes Karlsson from the Department of Meteorology of the Stockholm University (MISU), and Doctor Yuying Zhang from the Lawrence Livermore National Laboratory (LLNL, U.S.A.).

A few unstructured one-on-one meetings were very insightful and provided me with interesting ideas and suggestions, namely, the meetings in Boulder with Doctor George Kiladis, at the National Oceanic and Atmospheric Administration (U.S.A.), and with Doctor Gunilla Svensson (MISU), at NCAR; the meetings in Pasadena, at the Jet Propulsion Laboratory

(U.S.A.), with Doctors Edward Olsen, Eric Fetzer, and Brian Kahn; and a more recent meeting at NCAR with Doctor Peter Caldwell (LLNL / Program For Climate Model Diagnosis and Intercomparison [PCMDI], U.S.A.).

Finally, to my parents and sister, an infinite thank you for all the support and love, and, last but not least, to Doctor Sylvain Dupont: thank you for always being there (merci Vain!).

Abstract

The GPCI (GCSS / working group on numerical experimentation Pacific Cross-section Intercomparison) project offers a new approach for the intercomparison of models, by focusing the analysis on a single cross section in the NE Pacific ocean. It is targeted at the stratocumulus, shallow cumulus, and deep convection regimes, as well as the respective transitions. Three-hourly satellite observations and model simulations were prepared for GPCI for the JJA season. The seasonal mean results for variables such as total cloud cover, liquid water path, and outgoing longwave radiation show high scatter among models. Mean vertical velocity, and relative humidity, suggest good, overall, representation of the Hadley circulation. Still, differences exist between models (e.g., in the intensity of the deep convection, or humidity content in the boundary layer). The main cloud types are represented differently (e.g., too low stratocumulus clouds). The transitions between stratocumulus and shallow cumulus show two distinct behaviours (smooth versus abrupt with bimodal nature) reflecting distinct cloud parameterization approaches. None of them reproduces well the observations. Following GEPAT (Grade-based Empirical Pattern Analysis Technique), different cloud patterns were analyzed in terms of the means of associated parameters. Model relative humidity has negative biases in the boundary layer and subtropical mid troposphere. sBLT (sequential Boundary-Layer-Top determination scheme) offered a more thorough characterization of the boundary layer (top). Mean BLT height and strength show big spread among models. Models disagree in the time of the diurnal maxima of relative humidity, cloud fraction, and liquid water content. Precipitation lacks in diurnal amplitude in the deep convection area. The “Scinertia” concept was introduced, based on the analysis of diurnal cycle results for cloud cover and low tropospheric stability. GPCI proved useful for the work presented below, both in the characterization of model shortcomings, and in helping envision avenues for future investigation using models and observations.

Keywords: *GPCI, cloud regimes, GEPAT, boundary layer, sBLT, humidity structure, Scinertia*

Resumo

Apesar dos consideráveis avanços dos últimos 20 anos ao nível da parametrização de nuvens, a representação de nuvens ainda é um desfio para as comunidades de modelação do tempo e do clima. A urgência do desenvolvimento de parametrizações de nuvens para modelos de circulação geral (GCM) é reforçada pelo facto de a quantidade de nuvens gerada pelos modelos ter um impacto significativo no comportamento do sistema climático previsto pelos modelos. Em particular, os atuais modelos de clima tendem a responder de forma diferente em experiências de sensibilidade das mudanças climáticas. Deficiências nas parametrizações resultam igualmente numa representação inconsistente do ciclo hidrológico ao nível termodinâmico, o que acarreta importantes consequências para a simulação da circulação atmosférica tropical e subtropical. Estes tópicos são investigados por diferentes grupos do GCSS (Global energy and water cycle experiment Cloud System Study), cuja estratégia tem sido bem sucedida na definição e compreensão de regimes de nuvens fundamentais, e no desenvolvimento e melhoramento de parametrizações de nuvens. No entanto, o uso exclusivo de versões unidimensionais dos modelos atmosféricos, tradicionalmente feito no GCSS, não permite uma compreensão profunda do papel fundamental das nuvens no clima, o que implica que as parametrizações têm de ser testadas nas versões completas (tridimensionais) dos GCMs. Essa é uma tarefa que pode ter que envolver a análise de enormes quantidades de dados de simulações numéricas.

Neste contexto, o projeto GPCI (GCSS / working group on numerical experimentation Pacific Cross-section Intercomparison) oferece uma nova (e menos pesada) abordagem para a intercomparação de GCMs, focando a análise num número reduzido de localizações ao longo de uma secção, e permitindo uma integração de dados de modelos e de observações relativamente simples. GPCI tem estado centrado nos (sub)trópicos do sector NE do oceano Pacífico, e desenvolveu um programa especificamente dedicado à investigação de regimes de nuvens fundamentais que tipicamente ocorrem nas fronteiras orientais dos oceanos (sub)tropicais, nomeadamente, estratocúmulos, cúmulos pouco profundos, torres de convecção profunda, e as transições entre eles. O conhecimento ganho a partir de uma análise detalhada do comportamento destes sistemas de nuvens e dos ambientes dinâmicos e termodinâmicos a eles associados, recorrendo a dados de alta resolução temporal obtidos de observações e de modelos de previsão do tempo e do clima, deverá oferecer pistas para o desenvolvimento e melhoramento de novas parametrizações de nuvens, camada limite e convecção. Tendo sido

desenvolvida em estreita ligação com o projeto GPCI, a investigação apresentada nesta tese foi orientada segundo as linhas dos principais objetivos e questões científicas do projeto.

GPCI pode ser visto como um projeto de intercomparação de nível 2, em que todos os modelos participantes têm de seguir um conjunto comum de especificações e protocolos predefinidos. A condição básica imposta foi a de que os modelos deveriam correr em modo de clima, usando temperatura da superfície do mar (SST) prescrita como condição fronteira. O período de interesse corresponde a junho-julho-agosto (JJA). A região geográfica a estudar esta compreendida entre -5ºN a 45ºN e 160ºE a 240ºE, e inclui 13 localizações ao longo de uma secção. Os resultados das simulações numéricas foram pedidos numa resolução temporal de 3 horas para variáveis na forma de perfis verticais e para variáveis a um nível fixo. Mais de vinte instituições de previsão do tempo e do clima aderiram ao projeto e extensas quantidades de dados de satélite foram preparados para uso no GPCI. A análise de dados de modelos e de reanálises sugere que é possível estudar os principais aspetos da fenomenologia das nuvens, recorrendo apenas a uma secção individual alinhada com a circulação atmosférica associada à circulação da célula de Hadley na região em causa.

Uma análise preliminar de dados de modelos e de observações, com o objetivo de se obter uma visão geral das caraterísticas médias do ciclo hidrológico durante o verão na região GPCI, foi feita com particular enfase na distribuição vertical das nuvens, e nos processos que envolvem fatores dinâmicos e ambientais que têm um papel na manutenção dos campos de nuvens. As médias sazonais da maior parte das variáveis (e.g., cobertura nebulosa total [TCC], conteúdo de água líquida integrado na vertical [LWP], e radiação emergente de longo comprimento de onda [OLR]) são caracterizadas por um elevado grau de dispersão entre os vários modelos, que raramente mostram uma boa concordância com as observações em todos os pontos da secção. Perfis médios de velocidade vertical (w) e de humidade relativa (RH), sugerem que as características básicas da circulação atmosférica regional imposta pela célula de Hadley são, de um modo geral, bem representadas, apesar de, em detalhe, existirem diferenças substanciais entre os vários modelos (e.g., na intensidade da convecção profunda, ou no conteúdo em humidade na camada limite). Uma comparação da distribuição vertical de cobertura nebulosa (CF) nos vários modelos, mostrou bem os desafios da parametrização e simulação de nuvens em GCMs, com as simulações a mostrarem uma variedade de comportamentos ao nível da representação dos diferentes tipos de nuvens (e.g., estratocúmulos demasiado baixos) e das transições entre eles (e.g., presença de mais do que uma camada de nuvens nas áreas de transição). Estes resultados foram validados com observações da ocorrência de nuvens obtidas

com os satélites CloudSat e CALIPSO (Cloud-Aerosol Lidar and Infrared Pathfinder Satellite Observations). Um estudo ao nível dos processos físicos relevantes para as nuvens, revelou que, de um modo geral, existe uma resposta notória da circulação de larga escala a mudanças na SST prescrita nos modelos. As respostas de outras variáveis, tais como, balanço da radiação de pequeno comprimento de onda no topo da atmosfera (NSRTOA) e TCC, são ainda mais pronunciadas e variam de modelo para modelo. O facto de, na maior parte dos modelos, a resposta ao aumento da SST nem sempre ser coerente entre as diferentes variáveis, aponta para a necessidade de um melhor controlo do comportamento da simulação de importantes parâmetros relacionados com as nuvens, incluindo aqueles cruciais para a avaliação do forçamento radiativo das nuvens. Não foi encontrada (nos dados de 3-em-3 horas das simulações para JJA 1998) nenhuma relação óbvia entre as nuvens baixas (dos regimes de cúmulos pouco profundos e de estratocúmulos) a subsidência e a SST (ou mesmo a estabilidade estática da baixa troposfera [LTS]).

Foi feita uma análise de fundo da transição entre regimes convectivos, baseada no comportamento espaciotemporal das nuvens em simulações dos modelos, em reanálises e em observações de satélite. Com esse objetivo em mente, foram desenvolvidas várias técnicas para detetar transições de regime de nuvens, e ou, caracterizar a sua estrutura sazonal. Funções de distribuição de probabilidade, obtidas para TCC nas várias posições ao longo da secção GPCI, a partir de dados de 3-em-3 horas para a estação JJA 1998, mostram diferenças de modelo para modelo e apresentam importantes disparidades mesmo em posições onde os modelos mostram praticamente o mesmo valor na TCC média. Dois comportamentos distintos foram identificados ao nível da transição entre os estratocúmulos e os cúmulos dos ventos alísios: uma transição relativamente gradual da TCC; e uma variação mais abrupta, com carácter bimodal. Estes dois tipos de comportamentos são, provavelmente, um resultado da maneira como as nuvens são parametrizadas nos respetivos modelos. De qualquer maneira, nenhum destes comportamentos coincide com a forma como as transições se dão em dados correspondentes a observações da TCC do ISCCP (International Satellite Cloud Climatology Project). Estatísticas da cobertura nebulosa obtidas segundo uma metodologia desenvolvida para a deteção de fortes gradientes de TCC ao longo da secção, mostram uma diversidade de comportamentos entre os modelos, por exemplo, no valor médio do decréscimo de TCC, na sua frequência de ocorrência, ou nos histogramas da localização dessas transições em TCC (as reanálises também diferem do ISCCP). Adicionalmente, foi também efetuada uma análise espectral preliminar da série temporal correspondente a variações da localização das transições

abruptas em TCC ao longo da secção. Não tendo sido detetados picos importantes nos respetivos espectros, foi na forma da evolução temporal nas correspondentes séries, que os modelos mais se distinguiram (e.g., uma tendência, num dos modelos, para as transições ocorrerem mais para norte na secção no período final da estação JJA; ou a relativamente pequena amplitude das oscilações de localização encontradas num outro modelo). Em termos da evolução espacial da altura do topo das nuvens vista ao longo da secção, a média dos modelos está próxima dos dados de análise, apesar de, especialmente a sul das áreas de estratocúmulos, todos os resultados diferirem de observações MISR (Multiangle Imaging Spectroradiometer). Ainda no contexto da transição de regime de nuvens, foi desenvolvida uma nova abordagem de análise de padrões espaciais (GEPAT [Grade-based Empirical Pattern Analysis Technique]) com objetivo de se analisarem as condições ambientais associadas a diferentes estruturas espaciais da TCC identificadas pela nova técnica durante a estação JJA 1998. Foram assim encontrados seis diferentes padrões espaciais de cobertura nebulosa típicos da estação (cada um com diferente representatividade de ocorrência temporal). As correspondentes médias em termos de outras variáveis, tais como w aos 700 hPa, LWP, SST, LTS, e direção e intensidade do vento, foram analisadas, tendo sido encontradas diferenças, especialmente ao nível dos campos de w aos 700 hPa e LWP. Algumas ideias da aplicação futura da técnica incluem: a análise de outras estações e anos (separada ou conjuntamente); uma comparação de resultados para diferentes regiões; e o uso de dados puramente observacionais.

Foi dada especial atenção à estrutura da humidade na região GPCI, com o objetivo de uma maior compreensão do seu papel como um dos principais parâmetros no contexto do ciclo hidrológico, particularmente através da sua influência na formação e evolução das nuvens. Para esse fim, foram analisadas ao longo da secção, observações de satélite (AIRS [Atmospheric InfraRed Sounder]), simulações numéricas e análises da atmosfera, referentes a perfis de RH, obtidos para JJA (2003) na forma de médias sazonais, variância e evolução temporal. A comparação dos modelos com os dados AIRS mostrou diferenças significativas (e.g., valores bastante inferiores de RH nos níveis mais baixos da camada limite nas simulações, valores mais elevados do que as observações na tropopausa, e maior secura aos níveis médios da atmosfera nas regiões subtropicais nos modelos). No que diz respeito ao desvio padrão, ainda que, de um modo geral, os modelos apresentem maior variabilidade de RH, existem nas simulações, valores mais baixos na camada limite ao longo de toda a secção. Pensa-se que os valores mais elevados de desvio padrão apresentados pelos modelos imediatamente acima da

camada limite a norte da região dos cúmulos pouco profundos devam estar associados primariamente à relativamente fraca resolução vertical dos dados AIRS usados (mais do que serem uma consequência de deficiências nos modelos). A evolução temporal da distribuição vertical de RH parece apontar para a necessidade de se incluir na investigação das transições entre os estratocúmulos e os cúmulos dos ventos alísios, a influência, não apenas da estrutura da humidade nas camadas da troposfera logo acima da camada limite, mas também do perfil de humidade até às camadas superiores da troposfera. Mais especificamente em relação à estrutura da humidade na baixa troposfera, foi apresentada uma nova metodologia para a determinação do topo da camada limite sobre o oceano (sBLT [sequential Boundary-Layer-Top determination scheme]). Os resultados preliminares parecem promissores, especialmente pela sua abrangente aplicabilidade, e dado que a técnica permite uma maior caracterização da camada limite (e do seu topo) que outros métodos relacionados. Médias sazonais para a altura e a intensidade do topo da camada limite foram analisadas para modelos e análises ao longo da secção GPCI, e mostram dispersão considerável, exceto em termos da (praticamente comum) taxa de subida do topo da camada limite de norte para sul entre a área dos estratocúmulos e a dos cúmulos pouco profundos. As áreas de convecção profunda e dos estratocúmulos apresentam, respetivamente, o maior e o menor grau de definição (intensidade) do topo da camada limite. Segundo a classificação sBLT, foram encontradas nos modelos, e para as várias localizações na secção, diferenças na distribuição sazonal da representatividade dos vários tipos de camada limite. A esse respeito, apenas dois dos modelos se assemelham às observações AIRS. Foi ainda desenvolvida uma versão atualizada da técnica para deteção de mudanças abruptas na cobertura nebulosa ao longo da secção. A nova metodologia pareceu apresentar maior robustez no constrangimento dos resultados dos modelos para aquelas situações que efetivamente correspondem a transições espacialmente consistentes com a definição dos regimes de nuvens característicos dos estratocúmulos e dos cúmulos dos ventos alísios. Os valores da ocorrência das transições baixou drasticamente na maior parte dos modelos, e permitiu, uma melhor identificação dos impactos que diferentes filosofias de parametrização de nuvens têm no comportamento dos modelos a este nível. Por último, foram obtidos os perfis médios de RH correspondentes a cada um dos dois regimes de nuvens identificados, tendo sido verificadas importantes diferenças entre os dois regimes, para um determinado modelo, mas também entre os modelos, principalmente na forma como diferem os seus perfis de estratocúmulos e de cúmulos pouco profundos na média e alta troposfera. Foram propostas formas concretas de se estender a investigação dos potenciais impactos da estrutura da humidade da troposfera na transição entre os regimes de nuvens.

Um dos principais tópicos para o projeto GPCI é a representação, em modelos de previsão do tempo e do clima, de variações diurnas das nuvens e de parâmetros relacionados. Essas variações foram analisadas com base em dados de 3-em-3 horas obtidos dos modelos e de observações. O ciclo diurno médio na estação JJA foi descrito para diferentes localizações na secção GPCI. Foram apresentados resultados para: circulação atmosférica associada com a dinâmica de larga escala na região do Pacífico NE dominada pela célula de Hadley; perfis verticais de vários parâmetros de interesse para as nuvens; e anomalias médias do ciclo diurno em três posições da secção, representativas dos principais regimes de nuvens/convecção que caracterizam a região. A velocidade vertical aos 700 hPa apresenta, em geral, nos modelos e análises, um ciclo diurno marcado na zona de convergência inter-tropical (ITCZ). Nalguns modelos variações diurnas mais fracas foram também encontradas na região dos ventos alísios e nas regiões subtropicais. Num dos modelos o ciclo diurno de w aos 700 hPa é praticamente inexistente em qualquer das posições ao longo da secção. A intensidade e direção do vento na baixa troposfera mostrou variações diurnas características. A distribuição vertical de RH, CF, e conteúdo em água líquida das nuvens (CLW), mostrou alguma variabilidade diurna em todos os modelos analisados, especialmente abaixo dos 600 hPa na área de convecção profunda. Os modelos não concordam na altura do ciclo diurno em que simulam os valores máximos destas variáveis. Verificou-se, em geral, uma melhor concordância entre a variação diurna de CF e CLW nos estratocúmulos e nos cúmulos pouco profundos do que na ITCZ. Há, na região subtropical num dos modelos, CF simulada sem CLW associada. Em relação às anomalias médias diurnas de LTS, TCC, e precipitação (observações deste parâmetro foram obtidas de dados TRMM [Tropical Rainfall Measuring Mission]), os modelos tendem a concordar no primeiro parâmetro, mas diferem uns dos outros, e em relação às observações, nos outros dois.(e.g., na ITCZ, a TCC do ISCCP apresenta dois máximos relativos, sendo o mais pronunciado o que ocorre cerca das 16:00h locais, enquanto que nos modelos e análises, o pico de TCC mais importante dá-se tipicamente de madrugada). Nos estratocúmulos o ISCCP (TCC) tem a menor variação diurna, sendo a esse respeito, ultrapassado pelos modelos. De qualquer maneira, é nessa região que se verifica uma maior concordância entre modelos, análises e observações na altura do ciclo diurno em que se dá o máximo de TCC. No que diz respeito à taxa de precipitação, a maior parte dos resultados mostra um pico relativamente bem definido em todas as localizações ao longo da secção, mas apresentam, para os modelos, uma fraca amplitude diurna na ITCZ comparativamente aos dados TRMM. Finalmente, foi investigada a ligação, durante o ciclo diurno, entre a LTS e a cobertura nebulosa nos estratocúmulos para o caso particular de um modelo com um esquema de parametrização que

associa os dois, tendo-se argumentado sobre a existência de um certo grau de "inércia" na resposta da cobertura nebulosa subtropical em relação às variações diurnas de LTS. Do mesmo modo, e uma vez que a resposta (positiva) das nuvens à estabilidade estática do ambiente pareceu ser mais eficaz para a altura do ciclo diurno em que o valor de TCC era o mais baixo, inferiu-se qualitativamente sobre uma possível dependência dessa resposta no valor apresentado pela cobertura nebulosa. Até que ponto estará a "Scinércia" (ou "inércia dos estratocúmulos [Sc]" em relação à LTS) relacionada com a estrutura da humidade da (média) troposfera, foi uma questão deixada para investigação futura.

Dois pontos, para concluir. Primeiro, este trabalho mostra bem como os atuais modelos de previsão numérica do tempo e do clima ainda apresentam uma deficiente representação das nuvens e de processos relacionados. Segundo, a abordagem proposta pelo projeto GPCI provou ser útil na caracterização dos principais problemas dos modelos, e na definição de possíveis linhas de investigação futura, quer ao nível da modelação, quer na frente observacional.

List of Figures

List of Tables

List of Acronyms and Abbreviations

1D	one-Dimensional
2D	two-Dimensional
3D	three-Dimensional
AFES2	Atmospheric GCM for the Earth Simulator, version 2
AIRS	Atmospheric InfraRed Sounder
am	ante meridiem
AM2p12b	Atmospheric Model, version 2p12b
AMSR-E	Advanced Microwave Scanning Radiometer for the Earth observing system
AMSU	Advanced Microwave Sounding Unit
AR	Absolute Roughness of the cluster-size distribution
ARM	Atmospheric Radiation Measurement
ARPEGE	Action de Recherche Petite Echelle Grande Echelle
ASDC	Atmospheric Science Data Center
ASTEX	Atlantic Stratocumulus Transition EXperiment
Aus	Australia
BAM4.0.21	Bureau of meteorology unified Atmospheric Model, version 4.0.21
BL	atmospheric Boundary Layer
BLH	Boundary Layer Height
BLT	Boundary Layer Top
BMRC	Bureau of Meteorology Research Centre
BOMEX	Barbados Oceanographic and Meteorological EXperiment
CALIOP	Cloud-Aerosol Lidar with Orthogonal Polarization
CALIPSO	Cloud-Aerosol Lidar and Infrared Pathfinder Satellite Observations
CAM3.0	Community Atmosphere Model, version 3.0
Can	Canada
CBL	convective boundary layer
CCC	Canadian Centre for Climate modeling and analysis
CCCma	Canadian Centre for Climate modelling and analysis
CERES	Clouds and the Earth's Radiant Energy System

CF	Cloud Fraction
CG	Cluster Grade
CGUL	Center of Geophysics of the University of Lisbon
CLM	CLimate Model
CLW	Cloud Liquid Water content
CMC	Canadian Meteorological Centre
coupl.	coupled
CP	Centroid Pattern
CPR	Cloud Profiling Radar
CRCM	Canadian Regional Climate Model
CRF	Cloud Radiative Forcing
CRM	Cloud-Resolving Model
CSRM	Cloud-System-Resolving Model
CSU	Colorado State University
CTEI	Cloud-Top Entrainment Instability
CTH	Cloud-Top Height
CY23R4	model cycle 23R4
CY26R3	model cycle 26R3
DAAC	Distributed Active Archive Center
DBSCAN	Density-Based Spatial Clustering of Applications with Noise
DD	centroid-patterns' Degree of Dissimilarity
DIME	Data Integration for Model Evaluation
DISC	Data & Information Service Center
DMSP	Defense Meteorological Satellite Program
dNR	degree of Normalized Roughness
DS	centroid-patterns' Degree of Similarity
DWD	Deutsche WetterDienst
DYCOMS	Dynamics and Chemistry of Marine Stratocumulus
E	East
ECHAM5	ECmwf HAMburg, 5th generation

ECMWF	European Center for Medium-Range Weather Forecasts
ECMWFan	ECMWF analysis
EIS	Estimated Inversion Strength
EOS	Earth Observing System
EQ	equator
ERA-40	ECMWF 40 Year Re-analysis
ERBE	Earth Radiation Budget Experiment
ES9	ERBE-like Science product 9
ETH	Eidgenössische Technische Hochschule
EUROCS	European Cloud Systems Study
FCT	Portuguese Science and Technology Foundation
FIRE	First International satellite cloud climatology project Regional Experiment
fNR	factor to Normalize the absolute Roughness of the cluster-size distribution
FOV	Field Of View
FP	Full Profile
Fra	France
ftop	pressure at the RH-profile level just above the top level of the first subprofile
GCM	General Circulation Model
GCSS	Global energy and water cycle experiment Cloud System Study
GEM	Global Environment Multiscale
GEOPROF	CloudSat Geometrical Profiling Product
GEPAT	Grade-based Empirical Pattern Analysis Technique
Ger	Germany
GES	Goddard Earth Sciences
GEWEX	Global Energy and Water cycle EXperiment
GFDL	Geophysical Fluid Dynamics Laboratory
GFS	Global Forecast System
GISS	Goddard Institute for Space Studies
GISSIII3.3	Goddard Institute for Space Studies global climate middle atmosphere model III, version 3.3
GKSS	Gesellschaft für Kernenergieverwertung in Schiffbau und Schiffahrt

GME	Global Model Europe
GMS	Geosynchronous Meteorological Satellite
GOES	Geostationary Operational Environmental Satellite
GPCC	Global Precipitation Climatology Centre
GPCI	Global energy and water cycle experiment cloud system study / working group on numerical experimentation Pacific Cross-section Intercomparison
GPCP	Global Precipitation Climatology Project
GSFC	Goddard Space Flight Center
GSM0412	Global Spectral Model, version 0412
HadGAM	Hadley centre Global Atmosphere Model
ID	Identification
IPCC	Intergovernmental Panel on Climate Change
IPW	Integrated Precipitable Water
IR	InfraRed
ISCCP	International Satellite Cloud Climatology Project
ITCZ	Inter-Tropical Convergence Zone
JAMSTEC	Japan Agency for Marine-Earth Science and Technology
Jap	Japan
JIFRESSE	Joint Institute for Regional Earth System Science and Engineering
JJA	June-July-August
JK10	Karlsson et al. (2010)
JMA	Japan Meteorological Agency
jPDF	joint Probability Density Function
JPL	Jet Propulsion Laboratory
JSC	Joint Scientific Committee
KNMI	Koninklijk Nederlands Meteorologisch Instituut / Royal Netherlands Meteorological Institute
L2	Level-2
L3	Level-3
LCC	Low Cloud Cover
LES	Large-Eddy Simulation

LIDAR	Light Detection And Ranging
LLNL	Lawrence Livermore National Laboratory
LMD	Laboratoire de Météorologie Dynamique
local	lower cumulative average line
LST	Local Solar Time
lt	lower threshold
ltop	pressure at the RH-profile level just below the top level of the last subprofile
LTS	Low Tropospheric Stability
LWP	Liquid Water Path
MBL	Maritime atmospheric Boundary Layer
MG	Mean centroid-pattern Grade
MISR	Multiangle Imaging Spectroradiometer
MISU	Department of Meteorology of the Stockholm University
MMF	Multi-scale Modeling Framework
MOM3	Modular Ocean Model, version 3
MPI	Max Planck Institute for Meteorology
N	North
NASA	National Aeronautics and Space Administration
NCAR	National Center for Atmospheric Research
NCEP	National Centers for Environmental Prediction
NE	Northeast
Ned	The Netherlands
NOAA	National Oceanic and Atmospheric Administration
NSF	National Science Foundation
NSRTOA	Net Shortwave Radiative flux at the Top Of the Atmosphere
NVAP	National aeronautics and space administration water VApor Project
NW	Northwest
OLR	Outgoing Longwave Radiation
patcnt	pattern count
patgrd	pattern grade

patrep	pattern representativity
PCMDI	Program For Climate Model Diagnosis and Intercomparison
PDF	Probability Density Function
plt	(pressure) level of the lower threshold
pm	post meridiem
PNNL	Pacific Northwest National Laboratory
PP	Partial Profile
put	(pressure) level of the upper threshold
PWV	total Precipitable Water Vapor
RACMO2.1	Regional Atmospheric Climate MOdel, version 2.1
rec	record
refpat	reference pattern
RH	Relative Humidity
RHgrad	Relative Humidity gradient
RICO	Rain In shallow Cumulus over the Ocean
RMS	Root-Mean-Squared
RP	Reference Pattern
RSM	Regional Spectral Model
RSS	Remote Sensing Systems
S	South
S#	Sequential index used in sBLT
S!	BLT determined by the basic sBLT algorithm
sBLT	sequential Boundary-Layer-Top determination scheme
SCM	Single-Column Model
SCMS	Small Cumulus Microphysics Study
SE	Southeast
SI	Singleton Index
SRP	Starting Reference Pattern
SS	Smoothness of the cluster-size Distribution
SSM/I	Special Sensor Microwave Imager

SST	Sea Surface Temperature
SW	Southwest
TCC	Total Cloud Cover
TIROS	Television Infrared Observation Satellite
TMPA	TRMM Multi-satellite Precipitation Analysis
TOA	Top Of the Atmosphere
top	a given pressure value
TOVS	TIROS Operational Vertical Sounder
TRMM	Tropical Rainfall Measuring Mission
TWP	Tropical Western Pacific
TWV	Total column Water Vapor
UCLA	University of California Los Angeles
UCSD	University of California San Diego
UK	United Kingdom
UKMO	United Kingdom Meteorological Office
UL	University of Lisbon
UQM	University of Quebec at Montreal
ut	upper threshold
UTC	Universal Time Coordinated
US	United States of America
U.S.A.	United States of America
W	West
WCRP	World Climate Research Program
WGNE	Working Group on Numerical Experimentation

List of Symbols

#	number sign
%	percent
$\|x\|$	absolute value of x
b	width of an abstract rectangle
CH_4	methane
CO	carbon monoxide
CO_2	carbon dioxide
d	dimension in a pattern space
Dp	pressure difference
°C	degree Celsius
°N	degress north
g	gram
g	total number of measures of cluster validity
g_{ij}	grade between the the i^{th} and the j^{th} patterns
G	GEPAT global index of clustering validity
h	hour
hPa	hectopascal
$hS_0\%$	height of an abstract rectangle taken as the difference between $S_0\%$ and $S_0\%$ ($hS_0\% = 0$)
$hS_i\%$	height of an abstract rectangle taken as the difference between $S_0\%$ and $S_i\%$
i	the i^{th} pattern
I	number of iterations required for convergence in the basic K-means algorithm
j	the j^{th} pattern
K	kelvin
K	size of a clustering, or total number of clusters in a clustering
K'	undefined size of a clustering
K_0	a particular value for the size of a clustering
kg	kilogram
km	kilometre

l	a number of GEPAT experiments
$\leq$	less-than or equal to
m	metre
m	total number of patterns in a dataset
max	the max function
mb	millibar
min	minutes
mm	millimetre
n	total number of dimensions of a pattern space
N	number of standard deviations
N_2O	nitrous oxide
occ	occurrence
P	precipitation
Pa	pascal
ppmv	parts per million by volume
q	water vapor
$\overline{q}$	column water vapor
q_s	saturation water vapor mixing ratio
$\overline{q}_s$	column saturation vapor pressure
σ_d	standard deviation of the d^{th} components of all the pattern vectors
s	second
Sc	stratocumulus
ShCu	shallow cumulus
$S_0\%$	size of the most numerous cluster in percent of the total number of patterns in the dataset
S_i	size of the i^{th} cluster, or total number of patterns in the i^{th} cluster
$S_i\%$	size of the i^{th} cluster in percent of the total number of patterns in the dataset, also called representativeness of the i^{th} cluster
T	GEPAT grading threshold
T_0	a particular value for the GEPAT grading threshold
T_{sat}	GEPAT saturation threshold
μm	micrometre

v_{id}	the d^{th} component of the vector representing the i^{th} pattern
v_{jd}	the d^{th} component of the vector representing the j^{th} pattern
w	vertical velocity
W	watt
w700	vertical velocity at 700 hPa

Table of Contents

1 Introduction

1.1 Motivation and main goals

Notwithstanding the considerable improvement in cloud and cloudy boundary layer parameterization in the last 20 years (e.g., Tiedtke 1993; Del Genio et al. 1996; Fowler et al. 1996; Rasch and Kristjánsson 1998; Lock et al. 2000; Lock 2001; Bony and Emanuel 2001; Teixeira and Hogan 2002; Tompkins 2002), the representation of clouds is still a challenge for the weather and climate modelling communities (e.g., Teixeira 1999; Jakob 1999; Duynkerke and Teixeira 2001; Siebesma et al. 2004), thus underlining the continued need for observational methods and campaigns targeted at different cloud systems, along with the development of cloud parameterization in GCMs (General Circulation Models). This urgency is reinforced by the fact that the amount of cloud generated by the models has a significant impact on the predicted behaviour of the climate system (e.g., Cess et al. 1989; Slingo 1990). In particular, current climate models tend to respond differently in climate change sensitivity experiments, often showing diverging cloud-climate feedbacks, a situation explained, to a great extent, by significant differences in low (boundary layer) cloudiness (e.g., Bony et al. 2004; Bony and Dufresne 2005; Bony et al. 2006; Wyant et al. 2006; Stephens 2005). Parameterization deficiencies also result in thermodynamically inconsistent representation of the hydrologic cycle, which has important implications in the simulation of the (sub)tropical atmospheric circulation and its interplay with boundary layer and deep convection clouds (e.g., Philander et al. 1996; Ma et al. 1996; Larson et al. 1999).

These topics are investigated by different GCSS (Global energy and water cycle experiment Cloud System Study) working groups (boundary layer clouds, cirrus, frontal clouds, deep convection, and polar clouds), which have been successful in defining and understanding fundamental cloud regimes (e.g., Duynkerke et al. 1999; Bretherton et al. 1999; Bechtold et al. 2000; Redelsperger et al. 2000; Stevens et al. 2001; Randall et al. 2003; Siebesma et al. 2003), and in the development of new cloud and cloudy boundary layer parameterizations (e.g., Cuijpers and Bechtold 1995; Lock et al. 2000; Golaz et al. 2002; Teixeira and Hogan 2002; Cheinet and Teixeira 2003; Lenderink and Holtslag 2004; Bretherton et al. 2004b; Soares et al. 2004; Bretherton and Park 2009). Traditionally, four main steps characterize the GCSS strategy: *i)* creation of an observationally-based case study; *ii)* evaluation of CRM (Cloud-

Resolving Model) and LES (Large-Eddy Simulation) models for the case study; *iii)* evaluation of parameterizations using SCMs (Single-Column Models); and *iv)* develop and improve parameterizations using the statistics from the CRM and LES models.

However, the exclusive use of one-dimensional (SCM) versions of the atmospheric models does not allow a deep understanding of the fundamental role of clouds in climate (e.g., cloud-climate feedbacks) owing to the fact that the large scale dynamics is prescribed in the SCM and CRM models. This implies that parameterization testing has to be done in the complete (3D [three-Dimensional]) versions of weather and climate prediction models, which potentially entails the analysis of very large amounts of model simulation data. In this context, the GPCI (Global energy and water cycle experiment cloud system study / working group on numerical experimentation Pacific Cross-section Intercomparison) project offers a new and much lighter approach for the intercomparison of GCMs, by focusing the analysis on a reduced number of locations along a cross section in a carefully chosen geographical region, allowing for a relatively straightforward model and observational data integration. More precisely, the GPCI approach has, this far, been focused on the (sub)tropical NE Pacific ocean, although, in general, suitable for other similar regions (e.g., in the SE Pacific).

Cloud parameterization development and improvement resorting to high temporal resolution model output to allow the evaluation of the representation of the diurnal cycle, and the exploration and validation of state-of-the-art observational datasets to understand different cloud regimes and the transitions between them, are at the core of GPCI's motivations. In the long run this approach could also contribute to a better understanding of how the global changes in precipitation, evaporation, and hydrologic cycle are taking place.

Having been developed in tight connection with the GPCI project, the investigation presented in this thesis was oriented along the lines of GPCI's main goals and scientific questions (Section 3.1.2).

1.2 Outline

This thesis is divided into 8 main chapters.

The introductory chapter is followed by an overview of cloud climatology, cloud-related processes, and dedicated observational campaigns, given separately in a global, and in a regional perspective, with a special focus on (sub)tropical maritime low boundary-layer clouds. Also in Chapter 2, a brief description is given of the main physical processes thought to impact

the formation of low stratiform cloudiness over the subtropical oceans. The last section is dedicated to cloud parameterization, and presents a general view on some of the main aspects of the representation of clouds in numerical models.

Chapter 3 is dedicated to the GPCI project, and starts with some background, followed by the project's main goals. The project protocol is detailed, and information is presented on the participating models, and observational datasets used in this work. The chapter closes with a discussion on the representativeness of the GPCI cross section and concludes on the robustness of the GPCI approach.

The fourth chapter, is focused on a preliminary analysis of GPCI model and observational data, and discusses the corresponding results with the goal to give an overview of the mean characteristics of the summertime atmospheric hydrologic cycle in the (sub)tropical NE Pacific. Emphasis is also given to the vertical distribution of clouds, and to processes involving dynamical and environmental factors that play a role in the maintenance of total and low cloud fields on a seasonal time scale.

An in-depth analysis of convective regime transition, based on the spatiotemporal behaviour of clouds is attempted in Chapter 5, resorting to cloud data from model simulations, atmospheric reanalysis, and satellite observations. To gain insight into the question of the transition in (sub)tropical cloud regimes, several techniques are developed to detect the transitions, and or summarize their main seasonal features. Additionally, a preliminary spectral analysis of the seasonal record of spatial shifts in the location of sharp gradients in cloud cover is performed, and a novel approach to clustering of spatial patterns is introduced, and subsequently applied to total cloud cover along the GPCI transect, with the final goal to indentify main spatiotemporal features of the seasonal cloud cover, and compare associated environmental conditions.

Chapter 6 is dedicated to the study of the humidity structure in the GPCI region, with the goal to better understand its role as one of the main parameters in the context of the hydrologic cycle, particularly through its influence on cloud formation and evolution. State-of-the-art satellite observations are analyzed along the cross section, together with model simulations and atmospheric analyses. A number of results, based on the treatment of relative humidity data for the summer season, are presented, namely, seasonal mean profiles, variance, temporal evolution, boundary-layer properties, and potential impact on cloudiness structure and transition. The chapter introduces a new methodology for the determination of the top of the maritime boundary layer, and updates the technique for the detection of abrupt changes in the spatial distribution of clouds initially presented in Chapter 5.

As one of the main topics in GPCI, the representation, in weather and climate prediction models, of the diurnal variation of clouds and cloud-related parameters, is the focus in Chapter 7. Three-hourly model output and observational data are used to characterize the diurnal cycle, as seen in seasonal means at different locations along the GPCI transect. Results are presented for: atmospheric circulation associated with the large-scale dynamics in the Hadley-cell-dominated NE Pacific; a number of cloud-related vertically-distributed variables; and for June-July-August mean diurnal cycle anomalies at three specific locations in the cross section, representative of the main cloud/convection regimes found in the region.

The main conclusions of this work are presented in Chapter 8, followed by a list of the bibliography referenced.

A note on the contents of the CD-ROM with the appendixes to this work forms the Appendix, placed at the end of the thesis.

2 Convection and clouds over the (sub)tropical oceans

Clouds are known to be an important regulator of the climate system. They interact with the atmosphere in many ways, and influence its dynamic behaviour at different scales, from those at which they occur, to the global atmospheric circulation. Randall (1989) categorized the direct effects of clouds on the atmosphere in three "cloud forcing" mechanisms: radiative forcing, latent forcing, and convective forcing. The radiative forcing (Ramanathan 1987) describes the clouds' modulation on the solar and terrestrial radiative fluxes; the latent forcing describes the effects of vaporization and condensation latent heat that occur in clouds and precipitation; the convective forcing describes additional effects of heat, moisture, and momentum transport in convective clouds, associated with latent heat release, but treated separately from it. Through the combination of these three forcings, clouds profoundly influence the distribution of energy in the atmosphere, and the hydrologic cycle, and, therefore, the large-scale atmospheric circulation. Despite all the current knowledge, clouds are still one of the biggest challenges in climate research. The Intergovernmental Panel on Climate Change (IPCC) emphasized that one of the sources of uncertainty in global climate prediction is the incomplete knowledge of the mechanisms involved in the formation, dissipation, and radiative properties of clouds (Houghton et al. 1990; Houghton et al. 1992; Solomon et al. 2007).

The next two sections of this chapter present an overview of cloud climatology, cloud-related processes, and dedicated observational campaigns, in global (Section 2.1), and in regional (Section 2.2) perspectives, with a special focus on (sub)tropical maritime low boundary-layer clouds. In Section 2.3, the main physical processes thought to impact the formation of low stratiform cloudiness over the subtropical oceans are briefly described. Section 2.4 (Cloud parameterization) gives a general view on some of the main aspects of the representation of clouds in numerical models.

2.1 Global scale

The maritime atmospheric boundary layer (MBL) differs in many aspects from the atmospheric boundary layer (BL) over the continents. A few characteristics of the MBL, as compared to the continental BL, are typically highlighted, namely: a) the air close to the surface is moister, with relative humidity in the range of 75 % to 100 %; b) the diurnal cycle tends to be weaker

(though not negligible); c) except close to the coast, the difference in temperature between the air and the surface tends to be small (as a result of radiative cooling the air is usually up to 2 K cooler than the surface water, with significant temperature differences resulting in vigorous convection able to balance the effects of horizontal thermal advection [except in regions with strong sea surface temperature contrast], which makes for a neutral surface layer over most oceanic regions); d) more than 95 % of the global MBL has clouds, the exceptions being the coastal areas where warm and dry continental air is advected over a colder ocean, and some regions (e.g., in the western boundaries of the subtropical oceans) where air is advected from areas with relatively high sea surface temperature (SST) to areas with lower SSTs.

Boundary-layer clouds, or, in general, low clouds, occur frequently in the atmosphere, and are notably abundant in the MBL. The fact that they cover large areas of the globe make them particularly important for the radiative balance of the planet. A crucial climate topic is thus the understanding of the factors that control their abundance (e.g., Randall et al. 1984; Klein and Hartmann 1993; Bony et al. 2004; Sandu et al. 2010; Teixeira et al. 2011).

Shallow cumulus (ShCu), stratus, stratocumulus (Sc), and nimbostratus are the most frequent cloud types in the BL. Recent investigation suggests that the Sc and ShCu play an important role in the tropical and subtropical atmospheric circulation (e.g., Philander et al. 1996; Siebesma 1998; Larson et al. 1999). These two types of clouds are described in the next paragraphs.

Stratocumulus occurrence is particularly frequent over the oceanic regions and is generally associated with subsidence conditions in the subtropical regions and mid-latitudes. This is particularly notorious in subtropical regions in the eastern boundaries of the great oceans, where the descending branch of the Hadley cell circulation forces the subsidence of air over relatively cold surface waters, e.g., the regions to the west of California (NE Pacific), Peru (SE Pacific), Namibia (SE Atlantic), and Mauritania (NE Atlantic) (Hanson 1991; Klein and Hartmann 1993; Ma et al. 1996). Also noteworthy is the formation of Sc that occur during the Winter over the warm current regions of the western boundary of the big ocean basins (e.g., Kuroshio current [NW Pacific] and Gulf current [NW Atlantic]). In these regions, the contact of cold continental air masses with a relatively warm ocean surface results in strong heat and humidity fluxes that increase the depth of the MBL and favor convection, in contrast to what happens in the subtropical subsidence regions where convection is maintained by strong cloud-top radiative cooling (e.g., Klein and Hartmann 1993; Bretherton et al. 2004a). A third type of low stratiform clouds, Arctic stratus, forms essentially during the Summer, and, in many cases,

results from the radiative cooling of moist air reaching the Arctic from subpolar latitudes (e.g., Herman and Goody 1976; Curry et al. 1988). A unique characteristic of these stratus is the tendency to form multiple cloud layers, and the occurrence of humidity inversions with an increase of moisture from the base to the top of the inversion layer. Other types of stratus include those that occur during the Summer in the SE China plateau, and the maritime Summer stratus of the mid-latitudes between 45°N and 60°N.

Several observational campaigns and initiatives have been focused on improving the understanding of the Sc thermodynamic and turbulent structure, and chemistry, among them: FIRE (First International satellite cloud climatology project Regional Experiment [Albrecht et al. 1988]); ASTEX (Atlantic Stratocumulus Transition EXperiment [Albrecht et al. 1995]); and DYCOMS-II (the second Dynamics and Chemistry of Marine Stratocumulus field study [Stevens et al. 2003]). These have provided important data for a number of subsequent studies on Sc (e.g., Duynkerke and Driedonks 1987; Hignett 1991; Duynkerke and Teixeira 2001). More recently the use of Large-Eddy Simulation (LES) models has increased our understanding of fundamental mechanisms responsible for the formation and maintenance of Sc (e.g. Moeng et al. 1996; Stevens et al. 1998; Duynkerke et al., 1999). Climate research has reinforced the idea that Sc are important agents of its variability and dynamics (e.g., Philander et al. 1996; Clement and Seager 1999; Bony and Dufresne 2005).

Another type of low cloud with an important presence in the BL, and typically associated with convective boundary layer (CBL) situations is the ShCu. Its distribution affects on average, respectively, 12 %, and 5 %, of the area over the oceans, and continents (Duynkerke 1998). One peculiar aspect of ShCu is the fact that they typically occur in oceanic regions where the trade winds prevail, in which case they are commonly known as the *trade-wind cumulus*. These clouds often make the transition between Sc-dominated regions and the ITCZ (Inter Tropical Convergence Zone) associated with the ascending branch of the Hadley cell. In the continental mid-latitudes ShCu are frequent during the Summer, and can evolve into cumulonimbus when conditions are favorable for deep convection. By intensifying the vertical transport of heat, moisture, and momentum in the ITCZ, and contributing to the overall humidity and heat transport in the Hadley cell system, ShCu exert a direct influence on the global atmospheric circulation and hydrologic cycle (e.g., Tiedtke 1987; Siebesma 1998). ShCu also posses radiative properties that indirectly affect the radiative balance of the planet (e.g., Ackerman et al. 1981; Marshak et al. 1995).

Among the observational campaigns and initiatives dedicated to ShCu are: BOMEX (Barbados Oceanographic and Meteorological EXperiment [Kuettner and Holland 1969]); SCMS (Small Cumulus Microphysics Study [French et al. 1999]); ARM (Atmospheric Radiation Measurement [Brown et al. 2002]); and RICO (Rain In shallow Cumulus over the Ocean [Rauber et al. 2007]). Data from these campaigns were used in a number of research works (e.g., Warner 1977; Smith and Jonas 1995; De Roode and Duynkerke 1997). As with Sc, LES models are extensively used for the investigation of the CBL with ShCu (e.g., Sommeria 1976; Siebesma and Cuijpers 1995; Neggers et al. 2004).

Figure 2.1 presents an annual climatology of the global distribution of low stratiform clouds (stratus, stratocumulus, and fog) obtained from surface observations. In the next section, the focus is on the regional characterization of the cloud systems that typically occur close to the eastern boundaries of the big oceans, including the kind of low boundary-layer clouds whose regional maxima can be seen in Fig. 2.1 off the coasts of California, Peru, and Namibia.

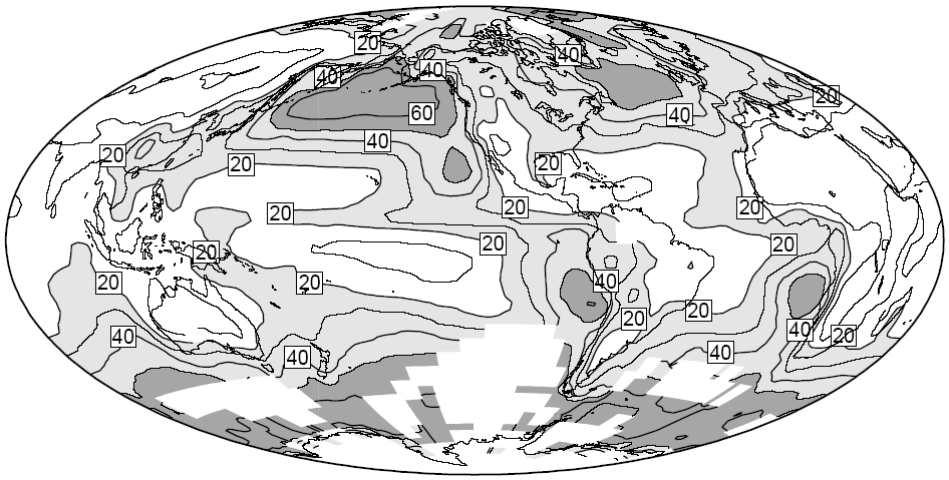

Figure 2.1 - Annual mean global distribution of low stratiform clouds (stratus, stratocumulus, and fog) obtained from surface observations (from Klein and Hartmann 1993).

2.2 Regional scale

The global distribution of low stratiform clouds patent in Fig. 2.1 clearly puts in evidence one of the most characteristic aspects of this type of clouds: the persistence of their occurrence to the east of the maritime subtropical anticyclones. Climatologically, these regions are marked by the presence of the (easterly) trade winds blowing (from the mid-latitudes) in the direction of the ITCZ. As mentioned in the previous section, stratus clouds form over the ocean in areas with relatively low SST, and below a strong temperature inversion at the top of the MBL. The inversion layer, also present in the trades, is maintained by the subsidence associated with the

descending branch of the Hadley circulation and imposes a (vertical) limit to stratiform convection forcing the clouds to stay relatively low (there is some evidence of a possible relation between the intensity of the temperature inversion and the amount of stratus in the MBL). The inversion strength is linked to the intensity of the Hadley cell, which, in turn is, in part, determined by deep convection in the tropics (Klein and Hartmann 1993). As the trades approach the ITCZ, and higher SSTs, the inversion layer gradually deepens and the temperature inversion becomes less pronounced. This is usually accompanied by an increase in convection activity resulting in the formation of cumulus clouds that become dominant to the detriment of stratiform clouds. The mechanisms behind this transition are a current topic of investigation (e.g., Karlsson et al. 2010; Sandu et al. 2010; Teixeira et al. 2011). An illustration of the basic interplay between the boundary layer clouds, the SST and the large-scale atmospheric circulation in thermally direct circulations such as the Hadley (/Walker) cell, is given in Fig. 2.2, with deep precipitating cumulus towers found (in the ITCZ / western tropical oceans) over warm waters near the equator (EQ) as mediators of the ascending branch of the direct circulation(s); stratocumulus clouds covering the relatively cold (eastern) subtropical oceans under the influence of the subsiding branch of the large-scale, and land/sea circulations; and trade-wind cumulus in between, in concomitance with a deepening of the MBL (as mentioned in the previous section, ShCu play an important role in the transport of heat and humidity that contributes to fuel the Hadley circulation).

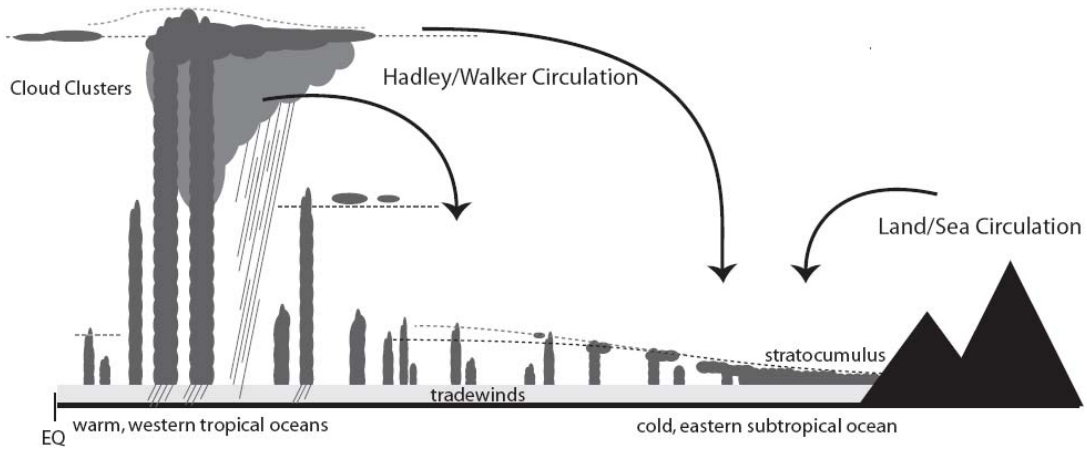

Figure 2.2 - Illustration of the main cloud regimes associated with thermally direct circulations between the tropics, and the subtropics of the eastern boundaries of the main oceanic basins (EQ for equator) (from Stevens 2005).

In the specific case of the Pacific region close to California, the conditions for the occurrence of stratocumulus during the Summer season seem to include a well defined subtropical anticyclone, trade winds blowing equatorward with divergence indicative of strong subsidence,

and a sharp temperature inversion at the top of a well mixed ~ 1000 m deep MBL (e.g., Klein and Hartmann 1993). A qualitative analysis of these aspects is given in the next paragraphs.

Note firstly, that, an intense subtropical anticyclone is favorable to an increase of BL cloudiness, since, along with increased subsidence, steadiness of the wind field, and advection of relatively cooler air, it dries the troposphere, and limits the disrupting influence mid-latitude cyclones have on the BL processes. Moreover, it seems that atmospheric circulation changes force SST variations, probably through the effects on the energy balance of the ocean mixing layer, of the conjunction of stronger surface winds, more vigorous surface fluxes, and cloud cover (Klein et al. 1995). It should be kept in mind, however, that it is inadequate to think of low clouds as being solely related with SST; in that point of view it would be tempting to infer the existence of a global climatic feedback from the negative correlation between low clouds and SST that happens in certain circumstances. There is no clear indication of such a feedback (e.g., Hartmann and Michelsen 1993; Klein et al. 1995; Bony et al. 1997).

Concerning, more specifically, the link between the strength of the inversion at the top of the MBL and stratiform cloud cover, the question is on its physical meaning. It is believed that the presence of the inversion layer forces the moisture that evaporates from the ocean surface to accumulate in the MBL and, eventually, reach saturation. Once a cloud is formed, convection is easily maintained, essentially owing to strong cloud-top radiative cooling (in the absence of clouds at higher levels, and, particularly, if the overlying free troposphere is relatively dry). Under these conditions the cloud will remain confined to the MBL because the inversion layer hinders its vertical (convective) development. It can then be concluded that an inversion layer is a necessary condition for the formation of (subtropical) MBL stratus. Still, it would be imprudent go much further and make a direct link between changes in inversion strength and changes in stratiform cloud cover. Another related aspect is the existence in the subtropical regions of a possible link between stratus and low tropospheric (static) stability (LTS, defined as the difference between the potential temperature at 700 hPa and at the surface). A positive feedback between both has even been suggested (Hanson 1991). In fact, this type of clouds help maintain the MBL relatively cool through longwave radiative cooling and scattering of shortwave energy from the Sun. This may cause an increase of the static stability, which can, in turn, be potentially responsible for a subsequent increase in stratus, and so on. The efficacy of such a feedback has to be evaluated taking into account that the MBL temperature is, to a great extent, determined by the SST. Knowing that the big heat capacity of the ocean implies that the SST is relatively unaffected by radiation changes (at least in shorter time scales), limits

the effectiveness of the proposed feedback (Klein and Hartmann 1993). In any case, it should be stressed that the association between stratus and static stability does not necessarily imply a causal relation (in any direction). Nevertheless, some studies have shown a significant link between maritime low cloud cover and measures of atmospheric vertical stability in the MBL. Klein and Hartmann's (1993) conclusions were drawn from the analysis of large areas of the maritime subtropics at the seasonal scale, showing a strong relation with LTS, while Wood and Bretherton (2006) showed improved connections using a variant of LTS, the estimated inversion strength (EIS).

Observations suggest that, there is, in the NE Pacific and similar regions, a relation between the behaviour of the cloud cover at a given location and environmental conditions the corresponding air mass experienced upwind along the trajectory of the trades. An immediate conclusion is the need to adopt a Lagrangean perspective to follow the history of the MBL atmospheric flow and understand its implications for the cloudiness (e.g., Klein et al. 1995; Mauger and Norris 2010). In that case, the prediction of MBL cloud properties in GCMs (General Circulation Models) must take into account, not only local boundary conditions, but also, the meteorological history of the MBL air. This points to the need for prognostic, instead of diagnostic, MBL cloud parameterization schemes (e.g., Tiedtke 1993).

Regarding the cloud transition that happens in the trades downwind from the regional Sc maximum, it has been mentioned that it is associated with a deeper MBL and with SSTs higher than those found in the Sc-dominated areas. In the transition region the stratiform clouds tend to be confined to a relatively thin layer immediately below the inversion layer, and are typically decoupled from the surface as a source of moisture, except during the presence of cumulus associated with intermittent convection (e.g., Bretherton 1992; Klein et al. 1995). Additional data on the thickness and temperature contrast of the inversion indicate that, as the MBL height increases, the intensity of the inversion, defined as the combination of those two quantities (Neiburger et al. 1961), decreases, which allows for an easier entrainment on the MBL of relatively dry air from the free troposphere above it. The combined effect of the decoupling from the surface and of the thinning of the stratiform cloud layer, is, by itself, responsible for an increased efficacy of the cloud dissipation by solar energy absorption, and, consequently, favors larger diurnal variations of cloud cover. This enhanced diurnal cycle of low cloudiness in the Sc-to-ShCu transition areas was observed during ASTEX (Albrecht et al. 1995).

However, the mechanism responsible for the restoration of the stratiform cloud layer, that occurs during the night, is less clear. The humidity flux associated with intermittent convective clouds could contribute for the renewal of the stratus layer in parts of the region where convection coexists with thin stratus, but, in regions where the diurnal cycle is more pronounced, there seems to be the need for an additional mechanism. A possible candidate is the nocturnal substitution of air heated during the day, by the advection of colder and saturated air from upwind (e.g. Wang et al. 1993).

Finally, since low clouds have a much more significant effect on top of the atmosphere shortwave radiative fluxes than on longwave radiative fluxes, the diurnal variations of the cloud cover associated with this type of clouds are particularly important to estimate cloud-induced changes in the planetary radiative balance. Seasonal variations of the diurnal cycle show that the largest diurnal cycle amplitudes occur during the summer months in both hemispheres (Rozendaal et al. 1995).

2.3 Physical processes

In Fig. 2.3, the key processes discussed above, whose interplay is thought to contribute to the formation, maintenance, and breakup of low stratiform cloudiness in the (subtropical) MBL, are illustrated. In addition, Fig. 2.3 introduces intermittent drizzle, longwave heating, and microphysical variability as fundamental factors for understanding cloud and cloudy boundary layer evolvement. A quick summary of the main physical processes and how they compete in determining the phenomenology of the cloudy MBL is given in the next paragraphs.

The longwave cloud-top radiative cooling is, to a great extent, responsible for driving the convective turbulence in the MBL, but also spurs turbulent entrainment of relatively warm and dry air from the overlying free troposphere. This entrainment tends to result in a deepening of the MBL, against the large-scale subtropical subsidence. The radiative cooling is counteracted by entrainment warming, and surface heat fluxes, while the drying effect of cloud-top entrainment is counteracted by surface moisture fluxes (e.g., DYCOMS-II [Stevens et al. 2003]; Stevens 2005).

Concerning the humidity structure of the free troposphere, the greater the moisture content of the overlying environment, the more downwelling longwave radiation will be felt at cloud top. This can offset the longwave radiative cooling, and potentially lead to a decrease of convective turbulence associated with cloud-top cooling. Such a situation tends to favor the decoupling of

the cloud layer from the surface as a source of moisture (Bretherton and Wyant 1997; Stevens 2000), and may result in a thinning of the stratiform clouds. On the other hand, if a moist overlying environment extends all the way down to the cloud level, the potential reduction of the drying of the cloud layer due to the entrainment of overlying (in this case relatively moist) air may, overall, counteract the effects of the aforementioned decoupling, and even favor cloud formation (e.g., Sandu et al. 2010).

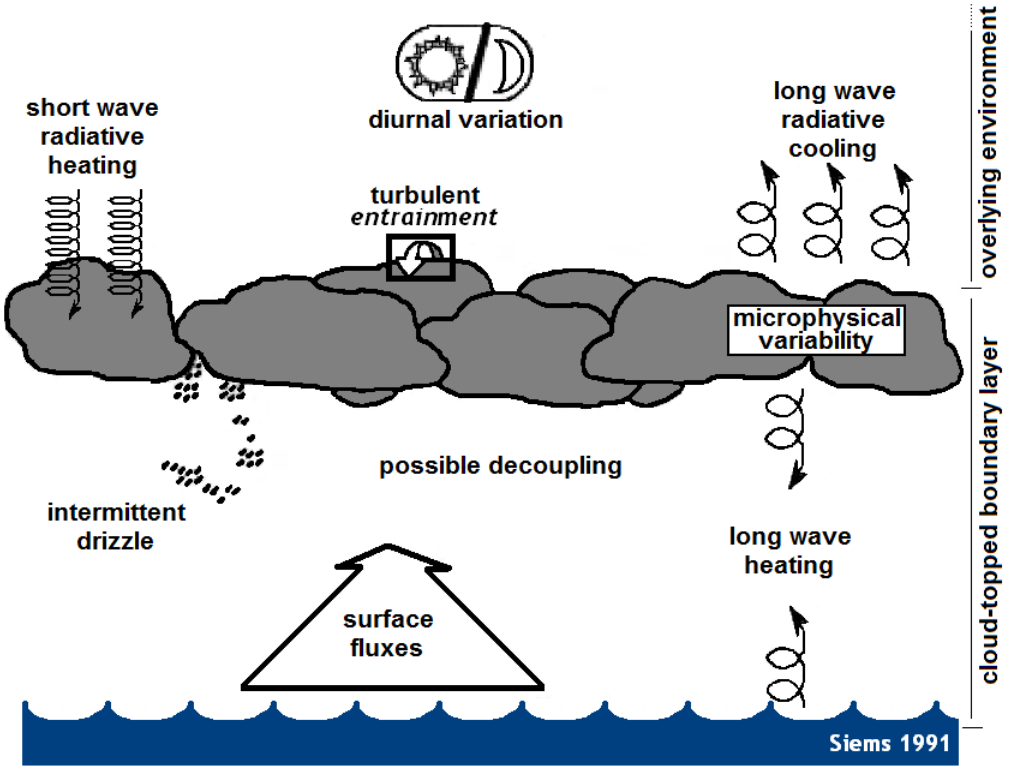

Figure 2.3 - Schematic representation of the physical and dynamical processes that affect the cloud-topped maritime boundary layer (adapted from Garratt 1992).

Another mechanism that may contribute to the breakup of this type of cloud layer, known as cloud-top entrainment instability (CTEI, Lilly 1968; Randall 1980; Deardorff 1980; Siems 1991, Kawai and Teixeira 2010), is thought to take place when subsaturated air, entrained in the cloud layer, is subsequently cooled by evaporation to the point of becoming negatively buoyant. The consequence is, potentially, the enhancement of the turbulent entrainment of more subsaturated air, in a positive feedback that ultimately results in a thinning, and eventual breakup, of the cloud layer (Yamaguchi and Randall [2008], question the effectiveness of this feedback as being responsible for cloud dissipation). It is also possible that the combination of (intermittent) drizzle (e.g., Paluch and Lenschow 1991) and latent heat release in the cloud layer (Bretherton and Wyant 1997), leads to MBL decoupling conditions, if they happen to

offset the effects of cloud-top radiative cooling on the convective turbulence. Once again, the cloud layer would undergo a thinning and, possibly, breakup.

As previously mentioned, thinner cloud layers are more prone to dissipation by solar energy absorption (shortwave radiative heating). This situation favors relatively large diurnal variations of cloud cover in regions where these thinner cloud layers tend to be more abundant (e.g., the Sc-to-ShCu transition areas of the maritime subtropics).

A deeper understanding of the interplay between the physical processes presented above, and of its modulation by the large-scale dynamics and environmental conditions, is crucial for the improvement of the numerical representation of clouds.

2.4 Cloud parameterization

In the first attempts at climate simulation with GCMs, clouds were prescribed. Their distribution was then usually introduced in the models as climatological values of zonal means, ignoring its spatiotemporal variation (e.g. Holloway and Manabe 1971). An important step forward in cloud modelling happened with the inclusion of the effects of important parameters such as relative humidity, vertical velocity, and static stability in the numerical schemes for the representation of clouds. That resulted in a more realistic simulation of cloud-related properties. The following paragraphs present a brief overview of some of the main topics of GCM cloud parameterization.

A fundamental aspect of atmospheric modelling is the difference between the two basic components of a GCM, the (large-scale) dynamics component, and the physics (parameterization) component. While the equations that govern the dynamics are well known (e.g., Navier-Stokes equations of motion), the lack of previously established equations for most of the physics, requires the use of (elaborate) conceptual schemes. This is, primarily, due to the fact that a number of physical process, such as, the ones associated with radiative transfer, turbulent mixing, orographic forcing, moist convection, surface fluxes, or clouds, which have a significant impact on the large-scale circulation, occur at spatial scales smaller than those typically resolved by atmospheric models. It is the need to somehow represent the effects on the atmospheric flow of these subscale mechanisms that is behind the development of parameterization schemes. Or, in other words, the combined influence of the subscale processes needs to be formulated in terms of the basic variables resolved by the models. The

simulation of boundary layer clouds by a GCM relies on a delicate balance between the different physical processes parameterized.

Three main types of cloud parameterization schemes have been used in climate and weather prediction models for some time: *i)* empirical "diagnostic" parameterizations in which the cloud cover is diagnosed as a function of relative humidity and some additional variables (e.g., Slingo 1980); *ii)* parameterizations in which cloud cover and cloud water are diagnosed based in the probability distribution of the subscale variability of thermodynamic variables – PDF (Probability Density Function)-based cloud schemes (e.g., Mellor 1977; Sommeria and Deardorff 1977); *iii)* "prognostic" parameterizations for liquid/solid water and or for the cloud cover (e.g., Sundqvist 1988; Tiedtke 1993).

The scheme proposed by Slingo (1980) is essentially based on the diagnostic relations between cloud cover and relative humidity. One of the main goals of the scheme was then try to represent stratocumulus in a realistic way, given their known importance in the climate system. This was one of the reasons why diagnostic information about the strength of the inversion at the BL-top was also included in the cloud cover parameterization. The link between the amount of stratiform clouds and the intensity of the inversion, briefly described in the previous sections for the subtropical latitudes, is based on observational data (e.g., von Ficker 1936; Klein and Hartmann 1993) whose climatology indicates that, except in the Arctic region, the season with more stratus is simultaneously the one for which the low troposphere static stability is the highest. However, there is in this diagnostic scheme the possibility of a strong positive feedback, since the cloud-top radiative cooling intensifies the inversion which, in turn, results in an increase in the amount of cloud, and so on. Slingo (1987) discusses this feedback in view of observations that suggest its occurrence in the BL. Notwithstanding, the parameterization scheme proposed by Slingo was probably the first one able to (with GCMs) realistically simulate cloud cover associated with stratocumulus.

Contrary to Slingo's diagnostic scheme, developed for GCMs, the Sommeria-Deardorff-Mellor (1977) scheme was initially applied in CSRMs (Cloud-System-Resolving Models) of the BL. Only later they were used in GCMs (e.g., Smith 1984). This scheme is based on the statistical description of subscale condensation processes. In its original paper, Sommeria and Deardorff (1977) proposed a scheme in which it was needed to evaluate double integrals, while Mellor (1977) demonstrated that the problem could be reduced to integration in a single variable.

PDF-based parameterizations constitute, theoretically, an ideal framework for the development of subscale cloud parameterizations, and for the coupling of its sources and dissipative

processes with parameterization schemes for convection and turbulence. Additionally, owing to the intrinsically continuous nature of a PDF, the problems with discontinuities, affecting many of the current cloud parameterization packages that deal with physical processes with associated critical limits (thresholds), can be avoided. The biggest issue with these methods is, however, the determination of the characteristics of the PDF itself, for different situations and cloud types. Some studies have showed that a careful choice of the probability distributions for each specific case yields good results, thus indicating the large applicability of this kind of schemes. See, for instance, the results of the investigation of the subtropical Sc-to-ShCu transition in Bechtold et al. (1995), and Cuijpers and Bechtold (1995).

A statistical scheme presents some advantages when compared to a prognostic scheme, primarily, because it is based on, fairly solid, physical and mathematical concepts, but also because it is diagnostic, thus needing less computational memory and being less prone to numerical instability. However, the implementation of these parameterizations in GCMs can be somewhat difficult, given the complexity of some of its components. Lastly, there is also the problem with the representation of other types of clouds other than the ones associated with the BL, for which the scheme has been validate (e.g., Teixeira 2000).

The implementation of prognostic schemes in GCMs is relatively recent. Until 1991, cloud prognostic schemes treated cloud cover through diagnostic relations (e.g., Sundqvist 1988). During that same year an alternative prognostic scheme for the cloud cover was firstly proposed (Tiedtke 1991; Tiedtke 1993). The scheme was inspired by the need to link the sources of liquid water and cloud cover to convection, and, essentially, consists of two prognostic equations, one for the liquid/solid water (allowing both to coexist), and the other one for cloud cover. In the scheme, the cloud production and dissipation (including BL clouds) is linked to the parameterized physical processes (convection, vertical movement, radiative heating, turbulence), which is desirable, and allows the representation of the main feedback processes among them. However, the intricacy of this link imposes added difficulty to the evaluation of the scheme's global performance, since errors in a certain component can be reflected on the parameters associated with cloud cover, which, in turn, will, potentially, be felt in the rest of the model (e.g., Jakob 1999).

An important limitation to the GCMs' ability of correctly representing clouds, is the vertical resolution adopted. It is well known that a realistic representation of the BL processes requires an adequate vertical resolution in the lower troposphere and, particularly, at the level of the inversion layer at the top of the BL. To tackle that issue, in addition to variable vertical

resolution, there is the need for adaptative grids able to adjust themselves to an inversion known to have important spatiotemporal variation (as discussed in the previous sections). Another important issue has to do with the fact that the different parameterization schemes that comprise the physics of a GCM, differ from each other in terms of the layers of the atmosphere were, ideally, they need higher vertical resolution (e.g. van Meijgaard and van Ulden 1998; Lenderink and Holtslag 2000).

3 The GPCI project

3.1 Introduction

The importance of atmospheric model intercomparison in climate studies was emphasized in 1989 by the Joint Scientific Committee (JSC) of the World Climate Research Program (WCRP). There was then the need for more comprehensive and standardized climate model intercomparison efforts. In 1992 the JSC endorsed the creation of GCSS (Global energy and water cycle experiment [GEWEX] Cloud System Study) as a long term program (Browning et al. 1993; Browning et al. 1994; Randall et al. 2003). GPCI (Global energy and water cycle experiment cloud system study / working group on numerical experimentation Pacific Cross-section Intercomparison) was established in 2004 and joined GCSS a year later (Teixeira et al. 2008a; Teixeira et al. 2011). GPCI is part of the GCSS's GCM (General Circulation Model) community and is dedicated to the intercomparison of three-dimensional (3D) global and regional models.

3.1.1 Background

The GPCI project can be seen as a follow-up to the 3D model intercomparison performed under the European Cloud Systems Study (EUROCS) along a similar cross section in the (sub)tropical NE Pacific ocean (Siebesma et al. 2004). The focus was on the June-July-August (JJA) season, but only monthly means at four times during the day were available during EUROCS. Although meaningful conclusions on model deficiencies could be drawn, the coarse temporal resolution didn't allow for a detailed study of the diurnal cycle. Moreover, there was a lack of observational data with which to validate important aspects of the model simulations, such as the vertical structure of tropospheric temperature and humidity, which had to be evaluated solely against reanalysis data (known to have limitations, especially over remote areas of the global oceans).

As will be seen below in more detail, at the core of GPCI's setup and project protocol is a request for high temporal resolution 3-hourly model output, and observational data. Also a step further from EUROCS is the recent availability of satellite retrievals of the vertical structure of important cloud-related parameters (e.g., temperature, humidity, cloud occurrence) from a new

generation of sensors and platforms (e.g., AIRS [Atmospheric InfraRed Sounder], and CloudSat).

Finally, GPCI is open to the participation of a larger number of atmospheric modelling centers, including American institutions (not present in EUROCS). Also, the inclusion in GPCI of more recent model versions from the centers that participated in EUROCS will allow for an evaluation of the respective model development efforts.

3.1.2 Main goals

As part of the GCSS community, the main goal of GPCI is to characterize deficiencies in the representation of (sub)tropical clouds and cloud-related processes in climate and weather prediction models, with an emphasis on different cloud and convection regimes and on the transitions between them. The GPCI framework is specifically set up for the investigation of three fundamental cloud regimes that typically occur over the eastern boundaries of the (sub)tropical oceans, namely, stratocumulus, shallow cumulus, and deep cumulus. Knowledge gained from a detailed analysis of the behaviour of these cloud systems, and associated dynamical and thermodynamical environments, in models and observations should offer insight for the improvement and development of new parameterizations of clouds, boundary layer, and convection.

A number of core scientific questions guide the progression of the GPCI activities, among them: what controls the diurnal cycle of cloud properties over the (sub)tropical oceans?; how do models represent these processes?; what is the humidity structure in the subtropical upper troposphere?; can models simulate it?; can the current tools for model diagnostic and validation, and available observational data, reveal the deficiencies in the cloud, convection, and boundary layer parameterizations used in state-of-the-art climate and weather prediction models?; how to make GPCI results a reference point for future model development efforts? To answer these questions GPCI is, at the present stage, primarily focused on: ● gathering model and observational data for the JJA season in the GPCI geographical location; ● developing and exploring methodologies for the study of important (sub)tropical cloud regimes (stratocumulus, shallow cumulus, and deep convection) and respective transitions; ● evaluating models and observations for a characterization of the hydrologic cycle; ● understanding the role of the interplay between the large-scale dynamics and environmental factors in the behaviour of the different cloud regimes; ● using and validating the newest generations of cloud-related satellite datasets, namely in what concerns the vertical structure of temperature,

humidity, and clouds; ● describing the (maritime) atmospheric boundary layer representation in models and in observations; and ● helping the participating centers in the development new parameterizations.

The GPCI approach has already proven useful in the fulfillment of some of these goals (e.g., Teixeira et al. 2008a; Karlsson et al. 2010; Teixeira et al. 2011).

3.2 Setup

3.2.1 The NE Pacific Summer

Given GPCI's main goals summarized above (Section 3.1.2), and the fact that the project envisioned the participation of a large number of modelling centers and the extensive use of a variety of observational datasets, there was the need to focus the investigation on a confined geographical area to avoid a computationally demanding data treatment and analysis. This, and the desire to include in the study fundamental (sub)tropical cloud systems, led to the choice of the (sub)tropical NE Pacific ocean region. In fact, the large-scale and environmental conditions found in the NE Pacific area, can, in general, be found in similar regions of the eastern boundaries of the (sub)tropical oceans (e.g., Klein and Hartmann 1993; Sandu et al. 2010).

More specifically, the GPCI region is confined between -5ºN to 45ºN and 160ºE to 120ºW, an area from the coast of California to the Equator, previously the focus of a number of studies of the maritime boundary-layer clouds and cloud-related processes (e.g., Riehl et al. 1951; Klein and Hartmann 1993; Fetzer et al. 2004; Siebesma et al. 2004; Karlsson et al. 2010; Sandu et al. 2010; Teixeira et al. 2011). In terms of the large-scale dynamics, the phenomenology in the region is dominated by the Hadley circulation, with deep convection in the inter-tropical convergence zone (ITCZ), and large-scale subsidence in the subtropics. Fundamental cloud regimes of interest for the GCSS can be found in this oceanic region reasonably well separated in three main cloud regimes, namely, stratocumulus, shallow cumulus, and deep cumulus, often showing characteristic cloudiness transition behaviour. The mean circulation in the region allows a study of the main features associated with the cloud phenomenology resorting only to individual cross sections aligned parallel to the low level trajectories of the atmospheric flow (see Section 3.5 Representativeness of the cross-section). Moreover, the persistency of a relatively well defined Hadley circulation implies that meaningful conclusions can be taken from the investigation of a time period of only a few months. Choosing JJA as the study period is, in part, based on: *i)* the fact that this season typically exhibits small sea surface temperature

(SST) anomaly in the region (1 K to 2 K, overall [see Fig. 4.1]); *ii)* it is the season of maximum occurrence of low clouds (Fig. 3.1); and *iii)* because the diurnal cycle presents its peak amplitude during the summertime (e.g., Rozendaal et al. 1995).

Figure 3.1 illustrates the location of the GPCI cross section in the NE Pacific from the coast of California to the equatorial region, superimposed on a JJA climatology of the low (boundary layer) cloud cover obtained from International Satellite Cloud Climatology Project (ISCCP) observational data.

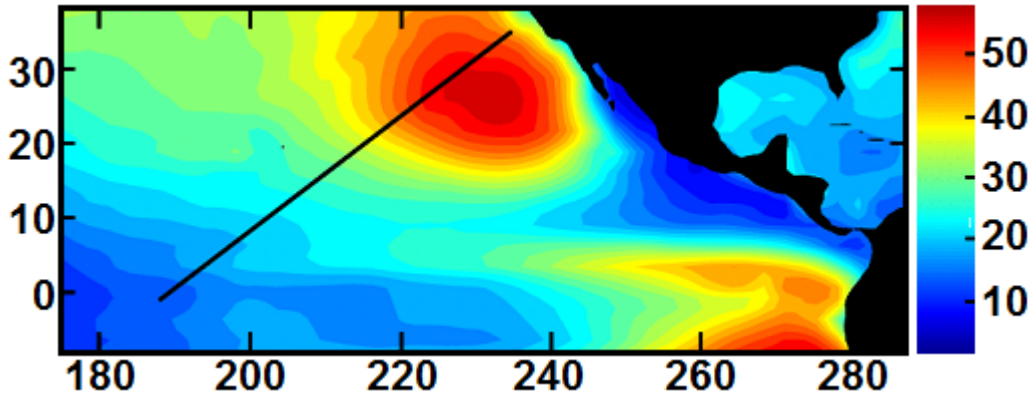

Figure 3.1 - Representation of the GCSS/WGNE Pacific cross section (black diagonal line), and ISCCP low cloud cover (%) climatology for the June-July-August season (courtesy Dr. Cecile Hannay).

3.2.2 Project protocol

GPCI can be seen as a level-2 model intercomparison project (Gates 1992) in which all the participating models have to follow the same line of predefined project specifications and protocols: *i)* simulations made under standard conditions; *ii)* common diagnostics in standard format; and *iii)* validation against common data.

Though standardized, the specifications are kept at a relatively generic level with the basic condition being that the models run in climate mode (i.e., without data assimilation) and using prescribed SSTs as boundary condition. As the period of interest is the JJA season (1998 and 2003), it is advised that the numeric simulations begin by the 20th of May. The requested output corresponds to the period between the 1st of June and the 31st of August. Regarding the geographical area of interest, it is requested that model data be sent for: *i)* 13 locations along the GPCI cross section, starting at 35ºN, 125ºW and moving southwestwards at 4º longitude and 3º latitude steps until -1ºN, 173ºW; *ii)* locations every 5 × 5 degrees in a grid ranging from -5ºN to 45ºN and 160ºE to 240ºE (referred to below as the 2D maps). Finally, the simulation

results are to be submitted in high temporal resolution (every 3 hours at 00, 03, 06, 09, 12, 15, 18, and 21 UTC), and at full vertical resolution, i.e., on model levels.

The following is a list of the different variables of the GPCI standard output.

Vertical profiles as a function of pressure (10 parameters): pressure (hPa), potential temperature (K), specific humidity (g/kg), relative humidity (%), zonal wind (m/s), meridional wind (m/s), vertical velocity (Pa/s), cloud cover (%), liquid water content (g/kg), ice water content (g/kg).

Single-level variables (18 parameters): sea surface temperature (K), outgoing longwave radiation (W/m^2), surface downward longwave radiation (W/m^2), net shortwave radiation at the top of the atmosphere (W/m^2), surface net shortwave radiation (W/m^2), surface downward shortwave radiation (W/m^2), surface latent heat flux (W/m^2), surface sensible heat flux (W/m^2), total cloud cover (%), total column water vapour (kg/m^2), liquid water path (g/m^2), ice water path (g/m^2), convective precipitation (mm/d), stratiform precipitation (mm/d), top of the atmosphere net clear sky shortwave radiation (W/m^2), top of the atmosphere clear sky longwave radiation (W/m^2), surface net clear sky shortwave radiation (W/m^2), surface net clear sky longwave radiation (W/m^2).

2D maps (for 7 parameters): outgoing longwave radiation (W/m^2), precipitation (mm/day), total cloud cover (%), total column water vapour (kg/m^2), liquid water path (g/m^2), relative humidity at 850 hPa (%), relative humidity at 200 hPa (%), vertical velocity at 300 hPa (Pa/s), vertical velocity at 700 hPa (Pa/s).

3.3 Participating models

Over twenty weather and climate prediction organizations have joined GPCI, sending model simulation output following the specifications of the project protocol presented above (Section 3.2.2). Table 3.1 gives a brief description of the participating models, including, model name, type, and horizontal and vertical resolutions. In addition, the table also lists two ECMWF analysis products, ERA-40, and AIRS e-suite, source of data for JJA 1998, and JJA 2003, respectively.

Model information					
Organization	Model	Type	Horizontal resolution	Vertical levels	Model reference
BMRC (Aus)	BAM 4.0.21	Global	T63	60	Zhong et al. (2001)
CCC (Can)	CCCma	Global	T47	35	von Salzen et al. (2005)
CMC (Can)	GEM	Regional	0.5º × 0.5º	53	Côté et al. (1998)
CSU (US)	BUGS	Global	2.5º × 2.5º	29	Colorado State University (2010)
CSU (US)	MMF	Global/MMF	T42	30	Khairoutdinov et al. (2005)
DWD (Ger)	GME	Global	59.9 km	31	Majewski et al. (2002)
ECMWF (UK)	ECMWF	Global	T399	62	ECMWF (2006)
ECMWF (UK)	ERA-40 (CY23R4)	Global	T159	60	Uppala et al. (2005)
ECMWF (UK)	AIRS e-suite (CY26R3)	Global	T511	60	McNally et al. (2006)
ETH-MPI (Ger)	ECHAM5	Global	T42	19	Roeckner et al. (2003)
GFDL (US)	AM2p12b	Global	2.0º × 2.5 º	24	Anderson et al. (2004)
GKSS (Ger)	CLM	Regional	50 km	32	Steppeler et al. (2003)
JAMSTEC (Jap)	AFES2	Global	T239	96	Kuwano-Yoshida et al. (2010)
JMA (Jap)	GSM0412	Global	T106	40	Matsumura et al. (2002)
KNMI (Ned)	RACMO2.1	Regional	0.5º × 0.5º	40	van Meijgaard et al. (2008)
LMD (Fra)	LMDZ4	Global	2.50° × 3.75°	19	Hourdin et al. (2006)
Météo-France (Fra)	ARPEGE	Global	T63	31	Gibelin et al. (2003)
NASA-GISS (US)	GISS III 3.3	Global	2.0º × 2.5º	32	Schmidt et al. (2006)
NCAR (US)	CAM 3.0	Global	T42	26	Collins et al. (2006)
NCEP (US)	GFS&MOM3	Global coupl.	T382	64	Saha et al. (2006)
NCEP (US)	GFS	Global	0.5º × 0.5º	64	Environmental Modeling Center (2003)
UCLA (US)	UCLAtm7.3	Global	2.5º × 2.0º	29	Gu et al. (2003)
UCSD (US)	RSM	Regional	180 km	17	Juang et al. (1997)
UKMO (UK)	HadGAM	Global	1.250º × 1.875º	38	Johns et al. (2004)
UQM (Can)	CRCM	Regional	180 km	29	Plummer et al. (2006)

Table 3.1 - Basic information about the models that joined GPCI, with a listing of the corresponding organizations, the model name and type, the horizontal and vertical resolutions used in the simulations, and the model references. The table also lists two ECMWF analysis products (ERA-40, and AIRS e-suite [ECMWFan]).

3.4 Observational datasets

In GPCI, a special attention is given to satellite data, seen as the truth against which to evaluate the model simulations. In fact, satellite observations have been a crucial tool for recent progress in the understanding of clouds as key players in the climate system (e.g., Ramanathan et al. 1989; Harrison et al. 1990; Rossow and Schiffer 1991; Rossow and Schiffer 1999; Wielicki et al. 1995; Chylek et al. 2007), and for the validation of climate and weather prediction models (e.g., Cess et al. 1997; Webb et al. 2001; Randall et al. 2003; Zhang et al. 2005).

A collection of satellite data has been prepared for GPCI by the GCSS Data Integration for Model Evaluation (DIME) initiative. These datasets include high temporal resolution data from

the International Satellite Cloud Climatology Project (ISCCP), together with daily products from the Special Sensor Microwave Imager (SSM/I), the Global Precipitation Climatology Project (GPCP), and the Television Infrared Observation Satellite (TIROS) Operational Vertical Sounder (TOVS). Given it's 3-hourly temporal resolution, the ISCCP cloud data has been particularly useful in the study of cloud regime transitions in the GPCI region. Note, however, that the model total cloud cover simulations have, this far, been directly compared against ISCCP total cloud cover information, without resort to the ISCCP simulator (Klein and Jakob 1999; Webb et al. 2001), a tool that converts cloud-related information from the models into ISCCP cloud properties (cloud top pressure, cloud amount, and cloud optical thickness). No ISCCP simulator output was requested because many of the participating centers had not implemented the tool in their respective models.

In fact, the bulk of the observational data used in this study was retrieved from the GCSS-DIME Web site in formats prepared for the GPCI project area of interest: see "CROSS-PAC" and "GPCI" at http://gcss-dime.giss.nasa.gov/. CERES (Clouds and the Earth's Radiant Energy System) ES9 (Earth Radiation Budget Experiment [ERBE]-like Science product 9) data were obtained from the Atmospheric Science Data Center (ASDC) at the National Aeronautics and Space Administration (NASA) Langley Research Center (http://eosweb.larc.nasa.gov/). The SSM/I data and images are produced by Remote Sensing Systems (RSS) and sponsored by the NASA Pathfinder Program for early Earth Observing System (EOS) products. SSM/I is onboard polar orbiting satellites, property of the Defense Meteorological Satellite Program (DMSP). Retrievals from three DMSP satellites carrying SSM/I (F11, F13, and F14) operational during JJA 1998 were used. RSS SSM/I can be found online at http://www.remss.com/ssmi/ssmi_description.html. The GPCP dataset combines precipitation information from several sources. Microwave estimates are based on SSM/I, infrared (IR) precipitation estimates are obtained from geostationary satellites and polar-orbiting satellites, and gauge data are assembled and analyzed by the Global Precipitation Climatology Centre (GPCC). A hierarchy of geostationary (GOES [Geostationary Operational Environmental Satellite], GMS [Geosynchronous Meteorological Satellite], Meteosat) and polar orbiting (NOAA [National Oceanic and Atmospheric Administration]) satellites are used by ISCCP to retrieve and calculate cloud related products.

Other important observational datasets used in GPCI are opportunely described in following sections of this thesis, whenever specifically applied for model evaluation, these include: cloud occurrence information from CloudSat and CALIPSO (Cloud-Aerosol Lidar and Infrared

Pathfinder Satellite Observations), cloud-top-height data from MISR (Multiangle Imaging Spectroradiometer), temperature and humidity profiles from AIRS, and 3-hourly precipitation information from TRMM (Tropical Rainfall Measuring Mission).

Table 3.2 gives basic information on the observational datasets used in this work, including, dataset name, horizontal and temporal resolution of the data products, and the parameters retrieved.

Observational Datasets					
Source	Dataset	Reference	Hor. res.	Δt	Parameter
ASDC	CERES ES9	Wielicki et al. (1995)	2.5° × 2.5°	Monthly	NSRTOA, OLR
GCSS-DIME	SSM/I	Wentz (1997)	0.25° × 0.25°	2-daily	TCWV, LWP
GCSS-DIME	ISCCP DX	Rossow and Schiffer (1999)	0.5° × 0.5°	3-hourly	TCC
GCSS-DIME	ISCCP PCTAU (D1)	Rossow and Schiffer (1999)	GPCI section	3-hourly	TCC
GCSS-DIME	GPCP v.2	Huffman et al. (1997)	1° × 1°	Daily	Precipitation
CloudSat	CWC RO4	Li et al. (2008)	1° × 1°	Daily	LWC
CloudSat	GEOPROF	Mace et al. (2007a)	2° × 2°	Monthly mean	Cloud occurrence
CALIPSO	GEOPROF-LIDAR	Mace et al. (2007b)	2° × 2°	Monthly mean	Cloud occurrence
ASDC	MISR level-2 wind-corrected CTH	Zong et al. (2002)	1 × 1 km^2	Daily	Cloud-top height
GSFC-DAAC	AIRS level-2 version 3.0	Fetzer et al. (2003)	~ 45 km	Dailly	Water vapor, Temperature
GES-DISC	TRMM 3B42	Huffman et al. (2007)	0.25° × 0.25°	3-hourly	Precipitation

Table 3.2 - Basic information on observational datasets used for GPCI model evaluation. This table lists the data center source of the observations, the dataset name, the horizontal and temporal resolutions of the data products, the parameters retrieved, and relevant product references.

3.5 Representativeness of the cross section

As mentioned above in the GPCI project protocol (Section 3.2.2), in addition to the data requested for the 13 locations along the GPCI cross section, seven parameters are requested for a larger domain, the "2D maps", encompassing the section and a broad area of the (sub)tropical NE Pacific. Two basic ideas are behind these maps: 1) the fact that a single cross section may miss relevant phenomena occurring in its vicinities (e.g., the diurnal cycle over the stratocumulus regions close to the coast of California may be modulated by subsidence caused by convection events over land, which can only be inferred from the analysis of the land portion of the 2D maps, since the GPCI transect is exclusively maritime); and 2) the need to answer the question about the representativeness of the transect, in the sense of, to what degree can any findings based solely on the analysis of data along the transect be extrapolated to the

broader area of the (sub)tropical NE Pacific. This last point is addressed in the next paragraphs resorting to two different types of results.

Firstly, ERA-40 winds are used to produce histograms of wind direction in a number of transect locations to infer the degree of alignment of the GPCI section relative to the low level trajectories of the atmospheric flow. More precisely, 1000 hPa and 900 hPa JJA 1998 winds were analyzed at six different locations, as shown in Fig. 3.2.

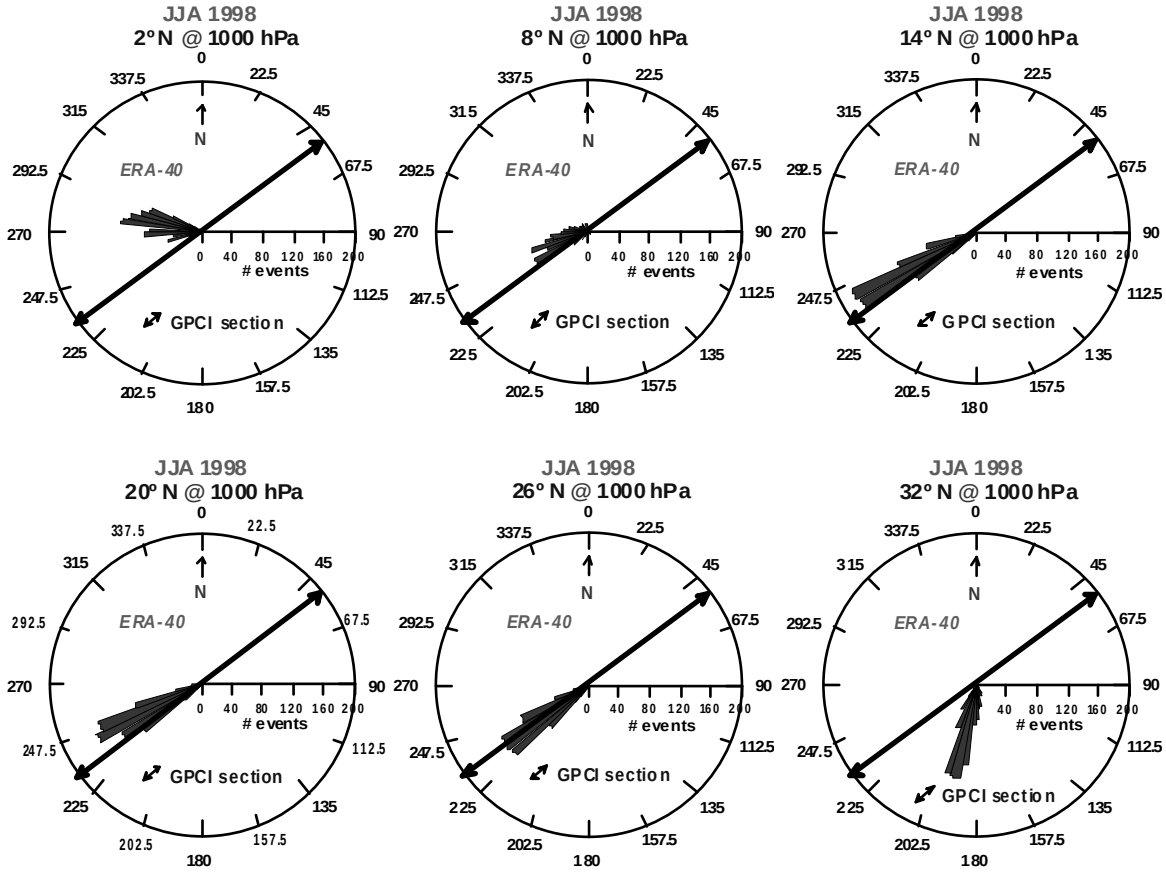

Figure 3.2 - Histograms of wind direction at 1000 hPa for six points along the GPCI transect from ERA-40 for June-July-August (JJA) 1998.

Figure 3.2 shows the wind direction histograms corresponding to the 1000 hPa level, for points 2°N, 8°N, 14°N, 20°N, 26°N, and 32°N. For the sake of brevity, the corresponding results for the 900 hPa level are not shown here. From these histograms it is apparent that, for most of its span, the winds tend to be reasonably parallel to the transect (especially between 8°N and 26°N, at 1000 hPa, and 14°N and 26°N, at 900 hPa). This comes in support of the, previously mentioned, argument that it is possible to study the main features associated with the cloud phenomenology in the GPCI region by resorting only to individual cross sections. Note, however, that, individually, the participating models may differ from ERA-40 in this regard, though, as shown in the next chapter, all of them simulate the main features of the regional

Hadley circulation (as seen in the respective seasonal means along the cross section), thus suggesting that the southeasterly advection of boundary layer air, is, in the models (as in ERA-40), fairly parallel to the GPCI cross section.

The second type of analysis resorts to information from the 2D maps to obtain histograms of cloud-related variables, such as total cloud cover (TCC) and precipitation, not only for the cross section locations but also for longitudinally adjacent points (5° to the east and to the west). Figure 3.3 shows, for the GFDL and the NCAR models, the precipitation histograms for one GPCI point (5°N, 195°E), and two adjacent points, obtained for JJA 1998. Figure 3.4 shows TCC histograms for the same models and season (the GPCI point is now 20°N, 215°E).

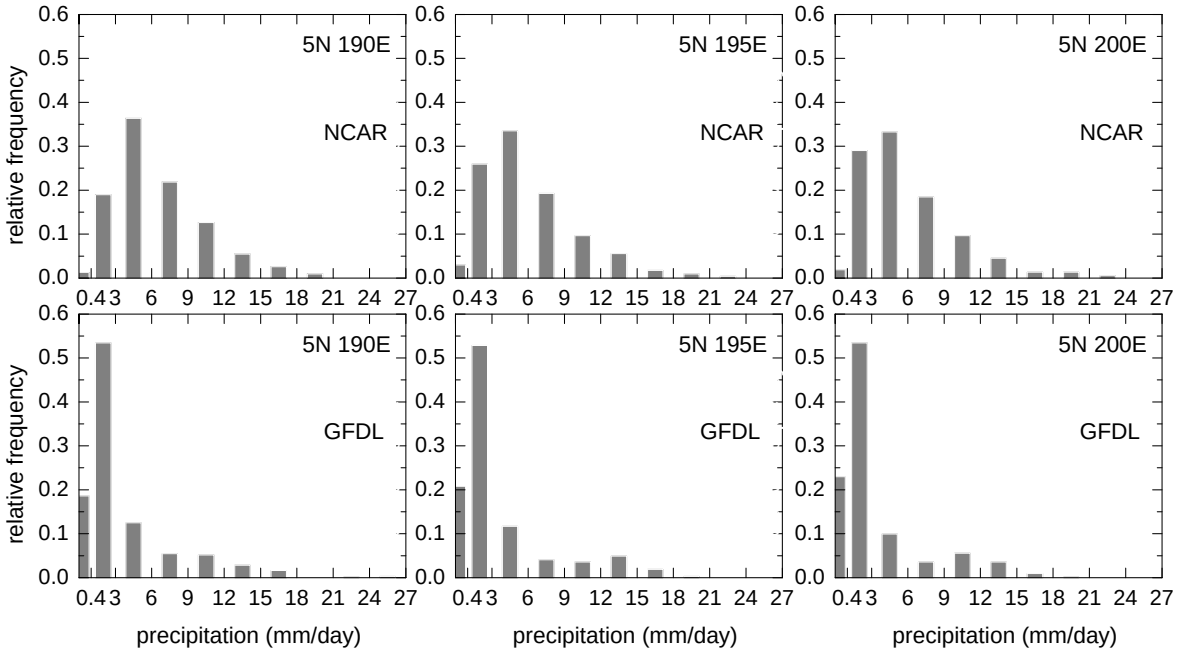

Figure 3.3 - Histograms of precipitation from the NCAR and GFDL models for one GPCI point (5°N, 195°E) and two adjacent (5° to the east and west along the same latitude) points for June-July-August 1998.

For the two parameters shown, there is a clear similarity of the respective histograms between adjacent points for a given model, though quite different results can be found between the two models presented. This is still the case for other transect points and models (not shown).

Once again, these results support the idea that the single-section approach used in GPCI may be able to provide robust conclusions on main model physical processes, not only for the cross section itself, but, as seen in Fig. 3.3 and Fig. 3.4, for the broader region of the (sub)tropics it represents.

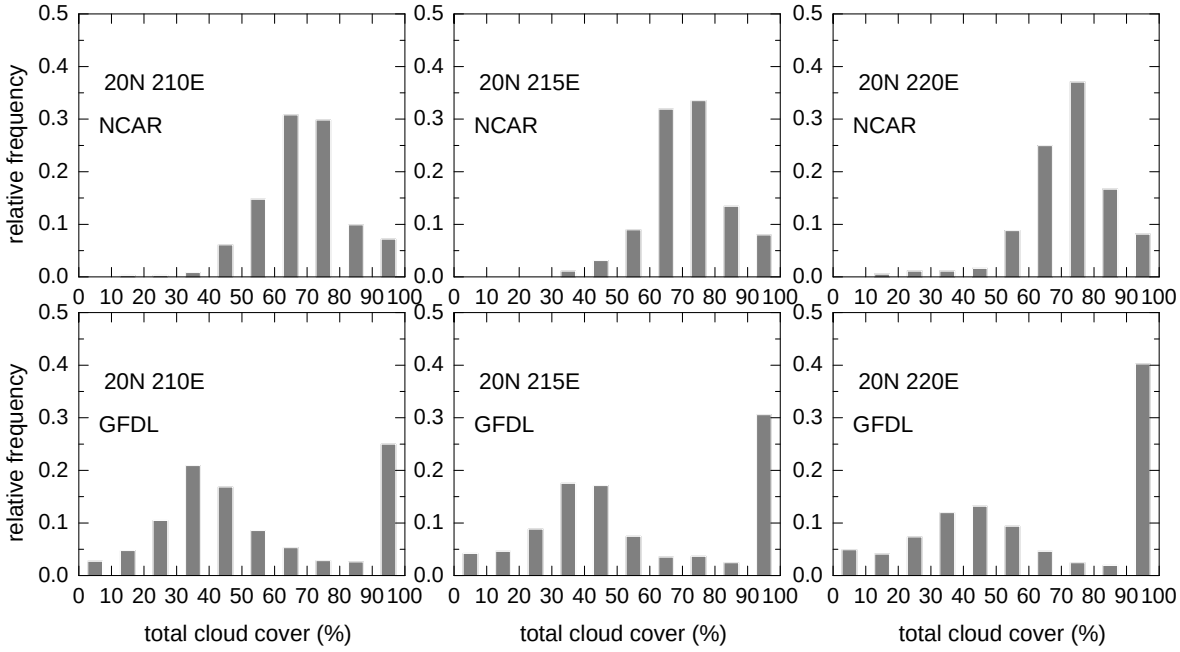

Figure 3.4 - Histograms of total cloud cover from the NCAR and GFDL models for one GPCI point (20°N, 215°E) and two adjacent (5° to the east and west along the same latitude) points for June-July-August 1998.

4 Description of the climatology in the GPCI simulations

This chapter focuses on the first results obtained for GPCI and is intended to give an overview of the mean characteristics of the summertime atmospheric hydrologic cycle in the (sub)tropical NE Pacific as seen in model simulations and in observations, with an emphasis on the vertical distribution of clouds, and on processes involving dynamical and environmental factors that play a role in the maintenance of total and low cloud fields on a seasonal time scale.

The analysis presented here is in part based on the results published in Teixeira et al. (2011), a work that benefited from substantial contributions from the author of this dissertation.

4.1 Sea surface temperatures

As stated in the previous chapter, the basic request for the numerical simulations for GPCI was the use of prescribed sea surface temperatures (SSTs) as a boundary condition for the climate runs, and, except for the coupled ocean-atmosphere version of the NCEP model, this was the case for the participating models, though resorting to the use of slightly different SST analysis datasets and implementation techniques. A quick look at the seasonal mean of the SSTs reported along the GPCI transect is presented below in Fig. 4.1 for June-July-August (JJA) 1998 and 2003.

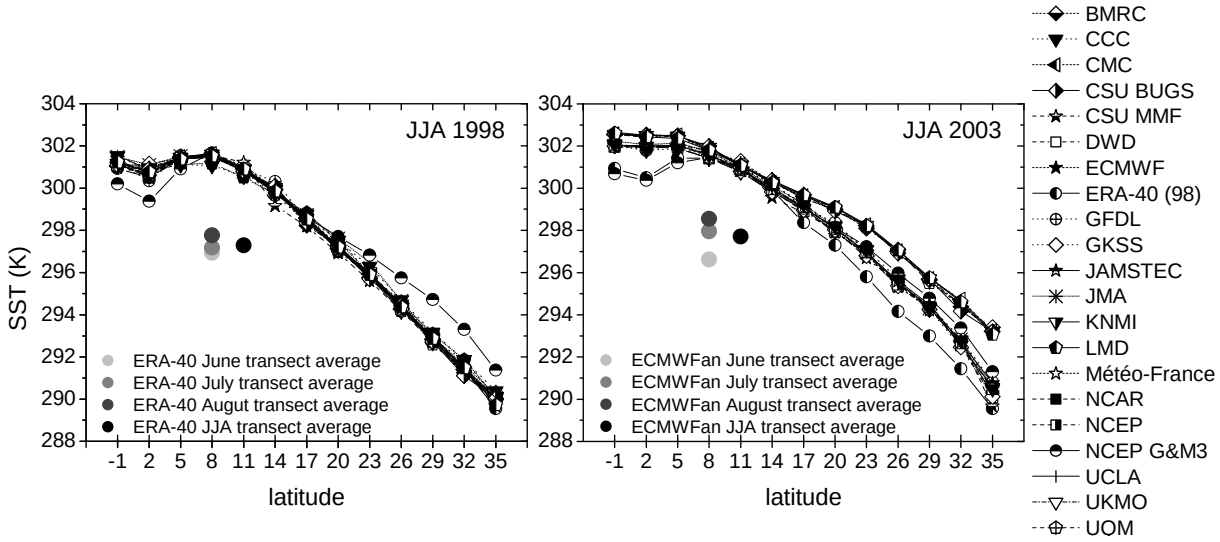

Figure 4.1 - Mean sea surface temperature (SST) along the GPCI transect for June-July-August (JJA) 1998 (left) and 2003 (right) from the participating models and ECMWF analysis.

Three main features can be identified in both plots in Fig. 4.1, namely: *i)* a quasi-linear southward increase of SST along the trade winds, from about 290 K of the relatively cold waters off the coast of California (35°N), to about 301 K, close to 10°N; *ii)* practically constant values in the area under the influence of the inter-tropical convergence zone (ITCZ) (5°N to 11°N); and *iii)* a slight decrease south of the ITCZ. There is, however, some dispersion among the values from individual models, particularly notorious north of 17°N for JJA 2003. Going from 1998 to 2003, there is an overall increase of the SSTs along the transect, more pronounced in its northern half, with an associated decrease in the mean latitudinal SST gradient. For illustration purposes, the monthly and seasonal mean "transect averages" are shown for two analysis products from ECMWF (ERA-40 [1998] and ECMWFan [2003]). These indicate that the increase in the seasonal "transect average" from 1998 to 2003 is mostly due to an accentuated monthly increase in the SSTs from June to July and August 2003 (note that the value for June is lower in 2003 than in 1998).

Finally, the SSTs obtained with the only coupled simulations available (NCEP GFS and MOM3 [NCEP G&M3, in Fig. 4.1]) show very small differences between 1998 and 2003, except in the southernmost portion of the transect, where, even though increased in 2003, the SSTs are still below those from the other models, and are, interestingly, more similar to the 1998 values from ERA-40. Regarding the relatively warm values obtained during JJA 1998 in the subtropical regions, it can be argued that these may in part be associated with underrepresentation of cloud cover probably linked to an important feedback between low clouds and the SST.

4.2 Single-level parameters

This section is dedicated exclusively to JJA 1998 results. Figure 4.2 shows the seasonal mean values of a number of single-level cloud-related parameters. A brief description of these mean fields along the GPCI cross section is given here. A more detailed view can be found in Teixeira et al. (2011).

The analysis starts with total column water vapor (TWV) shown in Fig. 4.2a. TWV's integral nature gives it a key role in the understanding of the atmospheric hydrologic cycle. TWV observations from SSM/I are shown along with reanalysis from ERA-40, and model simulation results represented by the model ensemble average, obtained from the individual seasonal means, and the across-model variability, as seen in the ensemble average plus or minus one

(ensemble) standard deviation and in the range (maximum and minimum) of model values in each one of the transect locations.

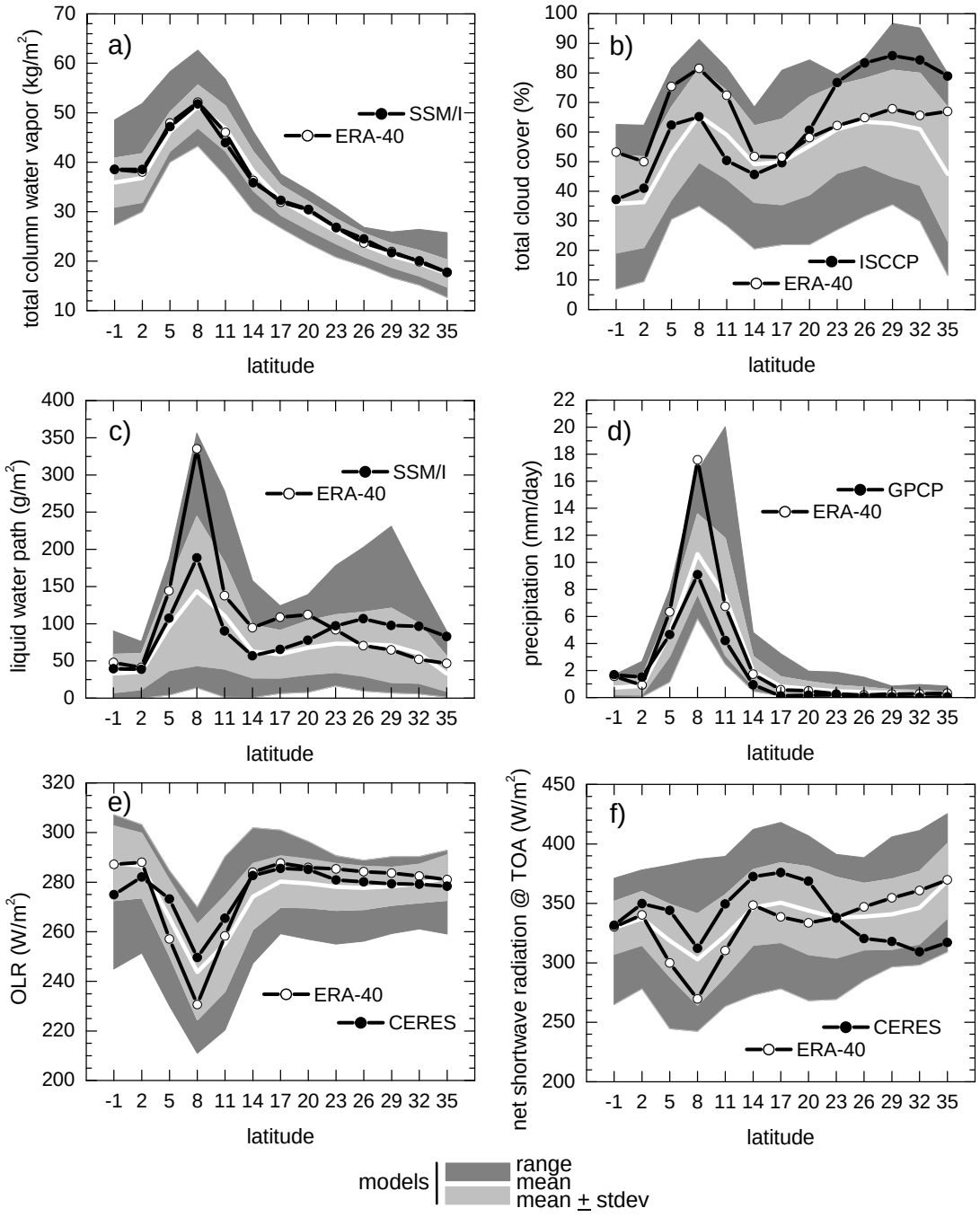

Figure 4.2 - (a) Total column water vapor from the models along GPCI for June-July-August 1998 together with ERA-40 and SSM/I, (b) as in (a) but for total cloud cover and ISCCP observations, (c) as in (a) but for liquid water path, (d) as in (a) but for precipitation and GPCP observations, (e) as in (a) but for outgoing longwave radiation (OLR) and CERES observations, and (f) as in (a) but for net shortwave radiation at the top of the atmosphere (TOA) and CERES observations. Results from the different models are shown as ensemble mean results, the mean plus or minus the standard deviation, and the maximum and minimum values attained by any model for a particular point (referred to as range).

TWV seems to mimic the behaviour of the SST field described above for the portion of the GPCI transect between the stratocumulus regions off California and the ITCZ. In SSM/I terms, the TWV increases from around 18 kg m^{-2} in the northernmost part of the transect (35°N) to about 50 kg m^{-2} at 8°N. Climatologically, these are major changes in the atmospheric column and are related to the transition from a shallow boundary layer, capped by a dry upper troposphere, to a regime characterized by fully developed moist convection events that reach deeper as one approaches the ITCZ. The good agreement between SSM/I and ERA-40 for TWC is worthy of notice and, although somewhat expected, given the fact that ERA-40 assimilates related observational information, can be seen as indicative of good quality of the SSM/I data, while suggesting that ERA-40 reproduces well the component of the hydrological cycle responsible for this integral parameter. Unfortunately, this high degree of agreement is uncommon for the other variables analyzed, as will be seen later. The TWV average for the ensemble of models is also very close to the observations and the reanalysis in all points of the transect, with a relatively small (as compared to other variables) across-model standard deviation. Note, however, that the model range reveal important departures from the observational truth, of concern especially in the stratocumulus regions (north of 29°N) and in the deep tropics (south of 11°N), where the range is O(20 kg m^{-2}). To a great extent, the situation in the stratocumulus is concomitant with the models' representation of the boundary layer, and particularly with its vertical reach, a key feature of the cloudy boundary layer. This will be discussed throughout the remainder of the chapter, and will receive a special focus in Chapter 6.

Figure 4.2b shows the seasonal mean total cloud cover (TCC) field along the GPCI transect for models, ERA-40, and ISCCP observations. Compared to the TWV results, TCC has an accentuated degree of scatter, as seen in the model range and standard deviation, confirming the poor ability of current weather and climate prediction models to simulate clouds. Both ERA-40 and the model ensemble average present important departures from the observations, in contrast with the results discussed above for TWV. More specifically, note in ERA-40 the negative bias in the stratocumulus and initial transition to cumulus (23°N to 35°N), and the positive bias in the ITCZ. In turn, the ensemble average follows the ISCCP TCC relatively well up to 20°N, but is even more negatively biased (-20 % to -30 % bias), as compared to the observations, than ERA-40 north of that location. Contributing to this situation, is the existence, among the available models, of extremely low values of seasonal mean TCC in the stratocumulus regime. Finally, it is important to bear in mind that the current ISCCP products

have uncertainties, particularly for tropical TCC, which is underestimated by about 10 % to 15 %, due to non detection of very thin cirrus (e.g., Stubenrauch et al. 1999). Nevertheless, at the present, it is believed that the ISCCP cloud cover product is more reliable than ERA-40, a reanalysis obtained without assimilation of explicit cloud information (more recent ECMWF reanalysis efforts have shown improvement in the representation of maritime low clouds [Köhler 2005; Hannay et al. 2009] relative to ERA-40).

In relative terms, what is said above about the behaviour of ERA-40 and model ensemble average TCC, as compared to ISCCP observations, is still valid for the liquid water path (LWP) parameter, shown in Fig. 4.2c with observations from SSM/I, namely: *i)* both ERA-40 and the ensemble average are below SSM/I in the stratocumulus regions; *ii)* ERA-40 overestimates LWP over the trade cumulus regions (unlike the ensemble average); *iii)* in the deep tropics, ERA-40 clearly exceeds SSM/I (350 g m^{-2} versus 200 g m^{-2}), where the ensemble average stays close to the observations. Apart from the absolute peak value in the ITCZ, the rest of the cross section (to the north) is characterized by a relatively modest variation of SSM/I LWP, with a minimum value of about 55 g m^{-2} at 14°N, a maximum value of about 110 g m^{-2} at 26°N, and a value of about 80 g m^{-2} at 35°N. That said, it should be noted that microwave instruments such as SSM/I do have significant uncertainties (see Li et al. 2008, for a comparison of LWP products from different satellite observations). The improvement of these observational issues depends on how successful more recent instruments, such as those onboard CloudSat (e.g., Stephens et al. 2002), will be, in helping to clarify and reduce the uncertainties that affect LWP.

Figure 4.2d presents seasonal mean precipitation with observations from GPCP. The first noticeable feature is the key difference (common to all datasets analyzed) between the subtropical regions, where (low) boundary layer clouds prevail, and the ITCZ, dominated by deep convection. In particular, the subtropics receive very small amounts of precipitation, except in the case of (at least) one model with maximum values close to 2 mm day^{-1} in the trade cumulus regions. In the ITCZ, GPCP amounts to around 9 mm day^{-1}, slightly below the model ensemble average, and about half the value for ERA-40. Traditionally, it has been difficult to obtain accurate observations of precipitation in relatively dry areas such as the subtropics (e.g., Adler et al. 2003) and for this reason the error bars for the GPCP product in these regions will be relatively large (e.g., Janowiak et al. 1998) and (percentwise) more important than in the ITCZ.

In Fig. 4.2e, outgoing longwave radiation (OLR) results are shown, with observations from CERES. For the subtropical regions, the model ensemble average, and ERA-40, give OLR values that are, respectively, lower, and higher, than the observations. In the ITCZ-dominated regions, ERA-40 has a negative bias of about 20 W m^{-2} relative to CERES data, while the ensemble average closely follows the observations. As expected, the underestimation of OLR in ERA-40 is consistent with ERA-40's positive biases of TCC, LWP, and precipitation in the ITCZ.

With observations from CERES, Fig. 4.2f presents results for the net shortwave radiative flux at the top of the atmosphere (NSRTOA). It is clear that the reanalysis and the ensemble average have similar values in the subtropical regions and all the way to 14°N, but, while in the stratocumulus areas (north of 23°N) both ERA-40 and the model average are above the observations by up to 50 W m^{-2} (owing to the negative bias in cloud cover and cloud water), in the shallow cumulus regions (between 14°N and 23°N), in turn, both underestimate NSRTOA. In ERA-40 this is consistent with the described overestimation of LWP in the trades. A possible explanation for the corresponding bias of the ensemble average may come from the fact that trade wind cumuli have been found to be too reflective in climate model simulations as compared to observations (e.g., Potter and Cess 2004; Karlsson et al. 2008). Further south, in the ITCZ area, the ensemble average is closer to CERES than ERA-40, which shows a negative NSRTOA bias of ~50 W m^{-2} (possibly in connection with the positive LWP and cloud cover bias found there). Finally, the high scatter among the models is, once again, problematic, and (more poignantly in the case of the shortwave radiation) points out to the need for greater model development efforts, especially thinking about the coupling between oceanic and atmospheric model components, with the purpose of seasonal and climate prediction (recall the case of the coupled model simulations in Fig. 4.1 [SSTs]).

4.3 Profiles along the section

In this section the results from three additional variables are analyzed. The focus is on their summertime seasonal distribution in the vertical along the GPCI cross section. Again, only a brief description of the mean fields is given, and for just a subset of the participating models. For a more comprehensive look, please refer to Teixeira et al. (2011).

Figure 4.3 shows the JJA 1998 seasonal mean subsidence field, as seen along the GPCI transect in model simulations and ERA-40 reanalysis. Qualitatively, the basic features associated with the regional Hadley circulation can be easily identified in all of the individual results presented: with upward motion in the ITCZ, and a broad area of downward motion characterizing the subtropical free troposphere. A closer look, however, reveals several substantial differences between the models, namely: very shallow upward-motion layers in the ITCZ (e.g., ETH/MPI); the width of the deep convection area (e.g., BMRC versus UKMO); and the strength of the deep convection (e.g. NCAR versus ERA-40).

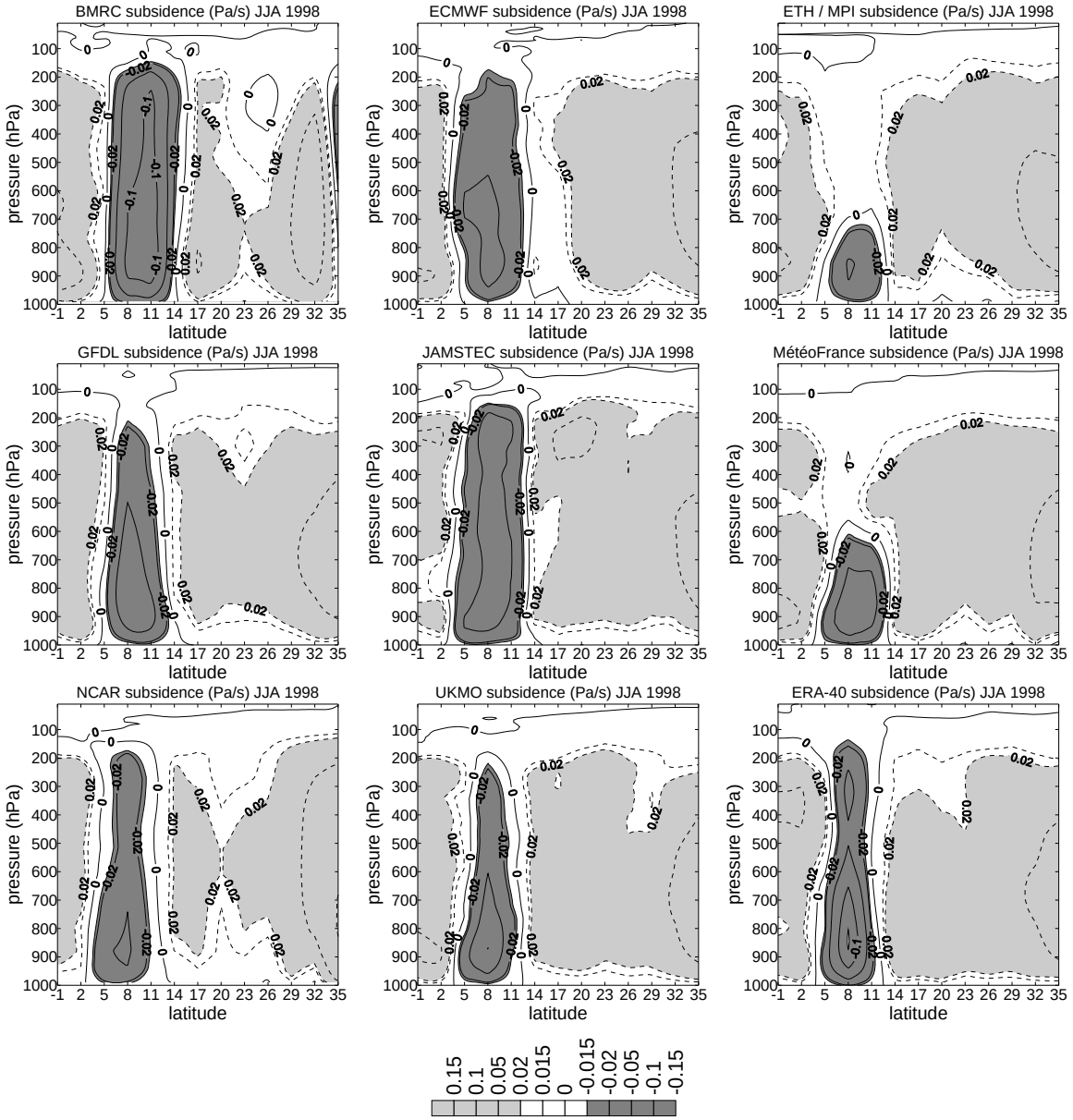

Figure 4.3 - Vertical cross sections of subsidence along the GPCI transect for June-July-August (JJA) 1998 from models and ERA-40.

Less pronounced, but still important, are also the differences in the subsidence field in the subtropics, particularly for the free-troposphere above the trades (17°N to 23°N).

Finally, note, how relatively low in the vertical profile, rather strong values of subsidence can be felt in ERA-40 (and to some extent in UKMO) between 14°N and 35°N. Knowing the role of the vertical structure of subsidence on the vertical extent of the (cloudy) boundary layer, the differences in model behaviour reported here can (at least) partly explain the differences in the simulated characteristics of boundary layer convection and clouds.

The figure that follows presents the results pertaining to the seasonal mean relative humidity for ERA-40 and the same models analyzed in Fig. 4.3.

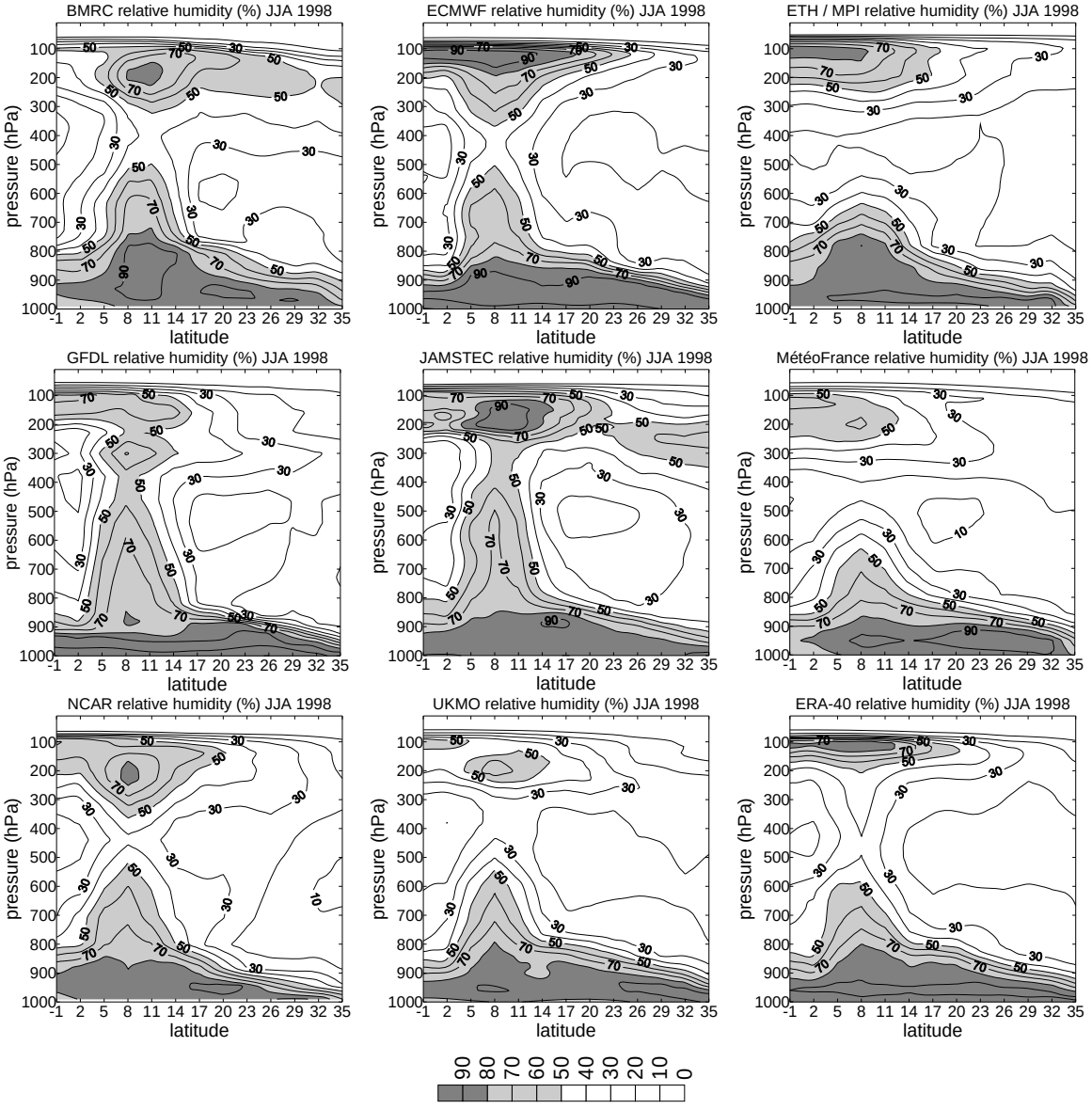

Figure 4.4 - Vertical cross sections of relative humidity along the GPCI transect for June-July-August (JJA) 1998 from models and ERA-40.

A first glance at these profiles reveals that, qualitatively, the models and ERA-40 reproduce the main features of a Hadley-like circulation including: a moist boundary layer that evolves from shallow, in the northern portion of the transect, to deeper, in the trades; an ITCZ with high relative humidity values throughout the troposphere; and a very dry subtropical free troposphere (a result of the large-scale subsidence that dominates the local dynamics). However, as seen in the subsidence results, a more detailed comparison shows significant differences among the models. It should be kept in mind that, as a key player in the hydrologic cycle, relative humidity can be very informative of model deficiencies in its characterization. In the case of the simulated boundary layer (as perceived from the relative humidity signature), the most striking difference is in the way it grows from the stratocumulus to the shallow cumulus regions. In the ITCZ area, the differences pointed out above for the vertical velocity field are now even more obvious, especially in what concerns the strength and width of the deep convection. Another interesting feature is the minimum in relative humidity around 400 hPa in the ITCZ (the models do not agree on its absolute value). To conclude, recall that a direct comparison between simulated and observed relative humidity is performed in Chapter 6, resorting to satellite (AIRS) data.

The last variable chosen for analysis in this section is (cloud) liquid water content, shown in Fig. 4.5 for models, ERA-40, and satellite observations from CloudSat (e.g., Stephens et al. 2008). The CloudSat results correspond to the climatology for JJA for the period 2006 to 2010. Known issues with this observing system, especially in getting information close to the ground (in the first km above the surface), and insufficient vertical resolution (~ 250-500 m), affect its reliability in what concerns the boundary layer liquid water content, and can explain a somewhat flat stratocumulus-to-cumulus transition, as compared to most models (though overall showing a similar content of liquid water). Further south, in the deep tropical regions, the variety of cloud liquid water vertical structures among the datasets shown is striking, with some models (e.g., JAMSTEC) showing virtually no liquid water in the lower troposphere, while reporting its existence erroneously high in the profile. Finally, it is apparent that UKMO is the model that most closely follows CloudSat's observations of liquid water content, especially south of 26°N and up to 700 hPa in the ITCZ region, and thus, can be considered the most accurate simulation among the different models. Bear in mind, however, that such a conclusion is somewhat superficial, given the fact that the CloudSat retrieval algorithm uses a fairly simple mixed-phase relation resorting to temperature information from ECMWF analysis.

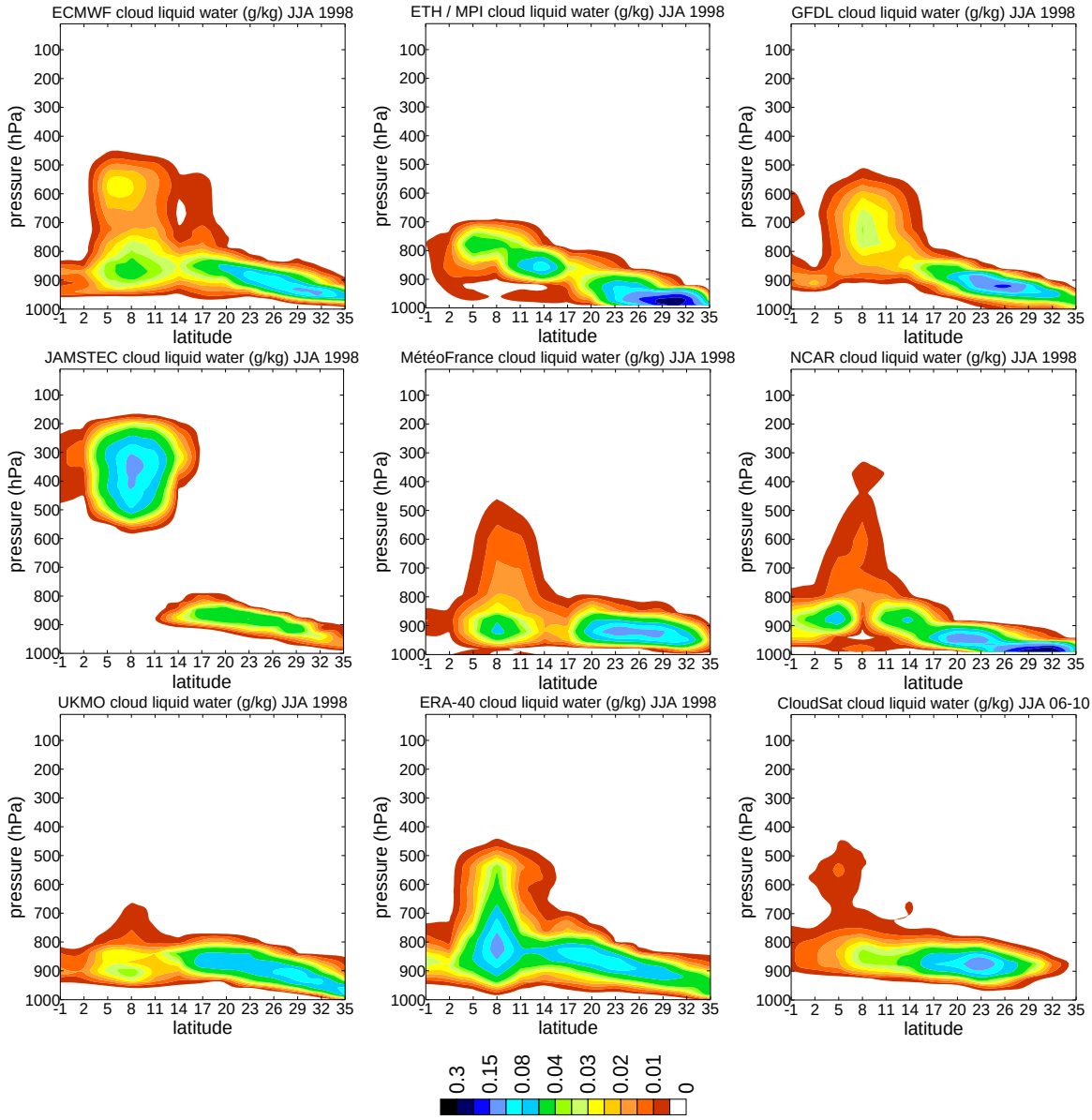

Figure 4.5 - Vertical cross sections of liquid water (content) along the GPCI transect for June-July-August (JJA) 1998 from models and ERA-40, and for JJA 2006-10 for CloudSat observations.

4.4 Vertical distribution of clouds

Having analyzed the vertical distribution of subsidence, relative humidity, and liquid water content along the GPCI transect in the previous section, the attention will now be directed to cloud fraction, a key parameter of the phenomenology associated with the thermodynamics of the hydrologic cycle. The section starts with a discussion of pertinent satellite observations, followed by analysis of results from the models and reanalysis (see Teixeira et al. [2011] for a more in-depth discussion).

Figure 4.6 shows the vertical distribution of clouds along the GPCI cross section, as inferred from cloud occurrence products retrieved by sensors on board the CloudSat and CALIPSO satellites during JJA 2006, together with the result from a combination of those two products. CloudSat and CALIPSO are members of the NASA's A-Train, a constellation of six satellites flying in formation and in close proximity. The differences found between the cloud distributions obtained by each satellite are associated with the specific targets the corresponding sensors where built to look at.

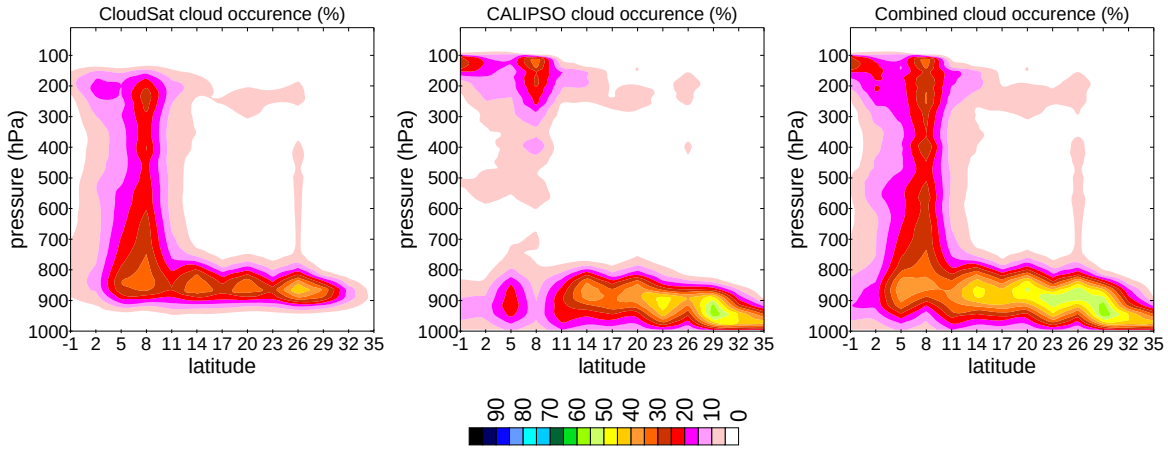

Figure 4.6 - Vertical cross sections of cloud occurrence along the GPCI transect for June-July-August 2006 from CloudSat (left), CALIPSO (center), and a combination of both (right) (see text for details).

With nearly identical orbits, CloudSat and CALIPSO carry two active sensors designed for the mapping of hydrometeors and aerosols, respectively, the Cloud Profiling Radar (CPR) (Im et al. 2006), and the Cloud-Aerosol Lidar with Orthogonal Polarization (CALIOP) (Winker et al., 2007). Essentially, the lidar detects optically thin cloud layers, but cannot penetrate very deep into (dense) cloud tops, while the radar is able to retrieve information from deeper in thick hydrometeor layers, but is limited by detection thresholds and contamination from surface clutter. These constraints are responsible for some of the features in the CloudSat and CALIPSO plots in Fig. 4.6, namely, less cloud occurrence in the ITCZ for CALIPSO, as compared with CloudSat, and the “clear” surface layer in CloudSat. Note that CALIPSO’s relatively high cloud occurrence in the subtropics (north of 23°N along the transect) is somewhat expected, and is an indication that stratocumulus decks form in the region in conditions unfavorable to the existence of upper-level optically-thick cloud layers.

There seemed to be enough reasons to envision the merging of information from CPR and CALIOP, especially in face of their virtually simultaneous measurements. The cloud occurrences shown in the right plot in Fig. 4.6 were extracted from a dataset obtained from the

combination of the CloudSat Geometrical Profiling Product (GEOPROF) (Mace et al. 2007a) with GEOPROF-LIDAR data (Mace et al. 2007b), a mapping of the CALIPSO cloud mask onto the radar footprint. These combined products play an important role in climate model validation efforts (e.g., Zhang et al. 2010). For GPCI, a more comprehensive view of the vertical structure of the cloud systems along the transect seems to emerge with this combined approach.

Figure 4.7 shows corresponding results for the vertical distribution of cloud fraction from a few of the participating models, and ERA-40, for JJA 1998.

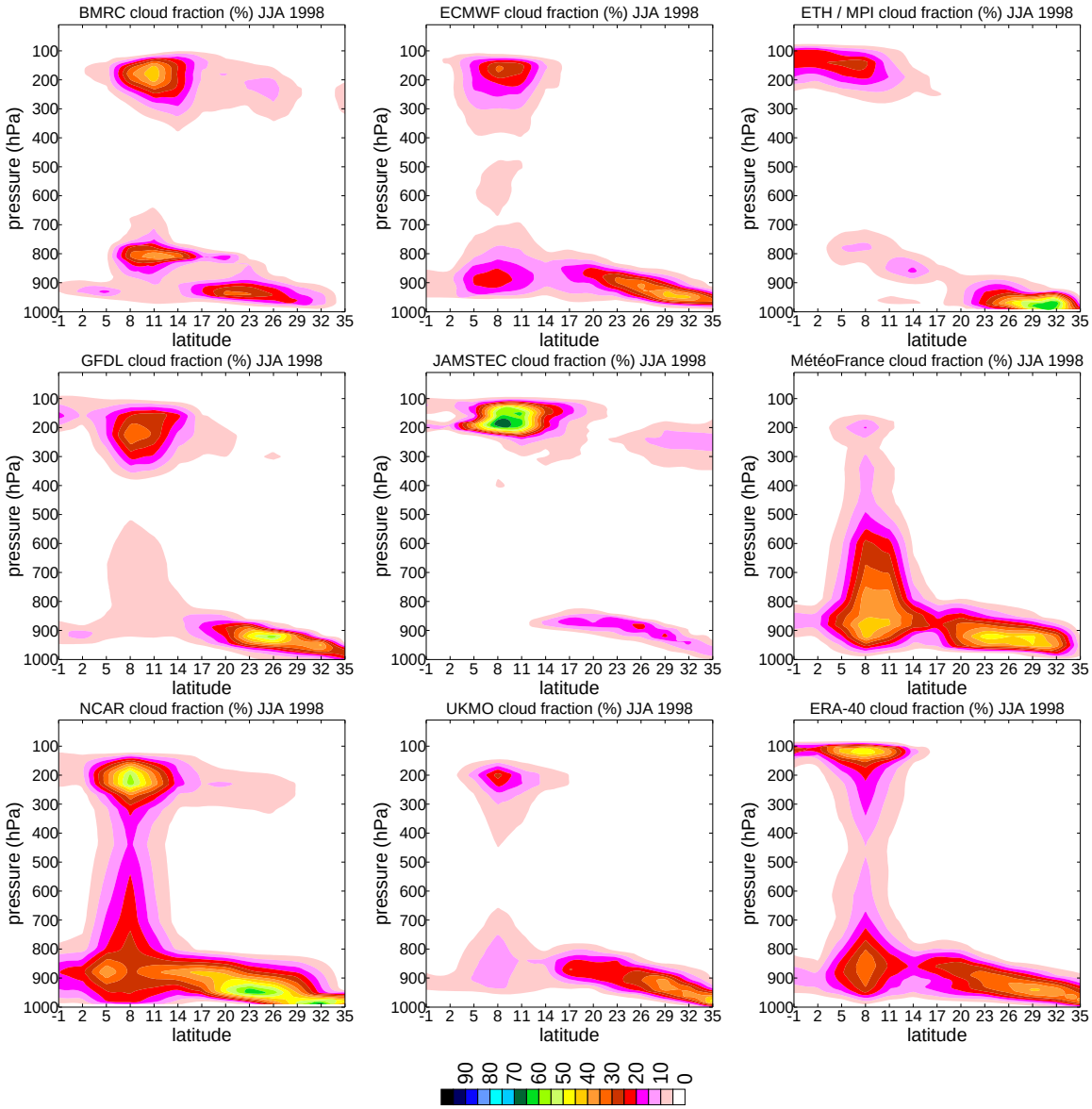

Figure 4.7 - Vertical cross sections of cloud fraction along the GPCI transect for June-July-August (JJA) 1998 from models and ERA-40.

The challenges in the parameterization and simulation of clouds in climate models are well illustrated in Fig. 4.7, with models showing a variety of behaviours in the representation of the

different cloud types and transitions that characterize the GPCI region. Moreover, the value of GPCI's relatively straightforward approach in trying to tackle these issues is well patent here, as it allows for the simultaneous evaluation of a number of important cloud and convection regimes.

Among the models shown, there is, in general, a qualitatively good representation of the evolution of the depth of the cloudy boundary layer going from the stratocumulus regions to the deep tropics, with ECMWF, GFDL, and UKMO more realistically getting the expected smooth and gradual deepening boundary layer (e.g., Karlsson et al. 2010). There are, however, some noteworthy issues including: *i)* too low stratocumulus clouds (e.g., NCAR); *ii)* presence of distinct cloud layers in the transition areas (e.g., between 14°N and 23°N in BMRC); and *iii)* very small cloud fraction (e.g., JAMSTEC). The differences in the ITCZ are significant, as well, with some models showing substantial cloud fraction at all levels in the column (e.g., NCAR), in contrast with models with negligible amounts in the lower troposphere, but with large values in the upper troposphere (e.g., JAMSTEC); or models with large values in the lower troposphere, but with relatively low amounts in the upper troposphere (e.g., Météo-France). Finally, a quick comparison with the results in the right plot in Fig. 4.6, reveals NCAR as the most accurate simulation of the vertical distribution of cloud fraction, even more so than ERA-40.

4.5 Process studies

Keeping the focus on the climatological characterization of the hydrologic cycle, as inferred from cloud and cloud-related parameters associated with the different regimes found along the GPCI cross section, a process-oriented study is proposed here to investigate the interplay between dynamical and environmental variables which potentially impact cloud formation and characteristics in the GPCI region. The main goal is to describe the models' response to a variety of large-scale and surface forcings. Given the fact that the analysis is based on a relatively limited time period (JJA 1998 and 2003), the results presented here should be regarded as only preliminary.

In Section 4.5.1, the influence of the (prescribed) SSTs, on the large-scale atmospheric circulation, and on a number of parameters, is investigated based on monthly means taken along the GPCI section. In Section 4.5.2, the investigation goes a step further and looks at the

relation among subsidence, cloud cover, SST, and atmospheric stability obtained directly from the available 3-hourly model and reanalysis data.

4.5.1 Monthly means versus SST

A relatively straightforward approach was taken to obtain, for the model simulations and ECMWF analysis, the relations between SST and, vertical velocity at 700 hPa (w700hPa), total cloud cover (TCC), liquid water path (LWP), precipitation (P), outgoing longwave radiation (OLR), and net shortwave radiation at the top of the atmosphere (NSRTOA), shown in Fig. 4.8.

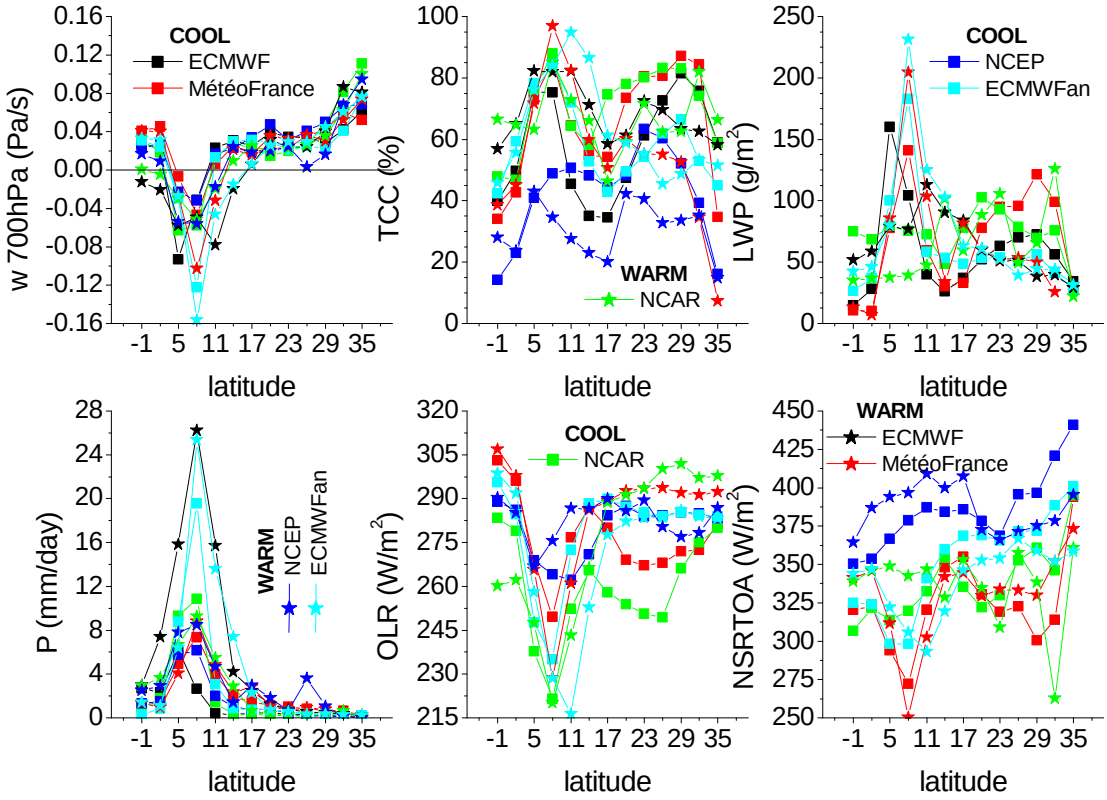

Figure 4.8 - Vertical velocity at 700 hPa (w700hPa), total cloud cover (TCC), liquid water path (LWP), precipitation (P), outgoing longwave radiation (OLR), and net shortwave radiation at the top of the atmosphere (NSRTOA) along GPCI from models and ECMWF analysis (ECMWFan) composited for the months with the coolest (spatially averaged) monthly mean SST (COOL [squares]) and warmest (spatially averaged) monthly mean SST (WARM [stars]) among June, July, and August from 1998 and 2003.

At a first step, the coolest and warmest months, in terms of the transect-averaged SST, were identified from the six months that comprise the two JJA seasons in 1998 and 2003 (the available periods for GPCI). For the months thus identified, the corresponding monthly means for the other parameters were then calculated at a second stage. In the results shown, the coolest- and warmest-SST months have been found to be June 1998 and August 2003, respectively (June 2003 and August 2003 in the case of the ECMWF analysis, for which only

2003 data were available). Essentially, all of the datasets have ~ 297 K for the coolest month, and ~ 299 K for the warmest month, which implies a ~ 2 K SST departure between the "cool" and "warm" fields presented in Fig. 4.8.

As stated above, the main goal here is to analyze how, in a climatological sense, cloud-related parameters change in relation to changes in large-scale dynamical and environmental variables. In this particular case, the investigation of changes between cool- and warm-SST months, basically follows an approach widely used in climate sensitivity studies, that tries to characterize the simulated model response to specific perturbations imposed to the (prescribed) SST field. Spatially uniform perturbations of +2 K and -2 K are traditionally used (e.g., Cess et al. 1996; Bony et al. 2004), complemented by more complex spatially and time varying SST perturbations (e.g., Wyant et al. 2006). From what is said in Section 4.1, the SSTs prescribed in the GPCI simulations correspond to analysis, and are thus quite realistic, in general showing, for 2003, not just an overall increase, as compared with 1998, but also an accompanying decrease in the along-transect gradient in the trades (Fig. 4.1). Recall, though, that there are slight dataset and implementation-technique differences among the different simulations used here. In the ideal situation all models use the same SSTs, as is done in the traditional approach.

The fields of vertical velocity at 700 hPa (w700hPa) produced for both "cool" and "warm" months are, overall, qualitatively similar, and, as expected, depict the ascending and descending branches of the Hadley circulation, with negative values of the pressure velocity in the ITCZ (~ 5°N to 11°N) and positive values elsewhere, that peak in the subtropics (32°N to 35°N). It is between 17°N and 29°N (mostly in the trades) that the different results agree the best. In terms of the differences going from the "cool" to the "warm" months, the results show: a general intensification (except for the maximum values for NCAR and ECMWF, that have a slight decrease) and widening (especially towards the north) of the deep convection area associated with the ITCZ; a decrease in subsidence at 17°N; in the trades, and all the way to 32°N, the datasets do not agree in their response, showing both slight decreases or increases in subsidence (except for NCEP, that shows a consistent decrease, and for ECMWFan, that shows an overall increase); at 35°N there is, in general, a marked increase in subsidence, the exceptions being ECMWFan, that basically doesn't change, and NCAR, that decreases. In fact, two mainly distinct behaviours can be found, on one side, NCAR simulates an overall weaker Hadley circulation in the warm month, in clear contrast with ECMWFan, that intensifies the Hadley circulation in response to the higher SSTs. In conclusion, there, is overall, a noticeable

response of the large-scale circulation to the change(s) in the prescribed SSTs in all the models (and analysis) shown.

Regarding the cloud cover response, the ITCZ shows a clear overall increase in TCC in all of the datasets (except for NCEP). To some extent, this is expected, given the fact that the warmer SSTs have been found to favor an increase in the deep convective activity in this area. Note that the decrease in the peak absolute value of w700hPa in the ITCZ (8°N) for NCAR is associated with a relatively shy increase in TCC, as compared with the responses in the other datasets. The response in the ITCZ is in contrast with the situation to the north of 17°N, where the models show lower values for the warm-month TCCs versus the cold-month TCCs. Again, this is to some extent expected in these regions, and a positive sign (from a climate modelling perspective) since warmer SSTs tend to be more favorable to shallow-cumulus clouds and less favorable to the formation of extensive stratocumulus cloud decks (at 26°N and 29°N all results agree in the TCC decrease). In this regard, and looking closer, a couple of results stand out in that they seem less intuitive, namely, the increases in TCC at 32°N and 35°N for NCAR, and at 35°N for ECMWFan. In NCAR this is even more striking, since, accompanying the increase in SST, there is also a decrease in the intensity of the subtropical subsidence (w700hPa). Assuming that the TCC at 29°N and 32°N is essentially associated with low boundary layer cloudiness, and taking into account ECMWF and ECMWFan in that area, one could argue that the fact that their (spatially-averaged) TCC decreases in the "warmer" SST month, even in face of relatively important concomitant increases in the local "warm-month" subsidence, are an indication of a cloud response more directly connected to the change in the thermodynamic state of the lower troposphere (e.g., its static stability [typically negatively correlated with the SST]) than with the change in the large-scale dynamics (at least as translated by w700hPa). This is in line with some of the findings by Sandu et al. (2010).

In terms of the LWP variable, ECMWFan, MétéoFrance, and ECMWF, show a behaviour similar to that of their respective TCC parameter. The responses in TCC and LWP aren't as clear for NCAR, with at least five locations along the transect showing LWP and TCC with opposing responses. Overall, it seems as if the previously described weakening of the Hadley circulation in NCAR entails lower values of simulated LWP in the GPCI region. There is, however, some interesting regional variation in NCAR's behaviour, especially in the distinct decreases in LWP between -1°N and 11°N (ITCZ included), in clear contrast with the average increase between 32°N and 35°N (well in the subtropical stratocumulus area) where, as stated above, TCC also increases. Again, NCAR seems to respond with increased cloud formation

(TCC and LWP) in the stratocumulus area, even under large-scale dynamic and environmental conditions traditionally agreed as less favorable to extensive low boundary-layer cloudiness (as discussed in the previous paragraph). The available NCEP LWP had bad-data, and or units problems and was not included in the plot.

The increase in precipitation (P) in response to warmer SSTs is noticeable, and, particularly for the ITCZ, shows a clear dependence with the concomitant intensification (and widening) of the deep convection region discussed above (for w700hPa). Quantitatively, the models show some interesting nuances in the ITCZ, with ECMWF being clearly overactive in its precipitation response, as compared with its response in the other parameters discussed. This is in contrast with the case of MétéoFrance, that shows a weaker intensification in precipitation, while being relatively more responsive in the increases in TCC and LWP, and intensification of |w700hPa|. Note that NCAR actually shows a decrease in the peak precipitation intensity in the ITCZ, at 8°N, while presenting at 11°N a significant increase in the precipitation rate in the warm month (~ 4 times higher) – a very clear response to the transition in the local dynamics regime, that goes from downward motion (~ 0.02 Pas^{-1}) in the "cooler" regime, to upward motion (~ -0.02 Pas^{-1}) in the "warmer" regime. Finally, to the north of the ITCZ, there is an increase in precipitation up to 20°N in all datasets, with basically unchanged precipitation rates to the north of 23°N, except for NCEP, that shows more precipitation at 26°N and 29°N, with the value at 26°N being almost as high as the values found in the deep convection area (e.g., at 11°N), and, again, probably in association with a relatively important decrease in the intensity of the subsidence at 26°N (~ 0 Pas^{-1} in the monthly mean response for the warm SSTs).

In the ITCZ (and generally south of 17°N) most results show the expected link between OLR and variables such as TCC, LWP, and precipitation, that is, coherent simulated increases/decreases in those three variables, are associated with decreases/increases in the corresponding response of the OLR parameter to the warmer SSTs. This is, however, not the case for NCEP, that shows relatively important increases in OLR between 8°N and 17°N, which is clearly more in line with the remarkable decrease in TCC, than with the increase in precipitation in that area (recall that NCEP LWP data wasn't available). In the shallow cumulus and stratocumulus areas (north of 17°N), however, NCEP's OLR (overall decrease) appears to be more sensitive to the precipitation changes (increase) than with the TCC changes (decrease) shown in response to the higher SSTs. The other datasets show the expected increase in OLR in response to the overall decrease in TCC (and LWP) to the north of 17°N (expect for ECMWFan, that shows no apparent change in OLR between the warm and the cool months to

the north of 23°N, in line with the shy response in its LWP). Finally, looking at 32°N and 35°N, NCAR's increase in OLR seems counterintuitive, given the increases in TCC and LWP, and raises a question about how high above the surface the associated cloudiness may have been simulated, since the lowest the cloudiness the lowest its expected impact on the OLR. The available ECMWF OLR had bad-data, and or units problems and was not included in the plot.

In the remaining set of results, there is, overall, the expected link between NSRTOA, TCC, and LWP. This is especially true for LWP, whose local response (increases, or decreases) to the warmer SSTs correlates well with the corresponding NSRTOA response (decreases, or increases, respectively). One noteworthy departure from this close link is seen at 29°N, for both NCAR and ECMWFan, that show decreases in NSRTOA, but also in both, TCC and LWP, in their simulated responses to +2 K SSTs. The available ECMWF NSRTOA had bad-data, and or units problems and was not included in the plot.

In summary, one main finding of the analysis presented above, is the fact that the general response to the increase in SST is not always coherent among the different variables, particularly at the local level at specific locations along the GPCI transect. This points out to the need to better constrain the simulated behaviour of important cloud-related variables, including those crucial for the evaluation of the cloud radiative forcing. Any improvements in this area would contribute to increase our understanding of the impacts and feedbacks of clouds in the hydrologic cycle, and ultimately of their key role in the climate system. Another important aspect of this study was the ability to, to some extent, qualitatively evaluate the relative impact of the increase in SST as compared to that of the (concomitant) changes in the large-scale dynamics (w700hPa), in the response of the cloud variables to the (+2 K) SST perturbation. A more complete analysis of these dependencies is beyond the scope of this section. Bony et al. 2004, and Wyant et al. 2006 offer further insight on this topic. Finally, it should be added that, although the vertical velocity field (e.g., w700hPa) can be seen as a meaningful proxy of the large-scale (sub)tropical circulation, and knowing its key role in the phenomenology of the difference tropical and subtropical cloud regimes, it is certainly not the only important large-scale factor that can impact the behaviour of cloud variables, others being, for instance, mid-tropospheric dry intrusions, and temperature lapse rate modifications.

4.5.2 Large-scale forcings

In this section the focus is more specifically on low cloud cover (LCC, obtained for each point in the GPCI transect simply from the maximum value of cloud fraction simulated in the layer

between the surface and 680 hPa). The investigation tries to understand to what extent the interplay between subsidence and SST, and alternatively, subsidence and low tropospheric stability (LTS, calculated at each location in the GPCI cross section taking the difference between the potential temperature at 700 hPa and the SST), relates to the model simulated low cloud cover in the segment of the GPCI transect between 14°N and 35°N (shallow cumulus and stratocumulus regions). The analysis is based solely on data for JJA 1998. Again, although one single season and year cannot offer statistically significant conclusions, it is worthwhile to explore the high temporal resolution (3-hourly) model output.

Figure 4.9 is based on Fig. 16 in Teixeira et al. (2011), but shows, in addition to low cloud cover as a function of SST and subsidence, low cloud cover as a function of LTS and subsidence, together with the joint probability density functions (jPDFs) for SST versus subsidence, and LTS versus subsidence. At least as a first approximation, the left and right ends of the SST axis in Fig. 4.9 can be seen as the northern and southern ends of the segment of the GPCI transect between the shallow cumulus and the stratocumulus, respectively (for the LTS it would be the other way around, although, most probably, to a lesser degree).

The jPDFs (in numbered contour lines) show, for all the results, the most representative bins in the 0 to 0.05 Pas^{-1} subsidence range, confirming that the region between 14°N and 35°N is dominated by large-scale downward motion. For the binning used, the peak values in the jPDFs seem more dispersed in the SST plots than in the LTS plots. Especially for the models shown (NCAR and UKMO), the largest values of subsidence are found in association with the coldest SSTs.

The value of the mean LCC for each bin in the jPDFs of subsidence versus SST, and subsidence versus LTS, is given by the color (%) scale. Although it is clear in all results that the colder SSTs (below ~ 295 K) are associated with the highest LCCs (above ~ 70 %), it seems difficult to find any obvious relation among the three parameters in any of the results shown. The NCAR results, show a more complex dependency of LCC on SST (and LTS), with a decrease in LCC for the coldest (highest) waters (LTS). Note, as well, that the peak LCC in NCAR is found for negative subsidence values (though in relatively rare events). Particularly for positive subsidence and in the vicinity of the most representative bins in the LTS plots (0 to 0.05 Pas^{-1} [subsidence] and 15 K to 17 K [LTS] for NCAR and UKMO, and 0 to 0.05 Pas^{-1} and 19 K to 21 K for ERA-40), these results do not show any specific dependency of LCC on the large-scale dynamics (vertical velocity at 700 hPa [mb]).

More comprehensive investigation on the interplay between cloud properties and measures of vertical stability has shown a significant relation between cloud cover and vertical stability in the cloudy boundary layer (e.g., Klein and Hartmann 1993; Wood and Bretherton 2006).

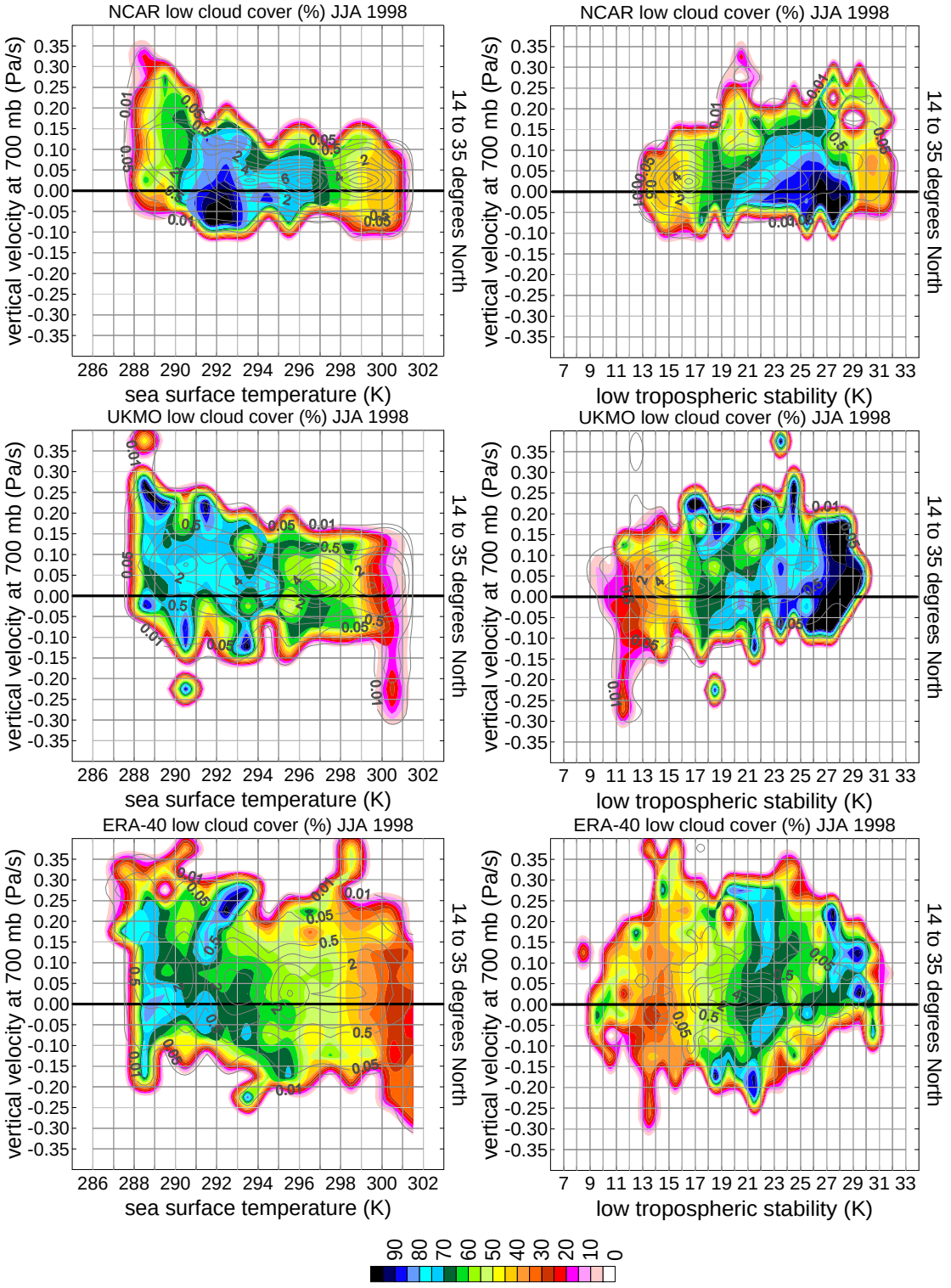

Figure 4.9 - Mean low cloud cover for jointly binned classes of vertical velocity at 700 hPa (mb) and: sea surface temperature (left column), and low tropospheric stability (right column) along the GPCI transect (14°N to 35°N) for June-July-August (JJA) 1998 for two models and ERA-40.

5 Cloud-based analysis of convective regime transition

Following a more traditional look at seasonal means of cloud-related parameters, presented in Chapter 4 to characterize the mean thermodynamic structure in weather and climate prediction models, the study will now turn to a more detailed analysis of the recurring transition in convective regime associated with the Hadley circulation, a prominent feature of the eastern boundaries of the (sub)tropical oceans (e.g., Sandu et al. 2010), discussed above specifically for the GPCI region.

The different cloud regimes associated with the large-scale overturning circulation (e.g., boundary layer clouds, deep convection towers, and the transitions between them) exert an important impact on the (sub)tropical atmospheric circulation, and thus on the climate system as a whole (e.g., Philander et al. 1996; Ma et al. 1996; Larson et al. 1999). One important aspect of these cloud systems is the relative contrast of their cloud radiative forcing (CRF) (e.g., Ramanathan et al. 1989; Hartmann et al. 1992) and feedbacks (e.g., Larson et al. 1999; Lindzen et al. 2001), two factors that make their relative spatiotemporal partitioning an important subject in climate change investigation. Climate change sensitivity experiments (e.g., doubling CO_2), show striking differences in the climate models' response in (low) boundary layer clouds, in many cases resulting in diverging cloud-climate feedbacks (e.g., Bony et al. 2004, Bony et al. 2006; Bony and Dufresne 2005; Wyant et al. 2006; Stephens 2005). In particular, it has been shown that the low-level cloudiness found in regions of moderate subsidence (e.g., trade-wind ShCu [shallow cumulus]) strongly influence modelled responses of CRF to prescribed ocean surface warming, mostly owing to their ubiquitous nature, and, hence, higher statistical weight (e.g., Bony et al. 2004). In this context, it can easily be argued that any changes in the (sub)tropical transitions between Sc (stratocumulus) and ShCu would have an impact on the tropical radiation budget, and therefore should be an important part of the investigation of cloud–climate feedbacks.

In the following sections, cloud data from model simulations, atmospheric reanalysis, and satellite observations are used in the GPCI framework to gain insight into the question of the transition in (sub)tropical cloud regimes. This is done by describing the observations, and evaluating and intercomparing the different models in view of their specific cloud and boundary-layer parameterizations. Several techniques to detect the transitions, and or summarize their main seasonal features, are proposed in Section 5.1. In Section 5.2, after the

presentation of results from a preliminary spectral analysis of the seasonal record of spatial shifts in the location of sharp transitions in total cloud cover (TCC), a novel approach to clustering of spatial patterns is introduced, and subsequently applied to TCC along the GPCI transect, with the final goal to indentify main spatiotemporal features of the seasonal tropical and subtropical TCC, and compare their respective environmental conditions.

The analysis presented in Sections 5.1.1, 5.1.2, and 5.1.3, is, in part, based on the results published in Teixeira et al. (2011). Section 5.1.4 discusses results published in Karlsson et al. (2010). The two publications were co-authored by the author of this thesis.

5.1 Representation of cloud transition

The brief sequence of results presented below is intended to characterize the spatiotemporal nature of the subtropical Sc-to-ShCu transitions, and how their presence and behaviour can be detected, or inferred, in different ways, depending on which aspect of its phenomenology one focuses on. Several approaches are then used to reveal different expressions of this transition, as seen in models and observations: from its impact on traditional seasonal climatologies of cloud cover (Section 5.1.1); to how it affects the summertime distribution of cloud cover values in different locations (Section 5.1.2); and how abrupt these transitions may actually be, as seen in high temporal resolution data (Section 5.1.3); or, more specifically looking at low boundary layer clouds, how their mean cloud-top height evolves along the GPCI transect (Section 5.1.4).

5.1.1 Seasonal mean cloud cover

As a starting point of the analysis of the cloud regime transitions, done in the next sections resorting to TCC information, Fig. 5.1 shows the individual model mean TCC behind the statistics presented in Fig. 4.2b (namely, model ensemble mean, ensemble mean plus and minus one standard deviation, and maximum and minimum values [range] at each location along the GPCI section).

The choice of TCC for this investigation, is partly based on the fact that the analysis is performed along the whole length of the GPCI transect, therefore encompassing the different cloud regimes (Sc to the north, ShCu in the transition areas, and deep convection towers in the inter-tropical convergence zone [ITCZ]). A corresponding study, using low cloud cover (LCC) instead, is not included here, owing to the lack of LCC output in the GPCI protocol (a simple

definition of LCC was used for the results presented in Fig. 4.9, knowing, though, that it may not be exactly the one in use in the different models). Note that, by looking at the features in the TCC field alone, one cannot directly infer on the nature of the associated convection regimes; it is only from the knowledge gained in the preceding chapters, that a close link between TCC and convection regimes can be reported. In this regard recall, for instance, the seasonal means of the vertical distribution of cloud fraction along GPCI presented in Fig. 4.7. Note that these results indicated that in the northern portion of the cross section, the TCC reported is probably very often mostly coming from the low cloudiness simulated during the June-July-August (JJA) 1998 season.

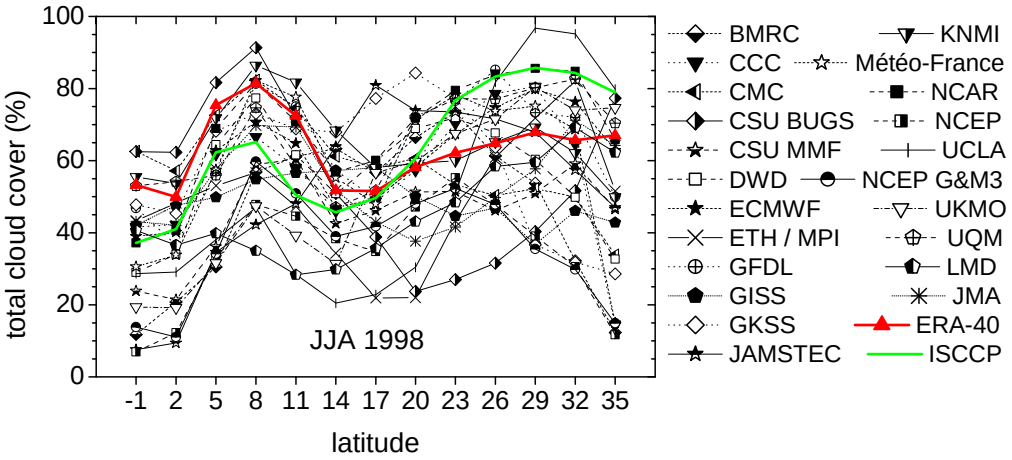

Figure 5.1 - June-July-August (JJA) 1998 mean total cloud cover along GPCI from each one of the participating models, ERA-40 reanalysis, and ISCCP observations.

It was stressed in Teixeira et al. (2011) that the large degree of scatter among the models' mean TCC is a clear indication of the serious problems current weather and climate prediction models have simulating clouds. Going a step further in that discussion, the question is now on whether the way in which the transitions between the different cloud regimes happen in the models contributes to the perceived model (and reanalysis) deficiencies. Can it (at least partly) explain the differences in TCC between NCAR and ERA-40 in the 17°N to 35°N portion of the transect (where NCAR is consistently above ERA-40)? How do the cloud transitions in Météo-France and UKMO compare to the ones in ISCCP between 20°N and 32°N (where the three datasets show relatively small TCC departures)?

5.1.2 Histograms

Although an important tool for a quick evaluation of first-order differences among corresponding results from different model simulations, seasonal mean diagnostics (e.g., the

TCC mean in Fig. 5.1), fall short of providing higher-order information such as temporal variability, which, usually, is valuable in further sorting out the relative performance of the models. In this section, TCC is analyzed from the perspective of its probability density function (PDF), taken individually at each location along the GPCI transect with the goal to further explain the nature of the cloud regime transition in the region, namely: 1) how is it being reproduced in the models; and 2) what do observations (e.g., ISCCP) show in this respect.

In Fig. 5.2, PDFs of TCC along the GPCI transect, obtained from 3-hourly data from JJA 1998, are presented, for models, reanalysis, and ISCCP observations.

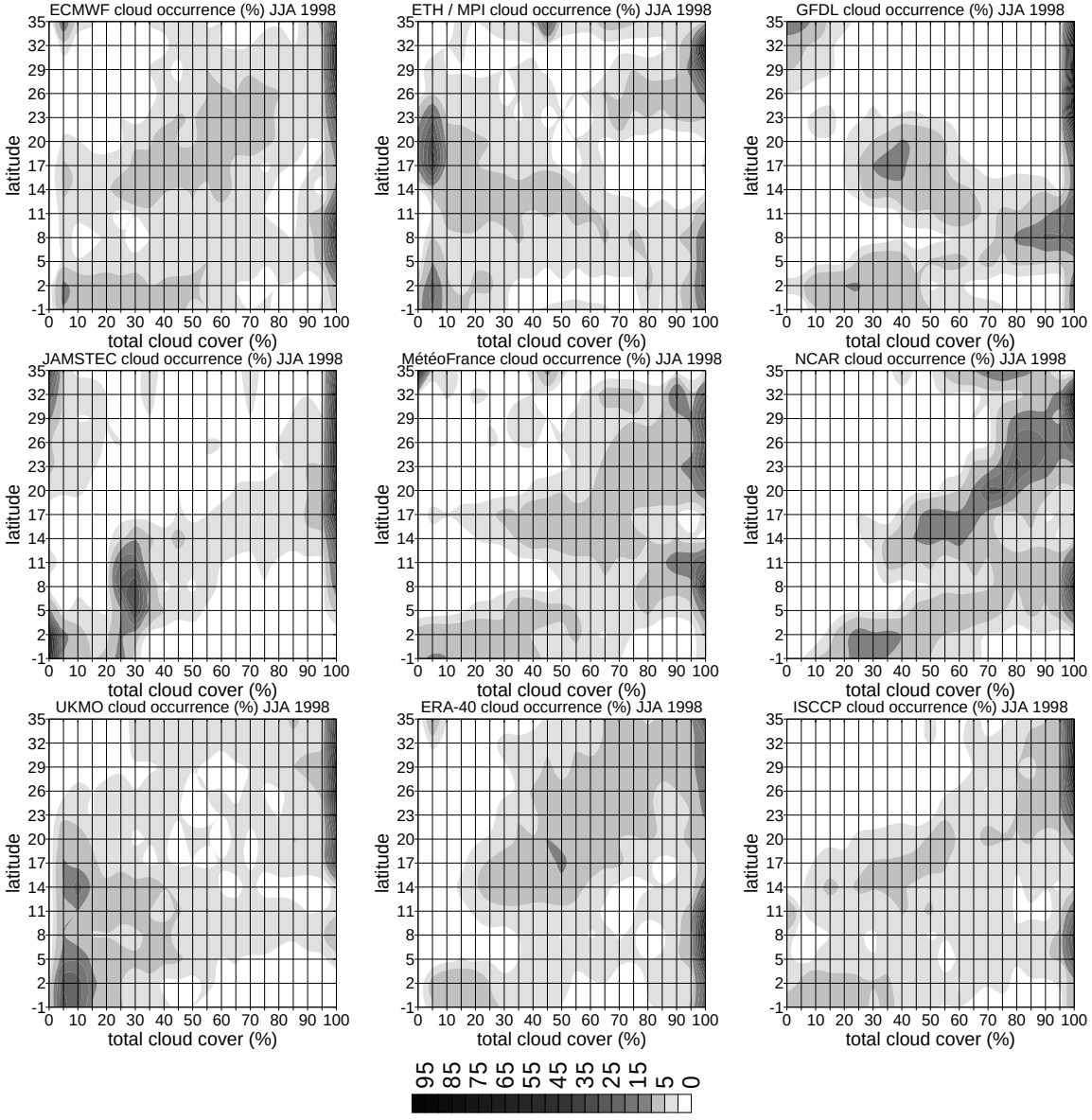

Figure 5.2 - June-July-August (JJA) 1998 histograms of total cloud cover along the GPCI transect for some of the models, ERA-40, and ISCCP.

The clear differences among these results, once again, confirm the variety of model behaviours in what concerns the simulation of clouds. Note that important differences in the TCC distributions can be found even in locations where models do show practically the same mean TCC (e.g., ECMWF, GFDL, and UKMO at 20°N [typical location for Sc-to-ShCu transitions] where all show ~ 60 % TCC). In more detail, and looking separately at each one of the three main cloud regime domains along the GPCI cross section, the situation is, for the Sc domain (26°N to 35°N): *i)* ISCCP, NCAR, and UKMO do not have any counts in the lowest TCC bins (TCC < 30 %); *ii)* GFDL and JAMSTEC preferably fall in the extreme TCC bins (TCC < 10 % and TCC > 95 %); while *iii)* ECMWF, ETH/MPI, ERA-40, and Météo-France fall somewhere in between those two situations. In the ShCu domain (14°N to 26°N): *i)* ECMWF, JAMSTEC, Météo-France, NCAR, ERA-40, and ISCCP show relatively smooth transitions, covering the bins between ~ 20 % and 90 % TCC; *ii)* overall, the TCC distributions are wider in ISCCP, ERA-40, ECMWF, and Météo-France, and relatively narrower for JAMSTEC, and (particularly) NCAR; *iii)* in contrast, the transitions in UKMO, ETH/MPI, and (particularly) GFDL are quite abrupt. Finally, in the ITCZ domain (5°N to 11°N): *i)* often high values of TCC (> 70 %) characterize the distributions for GFDL, NCAR, and Météo-France; *ii)* ECMWF, ETH/MPI, ERA-40, and ISCCP also show an important peak in the highest TCC bins, but have a wider spread in the overall distribution; *iii)* on the other hand, UKMO has a preference for lower TCC bins (TCC < 50 %), and shows a considerable spread in the deep convection TCC values; *iv)* JAMSTEC stands out as having its TCC distributed mostly between 20 % and 40 % TCC. In summary, two very distinct Sc-to-ShCu transitions can be identified in these TCC results, namely, a relatively smooth southward evolution (e.g., NCAR) and a more abrupt one with a bimodal character (e.g., UKMO).

Assuming that the main reason behind the differences in the TCC transition among the model results is mostly related to the way clouds are parameterized, a quick review of two distinct cloud parameterizations used in two of the models shown seems appropriate. In the case of the NCAR model, it could be argued that, to its smooth transition in the TCC evolution in the subtropics contributes the fact that its subtropical boundary layer cloudiness is, partly, parameterized in tight connection with the lower tropospheric stability (LTS, defined as the difference between the potential temperatures at 700 hPa and at the surface) – an empirical relation (e.g., Slingo 1980; Klein and Hartmann 1993) that has been adapted and used in climate modelling (e.g., Slingo 1987; Rasch and Kristjánsson 1998), but that, apparently, performs better at describing this link between low clouds and LTS, on larger spatiotemporal

scales (e.g., Kawai and Teixeira 2010). Recall that the results shown above, were obtained from the 3-hourly (and grid box) model output. That said, it is probable that NCAR is partly adjusting to the LTSs found along the GPCI transect (decreasing southward with increasing SSTs) by diagnosing corresponding climatological values of cloud cover, which then potentially leads to the smooth transition in TCC (the tight adjustment of [low] cloud cover to LTS may also be a reason for the relatively narrow seasonal TCC PDF distributions described above in the transition domain). It should be noted, however, that this parameterization may not always have the final word on the boundary layer cloud determination, and that, because TCC reported by models generally results from the application of cloud overlap assumptions of some sort, to the vertically distributed cloud fraction (including the boundary layer contributions), the overall impact of this parameterization on the final values of TCC cannot be fully understood from the available model output.

In the case of the UKMO model, the cloudy boundary layer parameterization is known to have been developed with the idea of the existence of a finite number of spatially separated subtropical physical regimes, such as those associated with stratocumulus, cumulus, and the transitions from cumulus to stratocumulus (e.g., Lock et al. 2000). This kind of simplification may be responsible for the bimodal nature of the TCC distribution along GPCI in the UKMO and (partly) in the GFDL results.

Going back to what ISCCP shows, although a final evaluation of the models in terms of these boundary layer cloud transitions would have to come from the study of a larger geographical area, and a longer time period, the preliminary conclusion is that none of these two very different model behaviours and parameterization approaches reproduces well the observed pattern in TCC distribution along the GPCI cross section for the JJA 1998 season.

5.1.3 Sharp gradients

The results presented in the two preceding sections showed well that the evolution of cloud cover along the GPCI transect is subject to changes that have a signature, not only in the mean values, but also in the nature of the local distributions of total cloud cover (TCC) – both shown to be quite different among the various datasets. Although undeniably useful for the study of the transitions in cloud regime, these two views of the TCC field are static by definition, and thus, cannot provide information on how the cloud cover values (coherently) change in time along the cross section during the season. Here, the investigation is taken to a new level resorting to the available high temporal resolution model output and observational data, so as

to produce estimates of how often the transitions are characterized by more or less abrupt discontinuities in the TCC field (known to be a manifestation of the subtropical maritime Sc-to-ShCu transitions).

The methodology proposed for the new kind of averaging can be divided into two main steps: (i) starting at the northernmost point (35°N, in the Sc region) and progressing southward along the cross section, determination of the location of the first significant decrease in TCC (e.g., above a given threshold of 30 % TCC); (ii) calculation of the average TCC to the northeast (NE) and southwest (SW) of the location determined in (i). This is performed for each one of the TCC records available 3-hourly. Note that, in step (ii), it is assumed that the TCC field is close to spatially uniform in the transect domains to the north and to the south of the transition location. Finally, the values for the seasonal mean TCC of the abrupt transition are obtained for the extreme north and south locations in the transect, respectively, from the means of all the NE and SW TCC averages; and for the mean location of the transition, as the mean of all the locations found in the 3-hourly data. Histograms of the transition location are computed as well. Bear in mind that, because the TCC field may actually not be uniform, the averaging of the TCC over the NE and SW domains mentioned above [step (ii)] can potentially result in a TCC difference between these domains lower than the threshold used to identify the abrupt decrease in TCC (this may even result in a SW TCC average higher than the one to the NE). An updated version of this methodology, developed to overcome this issue, is presented later in section 6.3.3.1.

Figure 5.3 presents, for ERA-40 and ISCCP, a summary of the main features associated with the occurrence of abrupt decreases in TCC along the GPCI transect, obtained by applying the methodology described in the previous paragraph to data for JJA 1998. Both ERA-40 and ISCCP show an important jump in TCC (left plot). These results show that this approach was able to capture discontinuities in the TCC field, whose magnitude and prevalence can, in part, be responsible for the TCC features that are typically seen in the more traditional seasonal means of TCC along the GPCI transect (note the high seasonal occurrence [occ] in both ERA-40 and ISCCP, shown in the plot to the right [location histograms]). It should be said that these results were practically unchanged using different values for the TCC threshold (e.g., 20% or 30% TCC), an indication of the robustness of the methodology. Recall, however, that the TCC values reported by the models may not (always) correspond to (low) boundary layer cloud cover (typically the cloudiness more directly subject to this kind of transitions), but can also (or exclusively) include information on high- and mid-level cloud cover.

Important departures between ERA-40 and ISCCP are highlighted in the context of this kind of analysis. In the left plot in Fig. 5.3, the two datasets differ, not only in the mean strength of the TCC gradients (~ 15 % and ~ 40 %, respectively for ERA-40 and ISCCP), but also in the mean TCC to the NE and SW of the abrupt decreases in TCC (ISCCP is ~ 10 % above ERA-40 to the NE, and ~ 15 % lower to the SW), and in the mean location of the gradients (~ 20°N in ISCCP and ~ 26°N in ERA-40). In what concerns the histograms of the location of the sharp gradients (right plot), it can be seen that the transition from Sc to ShCu occurs, in ERA-40, much more to the north (with the peak at 35°N, the northernmost point in the transect) than in ISCCP (with the peak at 23°N). In a lagrangian perspective this would mean that the break-up of the Sc decks into ShCu happens too early in ERA-40, as compared to ISCCP, and could be an additional reason for the negative cloud bias (ERA-40 vs. ISCCP) found in the subtropics – apart from the overall lower TCC values in the Sc areas shown in Fig. 5.2, and described in the previous chapter (Fig. 4.2b).

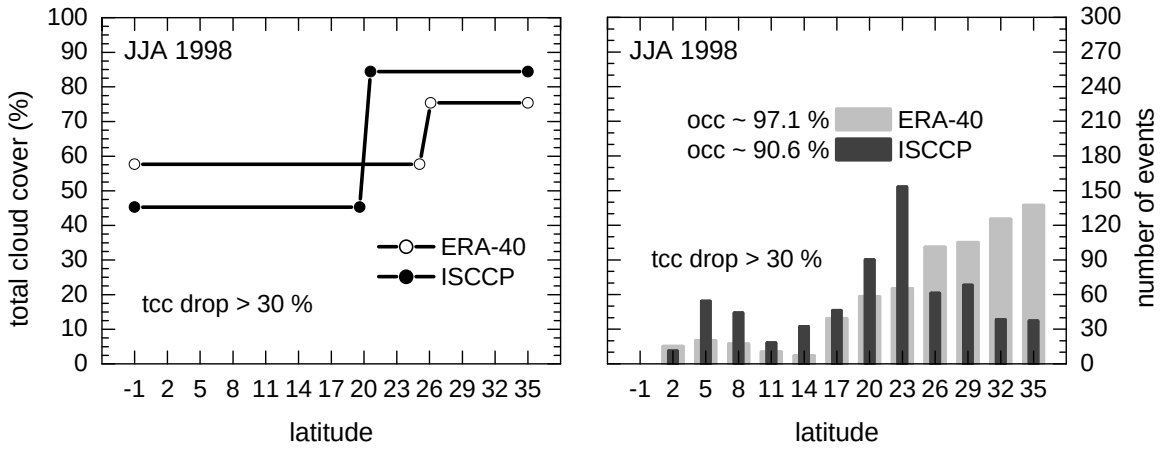

Figure 5.3 - June-July-August (JJA) 1998 ISCCP and ERA-40 cloud cover statistics obtained from a methodology based on the identification of large gradients of total cloud cover (tcc drop > 30 %) along the GPCI transect (see text for details): (left) seasonal mean values, and (right) histograms of the locations of the abrupt changes in total cloud cover (occ stands for occurrence [in percent]).

In Fig. 5.4, the results presented for (some of) the participating models show a diversity of behaviours in the sharp TCC transitions in all of the main features under investigation. Generally speaking: 1) the mean TCC decrease, as shown in these plots, is found to be between ~ 45 %, in the UKMO simulations, and ~ 15 % for Météo-France (for ISCCP it is ~ 40 % [Fig. 5.3]); 2) the seasonal frequency of occurrence (occ, in the plots) is between 86.7 %, for NCAR, and ~ 100 % in the other models; 3) the variability in the TCC values to the NE and SW of the mean gradient locations is large, and patent in the contrast between BMRC and ECMWF (the NE TCC in BMRC is about the same as the SW TCC in ECMWF [~ 55 % TCC]); and 4) the different histograms show one, two, or even three relatively well defined peaks.

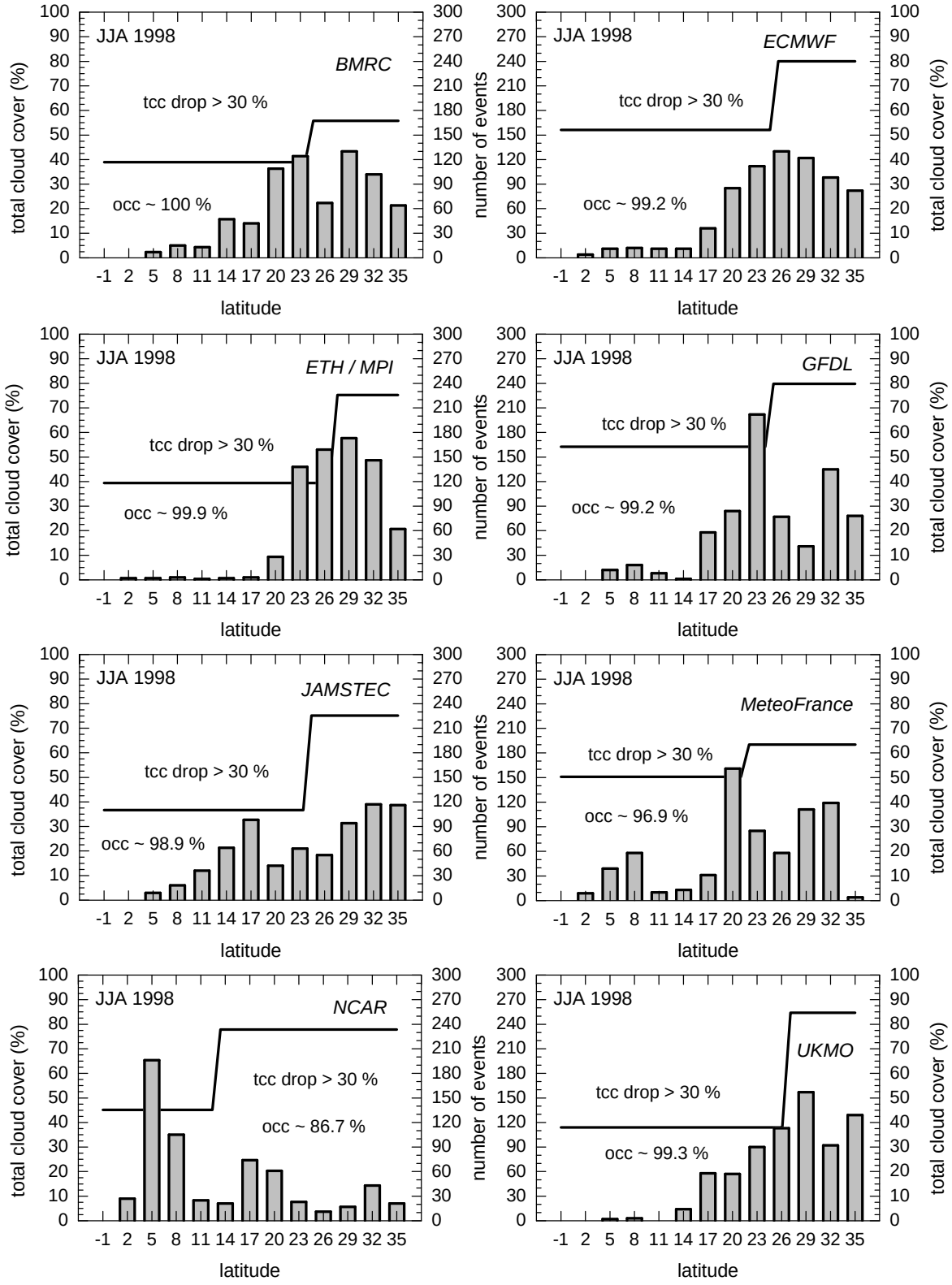

Figure 5.4 - Similar to Fig. 5.3, but for some of the GPCI models.

In more detail, it is worth noting that the overall good agreement between the location histograms for GFDL (Fig. 5.4), and ISCCP (Fig. 5.3), especially in what concerns the location of the main peak (23°N), happens in concomitance with two substantially different histograms of TCC along the transect (Fig. 5.2). To some degree, this is also the situation for ECMWF and ETH/MPI (with similar location histograms with one central peak between 26°N and 29°N, but different TCC histograms). The NCAR model clearly stands out from all the other models in the sense that the main peaks in its location histogram are found in the ITCZ area, at 5°N and 8°N, where the vast majority of sharp-gradient events happen. This is more easily understood in connection with the result shown in Fig. 5.2 (histograms of TCC along the transect), where it is apparent that the NCAR TCC only very gradually decreases from the Sc, in the northern portion of the transect, to the ShCu, and all the way to 14°N (recall NCAR's narrow TCC PDFs along the trades), from where it increases towards the ITCZ. This leaves the occurrence of abrupt decreases in TCC mostly to the area south of the deep convection region. Note that using LCC would probably eliminate the high peaks in the location histograms to the south of the ITCZ, and would probably (further) lower the absolute number of these events along the cross section. Again, this is partly a consequence of the way subtropical boundary layer clouds are parameterized in the NCAR model (see the discussion in Section 5.1.2).

The complementariness of the different techniques proposed for the investigation of cloud regime transitions along the GPCI transect is well patent – none of them can independently fully describe these transitions. In the next section, yet another perspective on the cloud transitions is presented, with the focus more specifically on changes in the low-cloud fields.

5.1.4 Cloud-top height

As qualitatively discussed in previous sections (e.g., Sections 4.2 to 4.4), the evolution of the cloud regimes along the GPCI cross section happens in association with a deepening of the maritime boundary layer from the Sc, to the north of the transect, to the ShCu, in the trades, and all the way to the vicinity of the deep convection area (ITCZ). Here a more quantitative analysis of the evolution of the boundary layer is presented. It relies on the assumption that the low clouds in the region are mostly confined to the boundary layer (particularly in the Sc regimes), and resorts to cloud top height (CTH) information to produce a climatological estimate of boundary layer depth, for observations and models along the GPCI transect. The CTH climatology constitutes an important model evaluation tool, that can provide insight on

how well the models treat the processes responsible for the maintenance of the cloudy boundary layer.

The results presented below are based on the findings reported in Karlsson et al. (2010), a paper co-authored by the author of this thesis.

On the observational side, the study is based on the level-2 wind-corrected CTH product obtained from the retrievals by the Multiangle Imaging Spectroradiometer (MISR) on the Terra satellite (Moroney et al. 2002; Davies et al. 2007). Terra is on a sun-synchronous polar-orbit and crosses the Equator at ~ 1030 local solar time (descending node). Operationally, MISR uses nine cameras at different angles to detect CTH reflectivity, that is then used in stereo-matching algorithms (Muller et al. 2002), and subsequently subject to geometrical adjustments to infer cloud motion and CTH (Zong et al. 2002). The CTH product used offers a horizontal resolution of 1×1 km^2, and a nominal accuracy of 6560 m (6300 for low-level clouds [Naud et al. 2004; Garay et al. 2008]). MISR CTHs have been reported to be accurate in the Sc and ShCu areas (Garay et al. 2008; Genkova et al. 2007). For this study, CTHs below 3000 m were accrued during JJA 2003, for each one of the 13 locations along the GPCI section (in 3° x 4° latitude, longitude domains). The spatial average of the CTHs for each domain was then converted to cloud-top pressure using geopotential and temperature data from atmospheric reanalysis.

For the model simulations (and ECMWF analysis) the low clouds' cloud-top pressure was obtained for each location in the cross section from the vertically distributed cloud fraction for the model levels > 700 hPa (below ~3000 m), provided that no clouds were reported above 700 hPa, and assuming the low clouds to be arranged in maximum overlap. Clouds with cloud condensate below 0.01 g kg^{-1} were disregarded, assuming that they would not be detected by the satellite instrument (other values for this threshold were tried). The final low-clouds' cloud-top pressure was then obtained from the weighted average of the half pressures above the model levels with (detectable) cloud fraction (the respective cloud tops are assumed to be located above the actual level where the cloud fraction is reported by the model), weighted by the respective amount of cloud fraction that would be seen from above in the case of a maximum cloud overlap.

In Fig. 5.5, the JJA 2003 CTH results along the GPCI transect are summarized for the models, ECMWF analysis, and MISR. In terms of the seasonal means (in plots a and b), there is an overall good agreement between the ECMWF analysis and the model ensemble. Basically, both show an increase in CTH along the entire transect from a value of ~ 950 hPa at 35°N to ~

875 hPa at 28°N, and a maximum of ~ 825 hPa at 5°N. MISR also shows an increase in CTH between 35°N (~ 925 hPa) and 20°N (~ 825 hPa), but has lower mean CTH to the south of 20°N, and gets closer to the simulated CTH between 17°N and 11°N (~ 875 hPa at 11°N), staying below the models, and analysis, in the deep convection area and south of it. MISR's much higher spatial resolution permits the detection of relatively fine spatial detail in the cloud scenes. It is thus speculated that the decreased CTH, south of 20°N (transition to the trades and ITCZ), is probably related with the detection of small cumuli that stay below the subsidence inversion (e.g., Genkova et al. 2007; Zhao and Di Girolamo 2007), a situation that may be associated with the decoupling between the (ocean) surface and the top of the maritime boundary layer, by an intermediate weakly-stable layer. Figure 5.5c shows only relatively small departures in CTH variability between MISR and the models (MISR's CTH variability is above [below] that from the models, and analysis, to the north [south] of 23°N [20°N]). The sharp decrease in MISR's variability, going from 23°N to 20°N, possibly indicates the area where the trasition from Sc to ShCu is more frequent (recall that ISCCP has at 23°N the maximum peak in its histogram of the location of abrupt decreases in total cloud cover [Fig. 5.3, for JJA 1998]).

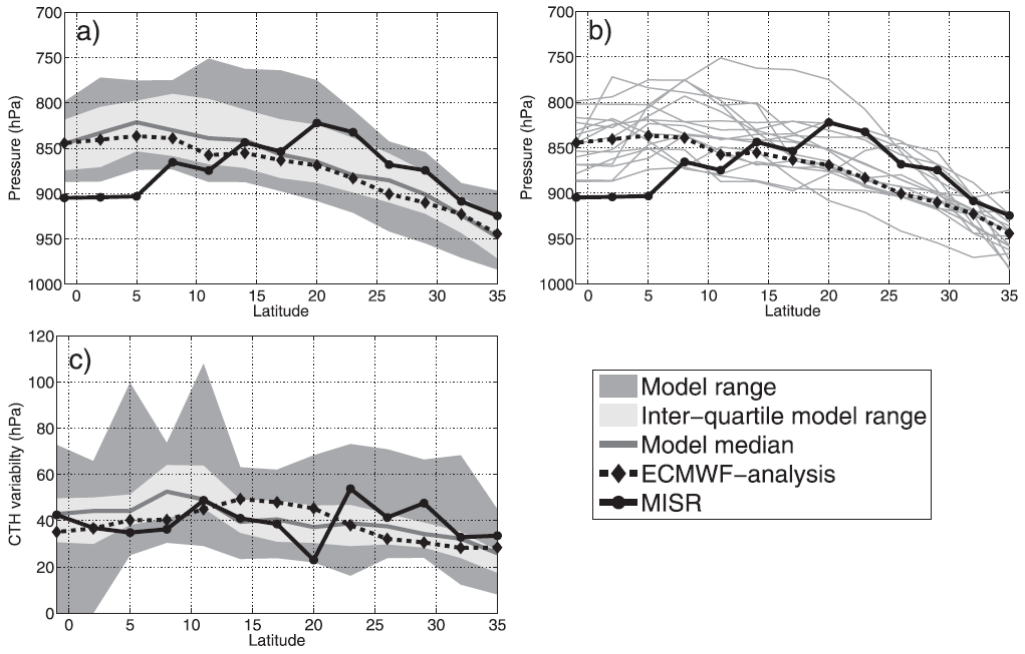

Figure 5.5 - Boundary layer height estimate based on the pressure at the top of low clouds, obtained along the GPCI transect for June-July-August 2003, for models, ECMWF analysis [dashed line], and MISR observations [solid black line]. The solid dark-gray line represents the median of the model ensemble, the light-gray envelope represents the interquartile model range, and the dark-gray envelope represents the range of model values: (a) mean values, (b) mean values for the models individually [gray lines], and (c) temporal variability (one standard deviation). (Figure taken from Karlsson et al. 2010).

Karlsson et al. (2010) show, in addition to CTH, results from an alternative technique to determine the top of the maritime boundary layer (BLT) and estimate its depth, "based on the height of the maximum vertical RH [relative humidity] gradient with respect to pressure." It was applied to humidity data from models, analysis, and satellite observations. Although equally promising for BLT investigation, a discussion of that technique, and corresponding results, is left to Section 6.3.1 (Relative humidity as a proxy for boundary layer depth), and Section 6.3.2 (A new scheme to determine the BLT), where an updated version of the methodology is introduced.

5.2 Refined analysis

To close the chapter, results from a more in-depth investigation of some of the aspects of the cloud regime transitions discussed above, are presented in the next couple of sections. Firstly, in Section 5.2.1 (Modes of temporal variability) the study tries to refine the characterization of abrupt changes in TCC done in Section 5.1.3 (Sharp gradients), and performs a spectral analysis of the corresponding 3-hourly record, with the goal to understand the dynamics of the TCC transition in terms of the variability of its location. This is presented to complement the static view offered by the location histograms (Figs. 5.3 and 5.4). Section 5.2.1 ends with proposals for future work, and suggestions on how to extend the analysis to other key parameters. Finally, Section 5.2.2 (Environmental conditions associated with main seasonal TCC fields) tries to go beyond the all-encompassing seasonal mean view of the TCC field presented in Section 5.1.1 (Seasonal mean cloud cover), and resorts to high temporal resolution (3-hourly) TCC data for the identification of spatiotemporal patterns corresponding to preferred modes of behaviour of the cloud regime transitions that occur along the GPCI cross section. This is done using a newly developed clustering technique, whose TCC results are then used to composite other cloud-related variables, to infer potential impacts of their interplay on the regime transitions that occur in the region.

5.2.1 Modes of temporal variability

The first step to prepare the data for the spectral analysis of the spatial variability of the sharp gradients in TCC (see Section 5.1.3 for details on how to detect these abrupt changes in TCC along the GPCI transect) was the subtraction, from the corresponding 3-hourly record, of the value of their seasonal mean location (all given in latitude along the cross section). The result is a record of location anomalies that allows for a relatively straightforward intercomparison

among different datasets. Figure 5.6 shows, for JJA 1998, the seasonal anomaly record for a few of the models, ERA-40 reanalysis, and ISCCP observations, and offers a quick view of the dynamics of the TCC transition in terms of the shifts in its location in complement of the information in the respective location histograms (Figs. 5.3 and 5.4). Note that in the abscissa axis (time) the minor ticks correspond to days (8 UTCs, 3-hourly), and the labels (located at the beginning of each week during the season) indicate the number of 3-hourly records up to that point in time. Also, keep in mind that a positive (negative) latitudinal displacement indicates a position along the transect to the north (south) of the seasonal mean location.

There are some noteworthy differences among the datasets shown in Fig. 5.6. For instance: in ISCCP, the latitudinal displacements are, overall, relatively large (between +16° and -16°), and the sharp decreases in TCC tend to stay for longer periods to the north of the mean location, a situation that changes dramatically in the last two weeks of August, when these consistently tend to stay to the south of the mean location; ERA-40 shows, overall, a highly changeable location of the sharp gradients, with displacements confined between +8° and -24°; in the second half of the season there is, in the reanalysis, a tendency of the sharp gradients to stay for longer periods in a given location (either to the north or to the south of the mean location); for NCAR, the displacements oscillate between -8° and +20°, and show a noticeable change in the last 4 weeks of the season, with the sharp gradients preferably staying to the north of the seasonal mean location (especially in the last week of August), probably a result of earlier (in a lagrangian sense) Sc-to-ShCu transitions, owing to the warming SSTs (lower LTS) experienced in the northern part of the transect towards the end of the JJA 1998 season (see the discussions in Sections 5.1.2 and 5.1.3); ETH/MPI shows the smallest latitudinal displacements (basically between +8° and -8°), and is the dataset whose sharp gradients happen continuously for longer periods in any of the sides of the mean location (e.g., a positive displacement for the whole fifth week of JJA); finally, in UKMO, the main feature seems to be the increase in the variability of the location of the sharp gradients towards the end of the season.

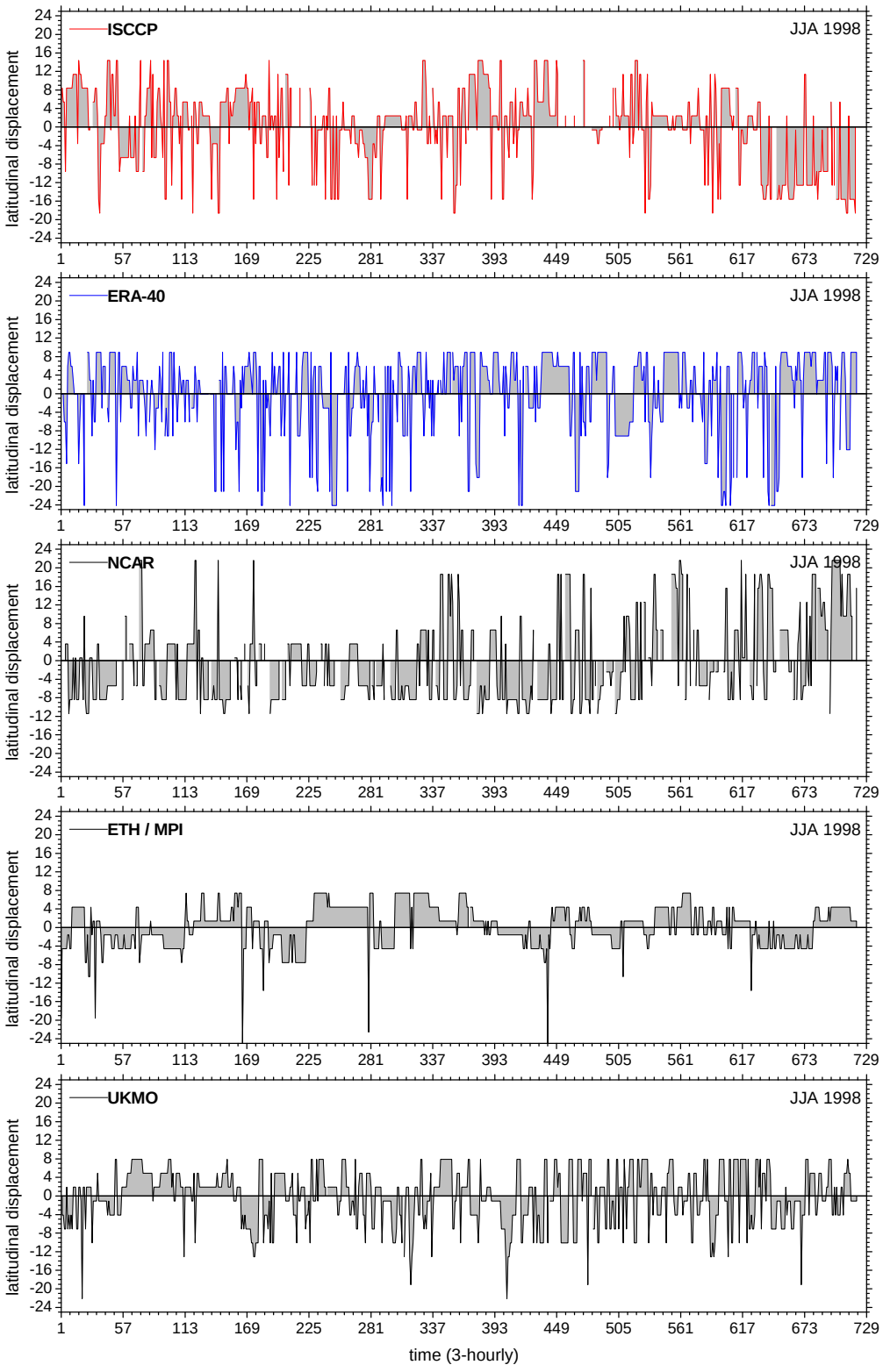

Figure 5.6 - June-July-August (JJA) 1998 time series of the location (relative to the seasonal mean position) of sharp gradients in total cloud cover (see text for details) for ISCCP observations, ERA-40 reanalysis, and some of the GPCI models (in the abscissa axis, minor ticks correspond to days, and labels, located at the beginning of each week during the season, indicate number of 3-hourly records up to that time).

Figure 5.7 presents the power spectra corresponding to the temporal series shown in Fig. 5.6, and, additionally, the power spectrum for Météo-France (whose temporal series is not shown in Fig. 5.6). It is apparent that there are no outstanding peaks in any of the plots. Nevertheless, relatively speaking, they show, overall, the expected behaviour when compared against the respective anomaly records analyzed above, e.g., ISCCP is generally slower (higher power in the lower frequencies) than UKMO or ERA-40, Météo-France is similar to ISCCP, and ETH/MPI has more power in the lowest frequencies than UKMO. In more detail, there is a relatively well define power peak in UKMO around a period of 12.5 days (10^{-2} in the frequency axis), while, for ERA-40, the most prominent peak is located around 6.25 days.

It would be interesting to extend this analysis to other cloud-related parameters of interest for the topic of the subtropical cloud regime transitions. Taking advantage of the 3-hourly model and reanalysis data, variables such as LTS, SST, and free tropospheric humidity could be spatially averaged in a domain upwind of the mean location of the sharp gradients in TCC (or LCC), and the record of their anomaly relative to the respective seasonal means be subject to the same kind of treatment proposed above (Figs. 5.6 and 5.7). Relevant questions could then be asked, for instance, about the correlations between each one of those anomaly records and the anomaly of the location of the sharp gradients of TCC (or LCC); or, how do their spectra compare. Finally, it seems imperative to perform this kind of investigation also for results obtained using more refined definitions of the sharp gradients in cloud cover, e.g., the one presented later in Section 6.3.3.1, more robust, and potentially able to provide better guidance for the compositing of the other key parameters.

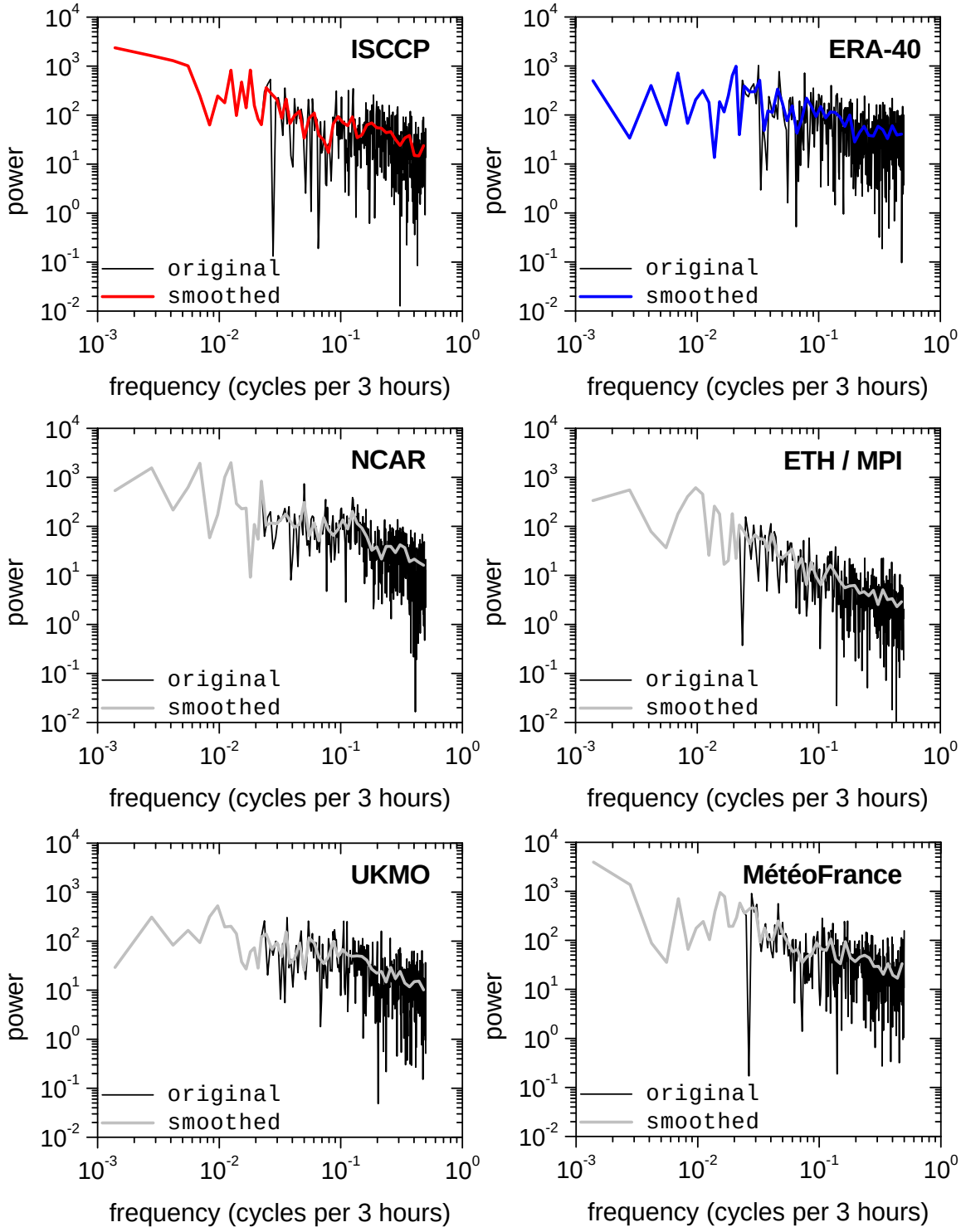

Figure 5.7 - Frequency spectra of the June-July-August 1998 time series presented in Fig. 5.6 for ISCCP observations, ERA-40 reanalysis, and some of the GPCI models (Météo-France is not shown in Fig. 5.6).

5.2.2 Environmental conditions associated with main seasonal TCC fields

The goal here is to describe the environmental conditions associated with distinct features of the cloud regimes (and respective cloud transitions) that occur during the JJA season in the tropical and subtropical NE Pacific ocean. A first step would have to do with the search for preferred spatiotemporal modes in the behaviour of the TCC field along the GPCI cross section. It was suggested that such investigation on the behaviour of the TCC field could be performed resorting to a clustering methodology. The decision to follow this kind of approach led to the development of GEPAT (Grade-based Empirical Pattern Analysis Technique), a novel cluster analysis technique introduced in Appendix A.4 to this thesis. Preliminary GEPAT results seem adequate for the accomplishment of that goal. It is in this context that ERA-40-versus-ISCCP GEPAT results for TCC are used for the compositing of key dynamical and thermodynamical variables believed to have an important role in the maintenance and evolution of the cloud phenomenology in the GPCI region. The analysis of these results is done in Appendix A.4 and tries to qualitatively infer potential impacts of the interplay of those key parameters, on the regime transitions that, generally, occur in maritime regions adjacent to the eastern boundaries of the subtropical oceans.

Figure 5.8 shows ERA-40 JJA 1998 seasonal mean fields of vertical velocity at 700 hPa (W700mb), liquid water path (LWP), sea surface temperature (SST), and low tropospheric stability (LTS) along the GPCI transect, together with section-averaged wind direction (direc) and speed.

Again, this figure is analyzed in Appendix A.4. It was included here for illustration purposes.

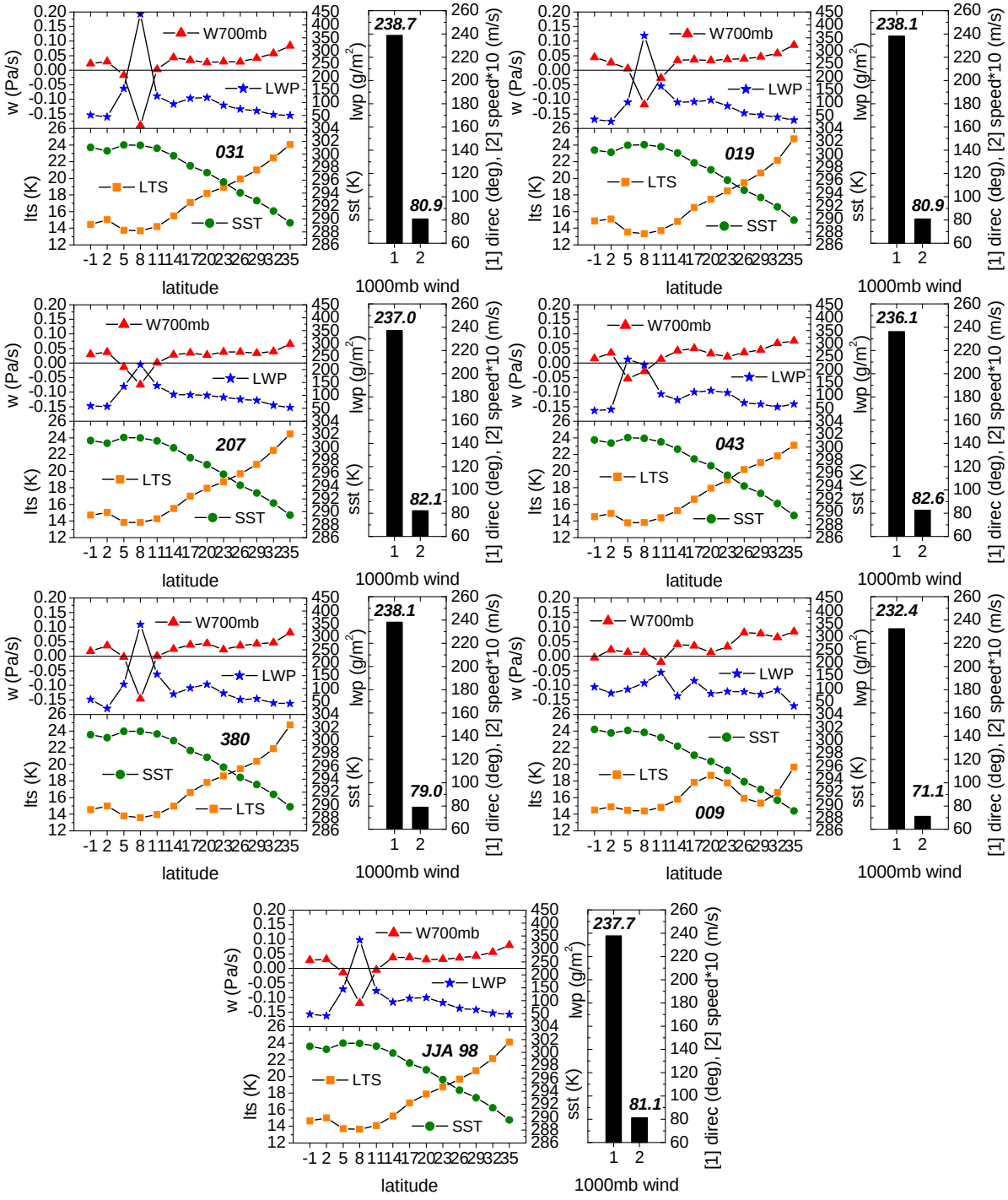

Figure 5.8 - ERA-40 June-July-August (JJA) 1998 seasonal mean fields of vertical velocity at 700 hPa (W700mb), liquid water path (LWP), sea surface temperature (SST), and low tropospheric stability (LTS) along the GPCI transect, together with section-averaged wind direction (direc) and speed, composited for each one of six clustering partitions of corresponding ERA-40 GEPAT results for total cloud cover. The bottom plot shows the means for the season as a whole (this figure is analyzed in Appendix A.4).

6 Examination of relative humidity and cloud cover changes

This chapter is dedicated to the study of the humidity structure in the (sub)tropical NE Pacific. The goal is to better understand its role as one of the main parameters in the context of the hydrologic cycle, particularly through its influence on cloud formation and evolution. For that end, state-of-the-art satellite observations are analyzed along the GPCI cross section, together with model simulations and atmospheric analyses. A number of results, based on the treatment of relative humidity data for the summer season, are presented, namely, seasonal mean profiles, variance, temporal evolution, boundary-layer properties, and potential impact on cloudiness structure and transition.

6.1 Validation of simulations of relative humidity

In this section, the Atmospheric InfraRed Sounder (AIRS) is introduced. This advanced remote sensing instrument constitutes an important source of satellite data for numerical weather prediction and for climate research, specifically for its strengths in providing, with unprecedented detail and on a daily basis, global profiles of temperature and humidity. The focus is on the use of June-July-August (JJA) 2003 relative humidity information to validate model simulations. The section ends with a discussion of some of the challenges of bringing together models and observations, in an integrated and meaningful way, in the particular context of the GPCI transect.

6.1.1 The Atmospheric InfraRed Sounder

Until recently, most large-scale water vapor climatological studies have depended primarily on analyses of radiosonde data. Radiosondes have good resolution in the lower troposphere in populated regions, but are notoriously unreliable, and are usually unsuitable for detecting trends of water vapor in the upper troposphere. Also, these traditional measurement systems lack over remote oceanic regions. More recently, substantial progress has been made using satellite observations to obtain total column water vapor, and (low-resolution) vertical profiles of humidity, from infrared and microwave sensors. One disadvantage of satellite observations comes from their inability to provide water vapor data for certain weather and cloud conditions, or above a number of surface types.

AIRS

AIRS (Aumann et al. 2003) is a state-of-the-art advanced infrared sounding system launched on May 4, 2002, on the NASA (National Aeronautics and Space Administration) Earth Observing System (EOS) Program's Aqua platform, into a nominal altitude of 705 km in a circular sun-synchronous near-polar orbit with equatorial crossings at 0130 local time, on the descending (southward moving) orbit, and 1330 local time, on the ascending (northward moving) orbit. Its period is 98.8 *min*, and orbital correction maneuvers maintain the orbit with a repeat cycle of 16 days. Together with other instruments on Aqua (e.g., AMSU [Advanced Microwave Sounding Unit]), AIRS forms an integrated cross-track nadir-scanning sounding system. This instrument suite combines infrared and microwave retrievals, a feature designed to allow for a significant reduction of the limiting effects of cloud contamination in the field of view of infrared sounders. The infrared spectrometer/radiometer covers the 3.7 μm to 15.4 μm spectral range with 2378 spectral channels. With the basic goal of supporting NASA's interest in process study and climate research, AIRS is, additionally, the first hyperspectral IR (InfraRed) radiometer designed to support NOAA (National Oceanic and Atmospheric Administration) / NCEP (National Centers for Environmental Prediction) requirements for operational numerical weather forecasting. At launch, AIRS had an expected seven-year lifetime. The sounding goals of AIRS were to produce 1 km tropospheric-layer mean temperatures with a root-mean-squared (RMS) error of 1 K, and layer precipitable water with a RMS error of 20 %, in cases with up to 80 % effective cloud cover (also called effective fractional cloud cover, or infrared cloud fraction, given by the product of the fraction of the field of view [FOV] covered by clouds and the cloud emissivity at 11 μm). It is the ability of the AIRS sounder to work in combination with the microwave sounder that enables the fulfillment of the "1 K/1 km" requirement for temperature, and 15 %/2 km humidity vertical resolution, globally, and under clear and cloudy conditions. In comparison to existing observations, AIRS brings high vertical resolution combined with global daily coverage.

Of the 2378 spectral channels of the AIRS instrument, 1524 are used to derive regression coefficients, and considerably fewer channels are used in the AIRS physical retrieval steps. AIRS retrieval algorithms deconvolve spectrally adjacent lines whose weighting function peaks are spaced closely in the vertical. Ultimately, the retrievals from the instrument suite are made available as data in the form of calibrated spectral radiances, radiance estimates from forward models of radiative transfer, and geophysical state estimated through retrieval algorithms. Those data are made available through the GSFC (Goddard Space Flight Center)

DAAC (Distributed Active Archive Center), mapped onto regular grids, referenced as "Level 1B" (calibrated radiances), "Level 2" (spot by spot retrievals with nominal 45 km resolution from the AMSU FOV), and "Level 3" (global gridded) data. The L3 data are given on a 1° × 1° latitude-longitude grid, and can be downloaded as 1-day, 8-day, or monthly mean segments (the ascending and descending orbits are gridded separately).

AIRS has been providing: ● atmospheric temperature profiles; ● specific humidity profiles; ● total precipitable water vapor; ● fractional cloud cover; ● cloud-top pressure and temperature; ● total ozone burden of the atmosphere; ● column abundances of minor atmospheric gases (e.g., CO_2, CH_4, CO, and N_2O); among other products. Of particular importance is the recognized ability of AIRS to measure water vapor in the upper troposphere between 300 hPa and 100 hPa.

Validation efforts

A number of relevant publications (e.g., Fetzer et al. 2003) have documented the comparison of AIRS retrieved products with collocated/contemporaneous independent data, to infer observational errors and establish the accuracy of those products. Radiosondes are the main source of such observational data. In general, the results validate the AIRS retrievals of temperature and humidity to within the design specifications.

Tobin et al. (2006) used high-quality dedicated radiosondes, launched for AIRS validation at the Atmospheric Radiation Monitoring (ARM) Tropical Western Pacific (TWP) site at Nauru (166.9°E, 0.5°S), and another ARM site in Oklahoma, and concluded that, at Nauru, biases between AIRS and radiosonde water vapor were in the range -4 % to 6 % in 2 km layers in the lower troposphere (with total precipitable water vapor biases of less than 5 %, surpassing the theoretical limit of 5 % [Aumann et al. 2003]). They showed that the biases had only a weak dependence on cloud amount. Divakarla et al. (2006) compared AIRS full retrievals against globally available operational radiosondes (including both land and water cases) and reported biases of less than about 10 % in 2 km layers. They also found potential temperature biases of ~ 0.5 K, at 600 hPa, and ~ -0.5 K, at 300 hPa (temporal variations in CO_2 absorption may have contributed to slight biases in the retrievals). McMillin et al. (2007) use GPS data to rescale radiosonde profiles, and find overall agreement between the AIRS and radiosonde integrated precipitable water (IPW) vapor observations, indicative of the good performance of AIRS as a water vapor sounder (consistent with the results published by Tobin et al. [2006] and Divakarla et al. [2006] mentioned above). Focusing on the upper troposphere, Gettelman et al. (2004) compared AIRS profiles collocated to in situ aircraft data in the upper tropospheric / low

stratospheric region. They found a good match between temperatures in the two data sets, showing no bias, and a standard deviation of 1.5 K. For water vapor below 150 hPa the standard deviation was around 20 %, without big departures, and, in the same way, relative humidity at 250 hPa (and below) was also unbiased, with a standard deviation of 9 %. Fetzer et al. (2003), using data from Vaisala operational radiosondes over water, shows AIRS full retrievals of water vapor with biases of -4 % to 4 %, in 2 km layers, between the surface and 500 hPa. Comparing AIRS with European Center for Medium-range Weather Forecast (ECMWF) reanalyses in the Eastern Pacific, and operational radiosondes in Southern California and Hawaii, Fetzer et al. (2004) showed biases of -5 % to 3 % for full retrievals in the surface-to-700 hPa layer. Fetzer et al. (2006), comparing matched AMSR-E (Advanced Microwave Scanning Radiometer for EOS) and AIRS independently-derived total precipitable water vapor (PWV) for two 16-day periods, showed RMS differences of about 0.2 kg/m^2 (a better agreement than the global mean difference seen by Amenu and Kumar [2005] between NVAP [NASA Water Vapor Project] and a model reanalysis). Again, they notice weak dependence of biases on inferred AIRS cloud amount, indicating that the AIRS cloud clearing methodology (Susskind et al. 2003) does not introduce significant cloud-dependent biases. On a regional scale, the work points out to the fact that the largest AIRS wet observational biases were located in regions more affected by persistent stratus cloud cover, and that trade wind cumulus regions had observational biases between AIRS and AMSR-E near zero (it is also in the trades that AIRS full-retrieval yields peak to values as high as 90 %).

Of special relevance for this work, is the generic conclusion that several comparisons of AIRS over-ocean full retrievals of water vapor against radiosondes, consistently indicate mean biases of only a few percent, usually irrespective to cloud amount up to 70 % to 80 % (AIRS effective fractional cloud cover). We note that previous examination of absolute differences in humidity, shows better agreement between AIRS and radiosondes over sea than over land, in line with the expectation that the AIRS retrievals should be more accurate over water (the higher surface reflectivities enhance the sensitivity of the microwave channels to changes in moisture).

Finally, regarding the global AIRS retrievals, it has been concluded that, at least for humidity, temperature, and related products, the primary source of sampling biases is clouds affecting AIRS infrared signal. From the results of the retrieval algorithms' calculations it is apparent that the percent of accepted geophysical parameters does decrease with increasing cloud fraction, in a manner that depends on the geophysical parameter. It can therefore be inferred that the fraction of AIRS full retrievals yields will vary with season and location.

The identification of these biases can be done recurring to (global) comparisons between AIRS and, other satellite data sets, model reanalyses, or even GCM (General Circulation Model) simulations (preferably with an ensemble of different models). In this perspective, this work can be, in part, seen as yet another such effort, in which AIRS observational data are subject to comparison with model simulations in addressing regional-scale climate processes of importance to global climate (change) studies.

6.1.2 AIRS relative humidity along GPCI

For this study, AIRS-version-4 humidity and temperature data were processed following Gettelman et al. (2006) to obtain a dataset of relative humidity (RH) throughout the troposphere in the (sub)tropical NE Pacific Ocean. The resulting RH dataset, with daily temporal resolution for JJA 2003, is analyzed and compared to weather and climate prediction model simulations in the GPCI framework.

More precisely, the first step for the calculation of RH profiles, was to gather available standard Level 2 (L2) profiles for which the infrared retrieval had been successfully completed. This is important, since, only the successful convergence of the algorithms during the final IR retrieval for the bottom-most part of the profile, can ensure full retrievals with the specified system accuracy of 1 K in 1 km layers (15 % in 2 km layers) over the entire temperature (humidity) profile (complete convergence occurs utilizing the full complement of microwave and infrared radiances from AMSU and AIRS, respectively). As mentioned, full retrievals occur more frequently under less cloudy conditions, and none are obtained for effective fractional cloud cover greater than about 80%. These water vapor (q) and temperature retrievals were then used to derive RH for each profile (RH = $q/q_s \times 100$, in percent, where q_s is the saturation water vapor mixing ratio). The calculations of RH were further restricted to regions where water vapor is greater than 10 ppmv, the nominal reported instrument sensitivity. The formulation of Goff and Gratch (1946) over water, for temperatures > 273 K (0 °C), and over ice, for temperatures < 253 K (-20 °C), was used to calculate q_s. A linear combination was used between 253 K and 273 K. Other alternative formulations exist, but the fact that this is identical to what is used in (some) GCMs, may facilitate comparisons. Given the fact that the AIRS retrievals provide a column water vapor ($\overline{q}$) between two pressure levels, and temperature on the corresponding (sub)layer edges, the RH profiles were calculated using a corresponding column saturation vapor pressure ($\overline{q}_s$) obtained from numerical integration of the saturation vapor pressure profile in the sublayer, assuming linear temperature

change between its two adjacent edges. Detailed sensitivity tests were conducted and the results are not highly sensitive to the method chosen (Gettelman et al. 2006).

Finally, the profiles of RH (at the AMSU nominal ~ 45 km spatial resolution) were binned into a 1° × 1° latitude–longitude grid, with longitude bins held constant at 111 km. Also, the ascending and the descending orbits of Aqua were commingled in a single daily record. The dataset comes in 20 pressure levels between 1000 hPa and 5 hPa (1000, 925, 850, 700, 600, 500, 400, 300, 250, 200, 150, 100, 70, 50, 30, 20, 15, 10, 7, and 5 hPa), but here only the information from the levels 70 hPa and below is used (it is believed that AIRS sensitivity to water vapor drops rapidly around 100 hPa). Bear in mind that, following the AIRS convention, these pressures refer to the bottom of the sublayers.

As discussed above, the limiting effects of the presence of clouds in the AIRS FOV, implies a reduction of the number of full retrievals with increasing cloud amount. In this work it is assumed that, for the model simulations, the value corresponding to the 80 % AIRS effective fractional cloud cover threshold is of the order of 70 % total cloud cover (TCC). The consequences of this constrain in the sampling characteristics of AIRS data, and the way it affects/defines the methodology of model validation and intercomparison, is discussed in the next section (6.1.3 Matching models and observations).

Figure 6.1 presents three samples of RH extracted for the GPCI cross section from the daily AIRS RH record. These are compared with GOES10 (Geostationary Operational Environmental Satellite 10) imagery in the infrared (channel 4, wavelength 10.7 μm). The three different days were chosen as representing three distinct synoptic meteorological situations typically found during JJA 2003 in the (sub) tropical NE Pacific. A straight black line is superimposed on the GOES images to schematically locate the GPCI transect. Taking into account that the AIRS data corresponds to an entire 24 hour period of measurements, it was desired to find GOES images showing persistent meteorological features, as captured in the 00 UTC (Universal Time Coordinated) and 12 UTC snapshots, corresponding to those same days in terms of the local time in the study area. The GOES images shown were all taken at 12 UTC, which, in local solar time, corresponds to approximately 03:40 am (~ 00:30 am) at the northernmost (southernmost) point in the cross section.

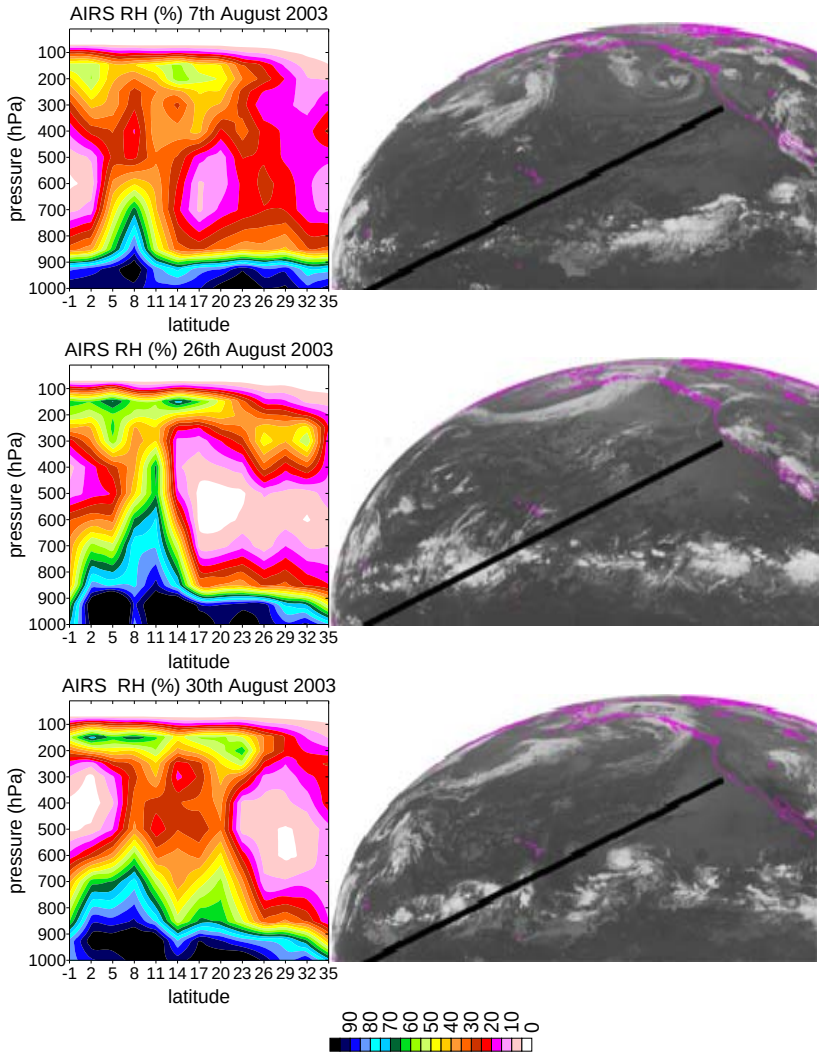

Figure 6.1 - Daily Atmospheric InfraRed Sounder (AIRS) relative humidity (RH) profiles along the GPCI cross section (black diagonal line), together with 12 UTC GOES10 satellite infrared snapshots for August 7 (top row), 26 (mid row), and 30 (bottom row), 2003 (see text for details).

In the first row in Fig. 6.1, dated August 7th, 2003, the GOES IR signal is relatively strong along the entire cross section, with the proximity of a low pressure system in the mid-latitude NE Pacific, broken packs of low level cloudiness all the way from the subtropical stratocumulus (Sc) regions (northern segment of the transect) to the equatorial central Pacific, and a dormant ITCZ (Inter-Tropical Convergence Zone), at least in terms of the intensity of the deep convection in the vicinities of the transect. Looking at the 25 % RH line (between red and brown in the color scale), the AIRS RH transect clearly depicts an ITCZ centered at around 8°N. Note also the relatively deep atmospheric boundary layer (BL), with a top (assumed, for the trades and the Sc areas to be [in a first approximation] the 50 % RH [e.g., Siebesma et al. 2004] line [between the yellow and green colors]) consistently at ~ 850 hPa to the north of 14°N. A prominent feature in this plot is the relative maximum in RH centered at 26°N,

connecting the top of the BL to upper-level relatively high values of RH. In the mid row in Fig. 6.1, dated August 26th, 2003, the GOES image shows, in contrast, an anemic infrared signal (basically spanning the entire portion of the tropical Pacific shown), associated with an active ITCZ, and a more homogeneous low level cloudiness field, extending southward along the cross section, from the subtropical Sc area to the trades (around 20°N, see the location of the Hawaiian Islands), where the cloudiness is broken, with the darker areas much probably associated with relatively clear skies. Note also the inexistence of any important mid-latitude cyclonic disturbance affecting the "area of catchment" of the section. Accordingly, and comparatively to the situation on August 7, the AIRS RH vertical cross section has a moister ITCZ, with a more well defined (and vertical) northern (RH) "boundary" (up until 300 hPa), and a generally lower BL top in the Sc area (especially to the north of 26°N). But, perhaps, the more striking aspect is now the very dry area, roughly between 750 hPa and 450 hPa, to the north of 17°N. Note the minimum above the trades (17°N to 23°N), with values of ~ 5 %, or less, RH. On August 30th, 2003 (bottom row in Fig. 6.1), four days after the previous situation described (mid row in Fig. 6.1), the region across the GPCI transect immediately to the east of the Hawaiian Islands, witnessed the peak strength of Jimena, by then a hurricane with sustained winds slightly over 160 km/h (http://www.prh.noaa.gov/cphc/summaries/2003/jimena/jimena.php). This is clearly the main departure from what is seen in the previous GOES image (note that the Sc decks appear even more well defined on August 30). Jimena shows in the AIRS profiles centered at 20°N, and lends the RH cross-section a look that resembles a double ITCZ.

In conclusion, the broad potential uses of the AIRS data are here undoubtedly displayed, even in view of some of the physical processes affecting cloud formation and evolution discussed in Chapter's 2 [Convection and clouds over the (sub)tropical oceans] Section 2.3 (e.g., the impacts of free tropospheric humidity on the subtropical Sc cloud decks).

6.1.3 Matching models and observations

A common feature of most of the studies referenced above (see [AIRS] *Validation efforts*, in Section 6.1.1) is the focus on the observational validation, i.e., an assessment based on collocated, usually contemporaneous, matches between AIRS retrievals and the chosen correlative truth. Of primary importance in climate studies, though, are the uncertainties and biases that may arise from the temporal and spatial sampling characteristics of a certain instrument, and or remote sensing platform, and, particularly, their potential

limitations/strengths under different atmospheric conditions. Moreover, in this context, it is frequently found that purely observational biases are only a small portion of total biases. Separating sampling induced misrepresentation of atmospheric state from the other error processes is one of the great challenges of validating and using satellite datasets.

On the other hand, in validating model results with observations it is usually recommendable to adapt the numerical simulations output to the spatial and temporal resolutions of the observational dataset. This is generally done by applying certain constrains, thresholds, or compositing the model record. Naturally, this mindset can be reversed in case the available model data is, in any particular perspective, more limited than the observational data. Relatively sophisticated methodologies have been developed with these concerns in mind, being the ISCCP simulator (see Section 3.4, Observational datasets) a good example of the efforts toward more meaningful comparisons of models and observations.

This section presents the methodologies followed to characterize the AIRS RH dataset prepared for GPCI introduced above. As the investigation of observational biases is outside the scope of this study, the main focus is on sampling biases, and potential consequences to the results presented in the following sections.

Spatial matching

Horizontal To spatially match the observational and the simulated records of relative humidity was the first task to be accomplished. First of all, the model data was made available by the different centers already along the cross section, following the GPCI specifications (which did not suggest any particular way to extract the results to the 13 points comprising the transect, or to the grid cells in the broader 2D maps [Section 3.2.2, Project protocol]). The participating centers reported the use of different techniques for that end (e.g., nearest grid point, bilinear interpolation). Table 3.1 shows the horizontal resolution and number of vertical levels of the different models. In the case of the AIRS data, the original 1° × 1° latitude-longitude grid had to be degraded to the 5° × 5° resolution of the 2D maps, and to the 13 locations along the GPCI transect. Given that the GPCI points coincided with grid nodes in the AIRS dataset, it was decided to take the average RH of the nearest 4 AIRS grid nodes to get the values for the 2D and transect locations.

Vertical Regarding the matching in the vertical, recall that the preliminary procedure followed to obtain RH from the AIRS temperature and specific humidity retrievals (Section 6.1.2), used an inferred (linear) temperature profile between adjacent (temperature) pressure

levels to calculate the column saturation vapor pressure from the humidity value for the corresponding sublayer. This means that the RH information on the AIRS vertical grid actually applies to the sublayer above the pressure levels themselves. To better correlate models and observations, the relative humidity profiles were linearly interpolated in the vertical (at each one of the GPCI locations) to a common 10 hPa -spaced regular pressure grid (the AIRS data was analogously interpolated in the vertical). The interpolated model simulations correspond thus to point values. An alternative would be to further integrate these values in the vertical for each (overlying) sublayer. This would require the assumption of a certain vertical profile for the relative humidity in the sublayers, a procedure that was not adopted in the this work, also to preserve a higher degree of detail in the vertical.

Temporal matching

To match the 3-hourly model output with the daily temporal resolution of the AIRS data, daily averages were calculated for the RH simulations. Apart from the seasonal averages and the percentages shown in the results that follow, all other calculations (e.g., variance [standard deviation], moving averages [temporal evolution]) were performed on the daily record.

Sampling matching

As previously mentioned, in this work it is assumed that, for the model simulations, the value corresponding to the 80 % AIRS effective fractional cloud cover threshold is ~ 70 % TCC. This value was then applied as an upper threshold for the selection, among the 3-hourly model output, of only those profiles of RH contemporaneous with values of the TCC parameter below 70 % (inclusive). The accrued RH profiles were then the basis for the calculation of the "constrained results" used for a more direct comparison with AIRS.

The top row in Fig. 6.2 shows, for some of the participating models, the (unconstrained) JJA 2003 mean TCC along the GPCI cross section. It also depicts the 70 % TCC (horizontal green) line, and the percentage of time TCC is less than or equal to 70 % at each one of the transect locations, which is also the percentage of "usable" RH profiles according to the TCC constrain (TCC70% hereinafter). As expected, the locations mostly affected by the TCC70% constrain, are those with the highest average TCC values, pronouncedly the ITCZ region (~ 8°N), where the number of usable profiles can be as low as ~ 20%, and the Sc regions (especially at 32°N). The trades (~ 17°N to 20°N) are less affected by the constrain, showing, in two of the models, values that surpass 70%. Note that these percentages were obtained from the 3-hourly record of simulation output.

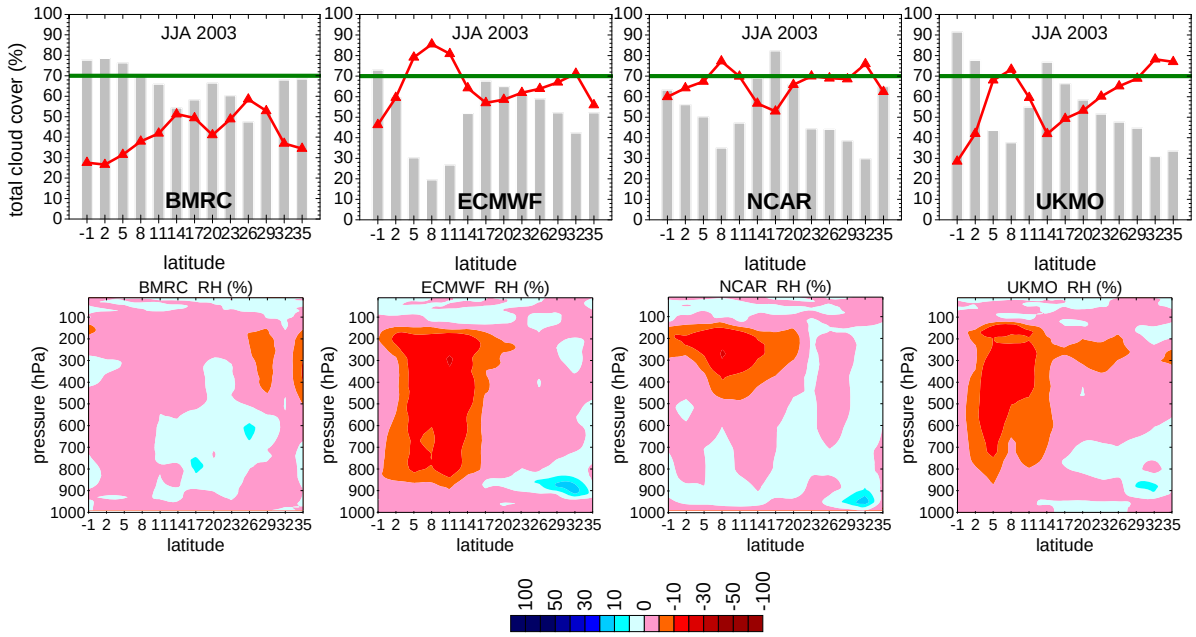

Figure 6.2 - Top row: June-July-August (JJA) 2003 mean total cloud cover (red line with triangles) along the GPCI cross section for four of the participating models (the horizontal green line marks the 70 % total cloud cover value), together with the respective percentages of occurrence of total cloud cover less than or equal to 70 % (gray columns). Bottom row: difference between constrained and unconstrained seasonal mean relative humidity (RH) (see text for details).

The bottom row in Fig. 6.2 presents, for the same models, cross sections of the difference between (TCC70%) constrained JJA 2003 mean RH and corresponding unconstrained RH. The results show a general dry bias, especially between levels 800 hPa and 200 hPa, and between 2°N and 17°N (around the ITCZ). This is in line with the fact that, in the ITCZ, higher values of TCC are typically associated with more intense deep convection and higher RH values at all levels in the vertical. The models seem to produce this (note, however, the slight moist bias at lower levels in the ITCZ in NCAR). Regarding the Sc region, it is interesting to notice that the models with the highest TCCs in those areas (to the north of ~ 26°N) show, in these plots, a wet bias right above the boundary layer. Again, this is, potentially, a good sign for these models, since it is expected that higher Sc cloudiness to be associated with a relatively dry free troposphere above the BL. BMRC shows clear departures from the other models in all features analyzed.

In conclusion, these model results depict quite well what was presented earlier regarding AIRS sampling biases in relation to weather and climatic patterns preponderant in different regions, most notably the findings in Fetzer et al. (2006), reporting that the largest AIRS (versus AMSR

-E) wet observational biases were located in regions more affected by persistent stratus cloud cover.

Bias, moving averages, and standard deviation calculation

To close, a few notions to support the analysis presented in the next section: 1) "observational bias" is defined as the difference "model minus observation", while "sampling bias" is defined, for a given dataset, as the difference "TCC70%-constrained minus unconstrained" (unless otherwise noted, the bias is evaluated directly from the seasonal means); 2) the moving averages used are simple unweighted previous moving averages that include the day in question and the previous 4 days (after preliminary investigation, the choice of a 5-days window seemed the best balance between the need to filter some transient meteorological signal and the availability of data in the constrained record of model-simulated RH); 3) for either the constrained, or the unconstrained records, the standard deviation is calculated, at the different locations along the cross section, individually for each level in the vertical profiles (the variance is evaluated from the daily averaged model output).

6.2 Mean structure and variability of relative humidity

This section presents a brief description of the main seasonal aspects of the summertime structure and temporal evolution of the vertical distribution of relative humidity in the GPCI region. It is based on model simulations and AIRS observations for JJA 2003.

6.2.1 Seasonal mean and variance

The left plot in Fig. 6.3 shows the seasonal mean AIRS RH along the GPCI section for the JJA 2003. It qualitatively depicts the RH signature of the thermally direct Hadley circulation of the (sub)tropical NE Pacific, with the ITCZ centered at 8°N (in June [not shown] the ITCZ is located between 5°N and 8°N, while in August [not shown] it is located between 8°N and 11°N), a moist BL, and a relatively dry free troposphere, capped by higher RH values in the tropopause. A look at the daily record of AIRS RH transects indicates that this (typical climatological) RH picture, not rarely, suffers disruption during the season, especially owing, for instance, to the influence of baroclinic disturbances, in the northernmost part of the section, and tropical depressions and hurricanes, in the lower latitudes (see Fig. 6.1). Still, it is, mostly, the sampling idiosyncrasy of the AIRS experiment (especially in what concerns the presence of clouds) that ultimately modulates the RH evolution in this particular dataset. In more detail, the

mean RH section is characterized by a very moist BL, with values above 70 % at 1000 hPa along the whole cross section (recall that, for AIRS, a value at 1000 hPa actually represents the layer between 1000 hPa and 925 hPa), being over 95 % between just north of 20°N and the ITCZ, a hint that the trades constitute an important source of the moisture that help fuel (via latent heat release) the deep convection in the ITCZ (recall that the low-level atmospheric flow blows along the trades in the direction of the ITCZ, and experiences increasing sea surface temperatures [SSTs]). Regarding the top of the BL (BLT), if one takes the 50 % RH line to be a proxy for its location (e.g., Siebesma et al. 2004), the BLT is at its lowest position at 35°N, at ~ 940 hPa, and deepens southward until a value of ~ 860 hPa, at 17°N. Noteworthy is also the (overall) southward intensification (weakening) of the vertical gradient of RH just below (above) the BLT between those two positions. For July (not shown) the southward deepening of the BL is the steepest, while for August (not shown) the BLT is close to 850 hPa for most of the transect between 20°N and 32°N. In the vertical, the seasonal ITCZ is characterized by a dome-shaped structure capped by a layer of RH with values as high as 50 % up to ~ 530 hPa. At 500 hPa, there is a minimum in the amount, and latitudinal extent, of the ITCZ RH, with the layers above showing the reverse picture until the tropical tropopause is reached at ~ 150 hPa (at 8°N). Finally, the driest portion of the vertical section is found in a layer between 650 hPa and 450 hPa (mid troposphere), essentially extending from the trades to the Sc (in the northern portion of the section), and showing values below 20 % RH. This minimum is associated with the large scale atmospheric subsidence that characterizes the dynamics of the subtropical free atmosphere. In June (not shown) that domain is even broader, both vertically and horizontally, and the RH falls below 10 % in a thin layer centered at 600 hPa between latitudes 26°N and 29°N.

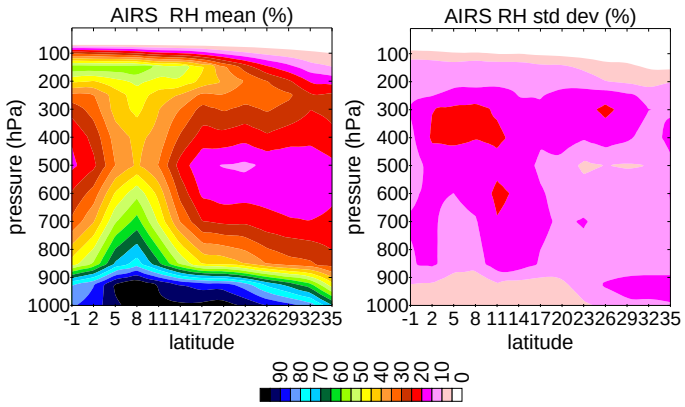

Figure 6.3 - June-July-August 2003 vertical structure of relative humidity (RH) along the GPCI cross section as seen in the mean (left plot) and standard deviation (right plot) taken from AIRS observations.

The right plot in Fig. 6.3 shows the corresponding RH standard deviation for JJA 2003. Note that both plots in this figure use the same color scale. There is an outstanding difference between the structure of the mean RH and the corresponding standard deviation field, with the standard deviation assuming notoriously lower values (below 25 %). One of the areas that shows the least variability in humidity extends from 23°N to (at least) the south end of the cross section, and is found generally below 900 hPa, coinciding with the area of highest mean RH values. In contrast, relatively high values of standard deviation (15 % to 20 %) are found in a layer with a constant top close to 890 hPa between 35°N and 26°N (Sc region). This feature is probably associated with the local variability in the location of the BLT. Lower standard deviation values (10 % to 15 %), homogeneously spread between 20°N and 35°N, and 870 hPa and 450 hPa, are an indication of the relative steadiness of the subtropical subsidence during JJA 2003. Another interesting detail in this plot is the minimum that extends in the vertical to about 600 hPa roughly between 2°N and 8°N, in clear contrast with the higher values found immediately to the north of it. This may, in part, be explained by the northward shift of the ITCZ during the season, an argument, in part, supported by the higher values in the vertical to the south of 2°N. Finally, the highest values of RH standard deviation for JJA 2003 are mainly found between 2°N and 11°N, centered between 300 hPa and 400 hPa, at the base (and mostly towards the south) of the upper-level relative maximum of (mean) RH associated with the tropical tropopause above the ITCZ.

Figure 6.4 shows, for the same four models presented in Fig. 6.2, JJA 2003 cross sections of seasonal mean RH, RH standard deviation, and the corresponding biases versus the respective AIRS results. Keep in mind that these are (TCC70%) constrained results. All the models show, in the RH means (column to the left), the general features associated with the RH signature of the Hadley circulation described above for AIRS (left plot in Fig. 6.3), and in a previous chapter, for the unconstrained model results (Fig. 4.4). Regarding the comparison with the AIRS seasonal mean RH (second column from the left), there are significant biases in these models, namely: *i)* a very important negative bias in the lowest portion of the BL (except to the north of 32°N); *ii)* in contrast with a strong wet bias immediately above it, along the whole transect (except for NCAR, with the wet bias confined between 11°N and 20°N), a situation associated with deeper BLs in the models than in AIRS; *iii)* in the deep convection area (around 8°N), there is (above a surface dry bias extending up to ~ 900 hPa) a wet bias between ~ 800 hPa and ~ 450 hPa, associated with, not just higher RHs going to higher levels, but also with wider ITCZs than in AIRS (the exception being ECMWF, with a slightly narrower ITCZ);

iv) the tropopause layer shows, overall, higher RHs in the models; *v)* the subtropical mid troposphere is, except for the BMRC model, generally drier in the models, especially immediately above the BL, with biases of up to -30 % RH relative to AIRS (this situation may be associated with a poor link between large-scale subsidence field and RH, and or with the misrepresentation of the influence of transient extratropical disturbances on the free tropospheric humidity structure [see top row in Fig. 6.1]).

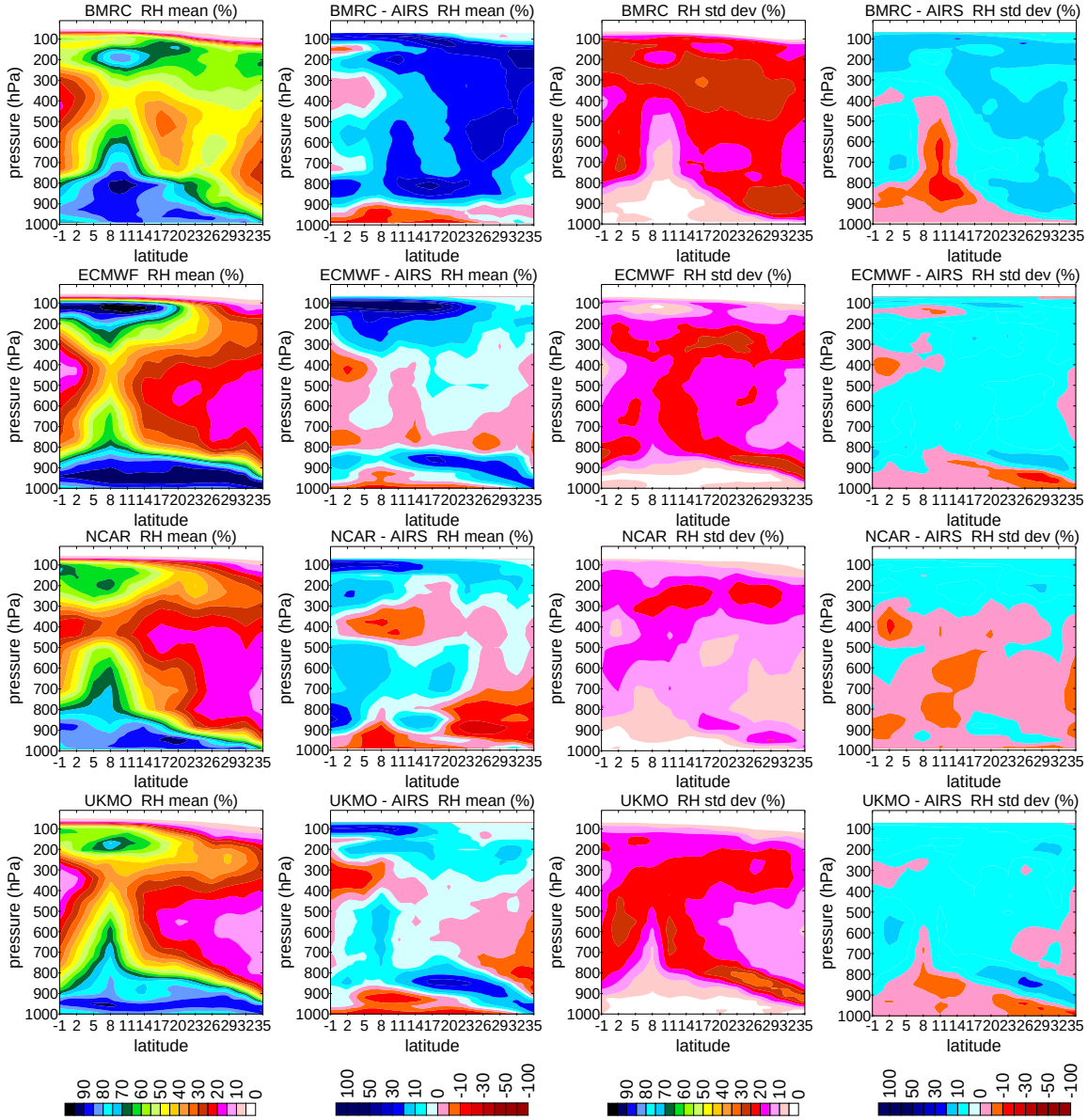

Figure 6.4 - For the same four GPCI models presented in Fig. 6.2, June-July-August 2003 cross sections of seasonal mean relative humidity (RH) (left column), RH standard deviation (std dev, in the third column from the left), and the corresponding biases versus the respective AIRS results (model - AIRS, in the second and fourth columns from the left, respectively).

In terms of the standard deviation (third column from the left), it should be noted that the general structure of the constrained and the unconstrained (not shown) cross sections compare very well for all the models, with only a slight decrease in variability in the constrained results.

It could probably be argued that this is also the case for AIRS, i.e., the sampling deficiencies result in a more static RH structure. Still, although the models show, overall, higher RH variability, there are distinct features in the comparison with AIRS. The right column in Fig. 6.4 shows a lack of variability in RH in the BL along the entire cross section, with models presenting negative standard deviation biases of up to -20 % in the subtropical BL (23°N to 35°N) (recall that the variance is evaluated from the daily averaged model output and not from the 3-hourly record). This is probably associated with the simulation of persistently deep subtropical BLs, as in the ECMWF and UKMO models. Another noteworthy feature is the positive bias just above the BL (particularly north of 20°N). More so than a model deficiency, this is probably associated with the relatively poor vertical resolution of this AIRS dataset, which may not the able to detect the finer detail in the variability of the vertical location of the BL top, particularly in the subtropics.

6.2.2 Intraseasonal evolution

To qualitatively investigate how the vertical structure of RH evolves during the JJA season, 5-day running means of the RH record were obtained for different locations in the GPCI cross section (the details are given above in *Bias, moving averages, and standard deviation calculation*). The corresponding JJA 2003 results for AIRS and two of the participating models are shown in Fig. 6.5. Again, the model results are obtained from the (TCC70%) composited RH profiles, being the vertical white columns in the plots, gaps arising from (at least) five consecutive days with TCCs above 70 %. From the discussion of Fig. 6.2, this situation is expected to occur more frequently in the NCAR model than in the BMRC model, and, for any of the models, more frequently in the deep convection and Sc regions, than in the trades.

Looking at the larger set of models, a general first conclusion is that, for the three locations shown (8°N, 20°N, and 32°N), there seems to be, overall, a better spatiotemporal correlation between any two given models than between the models and AIRS. It is also immediately apparent that the comparison of models and AIRS in terms of the humidity content in the BL, ITCZ, and subtropical mid troposphere, presented above, is still patent in these results, particularly in what concerns the model biases in the lowest levels along the transect, and the depth of the BL. What these plots put in evidence is essentially the fact that, at 32°N, the RH variations tend to be coherent throughout the entire profile, as opposed to having (especially at 20°N [trades]) periods when a drying of the mid troposphere is accompanied by a moistening at upper levels. This seems to point out to the need to include in the investigation of the

breakup of the Sc cloud decks that happens in the transition to the trade-wind shallow cumulus, the influence, not just of the humidity structure in the free troposphere immediately above the BL, but also of the humidity profile all the way to the upper troposphere. A synergistic approach between AIRS and other instruments onboard Aqua could be tried to tackle this issue.

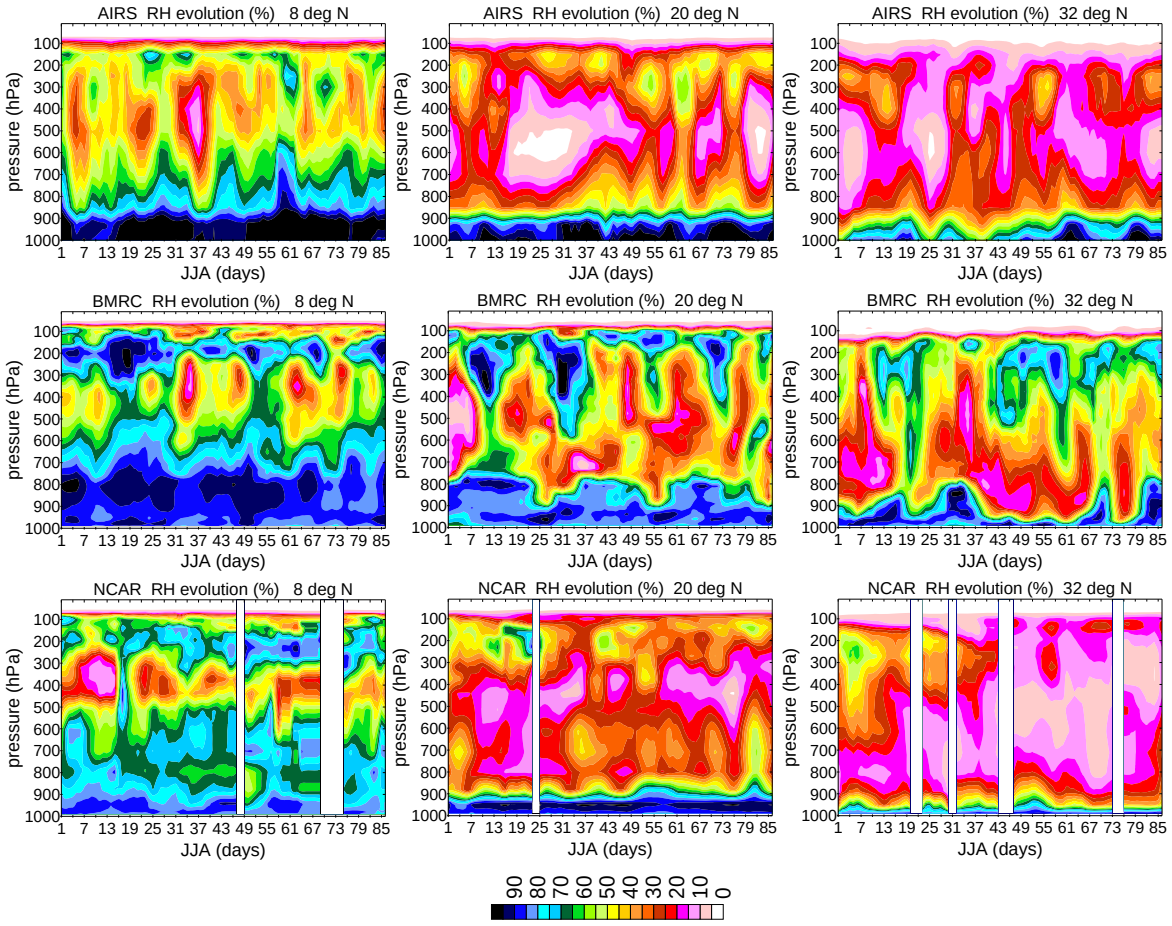

Figure 6.5 - June-July-August (JJA) 2003 5-day running means of the vertical distribution of relative humidity (RH evolution) at three different locations along the GPCI cross section (8°N, 20°N, and 32°N), for AIRS observations (top row) and two participating models (mid and bottom rows).

6.3 Is relative humidity a driver for cloud transition?

To answer this question, this section is divided into three main sections. Section 6.3.1 (Relative humidity as a proxy for boundary layer depth) presents a brief bibliographical review on boundary layer top determination. In section 6.3.2 (A new scheme to determine the BLT) the adequacy of relative humidity for the assessment of basic characteristics of the NE Pacific maritime atmospheric boundary layer, such as its depth and inversion strength, is explored resorting to a new scheme for the determination of the top of the boundary layer. The corresponding seasonal statistics for JJA 2003 are obtained along the GPCI cross section for

model simulations, atmospheric analysis, and AIRS observations. Section 6.3.3 (Cloud cover transitions) revisits the topic of abrupt transitions in cloud cover along the GPCI transect, firstly, by introducing an updated methodology for the location of these discontinuities in the cloud fields. The corresponding results are then used as guidance for the calculation of the spatial averages of relative humidity profiles, composited as located upwind, or downwind, of the location of the strong cloud cover gradients thus found during the JJA 2003 season in data from models and analysis.

6.3.1 Relative humidity as a proxy for boundary layer depth

Owing to the complexity of its phenomenology, the boundary layer has been given a great deal of attention in observational and in modelling studies. Simulation of boundary layer clouds in global climate models is still a challenge (e.g., Weare 2004; Bony and Dufresne 2005; Teixeira et al. 2008b; Karlsson et al. 2008), and would benefit from a better understanding of the observed behaviour of the planetary boundary layer. In this context a few related studies can be highlighted, namely: Seibert et al. (2000) thoroughly review and compare operational methods for the determination of the height of the atmospheric boundary layer (e.g., methods that use profile data from measurements [radiosonde profiles, sodar and wind profiler data] or from numerical model output, and mixing height parameterization using simple equations or models); Karlsson et al. (2010), present a cloud-top height (CTH) approach (discussed in Section 5.1.4 of this work) for the determination of the (sub)tropical maritime boundary layer top (BLT) from satellite observations, reanalysis data, and climate model simulations (an example among other satellite-based methodologies developed to tackle the issue of the determination of the BLT on a global scale from satellite data); passive-sensor CTH methods (e.g., Minnis et al. 1992; Wood and Bretherton 2004; Zuidema et al. 2009) have been successfully applied in regions dominated by low level (stratocumulus) clouds (e.g., Stevens et al. 2007); spaceborn lidars (active sensors) have been used to estimate the boundary layer height (BLH) from observed CTHs in stratocumulus areas (e.g., Ahlgrimm and Randall 2006; Lin et al. 2009); based on satellite retrieved vertical distributions of temperature and humidity, other studies have tried to locate the inversion that typically caps the maritime boundary layer, e.g., Fetzer et al. (2004), using AIRS, and von Engeln et al. (2005), using radio occultation data; in addition to CTH, Karlsson et al. (2010) present an alternative technique to determine BLT and estimate BLH from the vertical gradient of relative humidity.

More specifically, Karlsson et al. (2010) used "the height of the maximum vertical RH gradient with respect to pressure" found between the surface and 700 hPa. The method was successfully applied along the GPCI cross section to models, analysis, and AIRS observations, and the results showed, mostly in the subtropics, a fairly good agreement with the CTH-based BLT estimate for the same models and analysis, and MISR (Multiangle Imaging Spectroradiometer) observations. In the next section, an updated version of the RH-based methodology is introduced. It basically consists of additional conditions imposed to the evaluation of the RH profile in a sequence of stages of increasing constrain refinement. The methodology has thus been named sBLT, for *sequential Boundary-Layer-Top determination scheme*.

The introduction to sBLT starts with a brief overview of the main concepts behind its operation, followed by a description of the basic algorithm and subsequent steps for the determination of the BLT from a given RH profile. The section then proceeds to a discussion of a number of statistics to characterize the climatological BLT for a given location. After a few additional remarks, and the presentation of developments envisioned for the near future, preliminary results are discussed for a few case studies. sBLT statistics for JJA 2003 along the GPCI transect are analyzed for models, and atmospheric analysis. To close the section, the same kind of statistics are presented for the corresponding AIRS RH record.

6.3.2 A new scheme to determine the BLT

The RH results analyzed up to this point in the thesis, obtained from models and observations, either as seasonal climatologies, or at particular times during the JJA season (Fig. 4.4, Fig. 6.1, Fig 6.3, Fig. 6.4, and Fig 6.5), show that in the (sub)tropical NE Pacific the MBL is typically very moist, at least as seen along the GPCI cross section. Moreover, there is, for all of the transect locations in all those results, a marked upward decrease in RH at some point in the vertical profile, separating the moist lower levels from a relatively dry mid troposphere. It is known that these are important features of the (sub)tropical MBL, and that, in particular, the sharp decrease in RH is typically associated with the approximate location of its top. Locating the level of the strong decrease in RH has been the basic motive behind a number of RH-based BLT determination methods recently proposed in the literature (e.g., Karlsson et al. 2010, Martins et al. 2010). Introduced below, sBLT is yet another such proposal. RH is believed to be a befitting variable for this purpose owing to the fact that it depends on both temperature and humidity.

6.3.2.1 Basic concepts

Humidity Profile The sBLT methodology is solely based on the manipulation of relative humidity data (observational, or simulated) given in the form of vertical profiles spanning the layer from the surface to (ideally) the upper troposphere. In the first data treatment step, profiles are screened for bad values (inexistent data, or RH < 0 % [RH > 100 % is, at this stage, included in the analysis]), being disregarded if a bad data entry is found at one or more levels. In the second step, the RH information is interpolated to a regularly-spaced vertical grid (in what follows, the RH is assumed to be on a vertical pressure grid). The interpolation to a common vertical grid is especially useful when dealing with RH information from different sources, either used in combination, or for the purposes of comparison between different datasets. Specific issues arising from the interpolation procedure are discussed later (see Additional Remarks).

RH-Gradient Profile Once a RH profile has been screened and interpolated, it is used for the calculation of the corresponding RH-gradient (RHgrad) profile. The RH and pressure information for two adjacent levels is used such that the RHgrad for the layer bounded by the two levels is obtained dividing the RH difference between the top and bottom levels by the difference in pressure between the bottom and top levels. This value is then assigned to the mid level for that layer (this implies that the levels in the RHgrad profile correspond to the mid levels of the original RH profile). Given the pressure drop going up in the profile, this assures that a positive (negative) RHgrad corresponds to an increase (a decrease) in RH between the bottom and the top levels of the layer in question.

Upper Threshold For a given sublayer in the RH profile, the upper threshold (*ut*) is the RH value at the respective top level (this level is then called *put*).

Lower Threshold For a given sublayer in the RH profile, the lower threshold (*lt*) is the RH value at the respective bottom level (this level is then called *plt*).

Lower Cumulative Average Line For a given sublayer in the RH profile, the lower cumulative average line (*local*) starts at the respective *plt*, where it is equal to *lt*, and is built all the way to the bottom of the profile, taking, at each profile level, a value equal to the cumulative average of the RHs from all the levels between it (inclusive) and the *plt*. The *local* is also assigned to the corresponding RHgrad level, i.e., the midlevel of the sublayer in the RH profile. The *local* should be seen as a continuous line, with values between the profile levels obtained from the linear interpolation of the *local* values at respective adjacent levels.

S1 index A given level in the RHgrad profile is classified as S1 if the corresponding RHgrad is different than zero (irrespective of the sign). As an index, S1 can be 0, or 1, respectively when RHgrad is 0, or RHgrad is different than zero.

S2 index If a given level in the RHgrad profile is a S1, it will be classified (also) as a S2 if the corresponding RHgrad is negative (i.e., RH decreases between the bottom and the top [levels] of the respective sublayer in the RH profile). As an index, S2 will be 1 if RHgrad is negative, and 0 otherwise.

S3 index If a given level in the RHgrad profile is a S2, it will be classified (also) as a S3 if the corresponding *local* is never lower than the corresponding *ut* (in which case S3 = 1). In case the *local* gets to be lower than *ut*, S3 will be given a value between 0 (exclusive) and 1 (exclusive), obtained from the division of the difference in pressure between the point where the *local* (first [going from *plt* toward the bottom of the profile]) gets to be equal to *ut* and the *plt*, by the difference in pressure between the bottom of the RH profile and *plt*. S3 will only be 0 if S2 is equal to 0. S3 is the only continuous S# index.

S4 index If a given level in the RHgrad profile is a S2, it will be classified (also) as a S4 if, at the bottom of the RH profile, the corresponding *local* is not lower than *lt*. In that case S4 is equal to 1, being equal to 0 otherwise (i.e., if S2 = 0, or the *local* is lower than *lt* at the bottom of the RH profile). Note that there isn't, at this point, any direct link between S4 and S3, in the sense that a level in the RHgrad profile can be a S4 without it (fully) being a S3. The only commonality arises from the fact that both S3 (full or partial) and S4 need to be a S2. A link between S3 and S4 is imposed at a later stage in the scheme (as explained below at sS#).

S# Order There is an order implied in the S# classification. A level classified as a S4 is said to be higher in the classification order, than a level that could not be classified as being more than a S3, and so on.

S# Classification of the RHgrad Profile Before proceeding to the basic sBLT algorithm, each level in the RHgrad profile has to be classified following the sequence of S# indexes presented above. The input information for the basic algorithm is, for each level (mid level) in the RHgrad (RH) profile: 1) pressure; 2) RHgrad strength (absolute value of RHgrad); 3) RHgrad sign; 4) S1 index; 5) S2 index; 6) S3 index; and 7) S4 index.

The S Profile A S profile is obtained by locating in the RHgrad profile the levels with the strongest full S# indexes, that is, for each one of the (four) S# = 1, the one with the highest RHgrad strength (irrespective of the sign) is picked to represent S# in the S profile. It can then

happen that a S profile may not have a S3 determined (if all are $0 < S3 < 1$), even if it has a S4 determined. Another possible situation is the one for which the same level in the RHgrad profile is assigned all four S#, i.e., it has the strongest S1, which, in turn is also a S2, a (full) S3, and a S4.

The strict S# (sS#) If a level classified as a S4 is only a partial S3, i.e., $0 < S3 < 1$, then its sS# will only be a sS2, that is, it will, in the more strict sense, be classified as a sS2. This arises from the fact that, the sS# classification sequence starts at the lowest S# (S1) and chooses it as the sS# if S(#+1) is not 1, thus stopping at S2 if S3 is only partial, even if S4 is equal to 1. This imposes a tight link between sS3 and sS4, and ensures that, when analyzing the final sBLT results, any BLT classified as a sS4 is known to be a sS3 as well (i.e., a full S3 [S3 = 1]). More importantly, a sS# is never a sS(#+1). Even when only a partial S3, S4 levels are, nevertheless, useful for the purposes of initialization of the basic sBLT algorithm.

6.3.2.2 The basic sBLT algorithm

Four main steps comprise the basic sBLT algorithm, they are ordered as follows:

1: In the RHgrad profile, identification of the level with the strongest RHgrad (irrespective of the sign) among the levels with the highest S# classification (see S# Order above). The search is performed only on full S# indexes, i.e., S# = 1 (any S# = 0, or $0 < S3 < 1$, are disregarded at this step).

2: Using the level chosen at step 1: as a reference, proceed down in the profile, and elect it as the BLT if: the level is already the lowest level in the RHgrad profile; or, all levels below it are as high as it is in the S# classification order; or, all levels below it are either sS1, or S1 = 0.

3: If at step 2: no BLT has been determined, then, using the level chosen at step 1: as a reference, proceed down in the profile to the level with the strongest RHgrad that is stronger than the RHgrad of the reference level, chosen among the levels classified as S(r-1), being Sr the classification of the reference level. In case no level is found to meet the condition, the search is instead performed among the levels classified as S(r-2). And so on. The search stops at S2, i.e., this search is not to be performed among levels classified as S1.

4: If at step 3: a level has been found to meet the imposed condition, it is then taken to step 2: of the algorithm and subject to the same scrutiny going down the algorithm step sequence. On the other hand if no level has been found to meet the condition imposed at step 3:, the reference level from step 1: is chosen as the BLT for the profile being analyzed.

S! The following information is then stored for S!, the BLT determined by the basic algorithm: 1) pressure (keep in mind that this is a level of the RHgrad profile corresponding to a mid level of the original RH profile); 2) RHgrad strength (absolute value of RHgrad); 3) RHgrad sign; and 4) sS#.

Note that S! can only be a S1 if no level in the RHgrad profile has been classified as higher that S1.

6.3.2.3 BLT determination

Partial-Profile Looping In the partial-profile loop, S! are obtained for all and each one of the subprofiles that are embedded in the full RHgrad profile, that is, starting with the full RHgrad profile (i.e., the one with the bottom at the lowest RHgrad profile level and the top at the highest RHgrad profile level), each successive profile with the bottom at the lowest RHgrad profile level and the top at the RHgrad profile level right below the top level of the previous subprofile. The first subprofile in this sequence is then the full profile itself, the second subprofile will have its top at the level just below the top of the first subprofile, and so on. The final result is a catalogue of all the S! thus obtained, and, in particular, the number of times/subprofiles for which a given RHgrad level has been chosen as the S!.

S! Dp With the information from the partial-profile loop it is possible to determine, for each RHgrad level ever chosen as a S!, the corresponding lifespan, i.e., the RHgrad profile span comprised between the tops of the first and last subprofiles for which it has been chosen as the S!. Note that the operation of the basic algorithm described above implies that the RHgrad level in question was continuously chosen as the S! during the respective portion of the partial-profile loop sequence. Defining *ftop* as the pressure at the RH-profile level just above the top level of the first subprofile, and *ltop* as the pressure at the RH-profile level just below the top level of the last subprofile (recall that the RHgrad profile levels correspond to mid levels of the RH profile), Dp is calculate, for all RHgrad levels ever chosen as the S!, as the difference between the respective *ltop* and *ftop* (Dp = *ltop* - *ftop*).

7.S1 For the purposes of comparison of the sBLT results with the results that would be obtained following the RH-based BLT determination technique of Karlsson et al. (2010) (JK10 hereinafter), the strongest RHgrad for the subprofile with *ftop* = 700 hPa is identified. Once located, the level corresponding to this (strongest) RHgrad is stored as 7.S1, where S1 comes from the fact that this specific RHgrad is the S1 that would have been chosen for the S profile

(see details above at The S Profile) corresponding to the RHgrad profile with *ftop* at 700 hPa. Keep in mind that JK10 focused solely on the RH information below 700 hPa. Also, since JK10 does not make explicit reference to the sign of the gradient, it is here assumed that S1 would be their choice (recall that an S1 in the S profile may not necessarily be an S2).

7.S2 In addition to the search for 7.S1, it can be of interest to find 7.S2, which is the S2 that would have been chosen for the S profile (see details above at The S Profile) corresponding to the RHgrad profile with *ftop* at 700 hPa. Note that 7.S2 is the strongest RHgrad with negative sign, i.e., the strongest RH decrease with height, found in the RHgrad profile with *ftop* at 700 hPa.

PP*top* As will be seen below, it may be of interest to find, in the RHgrad profile, the level with the highest Dp. In a more general situation this search can be performed on only a specific (intermediate) portion of the RHgrad profile. In case the search is to be done between the bottom and a specific level of the RHgrad profile, the level with the highest Dp thus found is said to be associated with PP*top*, where PP stands for partial profile, and *top* is a given pressure value (e.g., 650 hPa). If *top* is the pressure at the top of the (full) RHgrad profile, PP*top* is called FP (for full profile). Note that, in either case (intermediate portion of the profile, FP, or PP*top*) the Dp values are the ones obtained from the analysis of the RHgrad profile as a whole.

Final sBLT Solution The final sBLT solution is the BLT corresponding to the RHgrad level with the highest Dp. As mentioned above, the choice can be made among only the RHgrad levels comprised between a particular portion of the RHgrad profile, although, typically, the final sBLT solution is obtained for, either the FP, or a given PP*top*. The following information is then stored for the final sBLT solution: 1) pressure (keep in mind that this is a level of the RHgrad profile corresponding to a mid level of the original RH profile); 2) RHgrad strength (absolute value of RHgrad); 3) RHgrad sign; 4) sS#; and 5) whether the final solution is, or not, the 7.S1 (the values for this parameter are then 1, or 0, respectively). It should be stressed at this point that a sS# is never a sS(#+1). But, as mentioned above [The strict S# (sS#)], a sS# is necessarily a sS(#-1). For instance, it can never happen that a level classified as a sS1 is simultaneously a sS2 (or above), meaning that a sS1 is strictly an increase in RH with height. This is in clear contrast with the situation for the S profile, for which a S# can be a S(#+1).

6.3.2.4 Climatological BLT characterization

The sBLT methodology can be applied to a single RH profile or to a number of profiles in a given spatiotemporal domain, in which case a number of statistics are typically obtained. Note that, a prerequisite for the statistical analysis, is that all individual elements of the sBLT solutions set, for a spatiotemporal domain of interest, need to have been found for a common PP*top*.

BLT Level The mean pressure for all the final sBLT solutions [point 1) of Final sBLT Solution above].

BLT Strength The mean RHgrad strength for all the final sBLT solutions [point 2) of Final sBLT Solution above (again, RHgrad strength is the absolute value of RHgrad)].

sS# Distribution The histogram of sS# for the final sBLT solutions [point 4) of Final sBLT Solution above].

not7.S1 Two things are evaluated for this statistic, one is the percentage (among the set of BLTs determined for the particular spatiotemporal domain) of final sBLT solutions that do not coincide with 7.S1 [a value of zero for the parameter in point 5) of Final sBLT Solution above], and the other is the percentage (among the set of BLTs determined for the particular spatiotemporal domain) of final sBLT solutions with pressures [point 1) of Final sBLT Solution above] less than 700 hPa.

6.3.2.5 Additional remarks

Strongest-S# Disambiguation In case the highest RHgrad strength for a given S# (with an index S# = 1) is found at two or more levels in the RHgrad profile, a disambiguation procedure is needed whenever it is desired to have only one level chosen. This is required, for instance, when trying to build a S Profile, or for the initialization of the basic sBLT algorithm, or to determine 7.S1. The currently adopted disambiguation procedure starts by looking at the value of the S(#+1) index for each one of the "ambiguous" levels, and chooses the level for which this index is the highest. If still there is the need for disambiguation in terms of the S(#+1) index values, the procedure then looks at the value of the S(#+2) index for each one of the remaining ("ambiguous") levels, and so on. If the procedure gets all the way to the evaluation of the last index in the S# sequence, i.e., S4, and still two or more levels remain ("ambiguous"), the one closest to the bottom of the profile is chosen. Note that the use of S3 as a continuous ($0 \leq S3 \leq 1$) index is only applied for the purposes of this kind of disambiguation. For any other uses, it is seen as a "0 or 1" index (like all the other S# indexes). In the particular

case the set of levels that need to be disambiguated are nonadjacent to each other, this final choice is based on the fact that the lowest level would (to the highest degree) be the one less marked by relatively dry sublayers below it. In the particular case the set of levels that need to be disambiguated are adjacent to each other (e.g., corresponding to sublayers obtained from the interpolation of a larger sublayer of the original RH profile with a given vertical rate of change for RH), the final choice is based on the (first order) assumption that, at the top of the boundary layer, the decrease of RH going up in the vertical is such that (locally) the corresponding (underlying [continuous]) RH curve is concave up, meaning that the highest decrease rate is found right at the BLT. This feature would then not be as clear in discrete RH profiles, such as the ones typically obtained from models and observations (especially if given in coarse vertical resolution). The disambiguation choice is then an attempt at getting closer to the actual BLT (this is revisited below at Future Developments).

Basic sBLT Algorithm Initialization By starting the basic algorithm at the level with the strongest RHgrad among the levels with the highest S# classification, the sBLT scheme tries to apply a first screening of the RHgrad profile for levels that overlay thick layers of dry air. Such RHgrad profile levels have the lowest probability of getting to the highest S# in the S# classification sequence. Extremely dry air intrusions are thus assumed to be atypical occurrences in the (subtropical) maritime boundary layers.

Regular p Profiles Although the linear interpolation makes the vertical distribution of RH smoother, the location of the main gradients in the profile should not change much if the new vertical grid is finer than the original grid.

PP*top* Choice Given the fact that, ultimately, sBLT bases its operation on geometrical considerations, it is possible that, for specific types of RH profiles, the BLT determined for the FP is at a level not realistic for a boundary layer. Taking this into account, testing has been performed to determine a reasonable value for PP*top*. For the current sBLT implementation, this value has been found to be *top* = 650 hPa, that is, PP650. Still, since the S! Dp values have to be calculated from the analysis of the RHgrad profile as a whole (see PP*top* above), in sBLT, no portion of the RH profile is discarded from analysis (contrary to JK10, that focused solely on the RH information below 700 hPa). Nevertheless, the FP results should always be analyzed, and can be potentially valuable to check for model and observational dataset deficiencies, namely, for the occurrence of unrealistically deep BLs.

sBLT versus JK10 It should be stressed that sBLT allows for a straightforward comparison of its results with those that would be obtained following JK10. In fact, JK10 is embedded in

sBLT. Note, however, that JK10 worked in model levels, and that no disambiguation procedure was reported in that publication. Another advantage of using sBLT comes from the fact that, even in the cases when sBLT and JK10 coincide, sBLT can still give additional information, useful to further characterize the BLT and the BL beneath it, namely in what concerns its sS# distribution statistic. This statistic is of special interest when comparing different spatial and or temporal domains, since it has information on, e.g., the kind of RH structure of the boundary layer, most typical in a given season or region.

sBLT versus Critical-Threshold Methods As mentioned above, with sBLT, the BLT is determined based on geometrical considerations. This seems to impart some robustness to the sBLT approach, particularly in the sense that it allows the determination of BLTs for a wider range of situations (especially in terms of the humidity content of the BL) than approaches that impose specific (typically minimum) thresholds to the vertical gradients of RH and or potential temperature (e.g., Martins et al. 2010).

6.3.2.6 Future developments

Testing sBLT is still in its development infancy. There is the need for further testing, especially on case studies with carefully chosen RH profiles, for which the sBLT results would be compared to the results from alternative RH-based (and other) methods (e.g., Fetzer et al. 2004, von Engeln et al. 2005, Karlsson et al. 2010).

Disambiguation Assumptions It would be important to assess the robustness of the assumption that, at the top of the boundary layer, the decrease of RH going up in the vertical is such that (locally) the corresponding (underlying [continuous]) RH curve is concave up (meaning that the highest decrease rate is found right at the BLT). This issue, first raised above at Strongest-S# Disambiguation, could be investigated resorting to fine resolution observation of the BLT, e.g., from dedicated radiosonde or satellite observational campaigns.

S1 In the current sBLT version, except for constant-RH profiles, a BLT is always determined, even if the S! out of the basic algorithm is a sS1. This implies that a BLT can be found in a profile characterized by a combination of constant-RH layers and layers showing an increase in RH with height, a case for which the BLT would end up corresponding to a RH increase with height (a situation not thought to be realistic [at least for the typical subtropical MBL]). A future development would then be to further constrain the algorithm to determine BLTs only for sS2, or above, S! solutions, or, at least, disregard sS1 “BLTs” in the evaluation

of the BLT Level and BLT Strength statistics, but still storing sS1 situations for supplemental information on the RH behaviour in the dataset in question.

sBLT Statistics Testing of sBLT results needs also to be done in a statistical framework. Development of additional sBLT statistics should be a priority.

not7.S2 This is an example of a statistic that would be interesting to implement. It is similar to the not7.S1 statistic, but with the focus on 7.S2, instead.

6.3.2.7 Case studies

Figure 6.6 presents four case studies, chosen to illustrate basic sBLT concepts, and the resulting sBLT BLT for specific RH profiles. In Fig. 6.6a, the S profiles are shown for the full (bottom to top) and the 700 hPa (bottom to 700 hPa) profiles. Recall that a S profile is obtained by locating in the RHgrad profile the levels with the strongest RHgrad for each S# index (S# = 1). f.S# and 7.S# are then the levels found for the full and the 700 hPa S profiles, respectively. Apart from the S profiles, the level for the BLT solution of the basic sBLT algorithm is also shown (S!), with an indication of the respective sS# (in light gray).

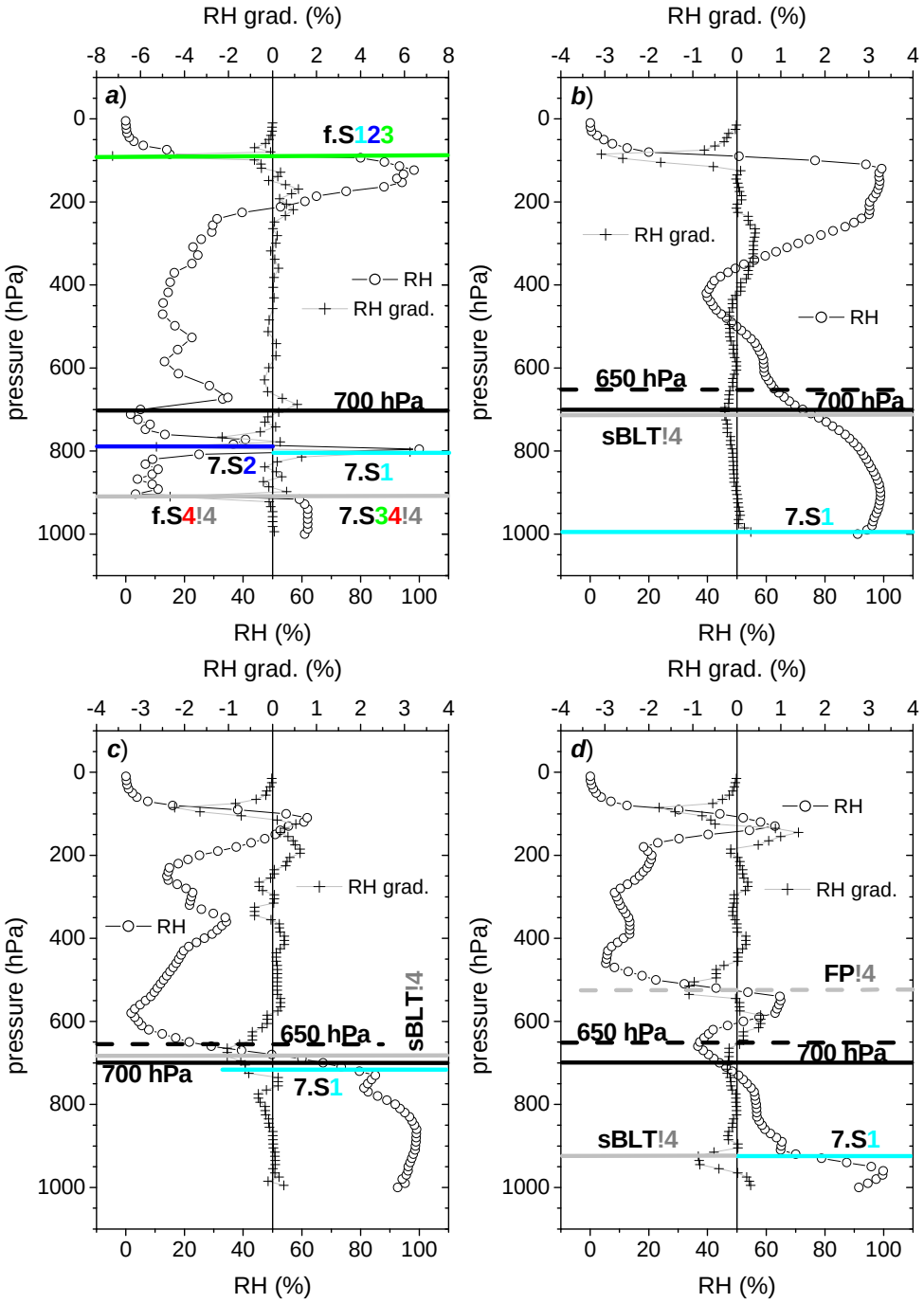

Figure 6.6 - Four vertical profiles of relative humidity (RH, black lines with open circles [at profile levels]), and respective profiles of the vertical gradient of relative humidity (RH grad., gray lines with black crosses [at the mid levels of the RH profiles]). The thick solid horizontal color lines indicate particular levels in the RH grad. profiles associated with the S# indexes with the same colors (the color shown is the one for the highest S# whenever different S#s fall in the same level). The thick black solid and dash lines indicate, respectively, the 700 hPa and 650 hPa levels (see text for details).

It is immediately apparent that, for this (Fig. 6.6a) RHgrad profile, the two S profiles differ substantially, except for S4, that is the same in both S profiles. Additionally, this same S4 is, for both, the solution of the basic algorithm. Note how f.S1, f.S2, and f.S3 coincide at the same

level, and how the thick dry layer below it doesn't allow it to be a S4, or at least, the strongest S4 in the full profile (f.S4). Note as well, that 7.S1 does not coincide with 7.S2 for the fact that the former corresponds to an increase of RH with height (a positive RHgrad.). As mentioned, this 7.S1 is assumed to be the JK10's solution. But perhaps the most striking thing about the case in Fig. 6.6a is the fact that 7.S2, the (mid) level with the strongest RH decrease in the 700 hPa profile, was not chosen by the basic sBLT algorithm as the BLT solution. This is an indication of the robustness of sBLT in being able to detect and manage intermediate dry layers (e.g., associated with residual layers, or with dry intrusions). Figure 6.6b, illustrates the use of a PP650. The final sBLT solution for this profile is indicated by the light gray thick line, sBLT!4. It is then the solution for a PP650 and corresponds to a sS4. Note how 7.S1 would not be an adequate BLT for this profile. Figure 6.6c, shows a case for which the sBLT solution is above 700 hPa. Finally, in Fig. 6.6d the FP sBLT solution seems unreasonable as a BLT, unlike the PP650 sBLT solution, which seems more realistic. For this profile, 7.S1 coincides with the sBLT solution, itself a sS4.

6.3.2.8 Model and analysis results

The results presented in the next two figures pertain to eight of the GPCI models and to one atmospheric analysis dataset (ECMWFan). These results were obtained from the available 3-hourly records.

In the left plot in Fig. 6.7, the sBLT BLT Level statistic is presented for models and analysis along the GPCI cross section as obtained for the JJA 2003 season. The transect average is also given for each model at the C position in the abscissa. The models included here are a subset of the models shown in Fig. 5 of JK10 (except for JAMSTEC, that wasn't included in that study). Although the models aren't individually identified in JK10, it can be said, looking at the model spread, that there is, overall, a good agreement between the sBLT results and the findings by JK10. All models show: a similar BLT growth rate between 35°N (Sc, ~ 940 hPa model mean) and 17°N (shallow cumulus [ShCu], ~ 840 hPa model mean); the ITCZ (8°N) dip (at 14°N in GFDL, and inexistent in MétéoFrance); and, higher BLTs to the south of the ITCZ. The biggest departure between sBLT and JK10 seems to be, for some of the models, deeper sBLT BLs found between 17°N and 20°N (in the trades). For the transect as a whole, NCEP and GFDL present the deepest and shallowest BLs, respectively; and, although deeper than MétéoFrance in the Sc and ShCu regions, JAMSTEC has a transect average below the former, owing to a significant decrease in BLT height south of 17°N. By looking at mean RH sections

for some of these models, it can be concluded that the dip in BLT height in the ITCZ is associated with a very moist surface overlaid by a relatively gentle RH decrease going up in the deep convection area. Finally, from the fact that all models tend to show, in these results, basically the same (close to constant) growth rate of BLT height, it could also be argued that (at least to a first approximation) their Sc BL representation in terms of simulated humidity content and BL depth is the main reason behind the departures found downwind in the ShCu BLTs.

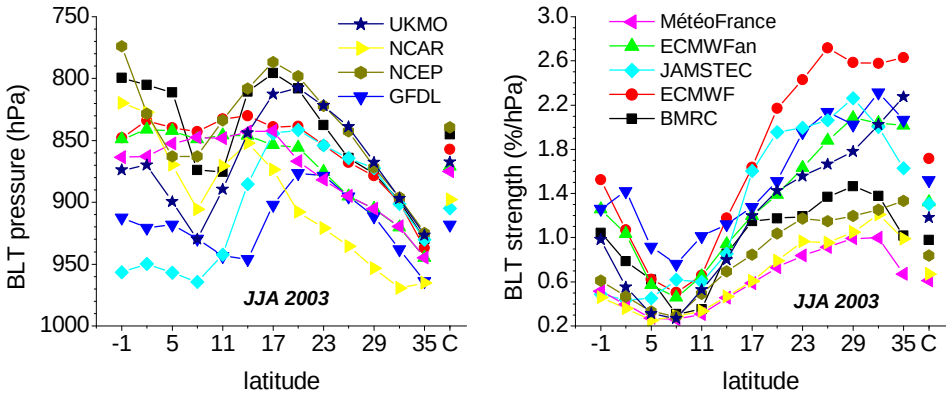

Figure 6.7 - Mean June-July-August (JJA) 2003 boundary layer top (BLT) pressure (left plot) and strength (right plot) along GPCI for eight participating models and ECMWF analysis (ECMWFan), determined using the sBLT methodology applied to relative humidity data (see text for details).

The right plot in Fig. 6.7, presents, for the same models and analysis, the sBLT BLT Strength statistic. The results show the ITCZ as the area with the weakest BLT strength, while the strongest BLTs are found somewhere between 26°N and 32°N (typically the area where the seasonal maxima of Sc are found [Fig. 5.1]). The comparison between the whole-transect results in both plots in Fig. 6.7 highlights some interesting differences among the datasets. Note, for instance, the case of ECMWFan and MétéoFrance, the two show in the left plot a practically coincident BLT in all points in the transect but differ substantially in the transect-averaged BLT strength with MétéoFrance showing lower values (note the striking departure in the Sc areas). Finally, NCAR shows not just one of the lowest BLTs, but also one of the weakest. In fact, MétéoFrance and NCAR follow each other very closely in terms of the mean BLT strength along the cross section, though NCAR has a lower BLT in any of the transect locations.

The sBLT sS# Distribution and not7.S1 statistics are presented in Fig. 6.8 for the same nine datasets.

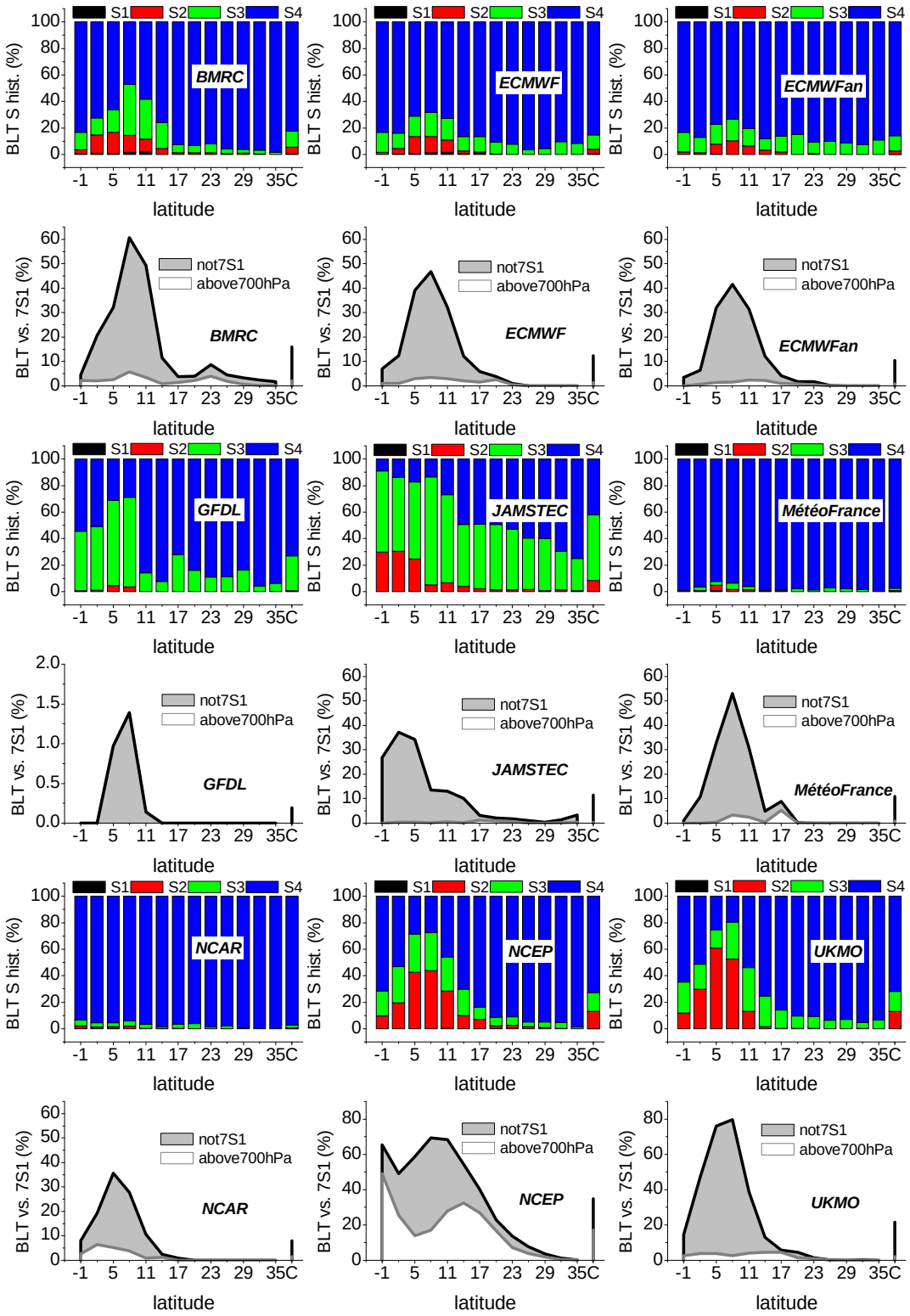

Figure 6.8 - June-July-August 2003 sS# Distribution (BLT S hist.) and not7.S1 (BLT vs. 7S1) statistics along GPCI for eight participating models and ECMWF analysis (ECMWFan), determined using the sBLT methodology applied to relative humidity data (see text for details).

The results in Fig. 6.7 contain information more directly related to BLT characteristics, namely height (pressure) and strength, in turn, while showing BLT-related information (e.g., "above700hPa" occurrence), Figure 6.8 presents, in addition, results that relate to the humidity (RH) characteristics of the BL itself, i.e., the portion of the atmosphere below the BLTs determined. The "BLT S hist." occurrence histograms show how often the different BL types occur at each one of the transect locations, and in the cross section as a whole (at C in the abscissa). For instance, a sS4 BL is one for which the vertically-averaged RH is equal to, or above, the highest of the two RH values used to evaluate the respective BLT strength (see the explanations above at S1, S2, S3, and S4 index, and at sS#). The first aspect in the results shown is the rare occurrence of sS1 BLs (sS# is in these plots denoted as S#). Only three of the models show sS1, essentially in the deep convection area, and with less than ~ 3 % seasonal occurrence. A second notorious feature in these results is that sS4 BLs clearly dominate, both spatially and temporally, the exception being the JAMSTEC model for which sS4 has, for the section as a whole, an occurrence of about 40 %. In this regard, the ITCZ (~ 8°N) is the area where sS4 BLs tend to occur less frequently, with five of the nine datasets showing values below 50 % seasonal occurrence. Overall, the second most dominant type of BL is sS3 that tend to occur more in the ITCZ. Models show important differences in the sS3 representation, with JAMSTEC as the only model for which sS3 is the dominant type. In NCEP and UKMO, sS3 is as representative as sS2, with the later dominating the deep convection region, the area where sS2 occur more frequently in all of the datasets shown. Recall that a sS2 is necessarily not a sS3, meaning that the sS2 BL is characterized by the presence of one or more layers of air with RH lower than the lowest of the two RH values used to evaluate the respective BLT strength. It is noteworthy that, for NCAR and MétéoFrance, sS4 dominates with more than 90 % occurrence in all of the transect locations. Still, although both models are very similar in terms of BLT strength, they differ in BLT height, with MétéoFrance showing deeper BLs, as mentioned above. Finally, recall that (only) geometrical considerations are implied in the sS# determination, such that, no information on the actual BL humidity content can be directly inferred from these results. The BL humidity content can be obtained from the kind of analysis presented in Fig. 4.4 (seasonal means of RH). Note, for instance, NCEP and UKMO, with practically the same BLT height, and very similar sS# histograms, to the north of 20°N, a segment where the two differ the most in BLT strength. This situation is probably associated with moister BLs in the UKMO simulations.

Regarding the "BLT vs. 7S1" results, it is evident that it is in the ITCZ that most frequently the sBLT solution differs from the 7.S1 BLT (for GFDL the peak value is only ~ 1.5 %). As these situations may arise from the simple fact that the sBLT solution falls above 700 hPa, the "above700hPa" line indicates how frequently that was the case. The difference between those two statistics (the gray segment) thus indicates, for each location in the cross section, the percentage of time sBLT didn't coincide with 7.S1 while being below 700 hPa. Note, for instance, that NCEP has, at 14°N, its mean BLT at ~ 810 hPa, well below 700 hPa, though having at the same location ~ 40 % occurrence of BLT above 700 hPa. To the north of 17°N both the "not7S1" and the "above700hPa" lines are below 10 % in all models except NCEP. Finally, note that UKMO has ~ 50 % sS2 occurrence at 8°N, where "not7S1" is ~ 80 %. This means that, at 8°N, for at least ~ 30 % of the time, an sS2 is not 7.S1. This can only occur in two different situations: 7.S1 is a sS1, i.e., an increase of RH with height; or, the level that initiated the basic algorithm was at least a S3, and was located below a 7.S1 that was, simultaneously, at least a S2. Only a not7.S2 sBLT statistic would allow a more definite answer in these cases.

6.3.2.9 Summertime statistics from daily AIRS data

The sBLT results for the JJA 2003 daily AIRS data are presented in Fig. 6.9.

For this AIRS dataset, no sS1 BLs have been determined, and the highest occurrence value for either sS2, or sS3 BLs is below 10 % (see the ITCZ area), meaning that sS4 BLs dominate, with more than 95 % occurrence in the cross section as a whole. This is an indication of consistently moist BLs, in the sense that the presence of intermediate dry layers is probably rare. This fact may also arise from the relatively coarse vertical resolution of the dataset in question. The models that most resemble these observations in terms of the type of BL most represented are NCAR and MétéoFrance. Note that the AIRS BLTs are rarely not at the level corresponding to 7.S1. BLTs above 700 hPa are also rare with a ~ 4 % occurrence in the deep convection area, and an isolated peak of ~ 1 % at 23°N. At about 0.46 %/hPa, the AIRS transect-averaged BLT strength is well below the value for most of the models (the minimum model value is ~ 0.65 %/hPa [MétéoFrance]). The seasonal mean BLT height along the cross section compares very well with JK10 (apart from a lower sBLT at 35°N ~ 950 hPa [~ 925 hPa in JK10]).

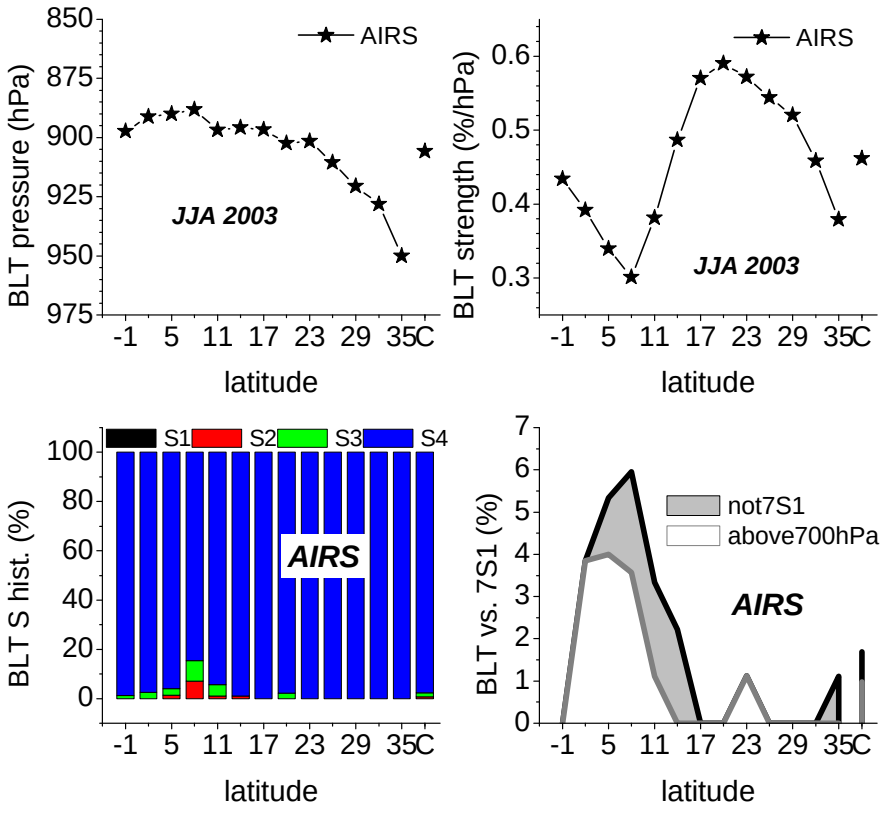

Figure 6.9 - Mean June-July-August (JJA) 2003 boundary layer top (BLT) pressure (top row left plot) and strength (top row right plot), together with the sS# Distribution (BLT S hist.) and not7.S1 (BLT vs. 7S1), statistics determined along GPCI using the sBLT methodology applied to AIRS relative humidity data (see text for details).

To close the section, and thinking about possible avenues for future applications of sBLT, first of all, it would be of interest to extend the kind of analysis proposed above to the broader domain of the NE Pacific, and even to the global oceanic (sub)tropical regions. Other seasons should also be investigated especially for a study of the spatiotemporal behaviour of the sBLT statistics. In particular, the sS# Distribution statistic could be used to composite BLT Level and BLT Strength for each one of the sS#. This compositing approach could also be tried for other key parameters such as BL moisture content, proxies for the large-scale dynamics, environmental conditions, cloud behaviour, and cloud-regime transition characteristics.

6.3.3 Cloud cover transitions

As mentioned, this section revisits the topic of abrupt transitions in cloud cover along the GPCI transect. Section 6.3.3.1 introduces a new methodology for the location of discontinuities in the cloud fields, a follow up of the technique presented in Section 5.1.3 (Sharp gradients), implemented constraining the definition of an abrupt cloud cover change. The results for the

cloud transition statistics (e.g., histograms of their location), are presented in the closing section, along with seasonal mean relative humidity profiles spatially averaged upwind and downwind of the transition locations determined from JJA 2003 3-hourly model and analysis data.

6.3.3.1 An updated version of the analysis of abrupt changes in cloud cover

Since the focus is now exclusively on subtropical cloud transitions, the analysis proposed here is limited to the segment of the GPCI transect comprised between 14°N and 35°N, that is, an area encompassing solely the ShCu and Sc domains. Recall that the results presented in Section 5.1.3 were obtained along the whole span of the section, thus including the deep convection area and the latitudes south of the ITCZ.

The new method comprises these steps: (i) determination of the location of the strongest (greater-than or equal to 30 %) southward decrease in TCC, calculated between two adjacent transect locations (as with the previous method, the TCC transition location is assigned to the position to the north, among the two adjacent transect locations used to calculate the TCC decrease [i.e., the one from where the TCC drops], furthermore, if two or more locations share the same strongest TCC decrease value, the one most to the south is chosen); (ii) check if all the TCC values to the north of the location determined in (i) (including the TCC value at the transition location), are above the average TCC calculated in the domain south of the transition location; (iii) if that is the case, verify if the average TCC for the domain north of the transition location (calculated including the TCC value at the transition location) is above the average TCC to the south of the transition location by at least 30 %. Only if all these conditions are met a TCC transition is said to occur. This is performed for each one of the TCC records available 3-hourly. Finally, the values for the seasonal mean TCC of the abrupt transition are obtained for the extreme north and south locations in the transect, respectively, from the means of all the TCC averages obtained for the north of and south sides of the transition locations. The mean location of the transition, is the mean of all the locations found in the 3-hourly data. Histograms of the transition location are computed as well.

That said, it is now clear that the mean TCC difference between the north and south domains will always be at least 30 %. This wasn't the case for the "old" method (Section 5.1.3), that could, potentially, result in a TCC difference between the two domains lower than the threshold used to identify the abrupt decrease in TCC, or even in a mean south-side TCC average higher than the mean north-side TCC average.

6.3.3.2 Relative humidity signature of sharp gradients in cloud cover

Contemporaneous with the calculation of the TCC averages for the north of and south sides of the transition locations found following the method described in the previous section, was the evaluation, for each one of the 3-hourly records with a TCC transition determined, of the respective spatially-averaged profiles of relative humidity. Figure 6.10 shows the JJA 2003 seasonal results for both the TCC transitions (occurrence, mean location, mean north and south TCC averages, and histograms of transition location) and the corresponding mean RH profiles for the north and south sides of the abrupt southward decreases in the TCC parameter.

Starting with the seasonal occurrence of abrupt TCC changes, it is evident that the values are, for the new method, and for all the datasets, much lower than those obtained previously, shown in Fig. 5.4 (for JJA 1998). This is the case, even taking into account only the transect segment between 14°N and 35°N. The occurrence values drop from above 90 % to values typically below 25 %, and indication of the robustness of the new method in constraining the model results to the situations with a spatially consistent cloud-regime transition. The UKMO model stands out from the rest with a an occurrence value of ~ 64 %, a feature probably associated with the peculiarity of its boundary layer cloud parameterization (see the discussion in Section 5.1.2). The histograms of the transition location are quite different among these datasets, with the main peaks found either close to 14°N, or at 35°N. The mean location for the transition falls between ~ 23°N (NCAR) and ~ 29°N (ECMWFan). The seasonal mean value of the TCC to the north of the transition locations found during the season is typically above 80 % (~ 100 % in GFDL), while the value to the south is ~ 40 % (below 30 % for BMRC and UKMO).

Regarding the RH profiles, these can be seen as representing the typical Sc (North) and ShCu (South) RH profiles, at least, for these sharp decreases in TCC. As expected, the ShCu show a deeper BL, with mean (vertically-averaged) BL RHs as high as, or even above, those found in the Sc BL. Close to the surface, both cloud regimes have similar RH values, with the maximum at the surface for the Sc, while for the ShCu the BL peak RH is above the surface, somewhere between 960 hPa and 920 hPa. It is above ~ 600 hPa that the biggest differences are found among the models in the comparison between the respective ShCu and Sc RH profiles. Between ~ 600 hPa and ~ 250 hPa, overall similar ShCu and Sc RH profiles are seen for ECMWFan, UKMO, and NCAR; consistently lower Sc RH characterizes ECMWF; and substantially higher Sc RH is found in the BMRC, and MétéoFrance models. The highest overall similarity between the Sc and ShCu RH profiles is found in the ECMWF and

ECMWFan datasets, which are also similar in the TCC transition statistics, except in terms of occurrence (ECMWF ~ 37 %, ECMWFan ~ 24 %).

This kind of investigation on the potential impacts of the tropospheric humidity structure on the (sub)tropical cloud regime transitions seems necessary to better constrain the models' boundary layer cloud behaviour. While there is the need for more observational insight on this (e.g., Sandu et al. 2010), extending the approach proposed above to analyze numerical simulations seems timely. A number of ideas in that direction conclude this section and chapter, namely: 1) find, additionally, the seasonal means of the RH profiles at the transition location, and just south of it, instead of averaging all the RH profiles in the domains to the north and to the south of the transitions; 2) perform these two types of analysis [in Fig. 6.10 and proposed in point 1)] individually for each location along the cross section, as a way to infer (for each model) any variations in how the Sc and ShCu RH profiles compare when the transitions occur later (more to the south) or earlier (more to the north) along the transect (the models should then be intercompared in this respect); 3) add to all these investigations, information on important parameters, such as, sea surface temperature, low tropospheric stability, proxies for the large-scale dynamics, low level winds, among others; 4) also, a comparison between the seasonal mean RH field for the 14°N-to-35°N segment of the GPCI cross section, and the mean RH fields for the same segment, composited separately for those times when the TCC transition falls in specific transect locations, could be tried (this would allow a broader view of the RH field, as opposed to looking at individual RH profiles).

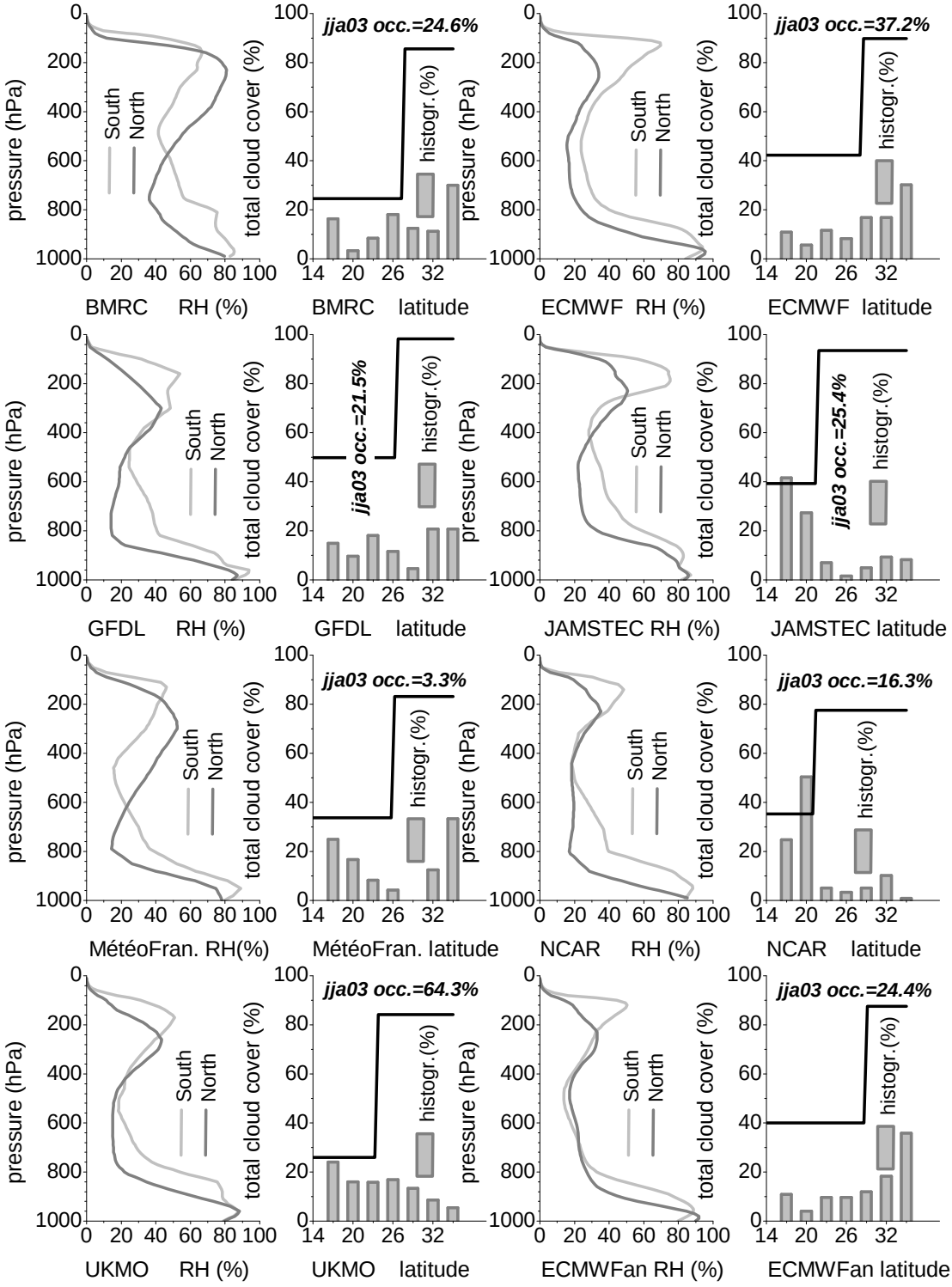

Figure 6.10 - June-July-August 2003 (jja03) statistics of total cloud cover transition (frequency of occurrence [occ.], location histograms [histogr.], means for location and north and south averages [black line]), together with mean profiles of relative humidity (RH) averaged to the north and to the south of the transition locations found during the season between 14°N and 35°N along the GPCI cross section (see text for details).

7 Diurnal oscillations in the models and in observations

Another important topic for GPCI is the representation, in weather and climate prediction models, of the diurnal variation of clouds and cloud-related parameters. As mentioned in Chapter 3 (The GPCI project), GPCI can be seen as a follow-up of the EUROCS (European Cloud Systems Study) climate model intercomparison, most notably in the much higher (3-hourly) temporal resolution of the requested model output and observational datasets. The 3-hourly model and satellite data have proven crucial in the characterization of the regional climatology of clouds, boundary layer, and large-scale dynamics and environmental conditions, done in previous chapters resorting to a number of traditional approaches and new methodologies, not possible with lower temporal resolution datasets (e.g., the cloud transition analysis, or the boundary layer statistics). In this chapter the focus is more specifically on the diurnal cycle, as seen in seasonal means at different locations along the GPCI cross section. Because, in the (sub)tropical NE Pacific the diurnal cycle presents its peak amplitude during the summertime, the data available for June-July-August (JJA) should prove useful for the preliminary evaluation of models and observations proposed in the next sections.

7.1 Seasonal mean characteristics

7.1.1 Atmospheric circulation

In an attempt to characterize mean diurnal changes in the large-scale dynamics associated with the Hadley circulation in the NE Pacific, models and reanalysis (ERA-40 [ECMWF 40 Year Re-analysis]) data for vertical velocity at 700 hPa (w700), and 1000 hPa -to- 850 hPa vertically averaged horizontal wind direction (defined as to where the wind is blowing to, and reported in degrees clockwise from North) and speed, were obtained for JJA 1998 at 8 different times during the day, for each one of the 13 locations along GPCI. The corresponding mean results, presented in Fig. 7.1, show: a discernible diurnal cycle of w700 in the ITCZ (Inter-Tropical Convergence Zone, 8°N), in ERA-40, and in the ECMWF and NCAR models, with minimum values between 6 UTC (Universal Time Coordinated) and 9 UTC (approximately between 7 pm and 10 pm, local solar time [LST]); a relative minimum in subsidence in the trades and subtropics (to the north of ~ 17°N) between 9 UTC and 15 UTC (at 26°N, 12 UTC ~ 3 am LST) in ECMWF and NCAR (3 hours earlier in GFDL); practically imperceptible diurnal

cycle in UKMO at any of the locations in the transect; an overall tendency for the trade winds (17°N to 23°N) to blow slightly more to the south between 3 UTC and 9 UTC (between ~ 5:30 pm and ~ 11:30 pm LST, at 20°N); also the period of the day when the winds are stronger generally to the north of 11°N (e.g., ERA-40).

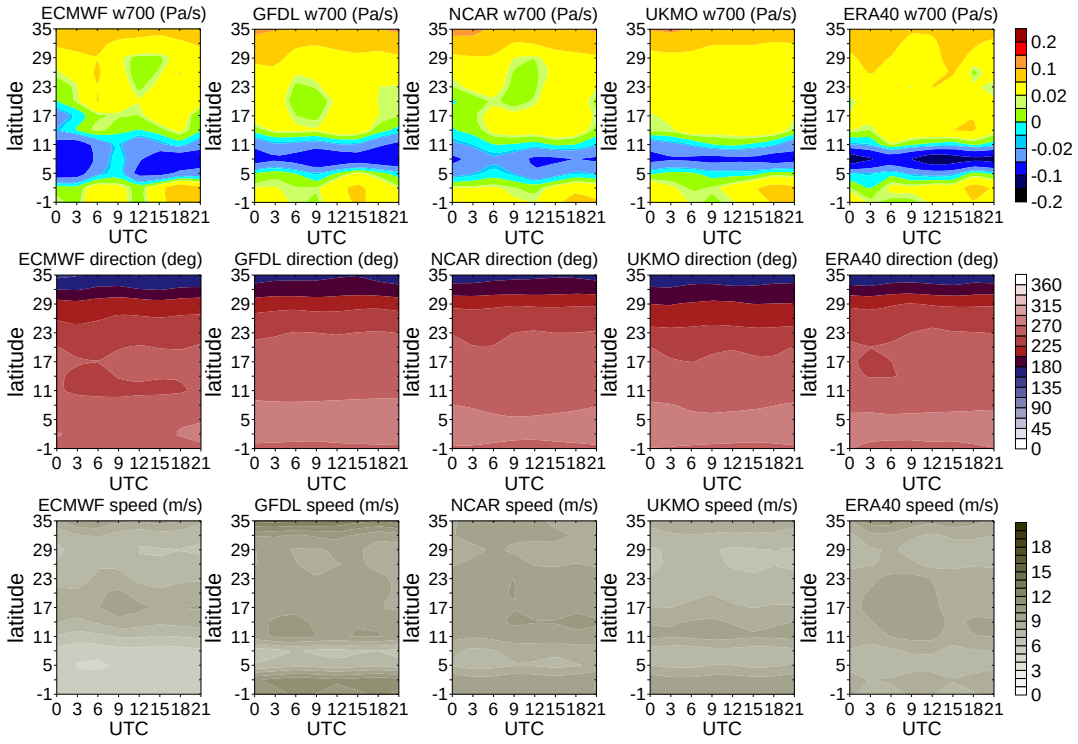

Figure 7.1 - For four of the participating models and ERA-40 reanalysis, June-July-August 1998 mean diurnal cycle of vertical velocity at 700 hPa (w700, top row), and horizontal wind direction (to where the wind is blowing to, in degrees clockwise from North, mid row) and speed (bottom row) vertically averaged in the 1000 hPa to 850 hPa layer, all at each one of the 13 locations along GPCI, and for 8 UTC (Universal Time Coordinated) 3-hourly during the day.

7.1.2 Full-profile parameters

The JJA 1998 mean diurnal cycle for three vertically distributed cloud-related variables is presented in Fig. 7.2, Fig. 7.3, and Fig. 7.4, for four participating models and ERA-40 reanalysis, and at three different locations in the GPCI cross section, respectively, the ITCZ (8°N), the shallow cumulus area (ShCu, 20°N), and the stratocumulus area (Sc, 32°N). The three variables are: relative humidity (RH), cloud fraction (CF), and cloud liquid water content (CLW).

In terms of the ITCZ RH, two models (GFDL, and UKMO [and to some extent NCAR]) show a moistening of the layer below 700 hPa that peaks around 15 UTC (~ 4 am LST). Those same models do not show any significant RH variations during the day in the ShCu, where, in turn,

ECMWF and ERA-40 show a slight moistening of the boundary layer (up to 900 hPa) between 12 UTC and 18 UTC (15 UTC ~ 5:30 am LST, at 20°N). For the Sc areas, a slight increase in RH close to the top of the boundary layer (see Fig. 6.7 for JJA 2003 mean boundary layer heights) is perceptible in NCAR between 12 UTC and 18 UTC (between ~ 3:30 am LST and ~ 9:30 am LST), while in ERA-40 the same period is characterized by a moistening of the boundary layer itself. Except maybe for ERA-40 in the ITCZ, and ECMWF in the ShCu, no significant changes in mid tropospheric (700 hPa to 400 hPa) humidity can be reported (in the Sc in NCAR there is a slight thickening of the dry layer [~ 600 hPa], with a peak about 9 hours prior to the peak in RH at the top of the boundary layer).

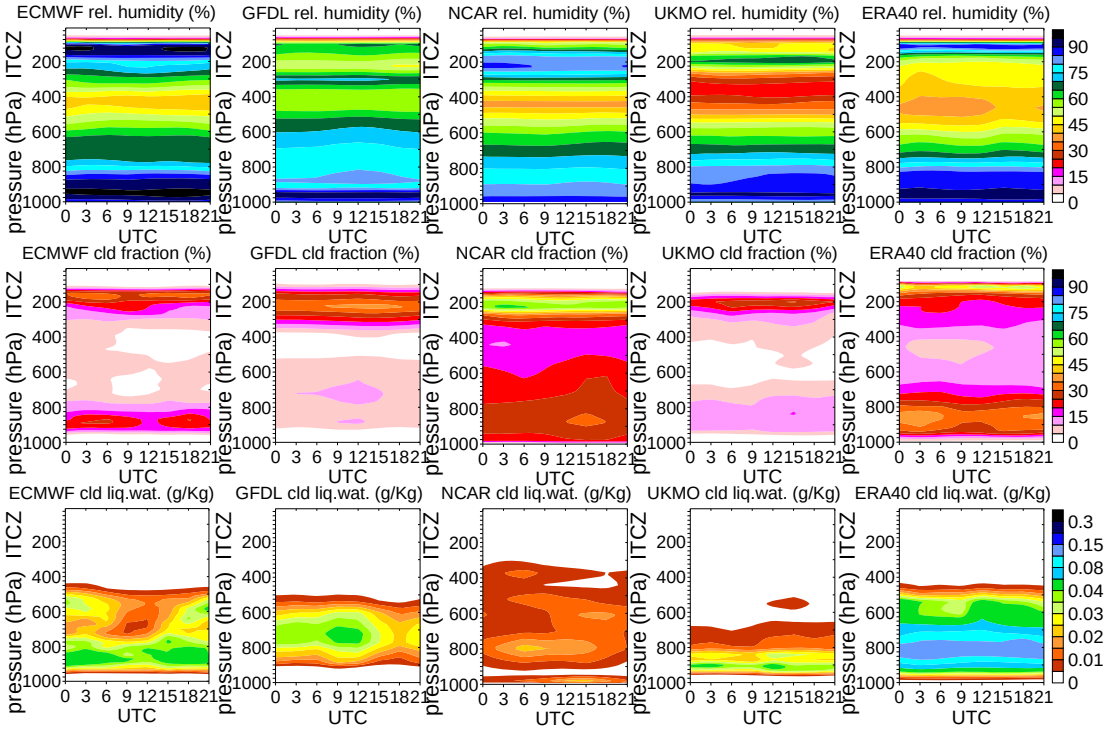

Figure 7.2 - For four of the participating models and ERA-40 reanalysis, June-July-August 1998 mean diurnal cycle of vertically distributed relative humidity (top row), cloud fraction (mid row), and cloud liquid water content (bottom row), for the Inter-Tropical Convergence Zone (ITCZ, 8°N) location in the GPCI transect, and for 8 UTC (Universal Time Coordinated) 3-hourly during the day.

In what concerns the CF and CLW parameters, in the ITCZ, and for all the datasets shown, below ~ 600 hPa, RH and CF seem to, to some extent, be correlated along the diurnal cycle. However, there are discrepancies in the UTC location of the relative maximums in CF, with a peak CF somewhere between 12 UTC and 15 UTC in GFDL, UKMO, and NCAR, precisely the period when ECMWF and ERA-40 show minimum values of CF. There is, overall, a good temporal agreement between the peak values of CF and CLW in ECMWF, ERA-40, and GFDL, contrary to the situation in UKMO, and, especially, NCAR (see the layer between 900 hPa and 700 hPa).

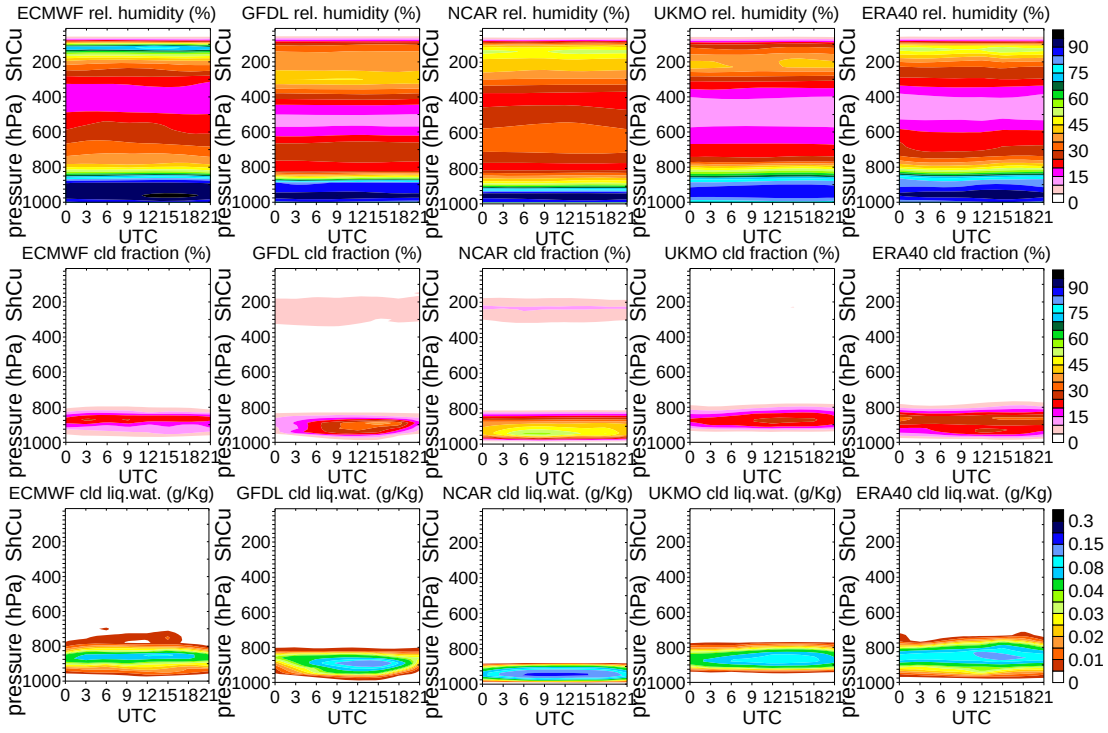

Figure 7.3 - For four of the participating models and ERA-40 reanalysis, June-July-August 1998 mean diurnal cycle of vertically distributed relative humidity (top row), cloud fraction (mid row), and cloud liquid water content (bottom row), for the shallow cumulus area (ShCu, 20°N) in the GPCI transect, and for 8 UTC (Universal Time Coordinated) 3-hourly during the day.

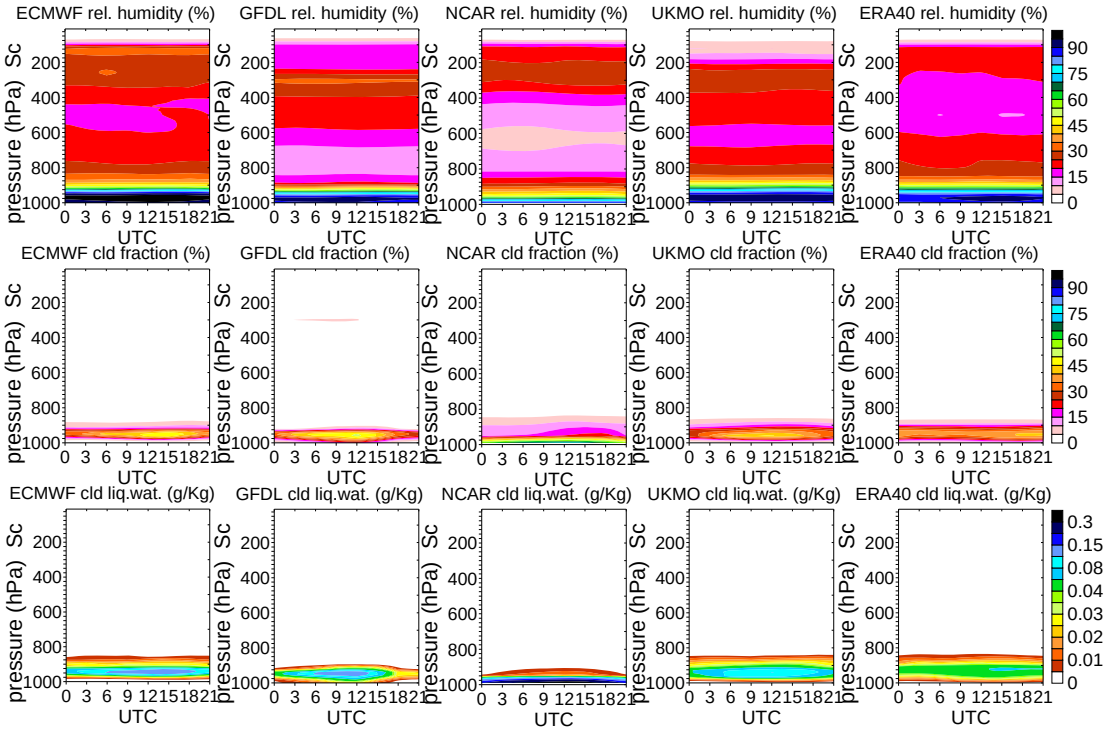

Figure 7.4 - For four of the participating models and ERA-40 reanalysis, June-July-August 1998 mean diurnal cycle of vertically distributed relative humidity (top row), cloud fraction (mid row), and cloud liquid water content (bottom row), for the stratocumulus area (Sc, 32°N) in the GPCI transect, and for 8 UTC (Universal Time Coordinated) 3-hourly during the day.

In the ShCu, most of the CF reported is below 800 hPa, and thus most probably associated with the boundary layer (Fig. 6.7). No specific relation is perceptible in ECMWF and GFDL between the diurnal variations of RH and CF. This is not the case in UKMO and ERA-40, that show a positive correlation between the two, with a peak in CF around 15 UTC. In NCAR, the maximum in CF between 6 UTC and 9 UTC happens ~ 3 hours earlier than a slight moistening of the lowest levels in the boundary layer. For the ShCu there is in all datasets a good agreement between CF and CLW, a situation still valid in the Sc areas.

Finally, the Sc results for NCAR show that the slight increase in RH close to the top of the boundary layer, between 12 UTC and 18 UTC, is accompanied by higher CF values, especially at the levels just above a very shallow boundary layer CF maximum. Also, the upper CF maximum happens ~ 3 hours later than the low-level maximum in CF. Note, however, that most CF simulated above 900 hPa doesn't have any CLW.

7.1.3 Diurnal anomalies from single-level variables

JJA 1998 mean diurnal cycle anomalies are analyzed in this section obtained from model simulations, ERA-40 reanalysis, and observations from ISCCP (International Satellite Cloud Climatology Project) and TRMM (Tropical Rainfall Measuring Mission). The results are given for three locations in the GPCI cross section, namely, one in the ITCZ (8°N), one in the ShCu area (20°N), and one in the Sc area (32°N). Three variables were chosen for analysis: low tropospheric stability (LTS), total cloud cover (TCC), and precipitation (P). The results are presented in Fig. 7.5.

Briefly, the precipitation observations used here, were extracted from the TRMM 3B42 precipitation rate product (Huffman et al. 2007), a 3-hourly, 0.25° × 0.25°, global (50°S to 50°N) dataset, covering the period from December 1997 to the present. 3B42 is obtained at fine intervals with the TRMM Multi-Satellite Precipitation Analysis (TMPA) combining microwave sensor precipitation estimates. Where unavailable, those estimates are substituted by infrared (IR) estimates from geostationary IR observations. These data are available online at the Goddard Earth Sciences Data & Information Service Center (GES-DISC).

The LTS variable (defined as the difference between the potential temperature at 700 hPa and at the surface), shows for all models and at any of the three locations along the GPCI transect, very similar mean diurnal variation behaviour, both in terms of amplitude and phase, with daily maxima typically found between 3 UTC and 6 UTC, and minima between 15 UTC and 21

UTC in the ITCZ, and 3 hours (UTC) earlier in the ShCu and Sc areas. ECMWF is the model with the least diurnal amplitude in the ITCZ, while showing in the other two regions, similar values as compared to the other datasets. The GFDL model shows, in all regions, the maximum and minimum LTS values shifted 3 hours earlier from the rest. No other variable shows this overall high degree of (intra-, and inter-model) diurnal coherence between the various regions.

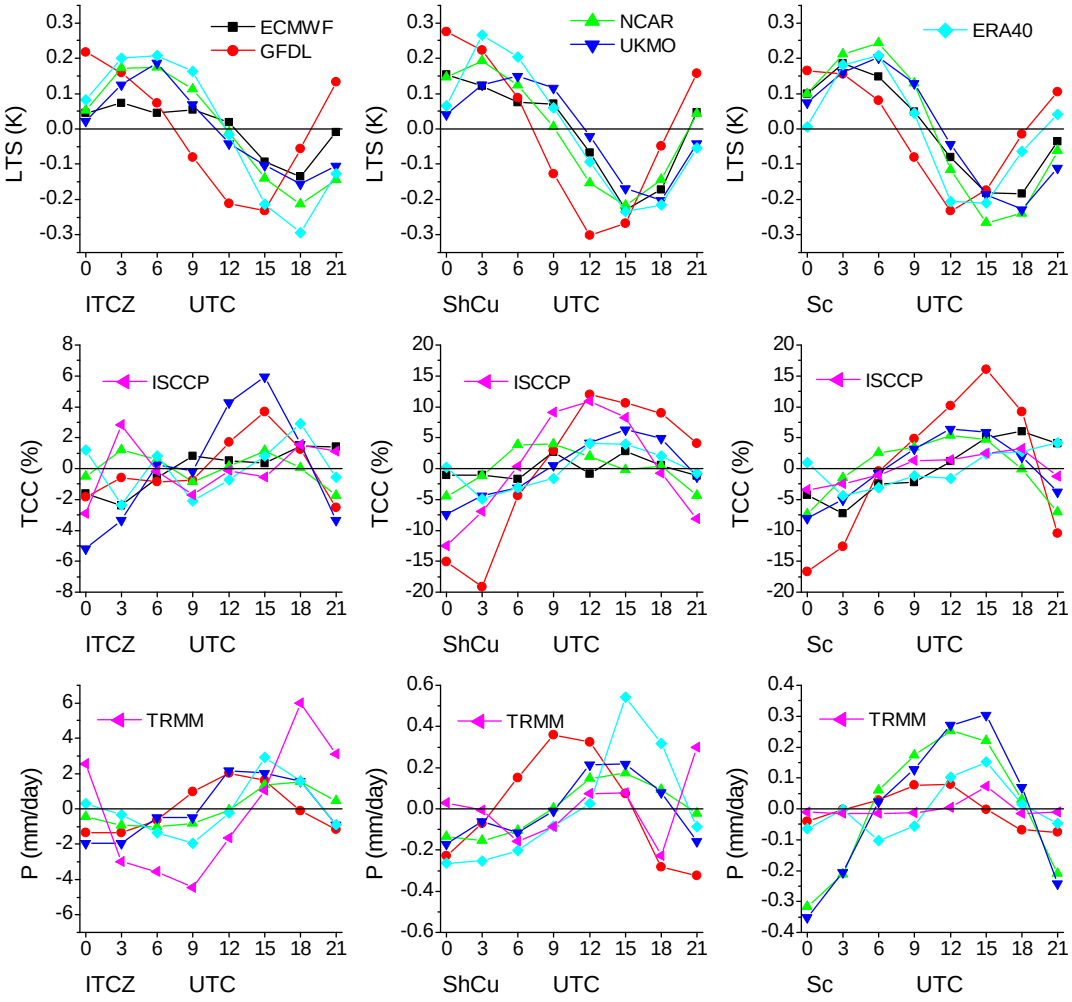

Figure 7.5 - For four of the participating models, ERA-40 reanalysis, ISCCP observations, and TRMM estimates, June-July-August 1998 mean diurnal cycle anomalies of low tropospheric stability (LTS), total cloud cover (TCC), and precipitation (P), obtained in three different areas along GPCI (Inter-Tropical Convergence Zone [ITCZ, 8°N], shallow cumulus [ShCu, 20°N], stratocumulus [Sc, 32°N]), and for 8 UTC (Universal Time Coordinated) 3-hourly during the day.

ISCCP's TCC in the ITCZ shows two relative maxima, the most pronounced being the one at 3 UTC (~ 4 pm LST), and a secondary one at 18 UTC (~ 7 am LST). The other datasets show two (or even three [ERA-40]) TCC peaks during the day, with the most pronounced peak in the early morning, instead of during the afternoon, as in ISCCP. In the ShCu and Sc areas the general tendency is for a single TCC cycle. ISCCP shows in the ShCu the biggest diurnal amplitude in TCC. The ISCCP maximum in the ShCu is centered at 12 UTC (~ 2:20 am LST).

NCAR has the ShCu peak (too early) between 6 UTC and 9 UTC, ECMWF, UKMO and ERA-40 show it ~ 3 hours later than ISCCP, and GFDL is, overall, the model that best follows ISCCP, both in phase and in amplitude (the other models lack in ShCu amplitude). It is in the Sc that ISCCP has the least diurnal variation in TCC, with models showing larger values in this respect (particularly GFDL with a diurnal amplitude as large as in the ShCu). Overall, there is, in the Sc, a better agreement between the datasets in the location of the daily maximum in TCC: 18 UTC (~ 9:30 am LST) in ISCCP, and ECMWF; 21 UTC (~ 12:30 pm LST) in ERA-40; and between 12 UTC (~ 3:30 am LST) and 15 UTC (~ 6:30 am LST) in UKMO, NCAR, and GFDL.

In terms of precipitation rate (ECMWF is not shown), most datasets show a (single) diurnal peak sometime between 12 UTC and 18 UTC at any of the three locations along the transect (about 3 hours earlier in the ShCu and Sc for GFDL). In the ITCZ, all datasets lack in diurnal amplitude as compared to TRMM, and, except for NCAR, are not in phase with the observations, showing the peak precipitation 3 hours earlier than TRMM. In general, the datasets are more in phase with TRMM in the Sc, although showing higher diurnal amplitudes. In the ShCu, TRMM has a principal peak t 21 UTC, and a secondary one between 12 UTC and 15 UTC. No other dataset has more than one precipitation peak in the ShCu (or at any of the other positions).

A final note about the Sc results, to highlight that, except between 0 UTC (~ 3:30 pm LST) and 6 UTC (~ 9:30 pm LST) for UKMO and NCAR, the diurnal evolution in TCC is basically out of phase with the diurnal variation in LTS. In fact, the peak TCC is found at a time close to the lowest diurnal value of LTS in practically all models and ERA-40. Assuming that TCC in the Sc is essentially associated with low level (boundary layer) stratiform cloudiness (see the cloud fraction results in Fig. 7.4), and looking more specifically at the NCAR results, a model that (at least in this version) is known to link this type of subtropical clouds to LTS (see the discussion in Section 5.1.2), it could be inferred that the Sc response to LTS is dependent, not only on the time of the day, but also (or perhaps, above all) on the (in this case) TCC value, that is, the (positive) cloud response to LTS is most effective for the lowest TCC values in the diurnal cycle (at 0 UTC in NCAR). Then, once the (increasing) cloud amount reaches a certain threshold (at 6 UTC in NCAR) the Sc become less sensitive to (the decreasing) static stability of the environment (that, for NCAR, happens between 6 UTC and 15 UTC), showing what could be called “Scinertia” (for “stratocumulus inertia”), i.e., a certain degree of inertia in the response to LTS (as mentioned, the TCC maximum in the Sc happens, for NCAR, between ~

3:30 am and ~ 6:30 am, LST, the later being the time when LTS is at its minimum). Naturally, other parameters should be taken into consideration in this type of analysis (e.g., to what degree "Scinertia" is related to the humidity structure of the free/mid troposphere?). Answers to some of these questions should be found in high spatiotemporal resolution observational and modelling efforts targeted at the subtropical Sc regime.

It is apparent that models differ from each other, and from ERA-40, ISCCP, and TRMM, mostly in TCC and precipitation, and particularly in the deep convection and trade wind regions. Given that there is an indication (both observational and modelling) that diurnal-scale processes can have an impact on phenomena occurring on longer time scales, these discrepancies should be given more attention by the climate prediction community, especially being the diurnal cycle the most distinct (forced) mode of variability in the atmosphere.

8 Summary and conclusions

Notwithstanding the considerable improvement in cloud parameterization in the last 20 years, the representation of clouds is still a challenge for the weather and climate modelling communities. The urgency for the development of cloud parameterization in GCMs (General Circulation Models) is reinforced by the fact that the amount of cloud generated by the models has a significant impact on the predicted behaviour of the climate system. In particular, current climate models tend to respond differently in climate change sensitivity experiments. Parameterization deficiencies also result in thermodynamically inconsistent representation of the hydrologic cycle., with important implications in the simulation of the (sub)tropical atmospheric circulation. These topics are investigated by different GCSS (Global energy and water cycle experiment Cloud System Study) working groups, whose strategy has been successful in defining and understanding fundamental cloud regimes, and in developing, and improving cloud parameterizations. However, the exclusive use of one-dimensional versions of atmospheric models, as traditionally done in GCSS, does not allow a deep understanding of the fundamental role of clouds in climate, which implies that parameterization testing has to be done in the complete (3D) GCMs, a task that potentially entails the analysis of very large amounts of model simulation data.

In this context, the GPCI (GCSS / working group on numerical experimentation Pacific Cross-section Intercomparison) project offers a new and much lighter approach for the intercomparison of GCMs, by focusing the analysis on a reduced number of locations along a cross section, allowing for a relatively straightforward model and observational data integration. GPCI has been focused on the (sub)tropical NE Pacific ocean, and developed a framework specifically targeted at the investigation of fundamental cloud regimes that typically occur over the eastern boundaries of the (sub)tropical oceans, namely, stratocumulus, shallow cumulus, deep cumulus, and the transitions between them. Knowledge gained from a detailed analysis of the behaviour of these cloud systems, and associated dynamical and thermodynamical environments, in high temporal resolution data from weather and climate prediction models and from observations, should offer insight for the improvement and development of new parameterizations of clouds, boundary layer, and convection. Having been developed in tight connection with the GPCI project, the investigation presented in this thesis was oriented along the lines of GPCI's main goals and scientific questions.

GPCI can be seen as a level-2 model intercomparison project, in which all the participating models have to follow the same line of predefined project specifications and protocols. The basic condition imposed is that models run in climate mode and using prescribed sea surface temperatures as boundary condition. The period of interest is the June-July-August (JJA) season. The focus geographical domain ranges from -5ºN to 45ºN and 160ºE to 240ºE, and encompasses 13 locations along the a cross section. The simulation results were requested in a 3-hourly temporal resolution for a number of variables, either as vertical profiles, or single-level variables. Over twenty weather and climate prediction organizations have joined the effort, and an extensive amount of satellite data has been prepared for GPCI. Analysis of model and reanalysis data suggest that it is possible to study the main features associated with the cloud phenomenology resorting only to an individual cross section aligned with the atmospheric circulation associated with the regional thermally-direct Hadley cell.

A preliminary analysis of GPCI model and observational data, with the goal to give an overview of the mean characteristics of the summertime atmospheric hydrologic cycle in the (sub)tropical NE Pacific, has been performed with an emphasis on the vertical distribution of clouds, and on processes involving dynamical and environmental factors that play a role in the maintenance of total and low cloud fields on a seasonal time scale. The seasonal mean results for most variables (e.g., total cloud cover, liquid water path, and outgoing longwave radiation) tend to be characterized by a high degree of scatter among the simulations, with models rarely showing good agreement with the observations in all of the transect locations. Mean profiles of vertical velocity, and relative humidity, suggest that the basic features associated with the regional Hadley circulation are, overall, well represented, though, in detail, substantial differences exist between the models (e.g., in the strength of the deep convection, or humidity content in the boundary layer). A comparison of the vertical distribution of cloud fraction highlighted the challenges in the parameterization and simulation of clouds in climate models, with simulations showing a variety of behaviours in the representation of the different cloud types (e.g., too low stratocumulus clouds) and transitions between them (e.g., presence of distinct cloud layers in the transition areas), these results were validated against observations of cloud occurrence from the CloudSat and CALIPSO (Cloud-Aerosol Lidar and Infrared Pathfinder Satellite Observations) satellites. Process-oriented studies indicate, overall, a noticeable response of the large-scale circulation to change in the prescribed sea surface temperatures in all of the models. The responses of other variables such as net shortwave radiation at the top of the atmosphere, and total cloud cover, are even more striking, and vary

from model to model. The fact that the general response to the increase in sea surface temperature is not always coherent among the different variables for a given model, points out to the need to better constrain the simulated behaviour of important cloud-related parameters, including those crucial for the evaluation of cloud radiative forcing. No obvious relation between low clouds in the stratocumulus and shallow cumulus regimes, and subsidence and sea surface temperature (or low tropospheric stability) has been found in 3-hourly model data for the JJA 1998 season.

An in-depth analysis of convective regime transition, based on the spatiotemporal behaviour of clouds, was performed resorting to cloud data from model simulations, atmospheric reanalysis, and satellite observations. To gain insight into the question of the transition in (sub)tropical cloud regimes, several techniques were developed to detect the transitions, and or summarize their main seasonal features. Probability density functions of total cloud cover along the GPCI transect, obtained from JJA 1998 3-hourly data, are different for the various models, presenting important departures even in locations where the models show practically the same mean total cloud cover. Two very distinct stratocumulus -to- shallow cumulus transitions could be identified (a relatively smooth southward evolution, and a more abrupt one with a bimodal character) and associated with two distinct parameterization approaches. None of the two model behaviours (or parameterizations) reproduces well the observed pattern seen in corresponding ISCCP (International Satellite Cloud Climatology Project) observations. Cloud cover statistics from a methodology based on the identification of large gradients of total cloud cover along the cross section show a diversity of behaviours among the models, for instance, in the mean cloud cover decrease, in their seasonal frequency of occurrence, or in the histograms of the location of the transition (ISCCP and reanalysis differ as well). Additionally, a preliminary spectral analysis of the seasonal record of spatial shifts in the location of these sharp gradients in cloud cover was performed. No outstanding peaks were found in the corresponding spectra, being the differences in the temporal evolution of the underlying record what mostly distinguished the models (e.g., the tendency for the abrupt transitions to occur more to the north of the transect toward the end of the JJA season, or the small amplitude in the location change). In terms of the evolution of clout-top height along the section, the model ensemble compared well with the analysis product used, though, especially south of the stratocumulus areas, all results departed from corresponding MISR (Multiangle Imaging Spectroradiometer) observations. Still in the context of cloud regime transition, a grade-based approach to clustering of spatial patterns was introduced (GEPAT [Grade-based Empirical

Pattern Analysis Technique]), and subsequently applied to total cloud cover along the cross section, with the final goal to indentify main spatiotemporal features of the seasonal cloud cover, and compare associated environmental conditions. Six different cloud-field patterns for JJA 1998, with different seasonal representativeness, were analyzed in terms of the respective means of vertical velocity at 700 hPa, liquid water path, sea surface temperature, low tropospheric stability, and wind direction and speed. Noteworthy differences were found mostly in the characteristics of the vertical velocity, and liquid water path fields. A few ideas for a future application of the technique include: the analysis of other seasons and years (separately or in combination); a comparison of results for different regions; and a more direct use of purely observational data.

The humidity structure in the GPCI region was given special attention, with the goal to better understand its role as one of the main parameters in the context of the hydrologic cycle, particularly through its influence on cloud formation and evolution. State-of-the-art satellite observations from AIRS (Atmospheric InfraRed Sounder) were analyzed along the cross section, together with model simulations and atmospheric analyses. A number of results, based on the treatment of relative humidity data for the summer season, were analyzed, namely, seasonal mean profiles, variance, and temporal evolution. The comparison with the AIRS seasonal mean relative humidity showed significant biases in the models (e.g., important negative bias in the lowest portion of the boundary layer, a positive bias in the tropopause layer, and a generally drier subtropical mid troposphere). In terms of standard deviation, although models show, overall, higher relative humidity variability, there is a lack of variability in the boundary layer along the entire cross section. A positive bias just above the boundary layer north of the trades, is argued to be probably associated with the relatively poor vertical resolution of the AIRS dataset used (more so than a model deficiency). The temporal evolution of the vertical distribution of relative humidity seems to point out to the need to include in the investigation of the stratocumulus –to- shallow cumulus transition, the influence, not just of the humidity structure in the free troposphere immediately above the boundary layer, but also of the humidity profile all the way to the upper troposphere. Regarding, more specifically, the humidity structure of the lower troposphere, a new methodology for the determination of the top of the maritime boundary layer was introduced (sBLT [sequential Boundary-Layer-Top determination scheme]). The results seem promising, especially for its broad applicability, and given that it permits a characterization of the boundary layer (top) not offered in other such methodologies. Seasonal mean boundary-layer-top height and strength

were analyzed for models and analysis along the GPCI cross section, showing considerable spread, except in the (practically common) rate of southward deepening of the boundary layer. The deep convection and the stratocumulus areas, present, respectively, the least, and the most well defined boundary layer tops. Following the sBLT classification, different seasonal distributions of the representativeness of the main boundary layer types, were found among models and for different locations along the transect. In this respect, only two of the models compared well with AIRS. An updated version of the technique to detect abrupt spatial changes in the cloud fields along the cross section was developed. It seemed more robust in constraining the model results to the situations with a spatially consistent cloud-regime transition. Much lower occurrence of the transitions was reported with the new technique, with big differences among the models (unlike the corresponding results for the previous version of the technique). It allowed for a better understanding of the impact of distinct cloud parameterization approaches on regime transition behaviour. Finally, relative humidity profiles composited for the two cloud regimes separated by the transition locations identified, showed marked differences between the two regimes for a given model, with the biggest differences among the models, found in the mid and upper troposphere. Concrete ways to extend the investigation of the potential impacts of the tropospheric humidity structure on the (sub)tropical cloud regime transitions were proposed.

As one of the main topics in GPCI, the representation, in weather and climate prediction models, of the diurnal variation of clouds and cloud-related parameters, was analyzed resorting to 3-hourly model output and observational data. The seasonal mean diurnal cycle was characterized for different locations along the GPCI transect. Results were presented for: atmospheric circulation associated with the large-scale dynamics in the Hadley-cell-dominated NE Pacific; a number of cloud-related vertically-distributed variables; and for JJA mean diurnal cycle anomalies at three specific locations in the cross section, representative of the main cloud/convection regimes found in the region. A discernible diurnal cycle of vertical velocity at 700 hPa could be identified in the inter-tropical convergence zone in reanalysis data, and in some of the models (weaker diurnal variations were also found in the trades and subtropics). One of the models showed practically no diurnal variation of this parameter at any of the locations in the transect. Wind intensity and direction also showed characteristic diurnal change. Vertically-distributed relative humidity, cloud fraction, and cloud liquid water content results, showed, some diurnal variability in all of the datasets, particularly in the deep convection areas and below 600 hPa. Models do not agree in the time of the diurnal maxima of

these variables. Temporal correspondence between cloud fraction and cloud liquid water content is, overall, better constrained in the shallow cumulus and stratocumulus areas than in the inter-tropical convergence zone. There is, in the subtropics in one of the models, cloud fraction reported in the boundary layer without any associated cloud liquid water content. As for mean diurnal anomalies of low tropospheric stability, total cloud cover, and precipitation (with precipitation rate observations from TRMM [Tropical Rainfall Measuring Mission]), models tend to agree well in the first parameter, but differ from each other and the observations in the other two (e.g., in the deep convection region ISCCP's total cloud cover shows two relative maxima, the most pronounced happening at ~ 4 pm, local solar time, while the other datasets tend to have the most pronounced peak in the early morning). In the stratocumulus ISCCP has the least diurnal variation in total cloud cover, being, in this respect, surpassed by the models. Overall, there is, in the stratocumulus, a better agreement between the datasets in the location of the daily maximum in total cloud cover. Concerning the precipitation rate, most datasets show a relatively well defined peak in all of the locations along the transect, but lack in diurnal amplitude in the deep convection area (as compared to TRMM). Finally, the link between stratocumulus and low tropospheric stability was discussed for a particular model known to bind the two, and led to the argument of the existence of a certain degree of "inertia" in the response of subtropical cloud cover to low tropospheric stability changes during the diurnal cycle. Also, since the (positive) cloud response to the stability of the environment seemed to be most effective only when total cloud cover was at its lowest values in the diurnal cycle, a possible dependence of the response on cloud amount was inferred. To what degree "Scinertia" (for "stratocumulus inertia") would be related to the humidity structure of the free/mid troposphere, was a question left for future research.

To conclude, two points. First, this work shows well how current weather and climate prediction models still suffer from deficiencies in the representation of clouds and cloud-related processes. Second, the GPCI framework proved useful, in the characterization of main model shortcomings, and in helping envision possible avenues for future investigation, both on the modelling side and on the observational front.

9 References

Ackerman, S. A., and S. K. Cox, 1981: Aircraft observations of the shortwave fractional absorptance of nonhomogeneous clouds. J. Appl. Meteor., 20, 1510-1515.

Adler, R. F., G. J. Huffman, A. Chang, R. Ferraro, P. Xie, J. Janowiak, B. Rudolf, U. Schneider, S. Curtis, D. Bolvin, A. Gruber, J. Susskind, P. Arkin, E. Nelkin, 2003: The Version 2 Global Precipitation Climatology Project (GPCP) Monthly Precipitation Analysis (1979-Present). J. Hydrometeor., 4, 1147-1167.

Ahlgrimm, M., and D. A. Randall, 2006: Diagnosing monthly mean boundary layer properties from reanalysis data using a bulk boundary layer model. J. Atmos. Sci., 63, 998–1012.

Albrecht, B. A., D. A. Randall, and S. Nicholls, 1988: Observations of marine stratocumulus clouds during FIRE. Bull. Amer. Meteor. Soc., 69, 618-626.

Albrecht, B. A., C. S. Bretherton, D. Johnson, W. H. Schubert, and A. S. Frisch, 1995: The Atlantic stratocumulus transition experiment - ASTEX. Bull. Amer. Meteor. Soc., 76, 889-903.

Amenu, G. G., and P. Kumar, 2005: NVAP and reanalysis-2 global precipitable water vapor products. Bull. Amer. Meteor. Soc., 86, 245-256.

Anderberg, M. R., 1973: Cluster analysis for applications. Academic Press, New York, 359 pp.

Anderson, J. L., V. Balaji, A. J. Broccoli, W. F. Cooke, T. L. Delworth, K. W. Dixon, L. J. Donner, K. A. Dunne, S. Freidenreich, S. T. Garner, R. Gudgel, C. T. Gordon, I. M. Held, R. S. Hemler, L. W. Horowitz, S. A. Klein, T. R. Knutson, P. J. Kushner, A. R. Langenhorst, N.-C. Lau, Z. Liang, S. Malyshev, P. C. D. Milly, M. J. Nath, J. J. Ploshay, V. Ramaswamy, M. D. Schwarzkopf, E. Shevliakova, J. J. Sirutis, B. J. Soden, W. F. Stern, L. T. Sentman, R. J. Wilson, A. T. Wittenberg, and B. Wyman, 2004: The New GFDL global atmosphere and land model AM2–LM2: Evaluation with prescribed SST simulations. J. Climate, 17, 4641-4673.

Aumann, H. H., M. T. Chahine, C. Gautier, M. D. Goldberg, E. Kalnay, L. M. McMillin, H. Revercomb, P. W. Rosenkranz, W. L. Smith, D. H. Staelin, L. L. Strow, and J. Susskind, 2003: AIRS/AMSU/HSB on the Aqua mission: Design, science objectives, data products, and processing systems. IEEE Trans. Geosci. Remote Sens., 41, 253–264.

Bechtold, P., J. W. M. Cuijpers, P. Mascart, and P. Trouilhet, 1995: Modelling of trade wind cumuli with a low-order turbulence model: toward a unified description of Cu to Sc clouds in meteorological models. J. Atmos. Sci., 52, 455-463.

Bechtold, P., J. L. Redelsperger, I. Beau, M. Blackburn, S. Brinkop, J. Y. Grandpeix, A. Grant, D. Gregory, F. Guichard, C. Hoff, and E. Ioannidou, 2000: A GCSS model intercomparison for a tropical squall line observed during TOGA-COARE. Part II: Intercomparison of SCMs and with CRM. Quart. J. Roy. Meteor. Soc., 126 , 865-888.

Bony, S., K.-M. Lau, Y. C. Sud, 1997: Sea surface temperature and large-scale circulation influences on tropical greenhouse effect and cloud radiative forcing. J. Climate, 10, 2055–2077.

Bony, S., and K. A. Emanuel, 2001: A parameterization of the cloudiness associated with cumulus convection: Evaluation using TOGA COARE data. J. Atmos. Sci., 58, 3158–3183.

Bony, S., J.-L. Dufresne, H. Le Treu, J.-J. Morcrette, C. Senior, 2004: On dynamic and thermodynamic components of cloud changes. Climate Dyn., 22, 71–86.

Bony, S., and J.-L. Dufresne, 2005: Marine boundary layer clouds at the heart of tropical cloud feedback uncertainties in climate models. Geophys. Res. Lett., 32, L20806, doi:10.1029/2005GL023851.

Bony, S., R. Colman, V. M. Kattsov, R. P. Allan, C. S. Bretherton, J.-L. Dufresne, A. Hall, S. Hallegatte, M. M. Holland, W. Ingram, D. A. Randall, B. J. Soden, G. Tselioudis, M. J. Webb, 2006: How well do we understand and evaluate climate change feedback processes? J. Climate, 19, 3445-3482.

Bretherton, C. S., 1992: A conceptual model of the stratocumulus-trade-cumulus transition in the subtropical oceans. Proc. 11th Int. Conf. on Clouds and Precipitation, Vol. I, Montreal, Quebec, Canada, Int. Comm. Clouds and Precipitation, 374-377.

Bretherton, C. S., and M. C. Wyant, 1997: Moisture. transport, lower troposphere stability, and decoupling of cloud-topped boundary. J. Atmos. Sci., 54, 148–167.

Bretherton, C. S., S. K. Krueger, M. C. Wyant, P. Bechtold, E. van Meijgaard, B. Stevens, and J. Teixeira, 1999: A GCSS boundary layer model intercomparison study of the first ASTEX Lagrangian experiment. Bound.-Layer Meteor., 93, 341–380.

Bretherton, C. S., T. Uttal, C. W. Fairall, S. E. Yuter, R. A. Weller, D. Baumgardner, K. Comstock, R. Wood, and G. B. Raga, 2004a: The EPIC 2001 stratocumulus study. Bull. Amer. Meteor. Soc., 85, 967-977.

Bretherton, C. S., J. R. McCaa, and H. Grenier, 2004b: A new parameterization for shallow cumulus convection and its application to marine subtropical cloud-topped boundary layers. Part I: Description and 1D results. Mon. Wea. Rev., 132, 864–882.

Bretherton, C. S., and S. Park, 2009: A new moist turbulence parameterization in the Community Atmosphere Model. J. Climate, 22, 3422–3448.

Brown, A. R., R. T. Cederwall, A. Chlond, P. G. Duynkerke, J. C. Golaz, J. M. Khairoutdinov, D. C. Lewellen, A. P. Lock, M. K. Macvean, C. H. Moeng, R. A. J. Neggers, A. P. Siebesma, and B. Stevens, 2002: Large eddy simulation of the diurnal cycle of shallow cumulus convection over land. Quart. J. Roy. Meteor. Soc., 128, 1075-1094.

Browning, K. A., A. Betts, P. R. Jonas, R. Kershaw, M. Manton, P. J. Mason, M. Miller, M. W. Moncrieff, H. Sundqvist, W. K. Tao, M. Tiedtke, P. V. Hobbs, J. Mitchell, E. Raschke, R. E. Stewart, and J. Simpson, 1993: The GEWEX Cloud System Study (GCSS). Bull. Amer. Meteor. Soc., 74, 387–399.

Browning, K. A., and Coauthors, 1994: GEWEX Cloud System Study (GCSS) science plan. IG PO Publ. Series No. 11, World Climate Research Programme, Geneva, Switzerland, 62 pp. and 3 appendixes.

Cess, R. D., G. L. Potter, J. P. Blanchet, G. J. Boer, S. J. Ghan, J. T. Kiehl, H. Le Treut, Z.-X. Liang, J. F. B. Mitchell, J.-J. Morcrette, D. A. Randall, M. R. Riches, E. Reockner, U. Schlese, A. Slingo, K. E. Taylor. W. M. Washington, R. T. Wetherald, and I. Yagai, 1989: Interpretation of cloud-climate feedback as produced by 14 atmospheric general circulation models. Science, 245, 513-516.

Cess, R. D., M. H. Zhang, W. J. Ingram, G. L. Potter, V. Alekseev, H. W. Barker, E. Cohen-Solal, R. A. Colman, D. A. Dazlich, A. D. Del Genio, M. R. Dix, V. Dymnikov, M. Esch, L. D. Fowler, J. R. Fraser, V. Galin, W. L. Gates, J. J. Hack, J. T. Kiehl, H. Le Treut, K. K.-W. Lo, B. J. McAvaney, V. P. Meleshko, J.-J. Morcrette, D. A. Randall, E. Roeckner, J.-F. Royer, M. E. Schelsinger, P. V. Sporyshev, B. Timbal, E. M. Volodin, K. E. Taylor, W. Wang, and R. T. Wetherald, 1996: Cloud feedback in atmospheric general circulation models: An update. J. Geophys. Res., 101, 12791-12794, doi:10.1029/96JD00822.

Cess, R. D., M. H. Zhang, G. L. Potter, V. Alekseev, H. W. Barker, S. Bony, R. A. Colman, D. A. Dazlich, A. D. Del Genio, M. Déqué, M. R. Dix, V. Dymnikov, M. Esch, L. D. Fowler, J. R. Fraser, V. Galin, W. L. Gates, J. J. Hack, W. J. Ingram, J. T. Kiehl, Y. Kim, H. Le Treut, X.-Z. Liang, B. J. McAvaney, V. P. Meleshko, J. J. Morcrette, D. A. Randall, E. Roeckner, M. E. Schlesinger, P. V. Sporyshev, K. E. Taylor, B. Timbal, E. M. Volodin, W. Wang, W. C. Wang, and R. T. Wetherald, 1997: Comparison of the seasonal change in cloud-radiative forcing from atmospheric general circulation models and satellite observations. J. Geophys. Res., 102, 16593-16603, 1997.

Cheinet, S., and J. Teixeira, 2003:Asimple formulation for the eddydiffusivity parameterization of cloud-topped boundary layers. Geophys. Res. Lett., 30, 1930, doi:10.1029/2003GL017377.

Chylek, P., U. Lohmann, M. Dubey, M. Mishchenko, R. Kahn, and A. Ohmura, 2007: Limits on climate sensitivity derived from recent satellite and surface observations. J. Geophys. Res., 112, D24S04, doi:10.1029/2007JD008740.

Clement, A., and R. Seager, 1999: Climate and the tropical oceans. J. Climate, 12, 3383-3401.

Collins, W. D., P. J. Rasch, B. A. Boville, J. J. Hack, J. R. McCaa, D. L. Williamson, B. P. Briegleb, C. M. Bitz, S.-J. Lin, and M. Zhang, 2006: The formulation and atmospheric simulation of the Community Atmosphere Model: CAM3. J. Climate, 19, 2144–2161.

Colorado State University, cited 2010: BUGS documentation. [Available online at http://kiwi.atmos.colostate.edu/BUGS/.]

Côté, J., S. Gravel, A. Méthot, A. Patoine, M. Roch, and A. Staniforth, 1998: The operational CMCMRB Global Environment Multiscale (GEM) model. Part I: Design considerations and formulation. Mon. Wea. Rev., 126, 1373–1395.

Cuijpers, J. W. M., and P. Bechtold, 1995: A simple parameterization of cloud water related variables for use in boundary layer models. J. Atmos. Sci., 52, 2486-2490.

Curry, J. A., E. E. Ebert, and G. F. Herman, 1988: Mean and turbulence structure of the summertime Arctic cloud boundary layer. Quart. J. Roy. Meteor. Soc., 114, 715-746.

Davies, R., Á. Horváth, C. Moroney, B. Zhang, and Y. Zhu, 2007: Cloud motion vectors from MISR using sub-pixel enhancements. Remote Sens. Environ., 107, 194–199.

De Roode, S. R., and P. G. Duynkerke, 1997: Observed lagrangian transition of stratocumulus into cumulus during astex: mean state and turbulence structure. J. Atmos. Sci., 54, 2157-2173.

Deardorff, J. W., 1980: Cloud top entrainment instability. J. Atmos. Sci., 37, 131–147.

Del Genio, A. D., M. S. Yao, W. Kovari, and K. W. W. Lo, 1996: A prognostic cloud water parameterization for global climate models. J. Climate, 9, 270–304.

Divakarla, M. G., C. D. Barnet, M. D. Goldberg, L. M. McMillin, E. Maddy, W. Wolf, L. Zhou, and X. Liu, 2006: Validation of Atmospheric Infrared Sounder temperature and

water vapor retrievals with matched radiosonde measurements and forecasts. J. Geophys. Res., 111, D09S15, doi:10.1029/2005JD006116.

Duynkerke, P. G., and A. Driedonks, 1987: A model for the turbulent structure of the stratocumulus-topped atmospheric boundary layer. J. Atmos. Sci., 44, 43-64.

Duynkerke, P. G., 1998: Modelling of Amtospheric Boundary layers. In Clear and Cloudy Boundary Layers, eds. A. A. M. Holtslag and P. G. Duynkerke, 85-110.

Duynkerke, P. G., P. Jonker, A. Chlond, M. C. van Zanten, J. Cuxart, P. Clark, E. Sanchez, G. Martin, G. Lenderink, and J. Teixeira, 1999: Intercomparison of three- and one-dimensional model simulations and aircraft observations of stratocumulus. Bound.-Layer Meteor., 92, 453-487.

Duynkerke, P. G., and J. Teixeira, 2001: A comparison of the ECMWF Reanalysis with FIRE I observations: diurnal variation of marine stratocumulus. J. Climate, 14, 1466-1478.

Environmental Modeling Center, 2003: The GFS Atmospheric Model. National Centers for Environmental Prediction, Washington D.C., NCEP Office Note 442.

European Centre for Medium-Range Weather Forecasts, cited 2006: The ECMWFintegrated forecast system documentation CY31r1. [Available online at http://www.ecmwf.int/research/ifsdocs/CY31r1/index.html.]

Fetzer, E. J., L. McMillin, D. Tobin, H. H. Aumann, M. R. Gunson, W. W. McMillan, D. E. Hagan, M. D. Hofstadter, J. Yoe, D. Whiteman, J. Barnes, R. Bennartz, H. Vömel, V. Walden, M. Newchurchm P. Minnett, R. Atlas, F. Schmidlin, E. T. Olsen, M. Goldberg, S, Zhou, H. Ding, W. Smith, Sr., and H. Revercomb, 2003: AIRS/AMSU/HSB validation, IEEE Trans. Geosci. Remote Sens., 41, 418-431.

Fetzer, E. J., J. Teixeira, E. T. Olsen, and E. F. Fishbein, 2004: Satellite remote sounding of atmospheric boundary layer temperature inversions over the subtropical eastern Pacific. Geophys. Res. Lett., 31, L17102, doi:10.1029/2004GL020174.

Fetzer, E. J., B. H. Lambrigtsen, A. Eldering, H. H. Aumann, and M. T. Chahine, 2006: Biases in total precipitable water vapor climatologies from Atmospheric Infrared Sounder and Advanced Microwave Scanning Radiometer. J. Geophys. Res., 111, D09S16, doi:10.1029/2005JD006598.

Fowler, L. D., D. A. Randall, and S. A. Rutledge, 1996: Liquid and ice cloud microphysics in the CSU general circulation model. Part 1: Model description and simulated microphysical processes. J. Climate, 9, 489–529.

French, J. R., G. Vali, and R. D. Kelly, 1999: Evolution of small cumulus clouds in Florida: observations of pulsating growth. Atmos. Res., 52, 143-165.

Garay, M. J., S. P. de Szoeke, and C. M. Moroney, 2008: Comparison of marine stratocumulus cloud top heights in the southeastern Pacific retrieved from satellites with coincident ship-based observations. J. Geophys. Res., 113, D18204, doi:10.1029/2008JD009975.

Garratt, J. R., 1992: The Atmospheric Boundary Layer. Cambridge University Press, 316 pp.

Gates, W. L., 1992: AMIP: The Atmospheric Model Intercomparison Project. Bull. Amer. Meteor. Soc., 73, 1962-1970.

Genkova, I., G. Seiz, P. Zuidema, G. Zhao, and L. Di Girolamo, 2007: Cloud top height comparisons from ASTER, MISR, and MODIS for trade wind cumuli. Remote Sens. Environ., 107, 211–222.

Gettelman, A., E. M. Weinstock, E. J. Fetzer, F. W. Irion, A. Eldering, E. C. Richard, K. H. Rosenlof, T. L. Thompson , J. V. Pittman, C. R.Webster, and R. L. Herman, 2004: Validation of Aqua satellite data in the upper troposphere and lower stratosphere with in situ aircraft instruments. Geophys. Res. Lett., 31, L22107, doi:10.1029/2004GL020730.

Gettelman, A., W. D. Collins, E. J. Fetzer, A. Eldering, F. W. Irion, P. B. Duffy, and G. Bala, 2006: Climatology of Upper-Tropospheric Relative Humidity from the Atmospheric Infrared Sounder and Implications for Climate. J. Climate, 19, 6104–6121. doi: http://dx.doi.org/10.1175/JCLI3956.1.

Gibelin, A., L. Déqué, and M. Dreveton, 2003: Anthropogenic climate change over the Mediterranean region simulated by a global variable resolution model. Climate Dyn., 20, 327–339.

Goff, J. A., and S. Gratch, 1946: Low-pressure properties of water from -160°F to 212°F. Trans. Amer. Soc. Heat. Vent. Eng., 52, 95-121.

Golaz, J.-C., V. E. Larson, and W. R. Cotton, 2002: A PDF-based model for boundary layer clouds. Part I: Method and model description. J. Atmos. Sci., 59, 3540–3551.

Gu, Y., J. D. Farrara, K. N. Liou, and C. R. Mechoso, 2003: Parameterization of cloud-radiative processes in the UCLA general circulation model. J. Climate, 16, 3357–3370.

Hannay, C., D. L. Williamson, J. J. Hack, J. T. Kiehl, J. G. Olson, S. A. Klein, C. S. Bretherton, and M. Köhler, 2009: Evaluation of forecasted southeast Pacific stratocumulus in the NCAR, GFDL, and ECMWF models. J. Climate, 22, 2871–2889.

Hanson, H., 1991: Marine stratocumulus climatologies. Int. J. Climatol., 11, 147-164.

Harrison, E. F., P. Minnis, B. R. Barkstrom, V. Ramanathan, R. D. Cess, and G. G. Gibson, 1990: Seasonal variation of cloud radiative forcing derived from the Earth Radiation Budget Experiment. J. Geophys. Res., 95 (D11), 18 687–18 703.

Hartmann, D., M. Ockert-Bell, and M. Michelsen, 1992: The effect of cloud type on Earth's energy balance: Global analysis. J. Climate, 5, 1281–1304.

Hartmann, D., M. Michelsen, 1993: Large-scale effects on the regulation of tropical sea surface temperature. J. Climate, 6, 2049–2062.

Herman, G., and R. Goody, 1976: Formation and persistence of summertime arctic stratus clouds. J. Atmos. Sci., 33, 1537-1553.

Hignett, P., 1991: Observations of the diurnal variation in a cloud-capped marine boundary layer. J. Atmos. Sci., 48, 1474-1482.

Holloway, J. L., Jr., and S. Manabe, 1971: Simulation of climate by a general circulation model. I. Hydrological cycle and heat balance. Mon. Wea. Rev., 99, 335-370.

Houghton, J. T., G. J. Jenkins, and J. J. Ephraums (eds.), 1990: Climate Change: The IPCC Scientific Assessment. Cambridge University Press, Cambridge, 365 pp.

Houghton, J. T., and S. K. Varney, 1992: Climate Change 1992. The Supplementary Report to the IPCC Scientific Assessment. Cambridge University Press, 200 pp.

Hourdin, F., I. Musat, S. Bony, P. Braconnot, F. Codron, J.-L. Dufresne, L. Fairhead, M.-A. Filiberti, P. Friedlingstein, J.-Y. Grandpeix, G. Krinner, P. LeVan, Z.-X. Li, and F. Lott, 2006: The LMDZ4 general circulation model: Climate performance and sensitivity to parametrized physics with emphasis on tropical convection. Climate Dyn., 27, 787–813.

Huffman, G. J., R. F. Adler, D. T. Bolvin, G. Gu, E. J. Nelkin, K. P. Bowman, Y. Hong, E. F. Stocker, D. B. Wolff, 2007: The TRMM Multi-satellite Precipitation Analysis: Quasi-Global, Multi-Year, Combined-Sensor Precipitation Estimates at Fine Scale. J. Hydrometeor., 8(1), 38-55.

Im, E., S. L. Durden, and C. Wu, 2006: Cloud profiling radar for the CloudSat mission. IEEE Aerosp. Electron. Syst. Mag., 20, 15–18.

Jain, A. K., and R. C. Dubes, 1988: Algorithms for Clustering Data. Prentice Hall Advanced Reference Series. Prentice Hall. Book available online at http://www.cse.msu.edu/~jain/Clustering_Jain_Dubes.pdf

Jakob, C., 1999: Cloud Cover in the ECMWF Re-Analysis. J. Climate, 12, 947-959.

Jakob, C., and G. Tselioudis, 2003: Objective identification of cloud regimes in the Tropical Western Pacific. Geophys. Res. Lett., 30, 2082, doi:10.1029/2003GL018367, 21.

Janowiak, J. E., A. Gruber, C. R. Kondragunta, R. E. Livezey, and G. J. Huffman, 1998: A comparison of the NCEP–NCAR reanalysis precipitation and the GPCP rain gauge–satellite combined dataset with observational error considerations. J. Climate, 11, 2960–2979.

Johns, T., C. Durman, H. Banks, M. Roberts, A. McLaren, J. Ridley, C. Senior, K. Williams, A. Jones, A. Keen, G. Rickard, S. Cusack, M. Joshi, M. Ringer, B. Dong, H. Spencer, R. Hill, J. Gregory, A. Pardaens, J. Lowe, A. Bodas-Salcedo, S. Stark, and Y. Searl, 2004: HadGEM1 – Model description and analysis of preliminary experiments for the IPCC Fourth Assessment Report. Hadley Centre for Climate Prediction and Research/Met Office Tech. Note 55, 74 pp.

Juang, H.-M., S. Y. Hong, and M. Kanamitsu, 1997: The NCEP regional spectral model: An update. Bull. Amer. Meteor. Soc., 78, 2125–2143.

Karlsson, J., G. Svensson, and H. Rodhe, 2008: Cloud radiative forcing of subtropical low level clouds in global models. Climate Dyn., 30, 779–788.

Karlsson, J., G. Svensson, S. Cardoso, J. Teixeira, and S. Paradise, 2010: Subtropical cloud regime transitions: Boundary layer depth and cloud-top height evolution. J. Appl. Meteor. Climatol., 49, 1845–1858.

Kawai, H., and J. Teixeira, 2010: Probability density functions of liquid water path of marine boundary layer clouds: Geographical and seasonal variations and controlling meteorological factors. J. Climate, 23, 2079–2092.

Khairoutdinov, M. F., D. A. Randall, and C. DeMott, 2005: Simulations of the atmospheric general circulation using a cloud-resolving model as a superparameterization of physical processes. J. Atmos. Sci., 62, 2136–2154.

Klein, S. A., and D. L. Hartmann, 1993: The seasonal cycle of low stratiform clouds. J. Climate, 6, 1587-1606.

Klein, S. A., D. L. Hartmann, and J. R. Norris, 1995: On the relationships among low-cloud structure, sea surface temperature, and atmospheric circulation in the summertime northeast Pacific. J. Climate, 8, 1140-1155.

Klein, S. A., and C. Jakob, 1999: Validation and sensitivities of frontal clouds simulated by the ECMWF model. Mon. Wea. Rev., 127, 2514–2531.

Köhler, M., 2005: Improved prediction of boundary layer clouds. ECMWF Newsletter, No. 104, ECMWF, Reading, United Kingdom, 18–22.

Kuettner, J. P., and J. Holland, 1969: The BOMEX project. Bull. Amer. Meteor. Soc., 50, 394-402.

Kuwano-Yoshida, A., T. Enomoto, and W. Ohfuchi, 2010: An improved PDF cloud scheme for climate simulations. Quart. J. Roy. Meteor. Soc., 136, 1583–1597.

Larson, K., D. Hartmann, and S. Klein, 1999: The role of clouds, water vapor, circulation, and boundary layer structure in the sensitivity of the tropical climate. J. Climate, 12, 2359–2374.

Lenderink, G., and A.A.M. Holtslag, 2000: Evaluation of of the kinetic energy approach for modelling turbulent fluxes in stratocumulus. Mon. Wea. Rev, 128, 244-258.

Lenderink, G., and A. A. M. Holtslag, 2004: An updated length scale formulation for turbulent mixing in clear and cloudy boundary layers. Quart. J. Roy. Meteor. Soc., 130, 3405–3427.

Li, J.-L. F., D. Waliser, C. Woods, J. Teixeira, J. Bacmeister, J. Chern, B.-W. Shen, A. Tompkins, W.-K. Tao, and M. Köhler, 2008: Comparisons of satellites liquid water estimates to ECMWF and GMAO analyses, 20th century IPCC AR4 climate simulations, and GCM simulations. Geophys. Res. Lett., 35, L19710, doi:10.1029/2008GL035427.

Lilly, D. K., 1968: Models of cloud-topped mixed layers under a strong inversion. Quart. J. Roy. Meteor. Soc., 94, 292–309.

Lin, W., M. Zhang, and N. G. Loeb, 2009: Seasonal variation of the physical properties of marine boundary layer clouds off the California coast. J. Climate, 22, 2624–2638.

Lindzen, R. S., M. D. Chou, and A. Y. Hou, 2001: Does the Earth have an adaptative infrared iris? Bull. Amer. Meteor. Soc., 82, 417–432.

Lock, A. P., A. R. Brown, M. R. Bush, G. M. Martin, and R. N. B. Smith, 2000: A new boundary layer mixing scheme. Part I: Scheme description and SCM tests. Mon. Wea. Rev., 128, 3187–3199.

Lock, A. P., 2001: The numerical representation of entrainment in parameterizations of boundary layer turbulent mixing. Mon. Wea. Rev., 129, 1148–1163.

Ma, C.-C., C. R. Mechoso, A. W. Robertson, and A. Arakawa, 1996: Peruvian stratus clouds and the tropical Pacific circulation: A coupled ocean–atmosphere GCM study. J. Climate, 9, 1635–1645.

Majewski, D., D. Liermann, P. Prohl, B. Ritter, M. Buchhold, T. Hanisch, G. Paul, W. Wergen, and J. Baumgardner, 2002: Icosahedral-hexagonal gridpoint model GME: description and high-resolution tests. Mon. Weather Rev., 130, 319-338.

Mace, G. G., R. Marchand, and G. L. Stephens, 2007a: Global Hydrometeor Occurrence as Observed by CloudSat; Initial Observations from Summer 2006. Geophys. Res. Lett., 34, L09808, doi:10.1029/2006GL029017.

Mace, G. G., Q. Zhang, M. Vaughn, R. Marchand, G. Stephens, C. Trepte, and D. Winker, 2007b: A Description of Hydrometeor Layer Occurrence Statistics Derived from the First Year of Merged CloudSat and CALIPSO Data. J. Geophys. Res., 114, D00A26, doi:10.1029/2007JD009755.

Marshak, A., A. Davis, and W. Wiscombe, 1995: Radiation smoothing in fractal clouds. J. Geophys. Res., 100, 26247-26261.

Martins, J. P. A., J. Teixeira, P. M. M. Soares, P. M. A. Miranda, B. H. Kahn, V. T. Dang, F. W. Irion, E. J. Fetzer, and E. Fishbein, 2010: Infrared sounding of the trade-wind

boundary layer: AIRS and the RICO experiment. Geophys. Res. Lett., 37, L24806, doi:10.1029/2010GL045902.

Matsumura, T., M. Ohizumi, H. Kitagawa, and M. Nakagawa, 2002: Outline of the operational numerical weather prediction at the Japan Meteorological Agency-Global Spectral Model (JMA GSM). Japan Meteorological Agency Rep. JMA-GSM0103.

Mauger, G. S., and J. R. Norris, 2010: Assessing the impact of meteorological history on subtropical cloud fraction. J. Climate, 23, 2926-2940.

McMillin, L. M., J. Zhao, M. K. Rama Varma Raja, S. I. Gutman, and J. G. Yoe, 2007: Radiosonde humidity corrections and potential Atmospheric Infrared Sounder moisture accuracy. J. Geophys. Res., 112, D13S90, doi:10.1029/2005JD006109.

McNally, A. P., P. D. Watts, J. A. Smith, R. Engelen, G. A. Kelly, J. N. Thépaut, and M. Matricardi, 2006: The assimilation of AIRS radiance data at ECMWF. Quart. J. Roy. Meteor. Soc., 132, 935–957.

Mellor, G. L., 1977: The gaussian cloud model relations. J. Atmos. Sci., 34, 356-358.

Minnis, P., P. W. Heck, D. F. Young, C. W. Fairall, and J. B. Snider, 1992: Stratocumulus cloud properties derived from simultaneous satellite and island-based instrumentation during FIRE. J. Appl. Meteor., 31, 317–339.

Moeng, C.-H., W. R. Cotton, C. S. Bretherton, A. Chlond, M. H. Khairoutdinov, S. Krueger, W. S. Lewellen, M. K. MacVean, J. R. M. Pasquier, H. A. Rand, A. P. Siebesma, R. I. Sykes and B. Stevens, 1996: Simulation of a stratocumulus-topped PBL: Intercomparison among different numerical codes. Bull. Amer. Meteor. Soc., 77, 261-278.

Moroney, C., R. Davies, and J.-P. Muller, 2002: Operational retrieval of cloud-top heights using MISR data. IEEE Trans. Geosci. Remote Sens., 40, 1532–1540.

Muller, J.-P., A. Mandanayake, C. Moroney, R. Davies, D. J. Diner, and S. Paradise, 2002: MISR stereoscopic image matchers: Techniques and results. IEEE Trans. Geosci. Remote Sens., 40, 1547–1559.

Naud, C., J.-P. Muller, M. Haeffelin,Y.Morille, and A. Delaval, 2004: Assessment of MISR and MODIS cloud top heights through inter-comparison with a back-scattering lidar at SIRTA. Geophys. Res. Lett., 31, L04114, doi:10.1029/2003GL018976.

Neggers, R. A. J., A. P. Siebesma, G. Lenderink, and A. A. M. Holtslag, 2004: An evaluation of mass flux closures for diurnal cycles of shallow cumulus convection. Mon. Wea. Rev., 132, 2526-2538.

Neiburger, M., D. S. Johnson, and C. Chien, 1961: Studies of the Structure of the Atmosphere over the Eastern Pacific Ocean in Summer. I: The inversion over the Eastern North Pacific Ocean. University of California Press, 94 pp.

Paluch, I. R., and D. H. Lenschow, 1991: Stratiform cloud formation in themarine boundary layer. J. Atmos. Sci., 48, 2141–2158.

Philander, S. G., D. Gu, D. Halpern, G. Lambert, N.-C. Lau, T. Li, and R. C. Pacanowski, 1996: Why the ITCZ is mostly north of the Equator. J. Climate, 9, 2958–2972.

Plummer, D., D. Caya, H. Côté, A. Frigon, S. Biner, M. Giguère, D. Paquin, R. Harvey and R. de Elia, 2006: Climate and Climate Change over North America as Simulated by the Canadian Regional Climate Model. J. Climate 19, 3112-3132

Potter, G. L., and R. D. Cess, 2004: Testing the impact of clouds on the radiation budgets of 19 AMIP models. J. Geophys. Res., 109, D02106, doi:10.1029/2003JD004018.

Ramanathan, V., 1987: The role of Earth radiation budget studies in climate and general circulation research. J. Geophys. Res., 92, 4075-4094.

Ramanathan, V., R. D. Cess, E. F. Harrison, P. Minnis, B. R. Barkstrom, E. Ahmad, and D. Hartmann, 1989: Cloud-radiative forcing and climate: Results from the Earth Radiation Budget Experiment. Science, 243, 57–63.

Randall, D. A., 1980: Conditional instability of the first kind upsidedown. J. Atmos. Sci., 37, 125–130.

Randall. D. A., J. A. Coakley Jr., C. W. Fairall, R. A. Kropfli, and D. H. Lenschow, 1984: Outook for research on subtropical marine stratiform clouds. Bull. Amer. Meteor. Soc., 65, 1290-1301.

Randall, D. A., 1989: Cloud parameterization for climate modeling: Status and prospects. Atmos. Res., 23, 245-361.

Randall, D. A., J. Curry, P. G. Duynkerke, S. Krueger, B. Ryan, D. Starr, M. Miller, W. B. Rossow, and B. A. Wielicki, 2003: Confronting models with data: The GEWEX Cloud Systems Study. Bull. Amer. Meteor. Soc., 84, 455-469.

Rasch, P. J., and J. E. Kristjánsson, 1998: A comparison of the CCM3 model climate using diagnosed and predicted condensate parameterizations. J. Climate, 11, 1587–1614.

Rauber, R. M., B. Stevens, H. T. Ochs, C. Knight, B. A. Albrecht, A. M. Blyth, C. W. Fairall, J. B. Jensen, S. G. Lasher-Trapp, O. L. Mayol-Bracero, G. Vali, J. R. Anderson, B. A. Baker, A. R. Bandy, E. Burnet, J. L. Brenguier, W. A. Brewer, P. R. A. Brown, P. Chuang, W. R. Cotton, L. Di Girolamo, B. Geerts, H. Gerber, S. Göke, L. Gomes, B. G. Heikes, J. G. Hudson, P. Kollias, R. P. Lawson, S. K. Krueger, D. H. Lenschow, L. Nuijens, D. W. O'Sullivan, R. A. Rilling, D. C. Rogers, A. P. Siebesma, E. Snodgrass, J. L. Stith, D. C. Thornton, S. Tucker, C. H. Twohy, and P. Zuidema, 2007: Rain in Shallow Cumulus Over the Ocean: The RICO Campaign. Bull. Amer. Meteor. Soc., 88, 1912–1928.

Redelsperger, J. L, P. R. A. Brown, F. Guichard, C. Hoff, M. Kawasima, S. Lang, Th. Montmerle, K. Nakamura, K. Saito, C. Seman, W. K. Tao, and L. J. Donner, 2000: A GCSS model intercomparison for a tropical squall line observed during TOGA-COARE. Part I: Cloud resolving models. Quart. J. Roy. Meteor. Soc., 126, 823-863.

Riehl, H., C. Yeh, J. S. Malkus, and N. E. LaSeur, 1951: The northeast trade of the Pacific Ocean. Quart. J. Roy. Meteor. Soc., 77, 598–626.

Roeckner, E., G. Baeuml, L. Bonaventura, R. Brokopf, M. Esch, M. Giorgetta, S. Hagemann, I. Kirchner, L. Kornblueh, E. Manzini, A. Rhodin, U. Schlese, U. Schulzweida, and A. Tompkins, 2003: The atmospheric general circulation model ECHAM5. Part I: Model description. Max-Planck-Institut für Meteorologie Rep. 349, 127 pp.

Rossow, W. B., and R. A. Schiffer, 1991: ISCCP cloud data products. Bull. Amer. Meteor. Soc., 72, 2–20.

Rossow, W. B., and R. A. Schiffer, 1999: Advances in understanding clouds from ISCCP. Bull. Amer. Meteor. Soc., 80, 2261–2287.

Rossow, W. B., G. Tselioudis, A. Polak, and C. Jakob, 2005: Tropical climate described as a distribution of weather states indicated by distinct mesoscale cloud property mixtures. Geophys. Res. Lett., 32, L21812, doi:10.1029/2005GL024584.

Rozendaal, M., C. Leovy, and S. A. Klein, 1995: An observational study of diurnal variations of marine stratiform cloud. J. Climate, 8, 1795-1809

Saha, S., S. Nadiga, C. Thiaw, J. Wang, W. Wang, Q. Zhang, H. M. van den Dool, H.-L. Pan, S. Moorthi, D. Behringer, D. Stokes, M. Pena, S. Lord, G. White, W. Ebisuzaki, P. Peng, and P. Xie, 2006: The NCEP Climate Forecast System. J. Climate, 19, 3483-3517.

Sandu, I., B. Stevens, and R. Pincus, 2010: On the transitions in marine boundary layer cloudiness. Atmos. Chem. Phys., 10, 2377-2391, doi:10.5194/acp-10-2377-2010.

Schmidt, G. A., R. Ruedy, J. E. Hansen, I. Aleinov, N. Bell, M. Bauer, S. Bauer, B. Cairns, V. Canuto, Y. Cheng, A. Del Genio, G. Faluvegi, A. D. Friend, T. M. Hall, Y. Hu, M. Kelley, N. Y. Kiang, D. Koch, A. A. Lacis, J. Lerner, K. K. Lo, R. L. Miller, L. Nazarenko, V. Oinas, J. P. Perlwitz, Ju. Perlwitz, D. Rind, A. Romanou, G. L. Russell, Mki. Sato, D. T. Shindell, P. H. Stone, S. Sun, N. Tausnev, D. Thresher, and M.-S. Yao, 2006: Present day atmospheric simulations using GISS ModelE: Comparison to in-situ, satellite and reanalysis data. J. Climate, 19, 153-192, doi:10.1175/JCLI3612.1.

Seibert, P., F. Beyrich, S.-E. Gryning, S. Joffre, A. Rasmussen, and P. Tercier, 2000: Review and intercomparison of operational methods for the determination of the mixing height. Atmos. Environ., 34, 1001–1027.

Siebesma, A. P., and J. W. M. Cuijpers, 1995: Evaluation of parametric assumptions for shallow cumulus convection. J. Atmos. Sci., 52, 650-666.

Siebesma, A. P., 1998: Shallow Cumulus Convection. In E. J. Plate et al. (eds.): Buoyant Convection in Geophysical Flows. Kluwer Academic Publishers, 441-486.

Siebesma, A. P., C. S. Bretherton, A. Brown, A. Chlond, J. Cuxart, P. Duynkerke, V. Grubisic, H. Jiang, M. Khairoutdinov, D. Lewellen, C.-H. Moeng, B. Stevens, and D. E. Stevens, 2003: A large-eddy intercomparison study of shallow cumulus convection. J. Atmos. Sci., 60, 1201-1219.

Siebesma, A. P., C. Jacob, G. Lenderink, R. Neggers, J. Teixera, J. Calvo, A. Chlond, H. Grenier, C. Jones, M. Köhler, H. Kitagawa, P. Marquet, A. P. Lock, F. Müller, D. Olmeda, C. Serverijns, 2004: Cloud representation in General Circulation Models over the Northern Pacific Ocean: A EUROCS intercomparison study. Quart. J. Roy. Meteor. Soc., 130, 3245- 3267.

Siems, S.T., 1991: A numerical Investigation of Cloud Top Entrainment Instability and Related Experiments, Ph.D. Dissertation, Department of Applied Mathematics, University of Washington, 116 pp.

Slingo, J. M., 1980: A cloud parameterization scheme derived from GATE data for use with a numerical model. Quart. J. Roy. Meteor. Soc., 106, 747–770.

Slingo, J. M., 1987: The development and verification of a cloud prediction scheme in the ECMWF model. Quart. J. Roy. Meteor. Soc., 113, 899–927.

Smith, R. N. B., 1984: An integrated approach to the representation of cloud processes. ECMWF workshop on Cloud Cover Parameterization in Numerical Models. November 1984, Reading, UK. 233-247.

Smith, S. A., and P. R. Jonas, 1995: Observations of the turbulent fluxes in fields of cumulus clouds. Quart. J. Roy. Meteor. Soc., 121, 1185-1208.

Soares, P. M. M., P. M. A. Miranda, A. P. Siebesma, and J. Teixeira, 2004: An eddy-diffusivity/mass-flux scheme for dry and shallow convection. Quart. J. Roy. Meteor. Soc., 130, 3365–3384.

Solomon, S., D. Qin, M. Manning, M. Marquis, K. Averyt, M. M. B. Tignor, H. L. Miller Jr., and Z. Chen (eds.), 2007: Climate Change 2007: The Physical Science Basis. Cambridge University Press, 996 pp.

Sommeria, G., 1976: Three-dimensional simulation of turbulent processes in an undisturbed Trade-wind boundary layer. J. Atmos. Sci., 33, 216-241.

Sommeria, G. and J. W. Deardorff, 1977: Subgrid-scale condensation in models of nonprecipitating clouds. J. Atmos. Sci., 34, 344-355.

Steppeler, J., G. Doms, U. Schättler, H. W. Bitzer, A. Gassmann, U. Damrath, and G. Gregoric, 2003: Meso-gamma scale forecasts using the nonhydrostatic model LM. Meteor. Atmos. Phys., 82, 75–96.

Stephens, G. L., D. G. Vane, R. J. Boain, G. G. Mace, K. Sassen, Z. Wang, A. J. Illingworth, E. J. O'Connor, W. B. Rossow, S. L. Durden, S. D. Miller, R. T. Austin, A. Benedetti, C. Mitrescu, and the CloudSat Science Team, 2002: The CloudSat mission and the A-Train. Bull. Amer. Meteor. Soc., 83, 1771–1790.

Stephens, G. L., 2005: Cloud feedbacks in the climate system: A critical review. J. Climate, 18, 237–273.

Stephens, G. L., D. Vane, S. Tanelli, E. Im, S. Durden, M. Rokey, D. Reinke, P. Partain, G. Mace, R. Austin, T. L'Ecuyer, J. Haynes, M. Lebsock, K. Suzuki, D. E. Waliser, D. Wu, J. Kay, A. Gettleman, Z. Wang, 2008: The CloudSat Mission: Performance of early science after the first year of operation. J. Geophys. Res., 113, D00A18, doi:10.1029/2008JD009982.

Stevens, B., W. R. Cotton, G. Feingold and C.-H. Moeng, 1998: Large-eddy simulations of strongly precipitanting, shallow, stratocumulus-topped boundary layers. J. Atmos. Sci., 55, 3616-3638.

Stevens, B., 2000: Cloud-transitions and decoupling in shear-free stratocumulus topped boundary layers. Geophys. Res. Lett., 27, 2557–2560.

Stevens, B., A. S. Ackerman, B. A. Albrecht, A. R. Brown, A. Chlond, J. Cuxart, P. G. Duynkerke, D. C. Lewellen, M. K. MacVean, R. A. J. Neggers, E. Sanchez, and D. E. Stevens, 2001: Simulations of trade- wind cumuli under a strong inversion. J. Atmos. Sci., 58, 1870-1891.

Stevens, B., D.H. Lenschow, G. Vali, H. Gerber, A. Bandy, B. Blomquist, J.-L. Brenguier, C.S. Bretherton, F. Burnet, T. Campos, S. Chai, L. Faloona, D. Friensen, S. Haimov, K. Laursen, D.K. Lilly, S.M. Loehrer, S.P. Malinowski, B. Morely, M.D. Peners, D.C. Rogers, L. Russell, V. Savic-Jovcic, J.R. Snider, D. Straub, M.J. Szumoswki, H. Takagi, D.C. Thorton, M. Tshudi, C. Twohy, M. Wetzel, and M.C. Van Zanten, 2003: Dynamics and chemistry of marine stratocumulus - DYCOMS-II. Bull., Amer. Meteor. Soc., 84, 579-593.

Stevens, B., 2005: Atmospheric moist convection. Annu. Rev. Earth Planet. Sci., 33, 605-643.

Stevens, B., A. Beljaars, S. Bordoni, C. Holloway, M. Köhler, S. Krueger, V. Savic-Jovcic, and Y. Zhang, 2007: On the structure of the lower troposphere in the summertime stratocumulus regime of the northeast Pacific. Mon. Wea. Rev., 135, 985–1005.

Stubenrauch, C. J., W. B. Rossow, F. Chéruy, A. Chédin, and N. A. Scott, 1999: Clouds as seen by satellite sounders (3I) and imagers (ISCCP). Part I: Evaluation of cloud parameters. J. Climate, 12, 2189–2213.

Sundqvist, H., 1988: Parametrization of condensation and associated clouds in models for weather prediction and general circulation simulation. In Physically-Based Modelling and Simulation of Climate and Climate Change, M.E. Schlesinger (ed.), Kluwer, 433-461.

Susskind, J., C. D. Barnet, and J. M. Blaisdell, 2003: Retrieval of atmospheric and surface parameters from AIRS/AMSU/HSB data in the presence of clouds. IEEE Trans. Geosci. Remote Sens., 41, 390-409.

Tan, P.-N., M. Steinbach, and V. Kumar, 2005: Introduction to Data Mining. Addison-Wesley, 769 pp.

Teixeira, J., 1999: Simulation of Fog with the ECMWF Prognostic Cloud Scheme. Quart. J. Roy. Meteor. Soc., 125, 529-553.

Teixeira, J., 2000: Boundary layer clouds in large scale atmospheric models: cloud schemes and numerical aspects. ECMWF, United Kingdom, 190 pp.

Teixeira, J., and T. F. Hogan, 2002: Boundary layer clouds in a global atmospheric model: Simple cloud cover parameterizations. J. Climate, 15, 1261–1276.

Teixeira, J., S. Cardoso, A. P. Siebesma, and the GPCI Team, 2008a: Results from the First 2 Years of the GCSS Pacific Cross Section Intercomparison. GEWEX News, No. 18(4), International GEWEX Project Office, Silver Spring, MD, 1–4.

Teixeira, J., B. Stevens, C. S. Bretherton, R. Cederwall, J. D. Doyle, J. C. Golaz, A. Holtslag, S. Klein, J. Lundquist, D. A. Randall, A. P. Siebesma, and P. M. M. Soares, 2008b: Parameterization of the atmospheric boundary layer: A view from just above the inversion. Bull. Amer. Meteor. Soc., 89, 453-458.

Teixeira, J., S. Cardoso, M. Bonazzola, J. Cole, A. DelGenio, C. DeMott, C. Franklin, C. Hannay, C. Jakob, Y. Jiao, J. Karlsson, H. Kitagawa, M. Köhler, A. Kuwano-Yoshida, C. LeDrian, J. Li, A. Lock, M. J. Miller, P. Marquet, J. Martins, C. R. Mechoso, E. van Meijgaard, I. Meinke, P. M. A. Miranda, D. Mironov, R. Neggers, H. L. Pan, D. A. Randall, P. J. Rasch, B. Rockel, W. B. Rossow, B. Ritter, A. P. Siebesma, P. M. M. Soares, F. J. Turk, P. A. Vaillancourt, A. Von Engeln, and M. Zhao, 2011: Tropical and Subtropical Cloud Transitions in Weather and Climate Prediction Models: The GCSS/WGNE Pacific Cross-Section Intercomparison (GPCI). J. Climate, 24, 5223–5256.

Tiedtke, M., 1987: The parameterization of moist processes. Part 2: The parameterization of cumulus convection. ECMWF Lecture Series, 56 pp.

Tiedtke, M., 1991: Aspects of cumulus parametrization. Proc. ECMWF Seminar on Tropical Extra-Tropical Interactions, Reading, United Kingdom, ECMWF, 441-466.

Tiedtke, M., 1993: Representation of Clouds in Large-Scale Models. Mon. Wea. Rev., 121, 3040-3061.

Tobin, D. C., H. E. Revercomb, R. O. Knuteson, B. M. Lesht, L. L. Strow, S. E. Hannon, W. F. Feltz, L. A. Moy, E. J. Fetzer, and T. S. Cress, 2006: Atmospheric Radiation Measurement site atmospheric state best estimates for Atmospheric Infrared Sounder

temperature and water vapor retrieval validation. J. Geophys. Res., 111, D09S14, doi:10.1029/2005JD006103.

Tompkins, A. M., 2002: A prognostic parameterization for the subgrid-scale variability of water vapor and clouds in largescale models and its use to diagnose cloud cover. J. Atmos. Sci., 59, 1917–1942.

Uppala, S. M., P. W. Kållberg, A. J. Simmons, U. Andrae, V. da Costa Bechtold, M. Fiorino, J. K Gibson, J. Haseler, A. Hernandez, G. A. Kelly, X. Li, K. Onogi, S. Saarinen, N. Sokka, R. P. Allan, E. Andersson, K. Arpe, M. A. Balmaseda, A. C. M. Beljaars, L. van de Berg, J. Bidlot, N.Bormann, S. Caires, A. Dethof, M. Dragosavac, M. Fisher, M. Fuentes, S. Hagemann, E. Hólm, B. J. Hoskins, L. Isaksen, P. A. E. M. Janssen, A. P. McNally, J.-F. Mahfouf, R. Jenne, J.-J. Morcrette, N. A. Rayner, R. W. Saunders, P. Simon, A. Sterl, K. E. Trenberth, A. Untch, D. Vasiljevic, P. Viterbo, and J. Woollen, 2005: The ERA-40 reanalysis. Quart. J. Roy. Meteor. Soc., 131, 2961-3012.

van Meijgaard, E., and A.P. van Ulden, 1998: A first order mixing-condensation scheme for nocturnal stratocumulus. Atmos. Res., 45, 253-273.

van Meijgaard, E., L.H. vanUlft, W. J. van den Berg, F. C. Bosveld, B. J. J. M. van den Hurk, G. Lenderink, and A. P. Siebesma, 2008: The KNMI regional atmospheric climatemodel RACMO, version 2.1. KNMI Tech. Rep. 302, 43 pp.

von Engeln, A., J. Teixeira, J. Wickert, and S. A. Buehler, 2005: Using CHAMP radio occultation data to determine the top altitude of the planetary boundary layer. Geophys. Res. Lett., 32, L06815, doi:10.1029/2004GL022168.

von Ficker, H., 1936: Die Passatinversion. Veröffentlichungen des Meteorologischen Institutes der Universitat Berlin, 33 pp.

von Salzen, K., N. A. McFarlane, and M. Lazare, 2005: The role of shallow convection in the water and energy cycles of the atmosphere. Climate Dyn., 25, 671–688.

Wang, S., B. A. Albrecht, and P. Minnis, 1993: A regional simulation of marine boundary layer clouds. J. Atmos. Sci., 50, 4022-4043.

Warner, J., 1977: Time variation of updrafts and water content in small cumulus clouds. J. Atmos. Sci., 34, 1306-1312.

Weare, B. C., 2004: A comparison of AMIP II model cloud layer properties with ISCCP D2 estimates. Climate Dyn., 22, 281–292.

Webb, M., C. Senior, S. Bony, and J.-J. Morcrette, 2001: Combining ERBE and ISCCP data to assess clouds in the Hadley Centre ECMWF and LMD atmospheric climate models. Climate Dyn., 17, 905–922.

Wielicki, B. A., R. D. Cess, M. D. King, D. A. Randall, and E. F. Harrison, 1995: Mission to planet earth: Role of clouds and radiation in climate. Bull. Amer. Meteor. Soc., 76, 2125–2153.

Winker, D. M., W. H. Hunt, and M. J. McGill, 2007: Initial performance assessment of CALIOP. Geophys. Res. Lett., 34, L19803, doi:10.1029/2007GL030135.

Wood, R., and C. S. Bretherton, 2004: Boundary layer depth, entrainment, and decoupling in the cloud-capped subtropical and tropical marine boundary layer. J. Climate, 17, 3576–3588.

Wood, R., and C. S. Bretherton, 2006: On the relationship between stratiform low cloud cover and lower-tropospheric stability. J. Climate, 19, 6425–6432.

Wyant, M. C., C. S. Bretherton, J. T. Bacmeister, J. T. Kiehl, I. M. Held, M. Zhao, S. A. Klein, and B. A. Soden, 2006: A comparison of low-latitude cloud properties and their response to climate change in three AGCMs sorted into regimes using mid-tropospheric vertical velocity. Climate Dyn., 27, 261-279.

Yamaguchi, T., and D. A. Randall, 2008: Large-eddy simulation of evaporatively driven entrainment in cloud-topped mixed layers. J. Atmos. Sci., 65, 1481–1504.

Zhang, M. H., W. Y. Lin, S. A. Klein, J. T. Bacmeister, S. Bony, R. T. Cederwall, A. D. Del Genio, J. J. Hack, N. G. Loeb, U. Lohmann, P. Minnis, I. Musat, R. Pincus, P.Stier, M. J. Suarez, M. J. Webb, J. B. Wu, S. C. Xie, M.-S. Yao, and J. H. Zhang, 2005: Comparing Clouds And Their Seasonal Variations in 10 Atmospheric General Circulation Models with Satellite Measurements. J. Geophys. Res., 110, D15S02, doi:10.1029/2004JD005021.

Zhang, Y., S. Klein, G. G. Mace, and J. Boyle, 2007: Cluster analysis of tropical clouds using CloudSat data. Geophys. Res. Lett., 34, L12813, doi:10.1029/2007GL029336.

Zhang, Y., S. A. Klein, J. Boyle, and G. G. Mace, 2010: Evaluation of tropical cloud and precipitation statistics of Community Atmosphere Model version 3 using CloudSat and CALIPSO data. J. Geophys. Res., 115, D12205, doi:10.1029/2009JD012006.

Zhao, G., and L. Di Girolamo, 2007: Statistics on the macrophysical properties of trade wind cumuli over the tropical western Atlantic. J. Geophys. Res., 112, D10204, doi:10.1029/2006JD007371.

Zhong, A., R. Colman, N. Smith, M. Naughton, L. Rikus, K. Puri, and F. Tseitkin, 2001: Ten-year AMIP-1 climatologies from versions of the BMRC atmospheric model. BMRC Research Rep. 83, 34 pp.

Zong, J., R. Davies, J.-P. Muller, and D. Diner, 2002: Photogrammetric retrieval of cloud advection and top height from the Multi-Angle Imaging Spectroradiometer (MISR). J.Amer. Soc. Photogramm. Eng. Remote Sens., 68, 821–829.

Zuidema, P., D. Painemal, S. De Szoeke, and C. Fairall, 2009: Stratocumulus cloud top height estimates and their climatic implications. J. Climate, 22, 4652–4666.

Appendix

A CD-ROM (SambingoCardoso_2013_PhDoutoramento) accompanies this thesis. It contains the following files:

SambingoCardoso_2013_PhDoutoramento_CV_Eng_Feb2013.pdf, with a Curriculum Vitae in English;

SambingoCardoso_2013_PhDoutoramento_CV_Port_Fev2013.pdf, with a Curriculum Vitae in Portuguese;

SambingoCardoso_2013_PhDoutoramento_Annex-1of4.pdf, with Teixeira et al. (2011)

Teixeira, J., S. Cardoso, M. Bonazzola, J. Cole, A. DelGenio, C. DeMott, C. Franklin, C. Hannay, C. Jakob, Y. Jiao, J. Karlsson, H. Kitagawa, M. Köhler, A. Kuwano-Yoshida, C. LeDrian, J. Li, A. Lock, M. J. Miller, P. Marquet, J. Martins, C. R. Mechoso, E. van Meijgaard, I. Meinke, P. M. A. Miranda, D. Mironov, R. Neggers, H. L. Pan, D. A. Randall, P. J. Rasch, B. Rockel, W. B. Rossow, B. Ritter, A. P. Siebesma, P. M. M. Soares, F. J. Turk, P. A. Vaillancourt, A. Von Engeln, and M. Zhao, 2011: Tropical and Subtropical Cloud Transitions in Weather and Climate Prediction Models: The GCSS/WGNE Pacific Cross-Section Intercomparison (GPCI). J. Climate, 24, 5223–5256;

SambingoCardoso_2013_PhDoutoramento_Annex-2of4.pdf, with Karlsson et al. (2010)

Karlsson, J., G. Svensson, S. Cardoso, J. Teixeira, and S. Paradise, 2010: Subtropical cloud regime transitions: Boundary layer depth and cloud-top height evolution. J. Appl. Meteor. Climatol., 49, 1845–1858;

SambingoCardoso_2013_PhDoutoramento_Annex-3of4.pdf, with Teixeira et al. (2008a)

Teixeira, J., S. Cardoso, A. P. Siebesma, and the GPCI Team, 2008a: Results from the First 2 Years of the GCSS Pacific Cross Section Intercomparison. GEWEX News, No. 18(4), International GEWEX Project Office, Silver Spring, MD, 1-4;

SambingoCardoso_2013_PhDoutoramento_Annex-4of4.pdf, with an introduction to GEPAT (Grade-based Empirical Pattern Analysis Technique);

SambingoCardoso_2013_PhDoutoramento_Thesis.pdf, with this thesis;

and

SambingoCardoso_2013_PhDoutoramento_Annex-0_AMS_copyright_policy_2010.pdf.